Title

Beam Steerable Antennas for CubeSats: Novel Synthesis Methods and Implementations of Reflectarrays and Transmitarrays

Author

Wang, Junbo

Publication Date

2023

Peer reviewed|Thesis/dissertation

UNIVERSITY OF CALIFORNIA

Los Angeles

Beam Steerable Antennas for CubeSats: Novel Synthesis Methods and Implementations of Reflectarrays and Transmitarrays

A dissertation submitted in partial satisfaction

of the requirements for the degree

Doctor of Philosophy in Electrical and Computer Engineering

by

Junbo Wang

2023

ABSTRACT OF THE DISSERTATION

Beam Steerable Antennas for CubeSats: Novel Synthesis Methods and Implementations of Reflectarrays and Transmitarrays

by

Junbo Wang
Doctor of Philosophy in Electrical and Computer Engineering
University of California, Los Angeles, 2023
Professor Yahya Rahmat-Samii, Chair

The advent of low-cost and lightweight CubeSats has opened up new possibilities to realize the Internet of Space (IoS), a vision that aims to establish a constellation of CubeSats in space to provide global network access. A key challenge for IoS realization is the development of beam steerable antennas that can meet the gain, bandwidth, and polarization requirements for IoS while complying with the small form factor of CubeSats. This work addresses this challenge by proposing innovative synthesis and implementation methods for reflectarrays and transmitarrays to empower low-profile wideband circularly-polarized (CP) beam steerable antennas. Two unique steerable antenna architectures are presented. The first design is a K-band mechanically steerable Risley prism antenna (RPA) constructed by two co-axially placed panels, i.e., a gradient-phase feed array (GPFA), and a gradient-phase transmitarray (GPTA). The in-plane rotation of the two panels creates beam scan that covers $0^\circ - 360^\circ$ in azimuth and $0^\circ - 60^\circ$ in elevation. To improve the CP bandwidth, a hybrid-phasing method is applied to design the GPFA, and an S-ring element unit cell is designed for the GPTA. The second design is an electronically steerable reflectarray antenna. Each unit cell can implement switches to reconfigure the connections among multiple Archimedean spiral arms, creating "element rotation" that leads to geometrically dependent CP phase shift. This allows the reflectarray to achieve wideband CP beam steering without any moving parts. Both antennas have been validated through prototypes and measurements to demonstrate their beam scanning capability and bandwidth potentials for CubeSat

applications. Besides, a generalized design methodology for switch-reconfigured unit cells (SRUC) to achieve the maximum phase resolution is established. It applies binary particle swarm optimization (BPSO) algorithm to optimize the topology of pixelated unit cells with embedded switches. Unconventional linearly-polarized (LP) and CP 2-switch 4-state SRUC for K-band beam steerable reflectarrays have been designed and thoroughly validated. Lastly, the novel charge-programmed multi-material (CPMM) additive manufacturing technology is applied to innovate antenna design and fabrication. Several ultra-lightweight CP transmitarrays achieving order-of-magnitude weight reduction and a compact CP horn antenna with uniquely designed 3D structures have been manufactured and measured. This dissertation addresses the cutting edges of CubeSat beam steerable antennas from several aspects, including the fundamental principles, synthesis methods, antenna architectures, and manufacturing methods.

The dissertation of Junbo Wang is approved.

Aydin Babakhani

Yuanxun Wang

Bahram Jalali

Yahya Rahmat-Samii, Committee Chair

University of California, Los Angeles

2023

To my family ...

for their unwavering love, support, and belief in me

And to whatever created the universe ...

for making it such beautiful and mysterious

TABLE OF CONTENTS

LIST OF FIGURES

LIST OF TABLES

ACKNOWLEDGMENTS

I wish to express my deepest gratitude and appreciation to my advisor, Prof. Yahya Rahmat-Samii, for his invaluable guidance, support, mentorship, and friendship throughout my journey to complete my doctoral study. A relentless educator and passionate researcher as he is, Prof. Rahmat-Samii has profoundly changed who I am. He taught me that "hard work and attention to details are the two paramount components in performing high-level research", but at the same time encouraged me to believe in sparks of ideas that may "sound absurd at the beginning". His profound knowledge and contributions, as well as enthusiasm in life, will continue to light my way up ahead. I want to thank Prof. Bahram Jalali, Prof. Ethan Yuanxun Wang, and Prof. Aydin Babakhani for their insightful feedback on my research and their valuable time dedicated to serving as my doctoral committee members. I would like to thank Prof. Xiaoyu Zheng for sharing the additive manufacturing technologies, which led to our fruitful collaborations on 3D-printed antennas. I also want to thank Prof. Tatsuo Itoh, who was my doctoral committee member but unfortunately passed away in 2021. His dedication to microwave research and education is an enduring legacy for us.

I am fortunate to have worked closely with a group of brilliant minds, and I'm grateful for the friendships and collaborations with my colleagues at the UCLA Antenna Lab: Jordan Budhu, Daisong Zhang, Vignesh Manohar, Lingnan Song, Yubin Cai, Anastasios Papathanasopolous, Dustin Brown, Botian Zhang, Tianjian Huang, Yusheng Luo, and Wenman Hu. I want to also thank my collaborators, Ryan Hensleigh, Zhenpeng Xu, and Zhen Wang for performing high-quality additive manufacturing work.

I would like to thank my partner, teammate, and girlfriend, Dr. Gaoyan Li, for her steady support in my life. I must mention our furry friend, Dahe (River) the cat, for always bringing joy and happiness to us. Lastly, and most importantly, I would like to thank my family from the bottom of my heart. Their steadfast love and constant support in all possible dimensions of my life keep me moving forward. None of my achievements would have been possible without them, and I share the joy and celebrate with them.

VITA

EDUCATION

2013–2017 **Zhejiang University (ZJU)** , Hangzhou, Zhejiang, China
- B.Eng. in Opto-Electronic Information Science and Engineering
- Final Overall GPA: 3.92/4

2017–2019 **University of California, Los Angeles (UCLA)**, Los Angeles, USA
- M.S. in Electrical & Computer Engineering
- Final Overall GPA: 3.90/4

AWARDS

2023 **Distinguished Ph.D. Dissertation Award in Physical & Wave Electronics**

2022 IEEE AP-S/URSI 2022 TICRA Foundation Travel Grant

2022, 2023 USNC-URSI Travel Fellowship

2021-2022 **UCLA Dissertation Year Fellowship**

2020-2021 **Samueli Excellence in Teaching Awards**

2021 **First Place in the '21 Ernest K. Smith USNC-URSI Student Paper Competition**

PUBLICATIONS

Y. Rahmat-Samii, **J. Wang**, J. Zamora, G. Freebury, R. E. Hodges and S. J. Horst, "A 7 m × 1.5 m Aperture Parabolic Cylinder Deployable Mesh Reflector Antenna for Next-Generation Satellite Synthetic Aperture Radar," *in IEEE Transactions on Antennas and Propagation*, vol. 71, no. 8, pp. 6378-6389, Aug. 2023.

J. Wang, Z. Xu, Z. Wang, X. Zheng and Y. Rahmat-Samii, "Development of a Low-Cost Lightweight Advanced K-Band Horn Antenna With Charge-Programmed Deposition 3D Printing," *in IEEE Antennas and Wireless Propagation Letters*, vol. 22, no. 8, pp. 1917-1921, Aug. 2023.

J. Wang, V. Manohar and Y. Rahmat-Samii, "K-band Circularly Polarized Beam Steerable Reflectarray Enabling Internet of Space: Conceptualization and Validation," *in IEEE Transactions on Antennas and Propagation*, vol. 70, no. 8, pp. 6703-6717, Aug. 2022.

J. Wang and Y. Rahmat-Samii, "A Simplified Configuration of Beam-Steerable Risley Prism Antennas: Principles and Validation," *in IEEE Antennas and Wireless Propagation Letters*, vol. 21, no. 11, pp. 2288-2292, Nov. 2022.

J. Wang, V. Manohar and Y. Rahmat-Samii, "Enabling the Internet of Things With CubeSats: A Review of Representative Beamsteerable Antenna Concepts," *in IEEE Antennas and Propagation Magazine*, vol. 63, no. 6, pp. 14-28, Dec. 2021.

J. Wang, Y. Rahmat-Samii, "Step-Like Structures in Electrostatic and Electrodynamic Implementation of Method of Moments: Some Unique Observations", *Progress In Electromagnetics Research B*, Vol. 85, 27-48, 2019.

J. Wang, B. Zhang, and Y. Rahmat-Samii, "Hexagonal Pixels Facilitating Topological Design of 2-bit 2-switch Phase-Reconfigurable Unit Cells," *2023 United States National Committee of URSI National Radio Science Meeting (USNC-URSI NRSM)*, Boulder, CO, USA, 2023, pp. 339-340.

Y. Luo, **J. Wang**, and Y. Rahmat-Samii, "The Significance of Nearby-term Approximation in Method of Moments: An Observation in 2D Electrodynamic Scenarios with TE Polar-

ization," *2023 United States National Committee of URSI National Radio Science Meeting (USNC-URSI NRSM)*, Boulder, CO, USA, 2023, pp. 319-320.

J. Wang and Y. Rahmat-Samii, "A Novel Reduced-Complexity Low-Profile mm-Wave Beam Steerable Risley Prism Antenna," *2022 Antenna Measurement Techniques Association Symposium (AMTA)*, Denver, CO, USA, 2022, pp. 1-6.

J. Wang, B. Zhang and Y. Rahmat-Samii, "Maximizing RF Switch Usage Efficiency in Electronically Reconfigurable Unit Cells: A Design using Binary Particle Swarm Optimization," *2022 IEEE International Symposium on Antennas and Propagation and USNC-URSI Radio Science Meeting (AP-S/URSI)*, Denver, CO, USA, 2022, pp. 1614-1615.

J. Wang, R. Hensleigh, Z. Xu, Z. Wang, X. Zheng and Y. Rahmat-Samii, "Fully 3D-Printed Lightweight Combination of a Circularly Polarized Transmitarray and a Feed Horn," *2022 IEEE International Symposium on Antennas and Propagation and USNC-URSI Radio Science Meeting (AP-S/URSI)*, Denver, CO, USA, 2022, pp. 645-646.

J. Wang, A. Papathanasopoulos, Y. Rahmat-Samii, R. Hensleigh, Z. Xu and X. Zheng, "Ultra-Lightweight Transmitarray Antenna Enabled by Charge-Programmed Three-Dimensional Multi-Material Printing," *2022 United States National Committee of URSI National Radio Science Meeting (USNC-URSI NRSM)*, Boulder, CO, USA, 2022, pp. 293-294.

A. Papathanasopoulos, **J. Wang** and Y. Rahmat-Samii, "Understanding the Far-Field Properties of Orbital Angular Momentum Beams through the Antenna Aperture Field Method," *2022 United States National Committee of URSI National Radio Science Meeting (USNC-URSI NRSM)*, Boulder, CO, USA, 2022, pp. 172-173.

J. Wang and Y. Rahmat-Samii, "A 3-State Broadband Circularly-Polarized Unit Cell Enabling Steerable Reflectarrays for CubeSats," *2021 IEEE International Symposium on Antennas and Propagation and USNC-URSI Radio Science Meeting (APS/URSI)*, Singapore, Singapore, 2021, pp. 561-562.

A. Papathanasopoulos, **J. Wang** and Y. Rahmat-Samii, "Transmitarray Antenna Generating Circularly Polarized Orbital Angular Momentum (OAM) Beams: Synthesis, Prototyping and Measurements," *2021 Antenna Measurement Techniques Association Symposium (AMTA)*, Daytona Beach, FL, USA, 2021, pp. 1-4.

J. Wang, V. Manohar and Y. Rahmat-Samii, "Beam Steerable Reflectarray Enabling CubeSat Internet of Space: Conceptualization and Design (Invited Paper)," *2020 14th European Conference on Antennas and Propagation (EuCAP)*, Copenhagen, Denmark, 2020, pp. 1-4.

J. Wang and Y. Rahmat-Samii, "Development of Novel K-band Beam Steerable Reflectarray for CubeSat Internet of Space," *2020 IEEE International Symposium on Antennas and Propagation and North American Radio Science Meeting*, Montreal, QC, Canada, 2020, pp. 1779-1780.

J. Wang and Y. Rahmat-Samii, "Meixner's Current Edge Behaviors and their Appearances in MoM Solutions: A Novel Step-Like Structure Creating Edges and Inner and Outer Wedges," *2019 International Conference on Electromagnetics in Advanced Applications (ICEAA)*, Granada, Spain, 2019, pp. 1300-1300.

J. Wang, Y. Rahmat-Samii, "Phase Method: A More Precise Beam Steering Model For Phase-Delay Metasurface Based Risley Antenna", *2019 URSI International Symposium on Electromagnetic Theory (EMTS)*, San Diego, CA, USA, 2019, pp. 1-4.

CHAPTER 1

Introduction

1.1 Satellite Constellation Supporting Global Network Coverage

The Internet has become a necessity for the conduct and progress of modern societies. However, there remains to be a vast area of land either under-developed or with low population density (referred to as "remote areas") that is not connected to the Internet. In fact, more than 40% of the global population have yet no access to the Internet, according to a recent report in 2020 [1]. The scarce network penetration in these areas is attributed to various reasons: extreme environmental conditions, low investment return, excessive cost for operation and maintenance, etc. The only feasible method of providing network coverage to such areas is via satellites. Thus, a vision of the Internet of Space (IoS) has been proposed to establish a constellation of satellites that provide global network coverage directly from space [2–5].

1.1.1 Satellite Constellation: Pioneers and Future Directions

Establishing a chain of satellites to support global network coverage requires hundreds or thousands of deployments. This was almost impossible with traditional satellites due to the economic and time cost associated with the development and deployment of such satellites. However, the recent advent of small satellites (Fig.1.1) has made IoS a realizable vision. Indeed, based on small satellites, there are several ongoing missions such as Starlink [6] by SpaceX and OneWeb Satellite Constellation [7] project by OneWeb, which target deploying a constellation of satellites to support affordable worldwide broadband network access. Starlink, as of 2023, has successfully deployed over 4000 satellites in 550 km LEO. Each satellite

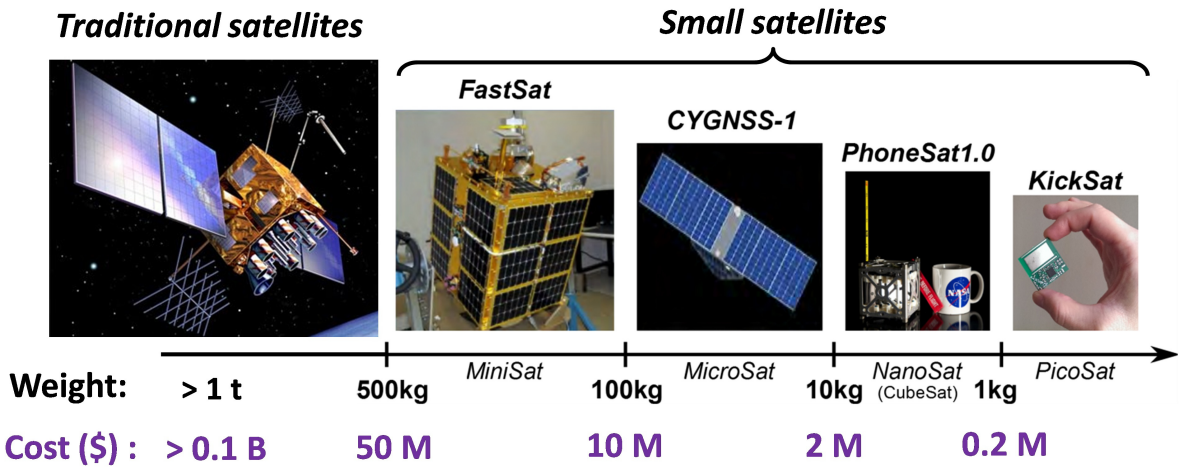

Figure 1.1 Representative mass and cost of each category of satellites. Adopted from [9] and modified based on [10].

for Starlink weighs around 200 kg and supports Ku- and Ka-band communication through 4 phased array antennas. The full deployment of the Starlink constellation is anticipated to complete by 2027. OneWeb constellation has deployed over 500 150-kg-satellites operating in Ku-band. These satellites are significantly miniaturized compared with traditional satellites, and fall in the category of MiniSats based on their mass according to Fig. 1.1. However, with these MiniSats it will still take tens to hundreds of launches and years to fulfill the desired satellite population for IoS. Employing smaller and more affordable satellite platforms such as CubeSats can bring many practical advantages, e.g., improving deployment efficiency, better affordability of the network service, improving revisit times [8], and reducing orbit blockage and astronomical pollution. Therefore, thus investigations in CubeSat-based network service hold substantial value.

1.1.2 CubeSats Enabling Internet of Space (IoS)

A typical CubeSat is built upon off-the-shelf modular blocks, each of which has a volume of 10 cm × 10 cm × 10 cm and a mass of approximately 1 kg [Fig. 1.2(a)]. This modular unit is commonly referred to as 1U. Stacking these 1U blocks allows the expansion of CubeSat volume (to 2U, 3U...) and thereby payload to meet the need of particular applications. The

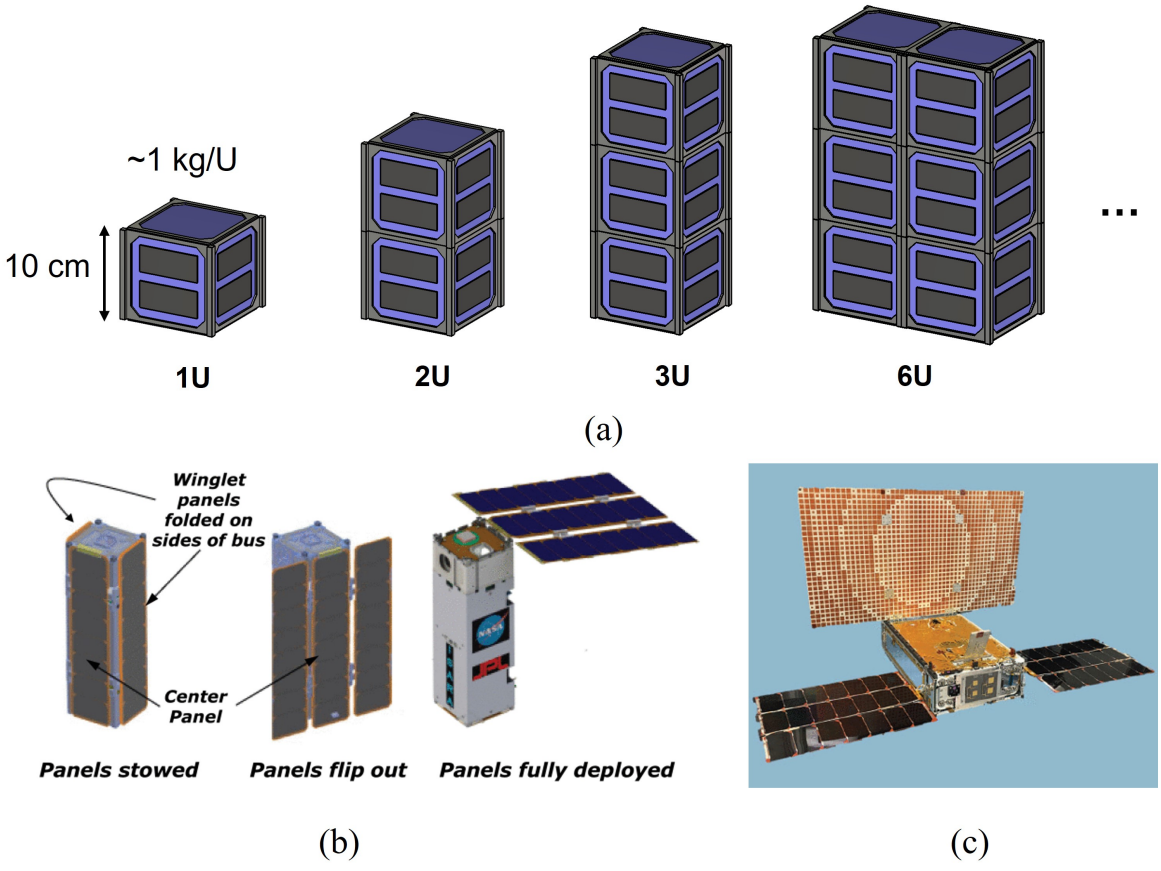

Figure 1.2 (a) Illustration of representative CubeSat chassis dimensions and the extension made through cascading modular units. (b) The ISARA [11] 3U CubeSat with a solar panel-integrated deployable reflectarray antenna (image acquired from [12]). (c) The MarCo [13] 6U CubeSat with a deployable reflectarray antenna.

small size and the economic affordability of CubeSat make it suitable for massive deployment, which is the foundation of establishing IoS. Therefore, CubeSats are envisaged to be the key enabler of IoS to provide Internet coverage across the globe [4, 5].

However, the compactness of CubeSats necessitates innovative designs in compatible electronics, especially the antenna. Low-gain antennas such as patch, dipole, etc. have been actively investigated for CubeSats [10, 14]. But achieving higher data rates necessitates the integration of high-gain aperture antennas with CubeSats, and this remains an open area of research. Several review articles that highlight the recent trends in antenna development for CubeSats can be found in [9, 12, 15, 16]. Some recent developments in the arena of high gain antennas for CubeSats for remote sensing and deep space missions are described in [17–22]. The feasibility of supporting high data-rate communication through CubeSats was well manifested by several successful missions [11, 13] led by Jet Propulsion Laboratory and NASA. In ISARA [11], a Ka-band reflectarray antenna was integrated with the solar panel and deployed on a 3U CubeSat, providing a 33.5 dBi gain at 26 GHz [Fig. 1.2(b)]. For MarCO [13], a circularly polarized X-band reflectarray antenna with 29.2 dBi gain was deployed on a 6U CubeSat, establishing a direct link between Mars and Earth [Fig. 1.2(c)]. These encouraging achievements motivated the expedition for CubeSat antennas under IoS scenarios, where more stringent requirements apply. As will be discussed in the following section, none of the antennas in current CubeSat missions has sufficient capability to meet all requirements raised by IoS. Certainly, the successful implementation of CubeSats necessitates innovations in various fields apart from antenna engineering, such as propulsion technologies [23], deployment mechanisms [24], formation control [25], etc. However, this dissertation will be focusing dominantly on tackling the challenges in CubeSat antenna designs.

1.1.3 Challenges and Technical Requirements on Antenna for CubeSats to Enable IoS

The realization of a CubeSat constellation supporting global network coverage challenges antenna design from the major aspects below:

a) **Beam steerability.** The antenna must be able to dynamically allocate its beam-pointing direction within a wide angular range. This is essential for the CubeSats to maintain stable data links while orbiting and to switch among dispersed user terminals.

b) **High gain, broadband circular polarization (CP) operation.** In order to sustain a high data-rate link to Earth, the antenna should provide a reasonable gain (> 20 dB) within a considerable bandwidth. Circular polarization (CP) is desired to guarantee efficient reception of signal regardless of the gesture of CubeSats.

c) **Capacity and power constraints.** The antenna system must be able to fit in the compact form factor of CubeSats while meeting the total mass limit of around 1 kg/U. The power consumption of the antenna should comply with the power constraint onboard CubeSats (typically less than 20 W).

These challenges translate into typical RF requirements on IoS CubeSat antennas that engineers in this field are currently pursuing (as shown in Table 1.1). Achieving data rates over a few hundred megabytes per second with the limited power onboard the CubeSat requires high gain antennas with CP beams for both the transmitting and the receiving bands of frequency. While there were discussions about using frequencies in E-band [26], the majority of recent works focused on K/Ka-band range of frequencies [8, 27–30]. Though achieving some of these requirements may be tangible with current techniques, assembling all the capabilities together while maintaining compatibility with CubeSat requires exotic antenna designs.

1.2 Overview of Beam Steerable Antennas

As stated in previous sections, antenna steerability is crucial for CubeSats to enable IoS. However, all of the so far reported CubeSat antennas provided fixed beams and thus are not qualified for CubeSats under IoS scenarios. In this section, we will begin with a brief review of the fundamental principles of beam steering. Then, an overview of mainstream steerable antenna techniques and a discussion of their potential for CubeSat application will

Table 1.1: Representative technical requirements for cubeSat antennas to enable IoS [8,27,30]

Specification	Typical Requirement
Frequency	17.8 - 20.2 GHz (Tx)
	27.5 - 31.0 GHz (Rx)
Polarization	RHCP/LHCP
Beam Coverage (Elevation)	$\pm 60^{\circ}$
Beam Coverage (Azimuth)	$\pm 180^{\circ}$
Axial Ratio	< 2 dB (broadside)
Power	≤ 20 W

be presented.

1.2.1 Fundamental Principles of Beam Steering

It is a well-acknowledged fact that the far field of an aperture antenna is related to its near field distribution by Fourier transform [31]. Based on this, scanning the far-field beam to a certain direction requires that the near field possess a phase gradient. In particular, for a target scan direction defined by θ_t and ϕ_t (elevation and azimuth) , the aperture phase (Φ) should ideally distribute as:

$$\Phi(x', y') = -(kx' \sin\theta_t \cos\phi_t + ky' \sin\theta_t \sin\phi_t) \tag{1.1}$$

where x' and y' represent aperture coordinates, and k represents the wave number ($= 2\pi/\lambda$) with λ being the wavelength. This means steerable antennas must incorporate some form of reconfiguration technique to dynamically synthesize the corresponding aperture phase distribution to achieve different beam scan directions. In general, beam scan is realized by: 1) mechanical rotation/displacement of the antenna/feed (e.g. scan with reflector antennas); 2) electronically switching among multiple feeds; 3) manipulating the phase shift of elements in an array (e.g., scan with phased array).

1.2.2 Beam Steerable Antenna for CubeSats: Potential Candidates

One of the most popular high-gain antennas for satellite missions is the parabolic reflector [32]. While a parabolic reflector performs reasonably well for scans up to several beamwidths (typically through feed displacement), the performance significantly degrades if larger scan angles are desired [33]. The only option, then, is to mechanically rotate the antenna. This necessitates the use of heavy motors and gimbals which are difficult to incorporate on CubeSats. In addition to this, the profile of the reflector needs sophisticated packaging and deployment mechanisms. While this is an option for conventional satellites [34], this is unfeasible for CubeSats.

Phased array, as an electronic approach, has been used widely for beam forming applications [35] and has gained some attention for CubeSats for its reconfigurability [36]. However, for CubeSat applications at our frequencies of interest, the loss in feeding networks, the complexity and cost associated with the massive use of active RF components for beam scan can be a major concern.

Other classes of aperture antennas, namely lenses, reflectarrays, and transmitarrays have thus drawn attention to facilitate IoS due to their ease of integration with CubeSat and their potential low-cost implementation. Lens antennas work on the principle of manipulating the phase of a spherical wavefront by engineering the effective dielectric distribution of the lens. Lenses, in general, can be made relatively low profile and light through profile optimization and 3D printing [37–39]. The beam scan, however, is typically achieved through some form of mechanical movement of the lens or the feed. While switching between multiple feeds is also a possibility for scanning with lens antennas, the number of beams that can be produced gets limited by the number of feeds.

Reflectarray and transmitarray both consist of an array of individual elements (typically sub-wavelength) that can be engineered to locally "correct" the phase of illumination so that the aperture re-radiates with the desired phase distribution. The advantages of planar profile and the low cost of these antennas make them appealing in various applications including CubeSats [40–42]. The beam scan with a reflectarray/transmitarray can be realized

by either mechanically repositioning or electronically switching the array elements. Steerable reflectarray and transmitarray antennas are free of RF phase shifters, and thus can potentially support more power-efficient operations. These features make reflectarray- and transmitarray-type antennas stand out as promising candidates for CubeSats. However, as will be reviewed in-depth in chapter 2, the existing beam steerable reflectarrays and transmitarrays can not yet fully satisfy the bandwidth, polarization, and mass requirements for IoS CubeSats. To further narrow down these technology gaps, the objective of this dissertation is then set forth to innovate low-profile beam steerable antenna technologies with reflectarrays and transmitarrays, particularly targeting the stringent requirements of IoS CubeSat.

1.3 Outline of This Dissertation: Beam Steerable Antennas for CubeSats

The organization of this dissertation is as follows: First, a comprehensive review of state-of-art steerable antennas that show potential for CubeSat applications will be presented in chapter 2. From an implementation standpoint, the advantages and challenges of each category of antenna architecture will be evaluated based on the requirements of IoS CubeSats. Two of the antenna architectures will be selected and investigated in this work, namely, a mechanically steerable, transmitarray-based Risley prism antenna (RPA) and an electronically steerable reflectarray antenna. In chapter 3, the common theoretical foundations that enable the antenna designs in this work will be articulated. The CP phase shift associated with element rotation will be revisited in radiating and scattering scenarios. This geometrical phase property largely benefits wideband CP applications and is implemented in various antenna designs of this work. In chapter 4, the fundamentals, design, and measurement results for a K-band two-component CP steerable RPA based on transmitarrays will be presented. An enhanced beam steering model is introduced to more accurately associate the beam scan direction and the orientation of the rotated panels. Beam scan capability, bandwidth, and beam scan resolution of the RPA will be characterized with the fabricated prototype. Chapter 5 presents the conceptualization, design, and characterization of K-band steerable reflectarray

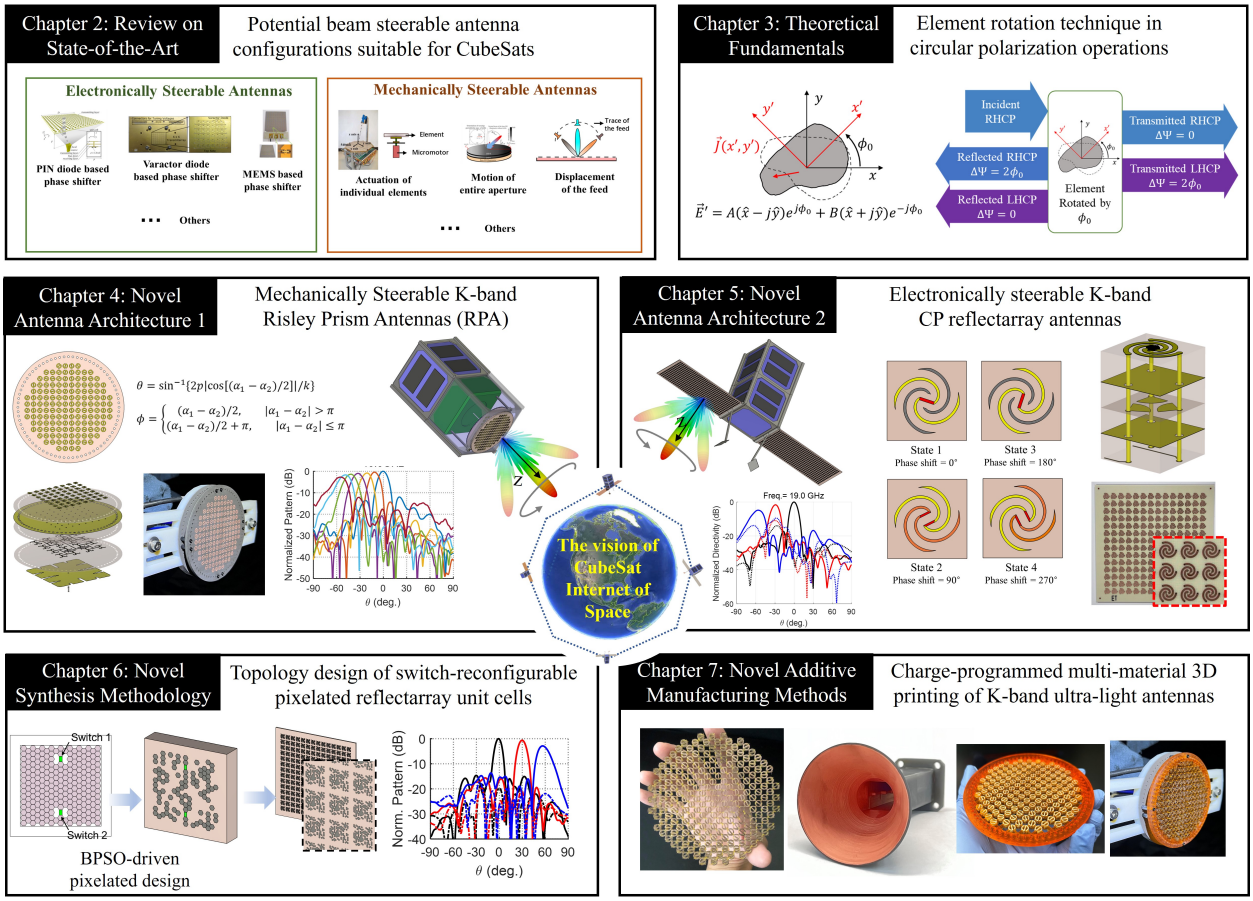

Figure 1.3 Overview of the major contributions of this research and the organization of this dissertation.

antennas that can be electronically reconfigured with p-i-n diode switches. The beam scan capability and bandwidth performance will be validated with manufactured prototypes. In chapter 6, a generalized design methodology for switch-reconfigurable unit cells (SRUC) will be introduced. Binary particle swarm optimization (BPSO) algorithm is utilized to optimize the topology of pixelated unit cells with integrated switches. Unconventional 2-switch 4-state SRUC for K-band beam steerable reflectarrays have been designed and thoroughly validated in simulations. In chapter 7, the novel charge-programmed multi-material (CPMM) additive manufacturing technology will be implemented for antenna fabrication. Several innovative K-band antennas are manufactured and characterized, including ultra-lightweight transmitarrays achieving order-of-magnitude weight reduction and a horn antenna with uniquely designed 3D structures. In Chapter 8, the major accomplishment of this research will be summarized.

CHAPTER 2

Beam Steerable Antennas Considering CubeSat Compatibility: State of the Art and Open Challenges

In this chapter, a comprehensive review on the state of the art steerable antenna architectures will be presented. In particular, it focuses exclusively on works that are able to, or have the potential to meet the requirements to enable CubeSat IoS. From a CubeSat implementation point of view, the antennas to be reviewed in this chapter will be divided into two major categories: mechanically steerable antennas and electronically steerable antennas. The advantages of each family of steerable antenna will be evaluated, the potential challenges to implementation on CubeSats will be addressed.

2.1 Mechanically Steerable Antennas

In this section, we focus on the antenna architectures that employ some form of mechanical motion in order to achieve the desired phase distribution in the aperture. Depending on the subject under movement, these works can be divided into three groups: (a) element motion, (b) aperture motion and (c) feed motion.

2.1.1 Element Motion

In this section, we elaborate on beam steerable aperture antennas that employ mechanical reconfiguration of individual elements. The feasibility of controlling the aperture phase by varying the height of individual patches in a reflectarray was shown in [43]. Recently in [44], a linearly polarized (LP) reflectarray capable of scanning to 60° (elevation) in C-band with a

bandwidth of 6.2% was experimentally realized with a dielectric shaft actuated element. As shown in Fig. 2.1, the unit cell consists of three layers: (1) a fixed top patch, (2) a movable slotted patch in between and (3) a fixed ground plane at the bottom. The slotted patches in between were actuated to vary their distances between the top and bottom layers to provide the required phase distribution. Due to this feature, the overall profile of the reflectarray remains unchanged. This concept was later adapted in [45] where each patch was pixelized and optimized to achieve improved performance.

Another approach of element level actuation is by element rotation, which largely supports CP operations. The concept originates from the special property that the phase shift of the co-polarized reflected/transmitted CP component has a linear dependence on the physical rotation angle of the scattering element [46, 47]. In [48], a CP reflectarray implementing mechanically rotated elements was shown to achieve a 60° scan with a simulated fractional bandwidth of 28.6% in X-band. Each element was addressed by a micro motor underneath and controlled individually (Fig. 2.2). It is worth noting that, despite the mechanical complexity, the type of elements used in [48] are strong candidates for efficient and broadband CP array antennas owing to their intrinsically frequency independent phase shifting mechanism.

2.1.2 Aperture Motion

There are multiple ways of scanning the beam by mechanically positioning a section of the aperture antenna. Among them, Risley prism antenna (RPA) [49–52] is a unique approach. The concept of RPA draws inspiration from optics: rotating a pair of prisms can steer a laser beam that propagates through the system. This concept was initially exercised in microwave using a pair of dielectric wedges [53]. More recently, planar transmitarrays pair have also been used to achieve beam steering [49–51]. In [49], linear phase shifting transmitarrays were used to produce beam deflection in a similar manner as prisms. At 30 GHz, the fabricated antenna achieved a beam scan over 70°. In [52], linearly graded dielectric (LGD) plate was incorporated as a prism, whose refractive index was engineered to provide the linear phase shift for expected beam deflection. Simulation results demonstrated a scan

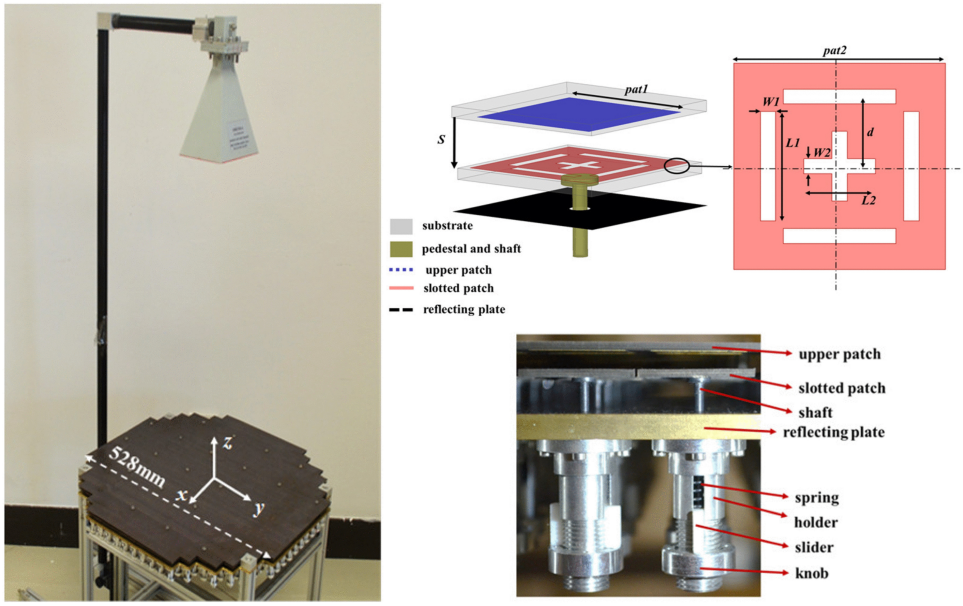

(a) (b)

Figure 2.1 Mechanically steerable C-band reflectarray via vertically shifting the element [44]. (a) Designed prototype. (b) Unit cell illustrating the element geometry and the motor mechanism.

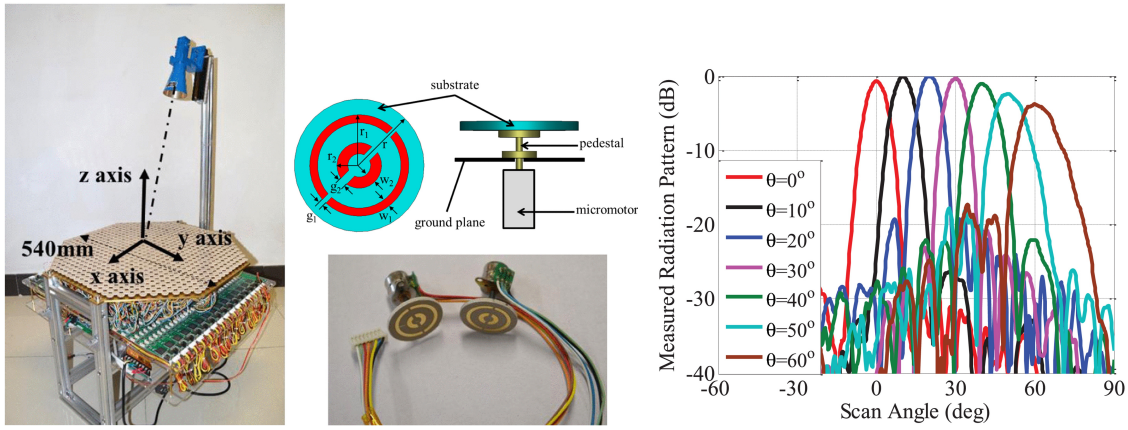

(a) (b) (c)

Figure 2.2 X-band reflectarray employing mechanically rotated elements to achieve the desired beam scans [48]. (a) Fabricated prototype. (b) Design of the unit cell showing the motor actuation mechanism. (c) Measured patterns at 8.3 GHz showing beam scan up to 60°.

up to 40° in X-band (Fig. 2.3). All the aforementioned works possess the potential of CP operation. A typical Risley prism antenna operates in transmitting mode, and requires two independent motions, i.e., the in-plane rotation of the first and second layer. Such a system significantly simplifies the circuitry for reconfiguration, since no element-wise control is required. However, novel mechanical designs must be carried out for practical implementation of RPA [52].

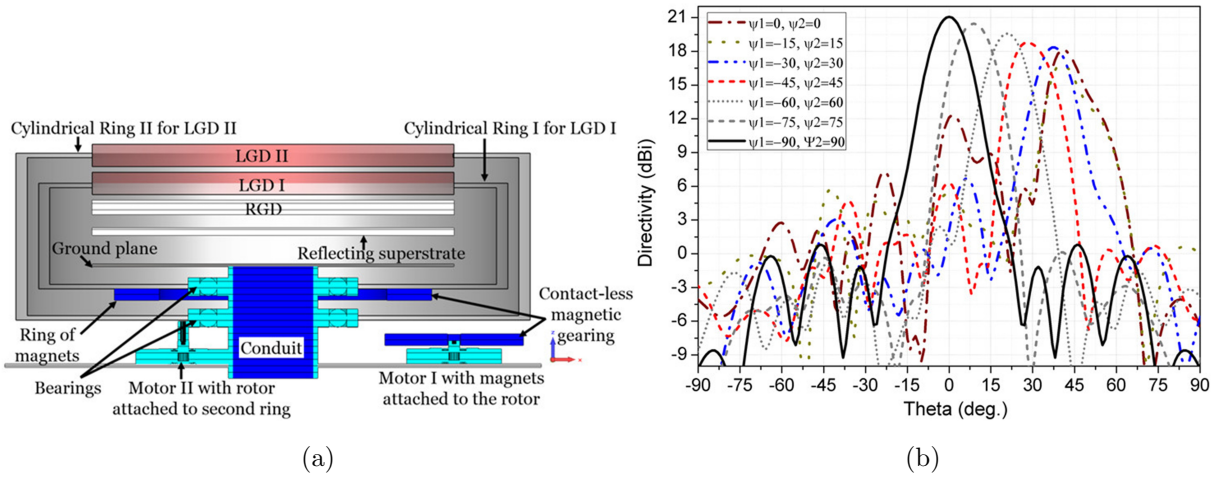

(a) (b)

Figure 2.3 Demonstration of a Risley prism antenna which uses the relative mechanical motion of two LGDs to achieve beam scans [52]. (a) Proposed mechanical implementation. (b) Simulated results showing multiple scanned beams at 11 GHz.

Another approach to achieve mechanical reconfiguration of the aperture is in-plane translation as was described in [54]. In this case, beam scanning was realized by translating a specially designed transmitarray over a fixed feed. At Ka-Band, a scan of CP beam in elevation up to 50° was achieved. This design can potentially allow 360° scan in azimuth by rotating the transmitarray. In-plane translation technique requires the movement of only a single layer, but at the expense of a larger physical aperture.

2.1.3 Feed Motion

This type of mechanical reconfiguration utilizes feed motion to scan the beam. This technique can be used for scanning with reflectarrays, transmitarrays and lenses. Traditionally, fixed-element reflectarrays are usually designed for a fixed feed position. The performance for

such reflectarrays can degrade significantly if the phase center of feed is displaced from the ideal position owing to the sensitivities involved with the phase response of individual elements [55]. In [56] an optimization process was developed in order to minimize the phase error as the feed moves along a circular arc over the reflectarray. The fabricated prototype achieved a LP beam scan up to 45° in one plane by moving the feed horn on a circular trace, with fixed-element reflectarray (Fig. 2.4). This work was demonstrated at 12 GHz and the 1-dB gain bandwidth was approximately 8%. Though full beam coverage in 3D cone with feed motion remains to be investigated, this work has demonstrated potential capabilities of reflectarrays.

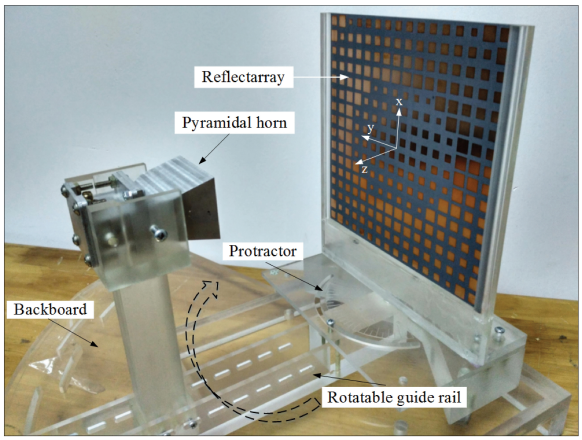

Figure 2.4 Mechanically steerable X-band reflectarray via motion of the feed [56].

2.1.4 Summary of Mechanical Reconfiguration Options

Mechanical reconfiguration, in general, bears the advantages of higher efficiency, ease of RF implementation and better phase resolution. It benefits from the absence of RF components and the continuity of physical motion. Element motion technique requires the independent translation/rotation of each element in the array. The motions are localized to element level; thus one expects no significant change in the lineament of the antenna. However, the key to implement this technique at higher frequencies is the availability of light weight and miniaturized actuators that can fit within the limited volume of a unit cell. Aperture motion technique utilizes the rotation or translation movement of (part of) the antenna, potentially

making the mechanical implementation more challenging. With this technique, the amount of variation in antenna profile as the beam scans may differ with the particular method chosen: for Risley prism type, the antenna profile is unaffected by pure rotation motions, whereas for in-plane translation type, the profile can vary by a considerable amount. Feed motion technique relies on the displacement of the feed and can cause a significant change in system profile. The implementation could thus raise concerns of blockage by the feed and support structures.

2.2 Electronically Steerable Antennas

Electronically steerable antennas can provide several desirable features such as fast switching, low weight and low mechanical complexity. These make them suitable for space missions and have attracted significant attention. The price paid for the relative ease of mechanical integration is the limited phase resolution. A study in [57], showed that 1-bit phase resolution (2 phase states) leads to a quantization loss around 3 dB, while 2-bit phase resolution (4 phase states) would reduce the loss to 1 dB. Numerous works have been reported in this domain with varied operation philosophies, and overall, the reconfigurations were mostly performed on the level of unit cell. Considering specific constraints on complexity, power and cost for CubeSats, we classify electronically steerable antennas into three mainstream classes based on their electronic building blocks: varactor, PIN diode and MEMS switch. As discussed previously, due to the complexities involved with implementations of active phase shifters, phased array is not discussed in this section.

2.2.1 Varactor Diode

Varactor diode generally serves as a DC voltage tuned capacitive load controlling the element phase shift. Two major unit cell configurations have been explored, in which the varactor detunes the resonance of the element [58, 59] or controls the phase shift of an internal phase shifter [60,61]. In the first kind of configuration, the variation in element phase is realized by shifting resonant frequency through varying varactor capacitance. Due to this nature, such

elements are usually narrow band [62–64]. Elements with multiple resonances have been investigated to increase the bandwidth of such elements [65]. Recently, a reflectarray with varactor-loaded split patch element [66] achieved a scan up to 45° at 13.58 GHz with a 1 dB gain bandwidth around 10% in simulations.

In the second kind of configuration, the unit cell employs a "Rx - phase shifter - Tx" arrangement, where the varactors (present in the phase shifter stage) control the phase shift. Using this concept, a transmitarray in [61] achieved scanning of a LP beam up to 60° at 5.4 GHz with a fractional bandwidth of 8.5% (Fig. 2.5). In [67], a CP transmitarray operating in the 4.75-4.85 GHz band has shown the capability of up to 45° scan.

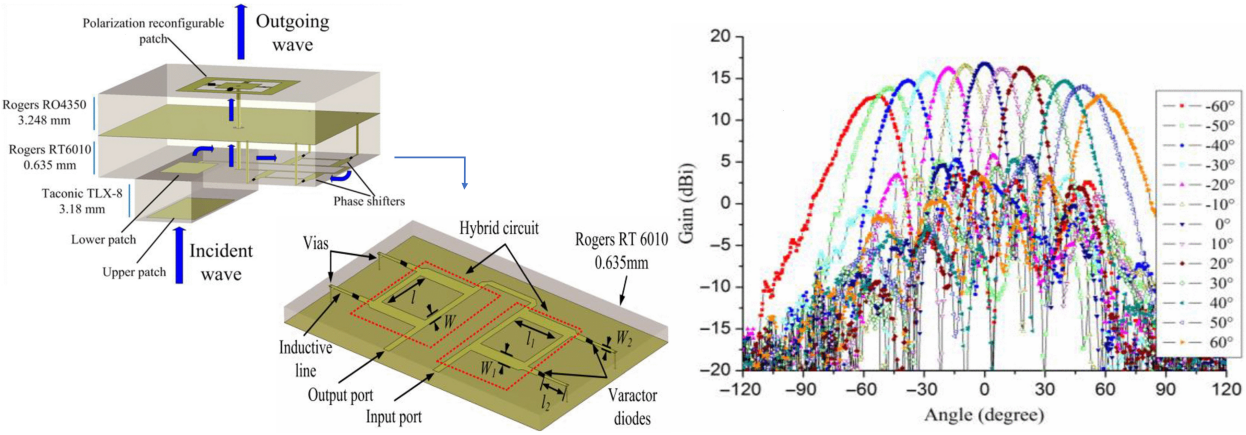

(a) (b)

Figure 2.5 Electronically steerable C-band transmitarray incorporating varactor diode phase shifter [61]. (a) Unit cell design and (b) representative measured results at 5.4 GHz demonstrating multiple scanned beams.

2.2.2 PIN Diode

PIN diode ideally works as a voltage controlled switch and has been extensively applied in reconfigurable antennas. It switches the current flow in the element which ultimately switches among different phase states. Since only a finite number of PIN diodes can be implemented in an unit cell, it intrinsically causes a discretization in the element phase shift. This leads to a trade-off between antenna efficiency and unit cell complexity. 1-bit phase reconfiguration is usually, though not necessarily, realized by single or double PIN diodes [68–70]. LP

beam steerable antenna with encouraging results have been achieved [71–77]. A successful implementation of 1-bit reconfiguration in [78] achieved a CP beam scan up to 60° at Ka-band within a bandwidth of 14.6% (Fig. 2.6).

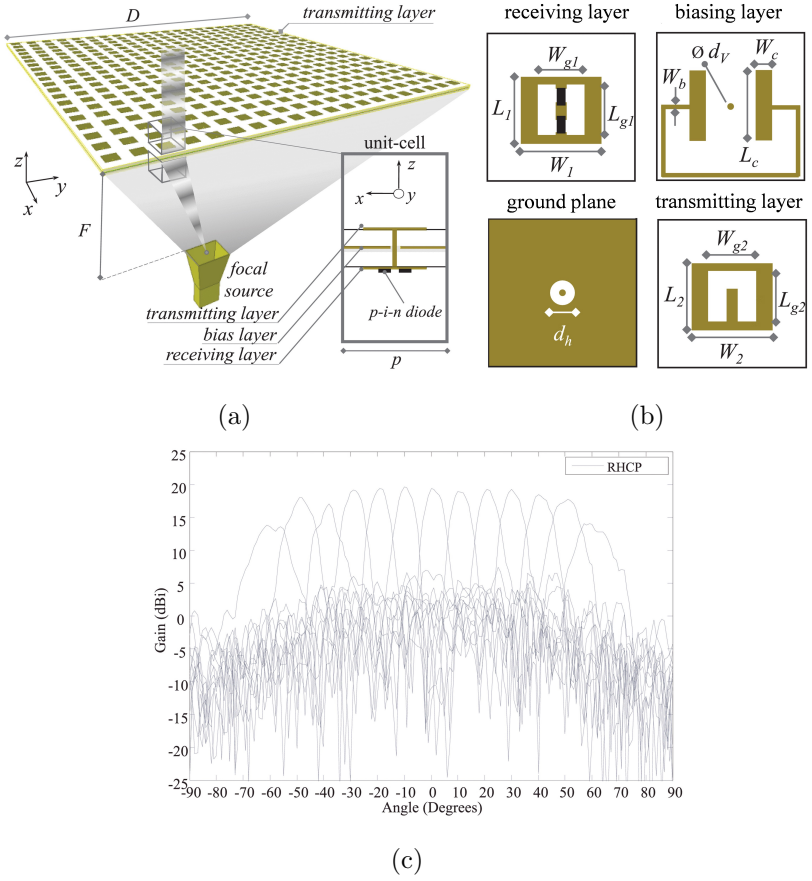

Figure 2.6 Electronically steerable Ka-band transmitarray using PIN diodes [78]. (a) The proposed transmitarray scheme (b) the unit cell design (of each layer) and (c) representative measured results at 29 GHz demonstrating multiple scanned beams.

Higher phase resolution (more than 1-bit) requires more PIN diodes in each unit cell, making the unit cell and bias network increasingly complex. A 2-bit reconfigurable antenna for LP operation was demonstrated in [30], and representative 2-bit unit cell designs with CP capability has been proposed in [79, 80]. Spiraphase element is one of the concepts that has been used for broadband CP elements. This concept is essentially the electronic realization of the element rotation technique described in Section 2.1. The unit cell packs multiple rotated copies of the same element. By electronically switching between these

copies, the element seen by the incident electromagnetic wave is electronically "rotated" thereby producing the required phase compensation. This idea was proposed decades ago in an L-band CP reflectarray [81] (Fig. 2.7), with which a wide angle scan to nearly 60° was achieved. While this design was successfully implemented at L-band, scaling the design to higher frequencies poses significant challenges due to the reduced size of the unit cell (limited space for switching network) and tight fabrication tolerances. Other works following the concept of spiraphase element at higher frequencies could be found in [82, 83]. In [83], a prototype with metal connections modeling "on" diodes has been fabricated as proof of concept at 36.5 GHz (Fig. 2.8).

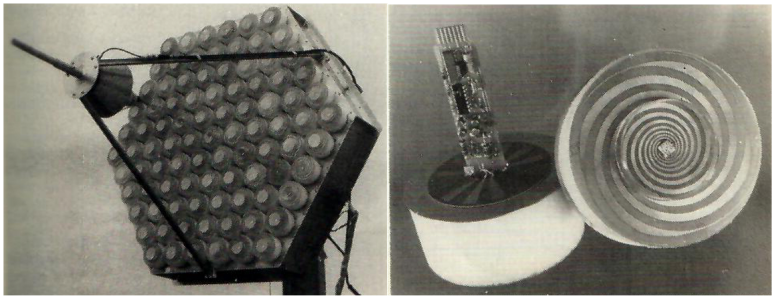

(a) (b)

Figure 2.7 Electronically steerable L-band reflectarray incorporating diode switched 2-bit spiraphase element [81]. (a) Manufactured reflectarray and (b) the unit cell.

2.2.3 MEMS Switch

The development of MEMS technology has enabled miniaturized MEMS switches to facilitate RF applications [84]. MEMS switch is conceptually similar to PIN diode, in that both behave as electronically controlled switches. Therefore, the concern of limited phase resolution exist in MEMS switched antennas as well [85]. The major advantages of MEMS switches are low loss, low power consumption and its capability of being monolithically integrated [86–88]. In [89], MEMS switch is monolithically integrated with a reflectarray antenna, and switch between broadside and 40° scanned beam was realized. This work was conducted at 25.6 GHz and the dimension of the MEMS switch is only 0.4 mm by 0.14 mm (Fig. 2.9(b)), which highlights the great potential of MEMS switch for high frequency applications.

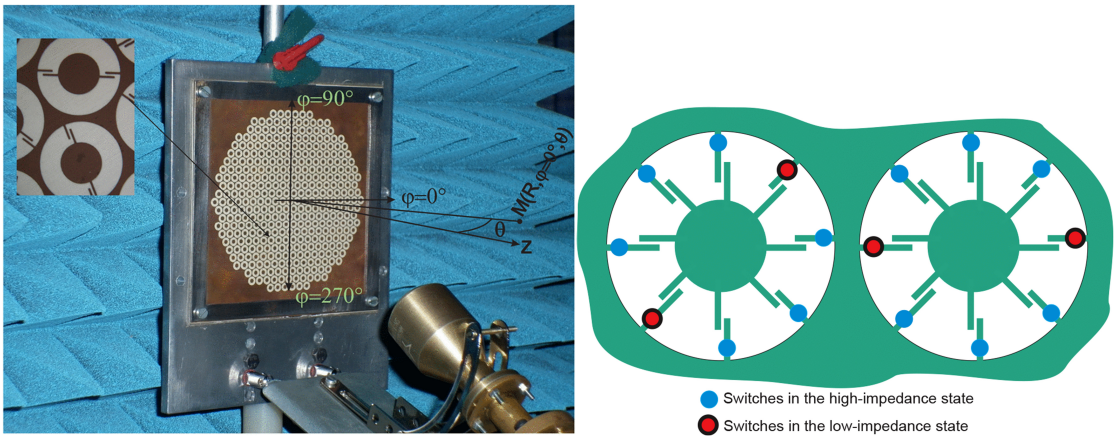

(a) (b)

Figure 2.8 Electronically steerable reflectarray at 36.5 GHz [83]. (a) Proof of concept prototype with 'on' and 'off' states modeled as open and short circuits respectively and (b) proposed PIN diode reconfigurable element.

2.2.4 Other Electronic Reconfiguration Techniques

Several technologies have emerged recently that perform antenna reconfiguration at millimeter-wave and THz frequencies with materials such as liquid crystal [90–92], graphene [93–97], thermally tunable material VO_2 [98–100], and etc. Optically reconfigured reflectarrays have also been demonstrated [101, 102]. In general, these techniques rely on the dependency of material property on external physical quantities, e.g., electric field, heat and optical illumination. However, most of the works are still proof-of-concept, and the feasibility of their application in real-life systems is yet to be explored. Particularly for satellite missions, the space compatibility of these novel materials (e.g., temperature dependence of the material) remains to be studied.

2.2.5 Summary of Electronic Reconfiguration Options

This section provides a comparison between varactor, PIN diode and MEMS switch from an implementation standpoint. Each one of them has their advantages and drawbacks. Varactor diode intrinsically enables higher phase resolution than PIN diode or MEMS switch, since the varactor capacitance is a continuous function of applied DC bias. However, the loss at

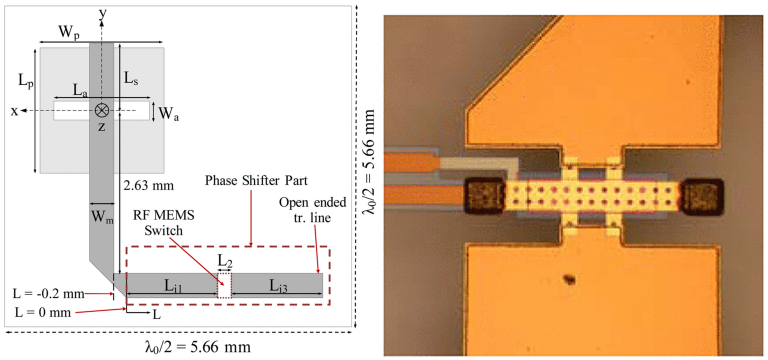

(a) (b)

Figure 2.9 Electronically steerable antenna at 26.5 GHz based on MEMS approach as presented in [89]. (a) Proposed element and (b) photo of fabricated MEMS switch.

high frequencies and narrow bandwidth may make it challenging for antennas using varactors to meet the desired RF specifications. PIN diode, on the other hand, introduces lower loss and is capable of achieving reasonably good bandwidth. However, to reduce quantization loss, phase resolution greater than 1-bit is favorable, which necessitates multiple diodes per unit cell, posing greater challenges for element and bias network design. MEMS switch is functionally similar to PIN diode, but provides the best RF isolation and lowest insertion loss among the three options. MEMS switch typically requires higher bias voltage [103], and its durability in the space environment is still being evaluated. Another important aspect of implementation of these electronic components is RF-DC isolation. Since varactor, PIN diode and MEMS switch all require DC bias, minimizing the impact of the inclusion of bias network becomes a critical task. Some discussion on biasing network design and techniques for RF-DC isolation can be found in [59, 73, 75, 104].

2.3 Summary and Open Challenges of Beam Steerable Antennas for CubeSats

The demands for wide band, circularly polarized, wide scanning angle antennas have evolved as the industry races to establish a CubeSat constellation to bring IoT to life. While many recent research works have shown a lot of potential, achieving all these RF requirements

Table 2.1: Summary of major steerable antenna architectures reviewed in this chapter

	Reconfiguration Techniques	Profile Variation	Expected Weight	Control System complexity	Reconfiguration speed	Quantization Loss	References
Mechanical Reconfiguration	Element Motion	low	medium	high	medium	low	[43–45, 48]
	Aperture Motion	low/medium	medium/high	medium	slow	N/A	[49–52, 54]
	Feed Motion	high	medium/high	medium	slow	N/A	[55, 56]
Electronic Reconfiguration	Varactor Tuned	no	low	high	fast	low	[58–67]
	Diode Switched	no	low	high	fast	$\leq$ 3 dB	[30, 68–83].
	MEMS Switched	no	low	high	fast	$\leq$ 3 dB	[84–89]

while being amenable to CubeSat integration remains an open challenge. In this chapter, we discussed two broad categories of antennas that show promise, namely mechanically steerable antennas and electronically steerable antennas. Mechanically steerable antennas, which incorporate some form of motor based actuation, can be desirable candidates if miniaturized motors that meet the CubeSat mass and power specifications are developed. Until then, electronically steerable antennas seem more conducive to CubeSats. However, a major challenge in electronic steering is that the circuit complexity increases exponentially as the number of switches increases. As discussed, a phase resolution greater than 1-bit is necessary to limit the quantization loss below 2 dB. This usually necessitates more than 2 switches per unit cell. Given that the wavelength of operation is of the order of a centimeter, such antennas can have hundreds of such unit cells, making physical implementation very complex and fabrication tolerance very critical. Apart from challenges associated with the antenna design, the extreme environmental conditions in space makes the selection of material a major concern. While in orbit, the antennas are subject to temperature extremes, static charges, etc. [105]. These conditions differ significantly from the environment on earth, and thus each antenna that is designed for space applications must be thoroughly evaluated for compatibility with the environment in space. This holds special relevance for dielectric based antenna designs

such as reflectarrays and transmitarrays. Substrates from several commercial suppliers such as Rogers have been suggested in the literature [16, 106] and have already proved their space qualification through past space missions [11, 13]. More comprehensive discussion over space antenna materials can be found in [105]. Aside from antenna substrate, active components such as switches (PIN diodes, MEMS, etc.) should also be carefully chosen for space environments. The testing of reconfigurable antennas conceptualized for IoT in space environment is also an area of future research. Addressing the challenges posed by IoS specifications to antenna engineers lays the foundation for major breakthroughs in the field of antenna engineering, and it also becomes the motivation of this dissertation.

CHAPTER 3

Fundamental Principles Enabling Wideband Circularly-Polarized (CP) Antenna Designs: Element Rotation and Resulted Phase Shift in the Radiated and Scattered Field

The RF performance of a reflectarray/transmitarray antenna is largely determined by the characteristic of the unit cell. The unit cell should maintain a high CP reflection/transmission coefficient over the entire frequency band of interest. Meanwhile, the unit cell should also be able to provide variable phase compensation (favorably $0 - 360°$). Though conventional reflectarray/transmitarray elements such as square and rectangular patches may support CP, they suffer from narrow bandwidth ($< 5\%$) and limited phase coverage because the phase shift is realized by the change in the element's resonant frequency (typically through the change of the element size). The need to alter the size of the element also makes these techniques unfeasible for element reconfiguration, which is critical for dynamic beam steering.

Alternatively, an interesting geometrical phase property that exists in CP operations has shown promise for broadband CP reflectarray/transmitarray unit cell designs [107, 108], and is gaining popularity for reconfigurable CP unit cell designs as well. This property states that: under CP wave illumination, a rotated object will introduce a phase shift to the reflected or transmitted CP component. This phase shift is exactly twice the rotation angle of the object and can thus always cover the $0 - 360°$ range. This geometrical phase phenomenon has been discussed since decades ago [109]. In [109], the underlying math of this property was revealed in a scenario where a single object was illuminated by a CP plane wave. It was later demonstrated that this property also applies to an array of objects. For

instance, in a reflectarray [110], each element was rotated differently to provide the desired local phase compensation. Since the phase shift depends only on the rotation of the element, the majority of the unit cell design work leans towards the optimization of the amplitude response, making it easier to realize broadband operations.

In this chapter, we discuss the effect of element rotation in two different scenarios: (1) a rotated, radiating object and the phase of its radiated CP field; (2) a rotated object scattering incident CP wave and the phase of its scattered field. The former is useful for the design of CP feed arrays, whereas the latter is critical in designing CP reflectarrays and transmitarrays. The detailed derivations for the phase-shifting property of rotated elements will be revisited and extended. It will be demonstrated that the geometrical phase exists generally in both CP reflection and transmission, except for a group of objects with special rotation symmetry. This chapter serves as the common theoretical foundation that has enabled various novel antenna designs presented in this dissertation.

3.1 The Radiation Phase of a Rotated Element

To begin with, we consider a radiating object and discuss how rotation changes the phase of its radiated field. Consider the object with its reference coordinate system shown in Fig. 3.1 (a). Suppose the object sustains a certain current distribution, and its radiation in the +z direction can be represented as:

$$\vec{E} = A(\hat{x} - j\hat{y}) + B(\hat{x} + j\hat{y}) \tag{3.1}$$

The radiated field is decomposed into RHCP and LHCP components, with complex coefficients A and B. When the object is rotated counter-clockwise by ϕ_0, the local coordinate for the object will also rotate to the primed coordinates, as shown in Fig. 3.1b. Assuming that the current distribution will remain the same in the primed coordinates, the radiated field of this rotated object can be expressed as:

$$\vec{E}' = A(\hat{x}' - j\hat{y}') + B(\hat{x}' + j\hat{y}') \tag{3.2}$$

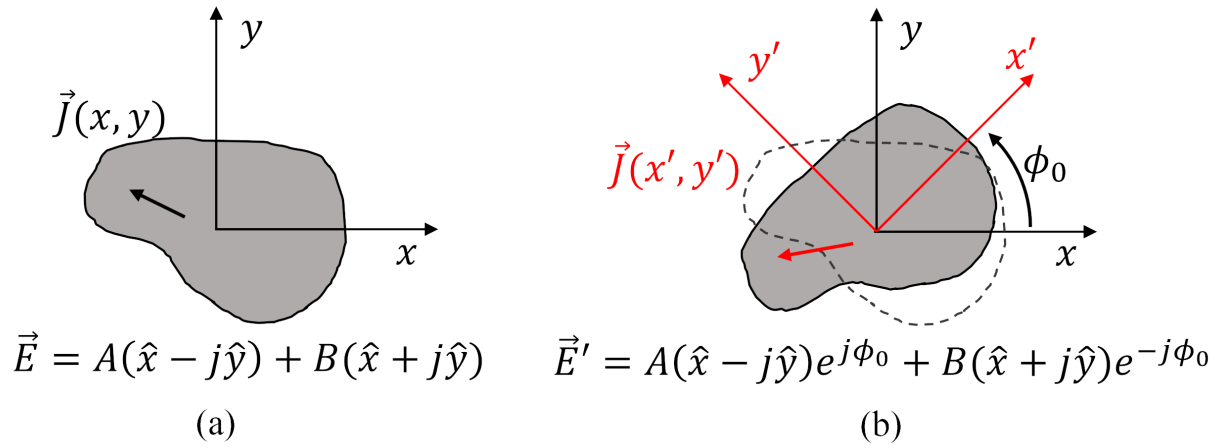

Figure 3.1 Illustration of a radiating object being rotated. The radiation is in the direction of +z. (a) The object in x-y plane with a specific current distribution. (b) The object rotated counter-clockwise by an angle ϕ_0, but having the same current distribution in its local coordinates.

Relating the unprimed coordinates to the primed coordinates, one can write:

$$\hat{x}' = \hat{x}\cos\phi_0 + \hat{y}\sin\phi_0 \tag{3.3}$$

$$\hat{y}' = -\hat{x}\sin\phi_0 + \hat{y}\cos\phi_0 \tag{3.4}$$

The radiated field $\vec{E}'$ in the original coordinates (global, unprimed coordinates) will become:

$$\vec{E}' = A(\hat{x} - j\hat{y})e^{j\phi_0} + B(\hat{x} + j\hat{y})e^{-j\phi_0} \tag{3.5}$$

The RHCP component thus gains an extra phase of ϕ_0 and the LHCP component gains an extra phase of $-\phi_0$. This is purely based on the geometrical relationships and is frequency independent. An example of the application of this property is the sequential rotation technique used to improve axial ratio (AR) bandwidth of a 2×2 patch antenna.

3.2 The Reflection and Transmission Phase of a Rotated Element Under CP Wave Excitation

Suppose a CP plane traveling in -z direction impinges upon an object lying in x-y plane, as shown in Fig. 3.2 (a). The expression of the incident CP wave is:

$$\vec{E}_R^i = \hat{x} + j\hat{y} \tag{3.6}$$

$$\vec{E}_L^i = \hat{x} - j\hat{y} \tag{3.7}$$

with the subscripts "R" and "L" corresponding to RHCP and LHCP wave respectively. We first focus on reflection, assume the reflected wave is still plane wave and takes the form of:

$$\vec{E}_R^r = A_r\hat{x} + jB_r\hat{y} \tag{3.8}$$

$$\vec{E}_L^r = C_r\hat{x} + jD_r\hat{y} \tag{3.9}$$

in which $\vec{E}_R^r$ and $\vec{E}_L^r$ are the reflected field due to RHCP and LHCP excitation, while the coefficients A_r, B_r and C_r, D_r are complex scalars that take into account of all the factors in this scattering problem (e.g., the geometry of the object).

We begin with considering RHCP plane wave incidence, the corresponding reflected wave takes the form in (3.8) and can be rearranged as:

$$\vec{E}_R^r = \frac{1}{2}(A_r + B_r)(\hat{x} + j\hat{y}) + \frac{1}{2}(A_r - B_r)(\hat{x} - j\hat{y}) \tag{3.10}$$

which effectively decomposes the reflected wave into RHCP and LHCP components. Note that since the reflected wave is traveling in +z direction, the first term in (3.10) is now LHCP and the second term become RHCP.

Then, as illustrated in Fig. 3.2 (b), the object is rotated about the origin of the coordinate by an angle of ϕ_0. The primed coordinate (marked red) follows the rotation of the object, and the new axes form an angle of ϕ_0 with the global (unprimed) axes. Now repeat previous procedures in the new coordinate but illuminating the rotated object with a new RHCP wave defined in primed coordinate ($\vec{E}_R^{i'} = \hat{x}' + \hat{y}'$), we should obtain the new reflected wave in the form of:

$$\vec{E}_R^{r'} = \frac{1}{2}(A_r + B_r)(\hat{x}' + j\hat{y}') + \frac{1}{2}(A_r - B_r)(\hat{x}' - j\hat{y}') \tag{3.11}$$

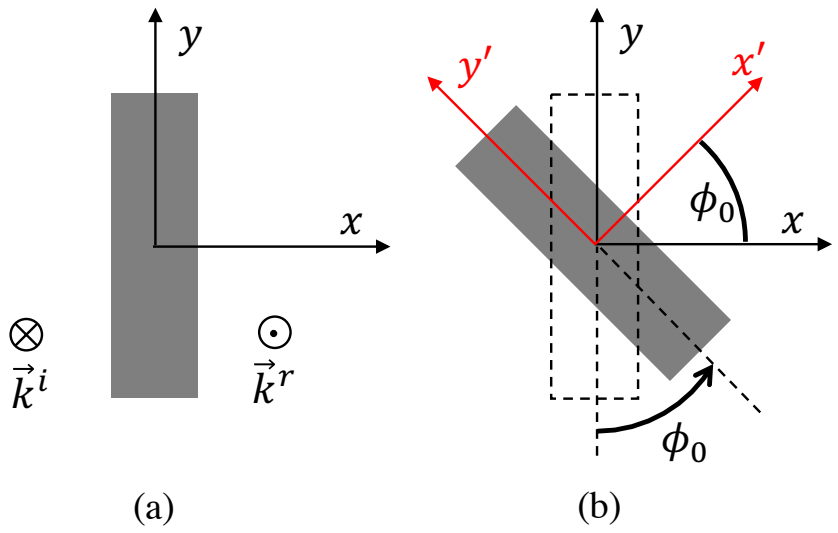

Figure 3.2 Illustration of a rotating object under CP plane wave incidence. (a) The object in x-y plane with the incident plane wave in the direction of -z. (b) The object is rotated counter-clockwise about the origin by an angle of ϕ_0.

which is again decomposing the reflected field into CP components in the new coordinate. The coefficients A_r and B_r are exactly the same as in (3.10) since in the new coordinate the rotated object now sees identical incident wave as before.

However, what we interest in is the reflected field from rotated object when it is excited by the original RHCP wave (E_R^i). Realizing the fact that the CP components defined in original coordinate and those in new coordinate are related as:

$$\begin{aligned}\hat{x} - j\hat{y} &= (\cos\phi_0\hat{x}' - \sin\phi_0\hat{y}') - j(\sin\phi_0\hat{x}' + \cos\phi_0\hat{y}') \\ &= e^{-j\phi_0}(\hat{x}' - \hat{y}') \qquad (3.12)\\ \hat{x} + j\hat{y} &= (\cos\phi_0\hat{x}' - \sin\phi_0\hat{y}') + j(\sin\phi_0\hat{x}' + \cos\phi_0\hat{y}') \\ &= e^{j\phi_0}(\hat{x}' + \hat{y}') \qquad (3.13)\end{aligned}$$

with which one can rewrite (3.11) as:

$$\begin{aligned}\vec{E}_R^{r'} =& \frac{1}{2}e^{-j\phi_0}(A_r + B_r)(\hat{x} + j\hat{y}) \\ &+ \frac{1}{2}e^{j\phi_0}(A_r - B_r)(\hat{x} - j\hat{y}) \qquad (3.14)\end{aligned}$$

$\vec{E}_R^i$ and $\vec{E}_R^{i'}$ are thus related as:

$$\vec{E}_R^i = e^{j\phi_0} E_R^{i'} \tag{3.15}$$

Therefore, when $\vec{E}_R^i$ is illuminating the rotated object, the reflected field will simply be (3.14) multiplied by a phase constant $e^{j\phi_0}$, which is:

$$\vec{E}_R^r = \frac{1}{2}(A_r + B_r)(\hat{x} + j\hat{y}) + \frac{1}{2}e^{j2\phi_0}(A_r - B_r)(\hat{x} - j\hat{y}) \tag{3.16}$$

What (3.16) suggests is that for an object under RHCP plane wave excitation, when the object is rotated by an angle of ϕ_0, the reflected RHCP component will obtain a phase shift of $2\phi_0$ whereas the reflected LHCP component will not experience any phase shift. Following similar procedures, one could also derive the expression of reflected wave under LHCP plane wave excitation:

$$\vec{E}_L^r = \frac{1}{2}e^{-j2\phi_0}(C_r + D_r)(\hat{x} + j\hat{y}) + \frac{1}{2}(C_r - D_r)(\hat{x} - j\hat{y}) \tag{3.17}$$

which means when the object is rotated by ϕ_0, a phase shift of $-2\phi_0$ will be introduced to the reflected LHCP component. In a word, the phase shift is introduced only to same-handed polarized component in reflected field.

Apparently, the derivations above is mathematically not specific to reflected field, and one should arrive at similar conclusions for transmitted wave as well. Indeed, by assuming the expression for transmitted field corresponding to RHCP and LHCP excitation:

$$\vec{E}_R^t = A_t\hat{x} + jB_t\hat{y} \tag{3.18}$$

$$\vec{E}_L^t = C_t\hat{x} + jD_t\hat{y} \tag{3.19}$$

and through similar derivations, one can obtain the expressions for the transmitted field under RHCP and LHCP excitation:

$$\vec{E}_R^t = \frac{1}{2}(A_t + B_t)(\hat{x} + j\hat{y}) + \frac{1}{2}e^{j2\phi_0}(A_t - B_t)(\hat{x} - j\hat{y}) \tag{3.20}$$

$$\vec{E}_L^t = \frac{1}{2}e^{-j2\phi_0}(C_t + D_t)(\hat{x} + j\hat{y}) + \frac{1}{2}(C_t - D_t)(\hat{x} - j\hat{y}) \tag{3.21}$$

Table 3.1: Summary of the "geometrical phase" property.

Incidence	Reflection	Transmission
RHCP	$\Delta\Psi = +2\phi_0$ in RHCP	$\Delta\Psi = +2\phi_0$ in LHCP
LHCP	$\Delta\Psi = -2\phi_0$ in LHCP	$\Delta\Psi = -2\phi_0$ in RHCP

An interesting observation from (3.20) and (3.21) is that: since the transmitted wave is propagating in -z direction, the phase shift is now introduced only to the polarization component orthogonal to the incident polarization. A summary of this phase shifting characteristic for different cases can be found in Table 3.1.

In reality, the "geometrical phase" property is widely applied in the design of reflectarrays or transmitarrays, where each element in the array is given a independent rotation angle to generate desired phase compensation. In these cases, it is often desired to maximize the amplitude of the component with phase shift (later referred to it as Co-Pol component) and minimize the component without phase shift (later referred to it as X-Pol component). To achieve this, the complex coefficients should satisfy:

$$\text{Reflection}: \begin{cases} \text{RHCP incidence}: & A_r = -B_r \\ \text{LHCP incidence}: & C_r = D_r \end{cases} \tag{3.22}$$

$$\text{Transmission}: \begin{cases} \text{RHCP incidence}: & A_t = -B_t \\ \text{LHCP incidence}: & C_t = D_t \end{cases} \tag{3.23}$$

which is to be achieved through proper design of the element. It is worth noting that, though the phase shift depends on rotation angle of the element but not frequency, there is still a frequency constraint when applying this property because condition (3.22) or (3.23) are potentially related with frequency.

3.3 Relating CP Coefficients to LP Coefficients

To better understand the physics of the phase shift characteristic and to facilitate the design of rotated elements, we will demonstrate the relationship between circular polarization coefficients A, B, C, D with linear polarization (LP) coefficients Γ and T. Taking reflection as example, let $\vec{E}^i = E_x^i\hat{x} + E_y^i\hat{y}$ to be the incident wave and $\vec{E}^r = E_x^r\hat{x} + E_y^r\hat{y}$ to be the reflected wave, a matrix equation can be written readily as:

$$\begin{bmatrix} E_x^r \\ E_y^r \end{bmatrix} = \begin{bmatrix} \Gamma_{xx} & \Gamma_{xy} \\ \Gamma_{yx} & \Gamma_{yy} \end{bmatrix} \begin{bmatrix} E_x^i \\ E_y^i \end{bmatrix} \tag{3.24}$$

where Γ_{mn} are the LP reflection coefficients. By substituting (3.6)-(3.9) in this matrix equation, one could relate the complex coefficients for CP to LP reflection coefficients Γ_{mn} as:

$$\begin{cases} A_r = \Gamma_{xx} + j\Gamma_{xy} \\ B_r = \Gamma_{yy} - j\Gamma_{yx} \\ C_r = \Gamma_{xx} - j\Gamma_{xy} \\ D_r = -\Gamma_{yy} - j\Gamma_{yx} \end{cases} \tag{3.25}$$

Assume one is designing a rotated element that reflects RHCP wave with a controllable phase shift, the goal for which is as we have proved: $A_r = -B_r$. With (3.25) we know that this goal is equivalent to:

$$\Gamma_{xx} = -\Gamma_{yy} \quad and \quad \Gamma_{xy} = \Gamma_{yx} \tag{3.26}$$

However, once condition (3.26) is satisfied, C_r will become equal to D_r as well. This implies that whenever an element is designed to work for either one of the CP polarized wave, this element will automatically work for both RHCP and LHCP wave.

Similar conclusions can be made for transmitted wave as well:

$$\begin{cases} A_t = T_{xx} + jT_{xy} \\ B_t = T_{yy} - jT_{yx} \\ C_t = T_{xx} - jT_{xy} \\ D_t = -T_{yy} - jT_{yx} \end{cases} \tag{3.27}$$

where T_{mn} are linear polarization transmission coefficients. The target of element optimization now become:

$$T_{xx} = -T_{yy} \quad \text{and} \quad T_{xy} = T_{yx} \tag{3.28}$$

The observations above suggest that it is possible to design rotated elements based on their LP reflection/transmission coefficients, though the rotation dependent phase shift is eventually gained by CP components.

3.4 Exceptions in Geometrical Phase Property

Exceptions in geometrical phase property exist in a group of objects with special rotation symmetry. For example, a pentagon as shown in Fig. 3.3 is an exception where the geometrical phase property does not hold. Such a pentagon rotated about its symmetry center by $2\pi/5$ (its rotation symmetry period) will become identical to itself before the rotation. This means the scattering problem before and after rotation should be identical. Assuming RHCP plane wave incidence and according to (3.16), one will end up with:

$$\begin{aligned} E_R^r|_{\phi_0=0} &= E_R^r|_{\phi_0=2\pi/5} \\ \Rightarrow (A_r - B_r) &= (A_r - B_r)e^{j4\pi/5} \end{aligned} \tag{3.29}$$

and (3.29) indicates that $A_r - B_r = 0$, which means this element will not reflect the desired Co-Pol component. Similar conclusions can be drawn for other excitation cases.

In fact, since the phase shift is twice the rotation angle, any object that possesses a rotation symmetry period less than π will encounter this issue and may not be used when rotated about its symmetry center. As illustrated in Fig. 3.4, there are in general 4 different combinations of object geometry and rotation center. Their characteristics are as follow:

1. As shown in Fig. 3.4 (a), the object has a rotation symmetry period less than π and is rotated about its symmetry center. Objects falls in this category will not provide the rotation dependent phase shift to Co-Pol component and should not be used as rotated element.

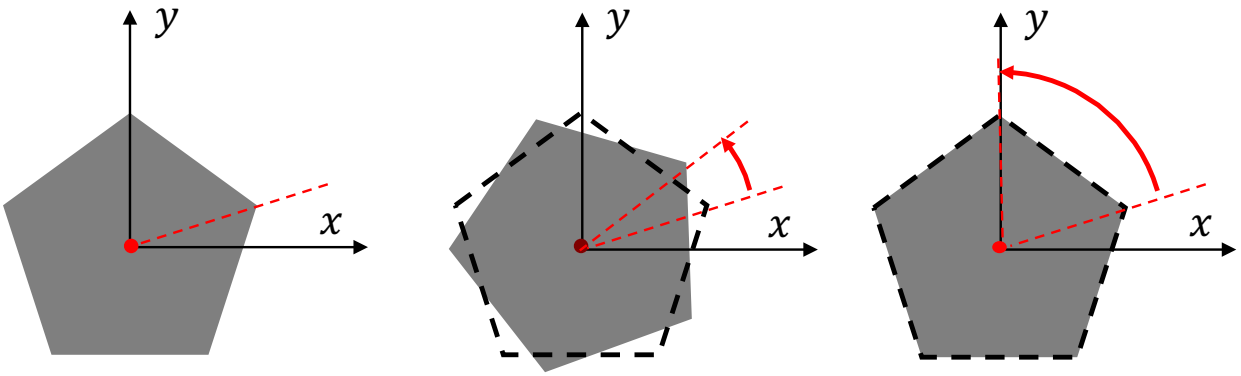

Figure 3.3 Pentagon as an example geometry that does not work with geometrical phase when rotated about its rotation symmetry center. The least angle to bring it back to itself is $2\pi/5$.

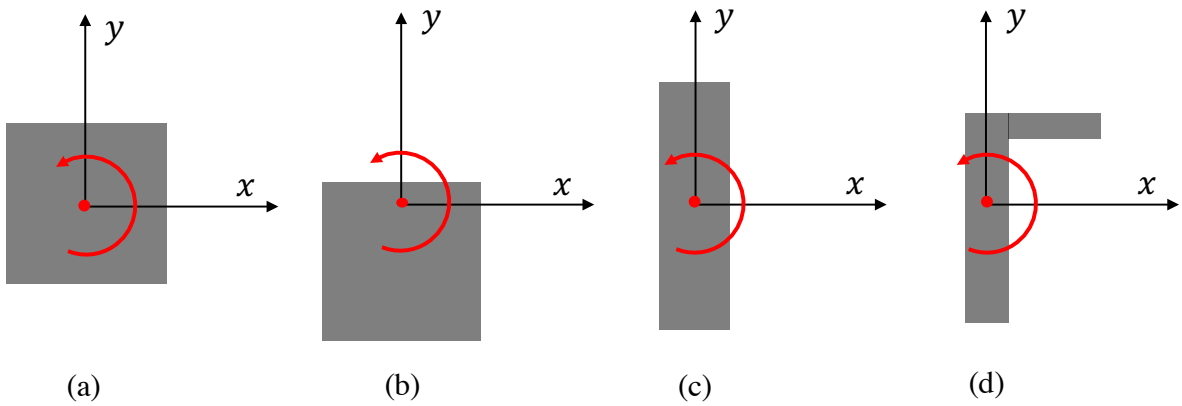

Figure 3.4 Four representative scenarios of rotated object. (a) An object that has a rotation symmetry period less than π and is rotated about its symmetry center. (b) An object that has a rotation symmetry period less than π but is not rotated about its symmetry center. (c) An object that has a rotation symmetry period equal to π and is rotated about its symmetry center. (d) An object that has a rotation symmetry period equal to 2π and is rotated about arbitrary center.

2. As shown in Fig. 3.4 (b), the object has a rotation symmetry period less than π but is not rotated about its symmetry center. In this case, the object will not overlap itself when rotated within $[0, \pi]$, therefore it is still possible to be used as rotated element providing phase shift.

3. As shown in Fig. 3.4 (c) and Fig. 3.4 (d), the object itself has a rotation symmetry period of π or 2π. In these cases, no matter which point is chosen as the center of rotation, the object will always manifest the rotation dependent phase shifting property.

To the best of the author's knowledge, all the elements employed in literatures so far reported complied the rules above [107, 108, 110].

3.5 Verification with Full-Wave Simulations

To verify the conclusions in previous sections, several representative elements are simulated in infinite array (using periodic boundary conditions) in CST Studio 2018. As a proof of concept, these elements are not necessarily designed to work in a particular reflectarray or transmitarray. In fact, we are focusing only on the reflection and transmission phase versus rotation angle of the element.

As shown in Fig. 3.5, a PEC rectangular as a representative geometry that has a rotation symmetry with a period of π is rotated. The phase of the reflection coefficient (S_{11}) and the phase of transmission coefficient (S_{21}) are shown. The curve labels, e.g.,"L(in) - R(out)" means that the curve is for "LHCP input to RHCP output", where "output" could be either reflection or transmission depending on which plot one is looking at. The phase curves manifests a linear dependence on rotation angle only for same-handedness polarized reflected wave and reverse-handedness transmitted wave. For the other cases, the phase remains constant, as the theory predicts. Shown in Fig. 3.6 is the reflection and transmission phase of a pentagon, whose rotation symmetry period is $2\pi/5$. As expected, the reflection phase and transmission phase no longer linearly depend on rotation angle. In Fig. 3.7, a spiral shaped element whose rotation symmetry period is 2π was rotated. In this case, both

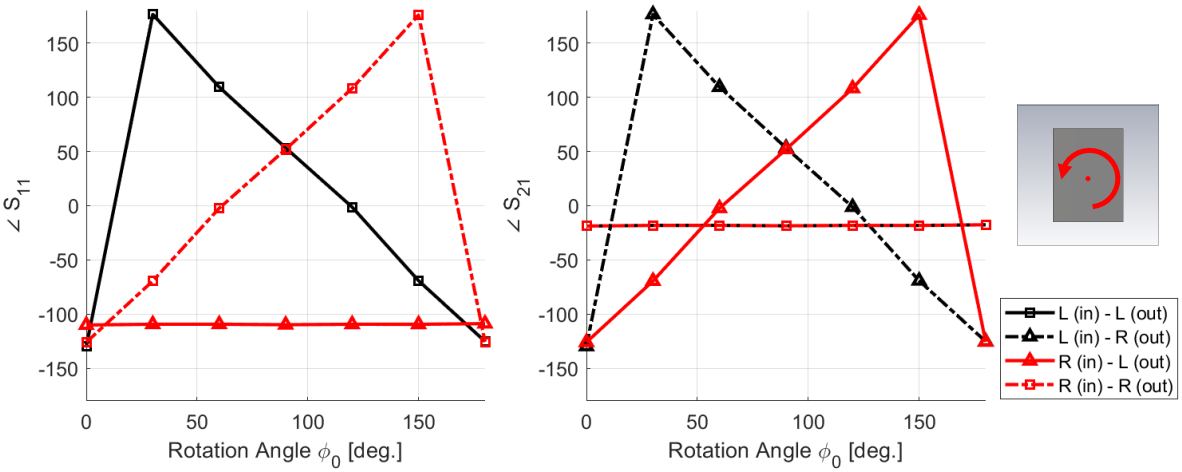

(a) (b)

Figure 3.5 The simulated (a) S_{11} phase and (b) S_{21} phase for PEC rectangular element. For reflected wave, the phase of same polarization component demonstrates linear dependence on rotation angle. For transmitted wave, the phase of orthogonally polarized component demonstrated linear dependence on rotation angle.

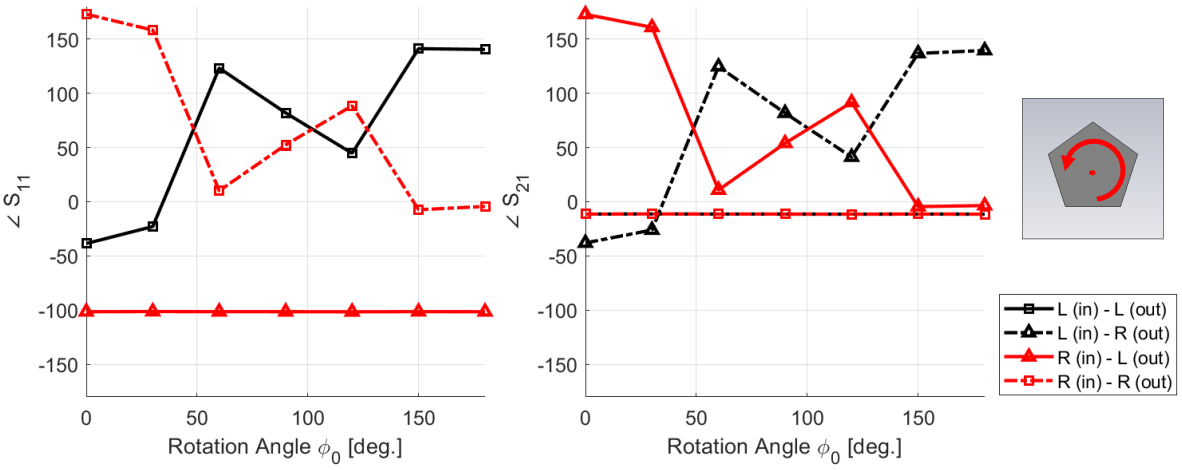

(a) (b)

Figure 3.6 The simulated (a) S_{11} phase and (b) S_{21} phase for PEC pentagon element. Linear dependence on the rotation angle is not observed.

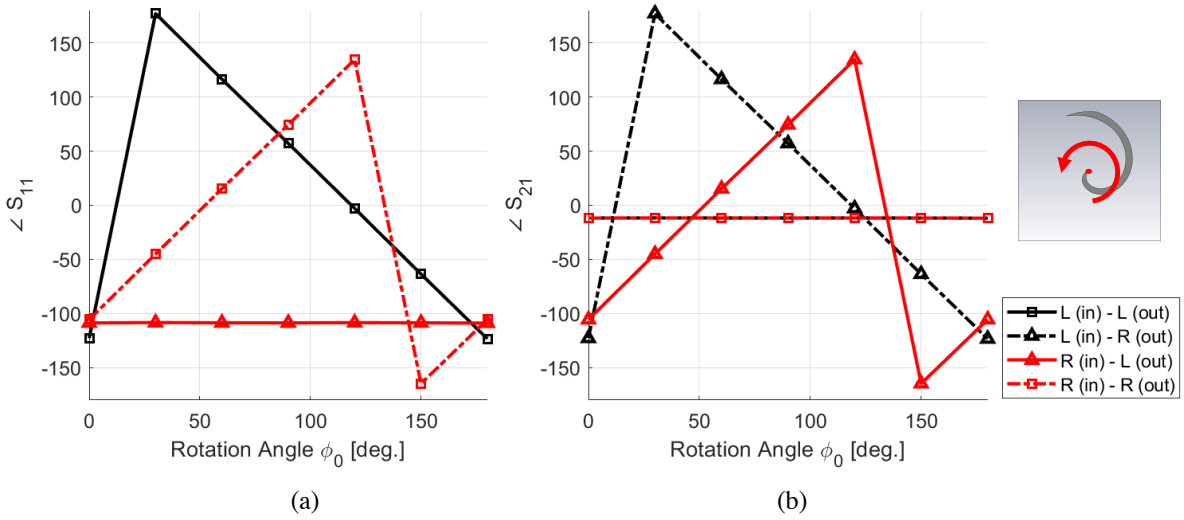

Figure 3.7 The simulated (a) S_{11} phase and (b) S_{21} phase for PEC spiral shaped element. For reflected wave, the phase of same polarization component demonstrates linear dependence on rotation angle. For transmitted wave, the phase of orthogonally polarized component demonstrated linear dependence on rotation angle.

the reflection phase and transmission phase behaved as predicted.

3.6 Summary on Element Rotation and Related Phase Response

This chapter revisited the CP phase shift effect of rotated objects, in self-radiating scenarios and in scattering scenarios. The radiated RHCP and LHCP components of a rotated object will experience conjugate phase shift, the absolute value of which equals the angle of rotation. Whereas when an object is illuminated by a CP wave, only one of the reflected/transmitted components gains a phase shift, the absolute value of which equals twice the angle of rotation. The CP phase shift's linear dependence on the angle of rotation offers numerous possibilities in the design of CP antenna arrays. However, in addition to this phase shift, it is of practical necessity to carefully design the geometry of the element to achieve maximum efficiency. For example, the reflection coefficient should be maximized for a reflectarray unit cell but minimized for a transmitarray unit cell. Implementing this property to achieve broadband reconfigurable CP unit cells also requires innovative designs. In the following chapters,

the phase shift related to rotation will be applied to design various novel beam steerable antennas.

CHAPTER 4

Low-Profile Mechanically Steerable Risley Prism Antenna (RPA) Enabled by Transmitarrays: Principles, System Simplification, Design, and Measurements

The recent advancements in mechanical beam steering technologies have refreshed the typical conception people have about mechanically steerable antennas (MSA): instead of antennas driven by bulky gimbals, novel MSAs exploring low-profile reconfiguration mechanisms and exploiting thin-panel transmitarrays/metasurfaces have been reported in recent literature [111]. Meanwhile, these MSAs maintain the advantages of lower cost, lower electronic complexity, and better efficiency compared to electronically steerable antennas such as phased arrays. Therefore, novel low-profile MSAs are considered competitive for many scenarios in next-generation communication platforms [111]. Risley prism antenna (RPA), also referred to as the near-field meta steering (NFMS) antenna, is a representative low-profile MSA technique that has gained much popularity [49–52, 112–118].

Risley prism (RP) is an optical beam steering concept that utilizes a pair of wedge prisms to scan a beam of light [119]. Every single prism has the effect of deflecting the incident beam by a certain angle. Combining two such prisms gives one the flexibility to control the output beam directions through the rotation of the prisms (as illustrated in Fig. 4.2(a)). This concept has gained interest is steerable antenna applications for its advantage that the beam steering is achieved purely mechanically without any active components or bias networks. In [53], a pair of rotated dielectric wedges which functions similarly as optical prisms were used to achieve beam scan at 12 GHz. Evolving from this concept, several recent works

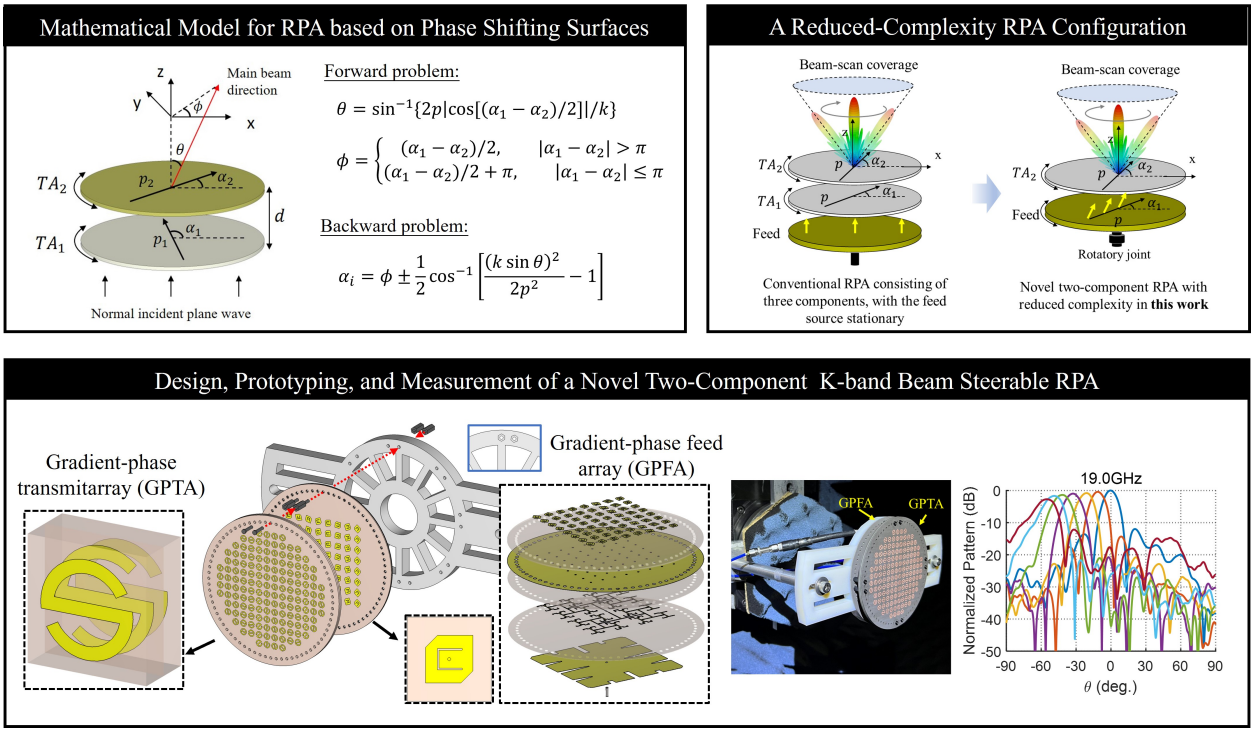

Figure 4.1 Summary of the outline and the key contributions of this chapter.

have demonstrated the feasibility of replacing the bulky dielectric wedges with planar phase shifting surfaces such as transmitarrays [49–51, 120] or graded-dielectric plates [52]. These phase-shifting surfaces function similarly to dielectric wedges in terms of providing beam deflection but with significantly reduced thickness and weight. In [49], an antenna under RP configuration was built with phase shifting surfaces whose thickness was only one-tenth of wavelength at 30 GHz (Fig. 4.2(b)). These antennas adopting the concept of RP will be referred to as Risley prism antenna (RPA) throughout this dissertation.

This chapter is organized as the following: first, the working principle of the RPA is elaborated. A novel mathematical model based on the phase method is established to explicitly relate the beam pointing direction, phase gradient of the "prisms", and the orientation of the "prisms"; Second, gradient-phase transmitarrays are designed to serve as the "prisms" of the RPA. Simulation results of the RPA are presented to verify the proposed beam steering model and to reveal its improvement over the paraxial method conventionally used. Third, a novel two-component RPA configuration is proposed to significantly reduce the complexity

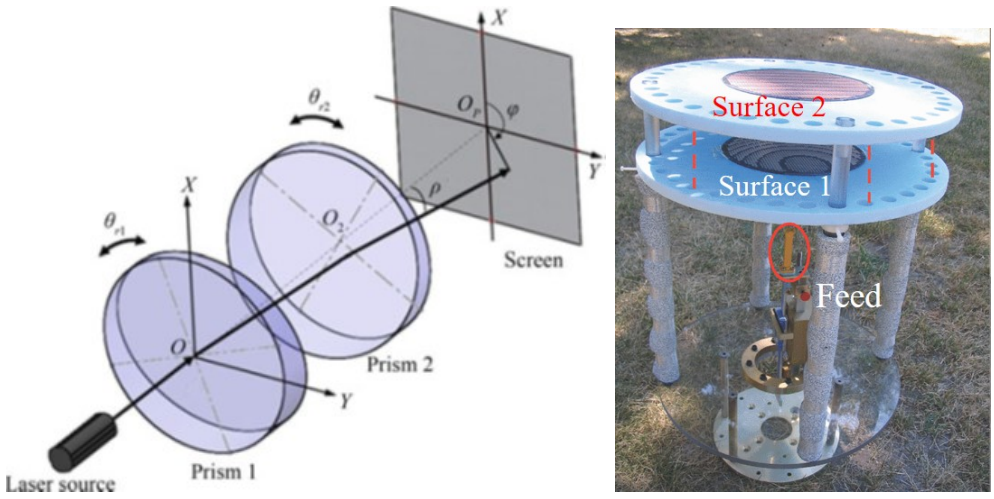

(a) (b)

Figure 4.2 (a) Conceptual view of an optical Risley prism system consists of two wedge prisms [119]. (b) A representative Risley prism antenna based on phase shifting surfaces at 30 GHz [49].

and weight of CP RPA systems. A novel hybrid-phasing gradient-phase feed array panel and a gradient-phase transmitarray panel are designed and manufactured, the constituent two-component RPA is extensively measured for its radiation pattern, beam scan range, and scan resolution, as well as bandwidth performance. The outline and key contributions of this chapter are also summarized in Fig. 4.1.

4.1 The Phase Method as a More Accurate Beam Steering Model for RPA based on Phase Shifting Surfaces

4.1.1 The Necessity of a Beam Steering Model for RPA and the Limitations of Existing Models

Beam steering with RP or RPA necessitates establishing a explicit description of the relationship between the orientation of the "prisms" and the beam pointing direction. This relationship contains a bi-directional problem [121]: (a) the forward problem is to predict the beam scan angle given the orientations of the prisms; (b) the backward problem, which is more concerned in real-world application, is to determine the prism rotation angles based

on a target beam direction. Comprehensive studies has been conducted in optical domain intended for establishing steering model for RPs. In [121], a sophisticated mathematical model was constructed by rigorously tracing the rays traveling through each face of the prisms. This method allows one to solve the forward problem accurately with analytical expression, but to solve the backward problem only through numerical methods. With certain level of approximation, the paraxial method [122] obtains simple and analytical expression for both the forward and backward problems. This approximated method applies well in optical RP systems and has also served as a reasonable prediction model for RPAs [50–52].

However, adopting beam steering models from optics for RF RPA can be questionable, especially for RPAs incorporating planar phase shifting surfaces such as transmitarrays. This concern originates from the fundamentally different beam deflecting mechanisms of a phase shifting surface compared to a wedge prism: a phase shifting surface tilts the beam by introducing a gradient phase shift, whereas a prism (dielectric wedge) deflects the beam through multi-refractions determined by Snell's law. Moreover, as has been observed [50,123] and as will be shown in this section, the accuracy of paraxial method degrades considerably at large scanning angles in elevation (e.g., $> 40^{\circ}$). In reality, mis-pointing of the beam can lead to failure in signal reception especially for high gain RPAs whose beamwidth can be too narrow to tolerate the pointing error. While array theory has been used to determine the beam directions for RPAs based on transmitarrays [49, 120], it was utilized only to predict beam direction for given surface orientations, and its analytical solution to the backward problem was not demonstrated. Moreover, array theory lacks generality since it does not work for RPAs implementing other types of surfaces that does not contain array elements (e.g., graded-dielectric plate). Motivated by the reasons above, this section will revisit the general beam steering mechanism for RPAs utilizing phase shifting surfaces, and propose an analytical model to more accurately relate the surface orientations with beam pointing angles using a method of phase.

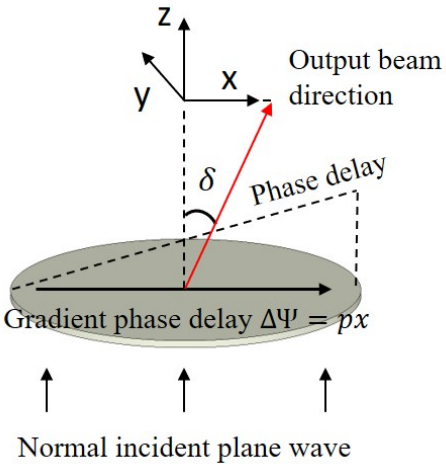

Figure 4.3 Illustration of a single phase shifting surface with a gradient phase delay along x. A normally incident plane wave will be deflected by an angle of δ towards the direction of gradient.

4.1.2 Development of the Phase Method for RPA Based on Phase Shifting Surfaces

An RPA is typically constructed with a pair of rotatable beam deflectors, the effect of each is to deflect the propagation direction of a incident beam by certain angle. In this section, we will focus exclusively on the specific type of beam deflectors realized with phase shifting surfaces. The mechanism of such a surface is as illustrated in Fig. 4.3. The surface deflects the beam by introducing a linear phase delay $\Delta\Psi(x, y) = px$ (gradient along x) to the transmitted wave, where p is the gradient of phase delay and is positive. We assume plane wave behavior for the input and output wave and assume p is polarization independent. Then, for a given incident wave $E^i = E_0 \exp(-jkz)$ the output wave can be written as:

$$\begin{aligned} E^o &= TE_0 \exp[-j(\Delta\Psi(x, y) + k_z^o z)] \\ &= TE_0 \exp[-j(px + k_z^o z)] \end{aligned} \tag{4.1}$$

where k is the free space wavenumber and T is the magnitude of transmission that is desired to be close to unity. Note that we refer to $\Delta\Psi(x, y)$ as "phase delay" such that the beam deflection aligns along the direction of the gradient. As a result, the corresponding "phase shift" to the transmitted wave becomes $-\Delta\Psi(x, y)$, which is consistent with the fact that a

"delay" in time creates negative offset in phase.

Let (k_x^o, k_y^o, k_z^o) be the corresponding components of the output wave vector and satisfy $k_x^{o2} + k_y^{o2} + k_z^{o2} = k^2$ to comply plane wave assumption. Note that in this case $k_x^o = p$, $k_y^o = 0$. The output beam direction in terms of elevation (θ) and azimuth (ϕ) can be then determined by:

$$\theta = \sin^{-1} \frac{\sqrt{k_x^{o2} + k_y^{o2}}}{k} = \sin^{-1} \frac{p}{k} = \delta \tag{4.2}$$

$$\phi = \tan^{-1} \frac{k_y^o}{k_x^o} + \xi\pi = 0 \tag{4.3}$$

where factor ξ depends on the sign of k_x^o as:

$$\xi = \begin{cases} 0, & k_x^o \geq 0 \\ 1, & k_x^o < 0 \end{cases} \tag{4.4}$$

It can be concluded that such a beam deflector will tilt the normal incident wave along the direction of its phase delay gradient by an angle of δ. This angle δ is conventionally used to characterize such a surface and, as will be demonstrated later, it also serves as a link to relate phase method with paraxial method.

A typical RPA can be constructed by assembling two of such beam deflectors, and its beam steering mechanism can also be understood with a method of phase. As depicted in Fig. 4.4, two beam deflectors TA_1 and TA_2 are placed in parallel with a spacing of d and with their axes aligned. TA_1 and TA_2 have phase delay gradient of p_1 and p_2 respectively. The two surfaces can be independently rotated, and we denote the angle formed between their phase delay gradient and x axis by α_1 and α_2. Then, the phase delay by each surface can be written as:

$$\Delta\Psi_1(x, y) = p_1 \cos\alpha_1 x + p_1 \sin\alpha_1 y \tag{4.5}$$

$$\Delta\Psi_2(x, y) = p_2 \cos\alpha_2 x + p_2 \sin\alpha_2 y \tag{4.6}$$

We assume the wave propagating through this system maintains a plane wave behavior, then with the same incident wave $E^i = E_0 \exp(-jkz)$, the wave at the immediate output of TA_1 becomes:

$$E_1 = T_1 E_0 \exp\{-j[\Delta\Psi_1(x, y) + k_z' z]\} \tag{4.7}$$

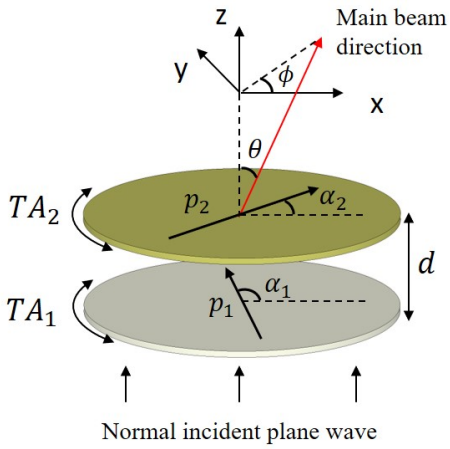

Figure 4.4 Illustration of an RPA consisting of two coaxially placed beam deflecting surfaces TA_1 and TA_2 with a relative spacing of d. TA_1 and TA_2 can be rotated, and the angles formed between their phase delay gradients and $\hat{x}$ direction are denoted as α_1 and α_2. The gradients of the two surfaces are p_1 and p_2. The output main beam direction is characterized by (θ, ϕ).

where T_1 is the transmission magnitude of TA_1 and $k_z' = \sqrt{k^2 - p_1^2}$. The wave at the immediate input of TA_2 gains a constant phase due to propagation:

$$E_2 = E_1 \cdot e^{-jk_z' d} \tag{4.8}$$

and this allows one to determine the output of TA_2 as:

$$\begin{aligned} E_{out} &= T_1 T_2 e^{-jk_z' d} E_0 \exp[-j(\Delta\Psi_1 + \Delta\Psi_2 + k_z^o z)] \\ &= T_1 T_2 e^{-jk_z' d} E_0 \exp[-j(k_x^o x + k_y^o y + k_z^o z)] \end{aligned} \tag{4.9}$$

Again, k_z^o should comply the condition $k_x^{o2} + k_y^{o2} + k_z^{o2} = k^2$, with the expressions of k_x^o and k_y^o being:

$$k_x^o = p_1 \cos\alpha_1 + p_2 \cos\alpha_2 \tag{4.10}$$

$$k_y^o = p_1 \sin\alpha_1 + p_2 \sin\alpha_2 \tag{4.11}$$

Eventually, the output beam direction in elevation and azimuth can be obtained by substi-

tuting (4.10), (4.11) into (4.2), (4.3):

$$\theta = \sin^{-1}\left\{\frac{1}{k}[p_1^2 + p_2^2 + 2p_1p_2\cos(\alpha_1 - \alpha_2)]^{1/2}\right\} \tag{4.12}$$

$$\phi = \tan^{-1}\left(\frac{p_1\sin\alpha_1 + p_2\sin\alpha_2}{p_1\cos\alpha_1 + p_2\cos\alpha_2}\right) + \xi\pi \tag{4.13}$$

in which ξ can be determined with (4.4), (4.10) and (4.11).

It can be observed from (4.12) that the minimum elevation angle θ of the beam can not reach 0 unless $p_1 = p_2$ and $\alpha_1 = \alpha_2$. For the beam scan range to cover the broadside direction, TA_1 and TA_2 must have the identical phase gradient, i.e., $p_1 = p_2 = p$. This condition leads to further simplification of (4.12) and (4.13):

$$\theta = \sin^{-1}\left\{2p\left|\cos\left[(\alpha_1 - \alpha_2)/2\right]\right|/k\right\} \tag{4.14}$$

$$\phi = \begin{cases} (\alpha_1 + \alpha_2)/2 & ,|\alpha_1 - \alpha_2| \le \pi \\ (\alpha_1 + \alpha_2)/2 + \pi & ,|\alpha_1 - \alpha_2| > \pi \end{cases} \tag{4.15}$$

Equation (4.14) and (4.15) indicate that the scan range of the RPA is $0^\circ \le \theta \le \sin^{-1}(2p/k)$ and $0^\circ \le \phi < 360^\circ$, corresponding to a conical solid angle range. For example, if the maximum elevation scan angle of the RPA is expected to be $\theta = 60^\circ$, the required phase gradient is $p = 0.433k$. The beam pointing resolution (BPR) is dominated by the angular resolution $\Delta\alpha$ of the mechanical rotations applied to TA_1 and TA_2. The resolutions in θ and ϕ can be estimated using (4.14), (4.15) and taking the derivative with respect to α_1 (or α_2):

$$\Delta\theta = \left|\frac{\partial\theta}{\partial\alpha_1}\right|\Delta\alpha = \frac{\Delta\alpha p\left|\sin\left[(\alpha_1 - \alpha_2)/2\right]\right|/k}{\sqrt{1 - 4p^2\cos^2\left[(\alpha_1 - \alpha_2)/2\right]/k^2}} \tag{4.16}$$

$$\Delta\phi = \left|\frac{\partial\phi}{\partial\alpha_1}\right|\Delta\alpha = \Delta\alpha/2 \tag{4.17}$$

While $\Delta\theta$ depends on α_1, α_2, it is no greater than $(p/k)\cdot\Delta\alpha$. Therefore, the BPR in both elevation and azimuth is no greater than half of the mechanical rotation resolution, i.e., $\Delta\alpha/2$.

In practice, it is necessary to calculate the required orientation angles of TA_1 and TA_2 based on a target beam scan angle (θ_t, ϕ_t). Using (4.14) and (4.15), the required rotation

Table 4.1: Mathematical expression of beam steering models derived with phase method and paraxial method as well as the approximations relating the two methods.

Phase Method (This Work)	$\Longrightarrow$	Paraxial Method [50]
$\theta = \sin^{-1}\left\{\frac{1}{k}[p_1^2 + p_2^2 + 2p_1p_2\cos(\alpha_1 - \alpha_2)]^{1/2}\right\}$	Take "$\sin^{-1} x \approx x$" and recall $\delta_i = \sin^{-1}(p_i/k) \approx p_i/k$	$\theta = [\delta_1^2 + \delta_2^2 + 2\delta_1\delta_2\cos(\alpha_1 - \alpha_2)]^{1/2}$
$\phi = \tan^{-1}\left(\frac{p_1\sin\alpha_1 + p_2\sin\alpha_2}{p_1\cos\alpha_1 + p_2\cos\alpha_2}\right) + \xi\pi$		$\phi = \tan^{-1}\left(\frac{\delta_1\sin\alpha_1 + \delta_2\sin\alpha_2}{\delta_1\cos\alpha_1 + \delta_2\cos\alpha_2}\right) + \zeta\pi$
$\xi = \begin{cases} 0, & p_1\cos\alpha_1 + p_2\cos\alpha_2 \geq 0 \\ 1, & p_1\cos\alpha_1 + p_2\cos\alpha_2 < 0 \end{cases}$		$\zeta = \begin{cases} 0, & \delta_1\cos\alpha_1 + \delta_2\cos\alpha_2 \geq 0 \\ 1, & \delta_1\cos\alpha_1 + \delta_2\cos\alpha_2 < 0 \end{cases}$
Special Case $p_1 = p_2 = p$	$\Longrightarrow$	Special Case $\delta_1 = \delta_2 = \delta$
$\theta = \sin^{-1}\left[2\frac{p}{k}\left\lvert\cos(\frac{\alpha_1 - \alpha_2}{2})\right\rvert\right]$	Take "$\sin^{-1} x \approx x$", "$\sin x \approx x$" and recall $\delta = \sin^{-1}(p/k) \approx p/k$	$\theta = 2\delta\left\lvert\cos(\frac{\alpha_1 - \alpha_2}{2})\right\rvert$
$\phi = \begin{cases} (\alpha_1 + \alpha_2)/2 & , \lvert\alpha_1 - \alpha_2\rvert \leq \pi \\ (\alpha_1 + \alpha_2)/2 + \pi & , \lvert\alpha_1 - \alpha_2\rvert > \pi \end{cases}$		$\phi = \begin{cases} (\alpha_1 + \alpha_2)/2 & , \lvert\alpha_1 - \alpha_2\rvert \leq \pi \\ (\alpha_1 + \alpha_2)/2 + \pi & , \lvert\alpha_1 - \alpha_2\rvert > \pi \end{cases}$
$\alpha_i = \phi \pm \frac{1}{2}\cos^{-1}\left[\frac{(k\sin\theta)^2}{2p^2} - 1\right]$		$\alpha_i = \phi \pm \frac{1}{2}\cos^{-1}\left[\frac{\theta^2}{2\delta^2} - 1\right]$

angles α_1, α_2 can be calculated as:

$$\alpha_i = \phi_t \pm \frac{1}{2}\cos^{-1}\left[\frac{(k\sin\theta_t)^2}{2p^2} - 1\right] \tag{4.18}$$

These expressions derived with phase method are summarized in in Table 4.1 and compared with the corresponding equations suggested by paraxial method [50] which is adopted from optics. Though the two methods rely on different characterization of the surfaces (phase method uses phase gradient p whereas paraxial method uses tilt angle δ), a strong resemblance between the expressions can be observed. Indeed, by recalling (4.2) and taking the first order approximation for the trigonometric functions, the equations by phase method can reduce to corresponding equations given by paraxial method. For consistency in format, a factor ζ which functions similarly to ξ is introduced in the general expression of ϕ by paraxial method. Another interesting observation from Table 4.1 is that under the special case of $p_1 = p_2$ the two methods have identical expression for the prediction of ϕ. These observations imply that the major discrepancy between the two methods lies in the prediction of elevation angle θ, and this difference will become more significant when gradient p is large

(in which case the first order approximation does not hold).

To manifest the difference between the two methods, we considered two cases: (i) TA_1 and TA_2 have relatively small phase gradients $p_1 = p_2 = 0.174k$ (equivalent to $\delta = 10°$); (ii) TA_1 and TA_2 have larger phase gradients $p_1 = p_2 = 0.423k$ (equivalent to $\delta = 25°$). For each case, we set $\alpha_2 = 0$ and vary α_1 continuously from 0° to 360°. This is effectively fixing TA_2 and rotating TA_1. We then calculated the beam directions (θ, ϕ) predicted by both methods using the equations in Table 4.1 and plotted the trajectories formed by (θ, ϕ) in polar plot as shown in Fig. 4.5(a). By varying only α_1, the predicted beam locations fall on a closed contour in $\theta - \phi$ plane. To provide a more intuitive representation of this beam scan behavior, we plotted in Fig. 4.5(b) the conical surfaces swept by the vector of main beam directions. Observations of both plots suggest that: when p is small, the two methods are mathematically similar; when p is large, the discrepancy between the two methods is revealed and this difference becomes more significant as the beam scans further away from broadside. The maximum difference in the prediction of θ can reach 7.9° in case (ii).

Fig. 4.5 demonstrated the representative beam scan behavior of an RPA when only single surface is rotated. It can be inferred that by rotating both surfaces, one is able to achieve more beam coverage. It is evident from (4.14) and (4.15) that the elevation angle θ of the beam is determine by the difference of α_1 and α_2, whereas the azimuth angle ϕ of the beam is determined by the average of α_1 and α_2. Therefore by properly rotating the two surfaces, the beam can cover full 360° in azimuth. However, the maximum reachable angle in elevation is limited by a θ_{max}, which can be determined by letting $\alpha_1 = \alpha_2$ in (4.14).

4.2 Design of a CP Transmitarray-Based RPA to Validate the Phase Method

In this section, we will demonstrate the design of a CP beam steerable RPA based on gradient-phase transmitarrays. The RPA will be designed at 19 GHz to realize 2D beam scan up to 60° from broadside. This RPA serves as an initial design for concept validation and will be used to verify our mathematical beam steering models proposed in the previous

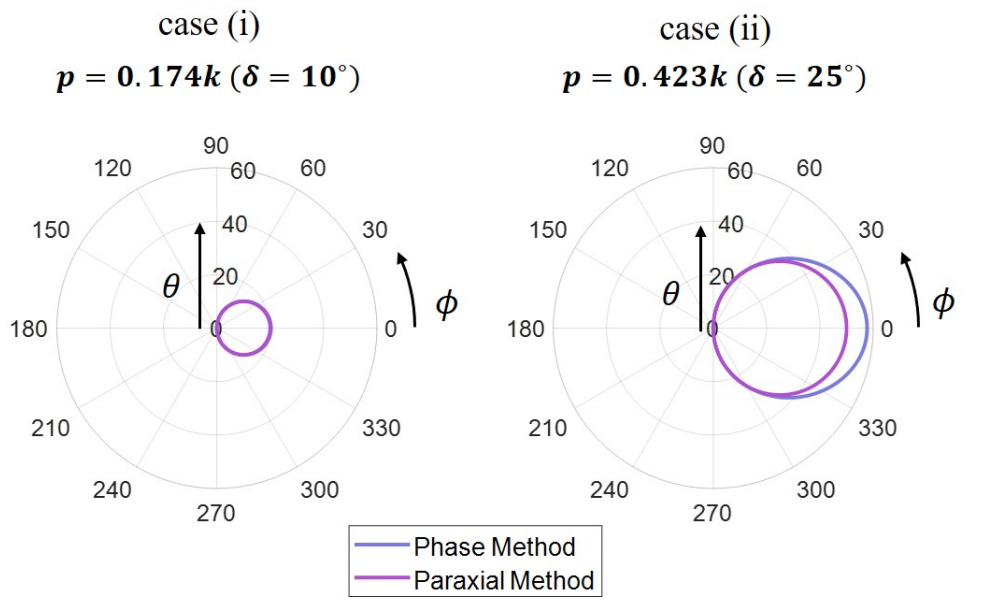

(a)

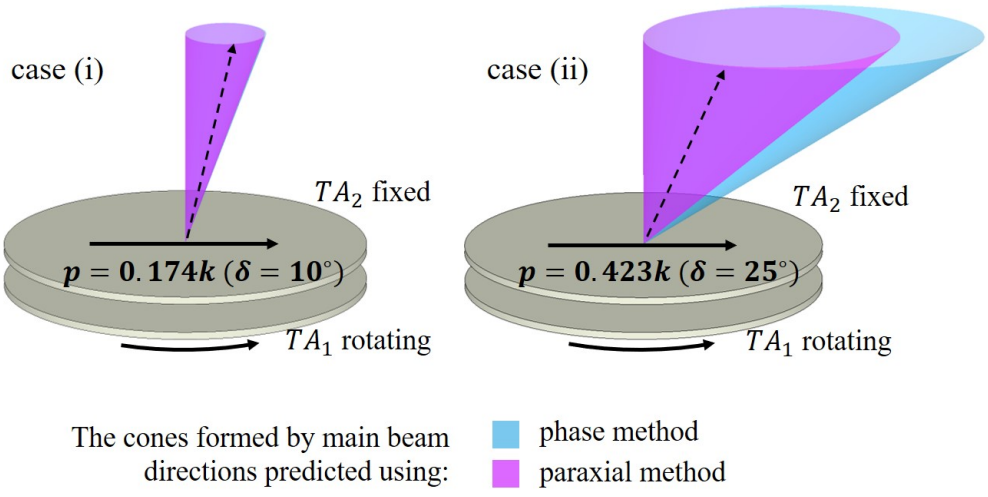

(b)

Figure 4.5 Representative beam scan directions calculated with phase method and paraxial method according to Table 4.1. Two cases were demonstrated: case (i) $p_1 = p_2 = 0.174k$ ($\delta = 10^{\circ}$); case (ii) $p_1 = p_2 = 0.423k$ ($\delta = 25^{\circ}$). For each case, the beam locations were calculated by letting $\alpha_2 = 0$ and varying α_1 continuously from 0° to 360°. (a) The contour formed by calculated main beam locations (θ, ϕ) presented in polar plot. (b) A conceptual illustration of the conical surfaces swept by the vector of main beam directions.

section.

4.2.1 Design of CP Transmitarray Unit Cell

A qualified transmitarray unit cell should have high transmission to the incident wave and be able to provide varied phase shift. We exploit the "rotation-phase" property [46] in the unit cell design, which allows one to achieve 360° CP phase compensation through the rotation of the element. In particular, when the element in an unit cell is rotated counter-clockwise (looking from incident side) by ϕ_0, the orthogonal CP components in the transmitted wave will gain a phase shift proportional to ϕ_0. To be specific, for RHCP incidence, the transmitted LHCP component will gain a phase shift of $2\phi_0$; for LHCP incidence, the transmitted RCHP component will gain a phase shift of $-2\phi_0$. This property can be summarized in the form of a transmission matrix:

$$\begin{bmatrix} E_L^t \\ E_R^t \end{bmatrix} = \begin{bmatrix} T_{LL}^{\phi_0=0} & T_{LR}^{\phi_0=0} e^{j2\phi_0} \\ T_{RL}^{\phi_0=0} e^{-j2\phi_0} & T_{RR}^{\phi_0=0} \end{bmatrix} \begin{bmatrix} E_L^i \\ E_R^i \end{bmatrix} \tag{4.19}$$

where E_L^i, E_R^i and E_L^t, E_R^t are the LHCP and RHCP components in the incident and transmitted wave; $T_{LL}^{\phi_0=0}, T_{LR}^{\phi_0=0}, T_{RL}^{\phi_0=0}, T_{RR}^{\phi_0=0}$ are the corresponding CP transmission coefficients before the rotation of the element. Although the rotation-dependent phase shift exists regardless of the transmission magnitude, one should properly design the geometry of the unit cell to maximize the transmission of desired CP component (i.e., to maximize $|T_{LR}|$ and $|T_{RL}|$).

The geometry of the unit cell is as shown in Fig. 4.6. The unit cell contains three identical "S-ring" shaped metallic elements which are separated by two dielectric layers of the same thickness. The element spacing P is 5.8 mm, which is approximately 0.37λ (λ: free space wavelength at 19 GHz). As illustrated in Fig. 4.6, the profile of the S-ring is carved out from a circular ring with outer radius R_{out} and inner radius R_{in}. The ring is opened in both sides by gaps corresponding to a sector angle of α. The trace width of the central line as well as the ring is w. The details of the parameters can be found in Fig. 4.6. Rogers RO3003 ($\epsilon_r = 3$) is chosen as the dielectric material and one of the standard thickness $t = 1.52$ mm

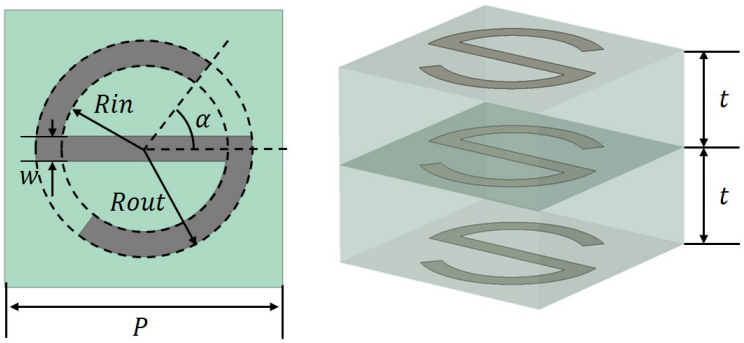

P	R_{out}	R_{in}
5.8 mm	2.26 mm	1.73 mm
w	α	t
0.53	53°	1.52 mm

Figure 4.6 Geometry of the S-ring element and the values for design parameters. The thickness of the substrate is exaggerated in the diagram for better illustration.

is used. For proof of concept, the dielectric loss is not considered and the metal layers are treated as PEC sheet with zero thickness. The unit cell was simulated in CST studio using periodic boundary conditions to obtain the CP transmission coefficients. The S-rings on three layers were rotated synchronously to provided different unit cell phase shift.

Fig. 4.7(a) shows the curves of $|T_{LR}|$ and $|T_{RR}|$ for different element rotation angle ϕ_0. At 19 GHz, it can be observed that the magnitude of T_{LR} remained close to unity and the magnitude of T_{RR} remained below -15 dB as the element rotates. The phase curves of T_{LR} are as shown in Fig. 4.7(b) for different ϕ_0. The phase curves are equally spaced with a relative increment around 90°, which justifies the phase shift's linear dependency on ϕ_0. Similar results can be observed for T_{RL} and T_{LL} in Fig. 4.7(c) and 4.7(d). Note that in this case, the phase curves manifest a relative decrement of 90°, which agrees with the negative sign in the linear dependency. These results validated the proposed unit cell.

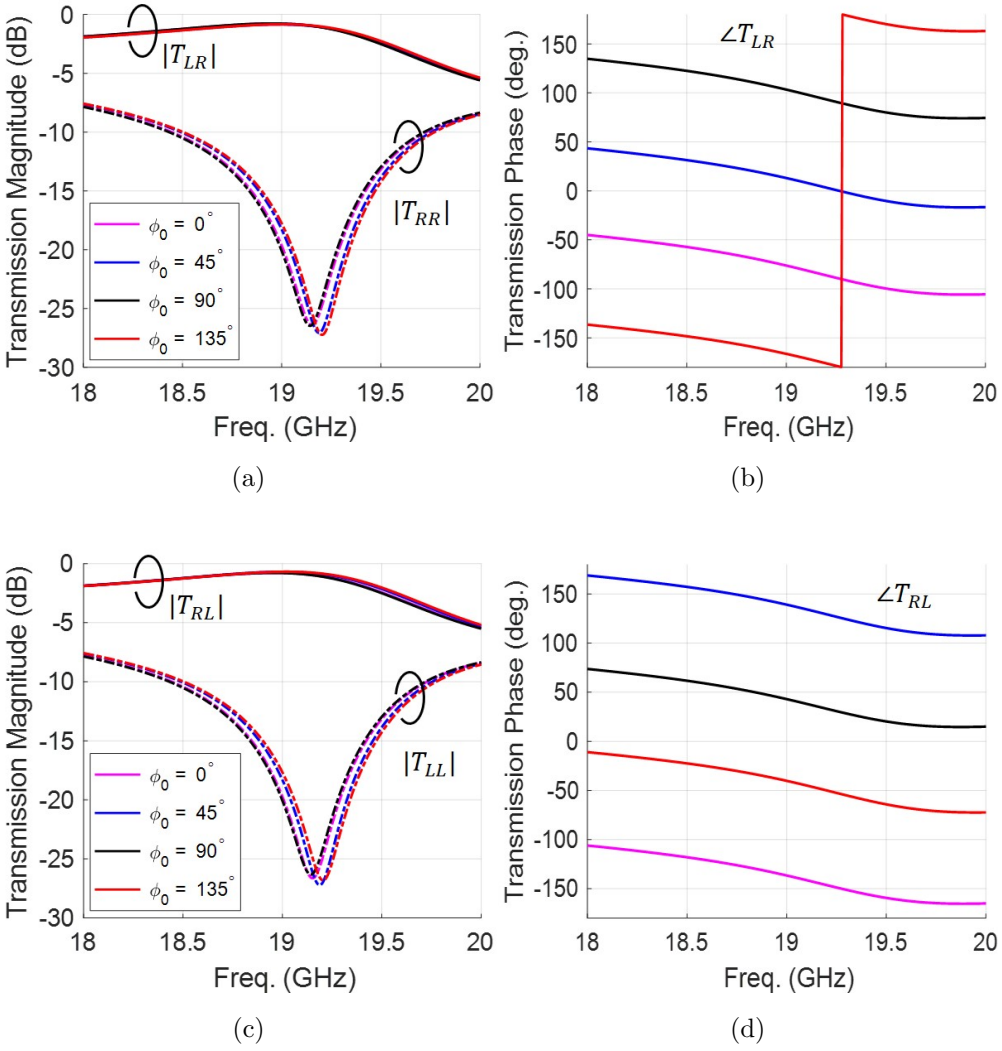

Figure 4.7 Unit cell transmission coefficient vs. element rotation angle ϕ_0. (a) The transmission magnitude $|T_{LR}|$ and $|T_{RR}|$; (b) The transmission phase $\angle T_{LR}$; (c) The transmission magnitude $|T_{RL}|$ and $|T_{LL}|$; (d) The transmission phase $\angle T_{RL}$.

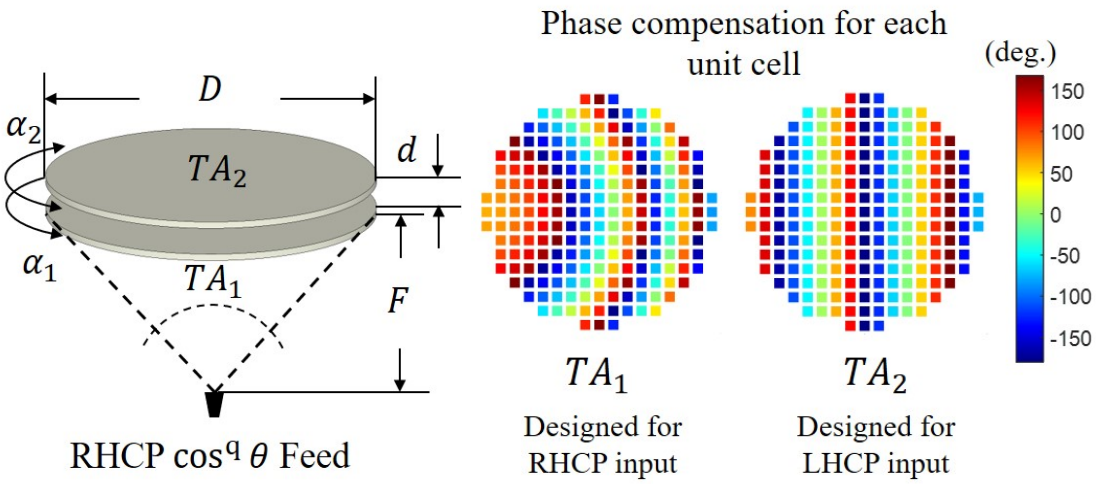

(a) (b)

Figure 4.8 (a) An illustration of the RPA configuration designed for simulation. (b) The required unit cell phase compensation calculated for TA_1 and TA_2. TA_1 compensates the spherical phase from the feed to uniform, and introduces a gradient phase to deflect the beam. TA_2 simply introduces a gradient phase to deflect the beam.

4.2.2 Design of the RPA

The configuration of the RPA proposed in this work is depicted in Fig. 4.8(a). The RPA has a circular aperture with a diameter of $D = 10$ cm ($\approx 6.33\lambda$). Two gradient-phase transmitarrays TA_1 and TA_2 are coaxially placed with a spacing d to be determined. For concept validation, an ideal RHCP feed with $\cos^q(\theta)$ pattern [124] will be used to illuminate the RPA symmetrically with a $F/D = 1$. The focal length F is measured from the phase center of the feed to the center of the first face of TA_1. For the $\cos^q(\theta)$ model we set $q = 10.32$ to provide a edge taper around -10 dB.

It is evident from the derivations in Section 4.1.2 that phase of the input wave plays an important role in the proper steering of the beam. Phase method assumes normal incident plane wave whose phase is uniform at the input of the RPA. However, the $\cos^q(\theta)$ feed used for our simulation as well as most feed sources in reality do not satisfy this uniform phase assumption. This necessitates an extra phase correction to obtain the uniform phase distribution as needed. While this can be realized by introducing an extra layer of phase shifting surface between the feed and TA_1, we embedded this correction effect into TA_1 and

avoided the addition of new structures. The phase correction of TA_1 is the combination of a spherical phase correction and a linear gradient phase correction:

$$\Delta\Psi_1(x,y) = -k\sqrt{x^2+y^2+F^2} + px \tag{4.20}$$

In (4.20), the first part is used for transforming the spherical phase from the feed to uniform, and the second part is responsible for giving the output beam a tilt angle. Note that the spherical phase compensation is independent of the orientation of TA_1 due to the symmetric feeding configuration. The design of TA_2 is then to simply introduce a linear gradient phase correction:

$$\Delta\Psi_2(x,y) = px \tag{4.21}$$

Both TA_1 and TA_2 are designed to provide a phase delay gradient of $p = 0.433k$ (equivalent tilt angle $\delta \approx 25.7°$), which should allow the RPA to provide a maximum scan angle of $\theta_{max} = 60°$ according to (4.14). First, $p = 0.433k$ was used in (4.20) and (4.21) to calculate the phase compensation for each unit cell in TA_1 and TA_2. The determined phase compensation for TA_1 and TA_2 is shown in Fig. 4.8(b). The S-ring elements were properly rotated based on the calculated phase compensation. The constructed TA_1 and TA_2 were first simulated individually to verify their deflect angle. TA_1 was simulated with the $\cos^q(\theta)$ source and provided a beam at $\theta = 25.4°$. TA_2 was simulated with a aperture source with uniform phase and provided a beam at $\theta = 25.3°$. The slight angle differences is mainly caused by the non-isotropic element pattern and array effect, rather than error in phase gradient. This phenomenon occurs for scanned arrays, especially at large scan angles [57]. This is because in general an element's pattern is not isotropic, but rather tapers down as elevation angle increases (usually modeled as $\cos^q(\theta)$). This element pattern, when multiplied with the array factor, will cause the total array pattern to shift slightly toward a smaller angle in elevation. For the following calculations with phase method and paraxial method, we will still use $p = 0.433k$ or $\delta = 25.7°$ for calculations.

Another interesting fact with the use of this S-ring element is that the handedness of polarization is always flipped in the transmitted wave. This means, with an RHCP feed

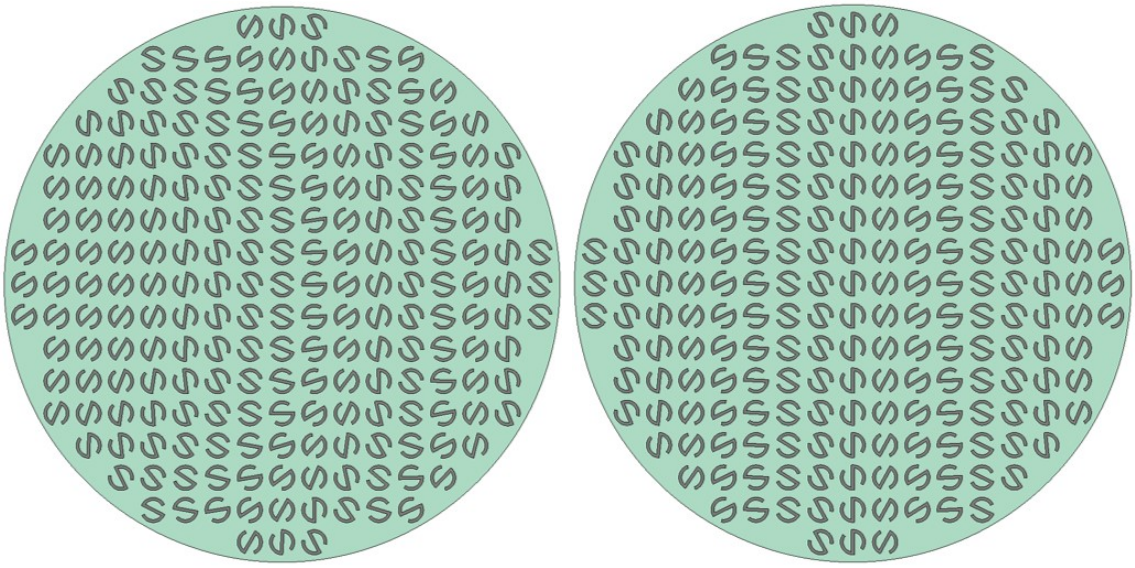

(a) (b)

Figure 4.9 The front view of the designed transmitarrays: (a) TA_1 and (b) TA_2. (Looking from the side of the feed.)

source, the output of TA_1 becomes dominantly LHCP. Consequently, TA_2 should be designed for LHCP input and produces RHCP output. Eventually, the output beam of the system is polarized in the same handedness as the feed source. Shown in Fig. 4.9(a) and 4.9(b) are the front view of TA_1 and TA_2. Each transmitarray contains 213 unit cells and has a thickness of 3.04 mm.

4.2.3 Simulation Results of the Transmitarray RPA

We began with the determination of spacing d between TA_1 and TA_2. We fixed the beam pointing direction to broadside (by letting $\alpha_1 = 0°$ and $\alpha_2 = 180°$) and varied the value of d. By sweeping d from 3 mm to 1 mm, the simulated directivity of the RPA appeared to slightly increase from 23.73 dBi to 23.83 dBi. We chose to maintain a reasonable gap between the two rotating surfaces and set d to be 2 mm. We then rotated TA_1 and TA_2 for the RPA to scan to different target angles θ_t in $\phi = 0$ plane. Phase method was used to calculate the rotation angles for TA_1 and TA_2. The simulated RPA patterns at 19 GHz for multiple scanned cases are presented in Fig. 4.10. The simulated RHCP directivity of broadside beam

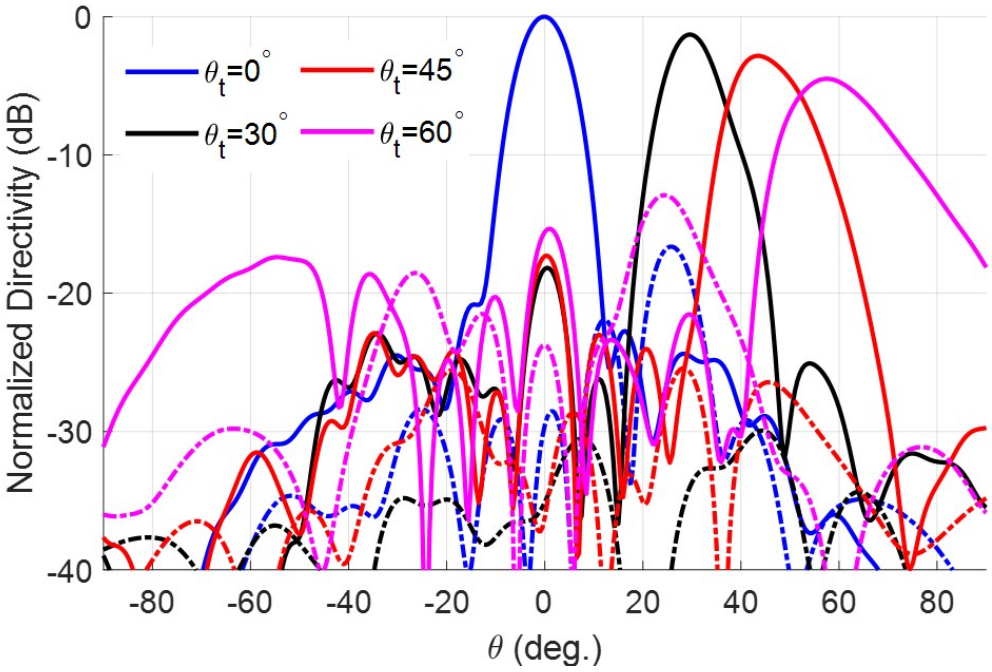

Figure 4.10 Normalized directivity of the simulated RPA showing multiple scanned beams in $\phi = 0°$ cut at 19 GHz. Solid lines represent the RHCP (Co-Pol) patterns and the dash lines represent the LHCP (X-pol) pattern. The directivity for the broadside beam is 23.7 dBi.

is 23.70 dBi, corresponding to an aperture efficiency of 59.3%. Beam scan up to $\theta = 57.5°$ was achieved with a scan loss of -4.5 dB compared to broadside beam. Cross-polarization (LHCP) level is below -12 dB for all the scanning cases. Due to the symmetric configuration of this system, the beam scan patterns in other azimuth planes were similar and will be saved for brevity. These encouraging results have well validated our CP RPA design. We will then use this RPA to verify the proposed phase method and compare it against paraxial method in terms of their prediction accuracy of beam direction.

4.2.4 Phase Method vs. Paraxial Method for Transmitarray RPA

The accuracy of phase method and paraxial method was evaluated through the solving of a practical problem designed as follows:

1. Set a target direction (θ_t, ϕ_t) and obtain the surface orientations using two methods respectively. The calculated surface orientations by phase method are denoted as

Table 4.2: Simulated pointing direction and corresponding pointing error by phase method and paraxial method for scans in $\phi = 0^\circ$ plane.

Target Angle	By phase method		By paraxial method	
θ^t	θ^p	$\lvert\theta^p - \theta^t\rvert$	θ^a	$\lvert\theta^a - \theta^t\rvert$
0.0°	-0.1°	0.1°	-0.1°	0.1°
30.0°	29.6°	0.4°	29.8°	0.2°
40.0°	40.9°	0.9°	42.0°	2.0°
45.0°	43.5°	1.5°	49.5°	4.5°
50.0°	50.1°	0.1°	55.7°	5.7°
55.0°	53.7°	1.3°	–	–
60.0°	57.5°	2.5°	–	–

(α_1^p, α_2^p), and those calculated by paraxial method are denoted by (α_1^a, α_2^a).

2. Use the calculated surface orientations (α_1^p, α_2^p) and (α_1^a, α_2^a) for two identical RPA systems respectively and obtain the corresponding simulated main beam directions. We use (θ^p, ϕ^p) to denote the beam direction of the RPA taking (α_1^p, α_2^p), and use (θ^a, ϕ^a) to denote the beam direction of the RPA taking (α_1^a, α_2^a).

3. The prediction error for each method is then measured by taking the difference between the simulated beam direction and the target direction (θ_t, ϕ_t).

In the calculations above, $p = 0.433k$ was used for phase method and $\delta = 25.7^\circ$ was used for paraxial method. A set of target beam directions in $\phi = 0^\circ$ plane were chosen, i.e., we fixed $\phi_t = 0^\circ$ and varied θ_t. As has been discussed in Section 4.1.2, the major discrepancy of the two methods lies in their prediction in elevation angle. It was also verified through simulations that both methods were able to accurately position the beam in $\phi = 0^\circ$ plane. Therefore, we will focus dominantly on pointing error in elevation, as shown in Table 4.2.

It can be observed that for small steering angels, e.g., $\theta^t \leq 30^\circ$, the pointing error of both methods was less than 1°. When larger scan angle θ^t was desired, the pointing error of the RPA using paraxial method started to increase and reached an error of 5.7° for $\theta^t = 50^\circ$;

whereas the RPA using phase method manifested a stable error below 1.5° till a target angle of $\theta^t = 55°$. It is worth noting that, the maximum scan angle that can be predicted with paraxial method is $2\delta = 51.4°$ according to the equations in Table 4.1. One will not obtain a valid solution of (α_1^a, α_2^a) with paraxial method if a θ^t beyond 2δ is desired, and this explains why the last two rows in Table 4.2 are missing under paraxial method. In fact, the simulations suggested that the RPA was capable of scanning beyond 51.4°. The maximum scan angle of this RPA was 57.5°, corresponding to the maximum prediction error of 2.5° by phase method. As far as $\theta^t = 50°$ is concerned, an improvement of 5.6° in accuracy was achieved with phase method.

Though the exact pointing error may vary in particular RPA systems, it is evident with these results that the proposed phase method is capable of improving the beam pointing accuracy by several degrees. Such improvement can be significant especially for high gain RPAs with narrow beamwidth, in which case missing a few degrees can dramatically diminish the power reception.

4.3 A Novel K-band, Reduced-Complexity, Two-Component Risley Prism Antenna: Configuration, Prototyping, and Validations

A typical RPA consists of two independently rotatable gradient-phase surfaces and a stationary feed source [Fig.4.11 (a)]. As has been discussed in depth in section 4.1, the feed source creates a illumination with a uniform phase, and the two gradient-phase surfaces each provide a gradient phase shift to the transmitted wave. The combined phase at the aperture forms a new gradient that results in a scanned beam. By rotating the two surfaces, one controls the distribution of the aperture phase gradient and consequently scans the beam.

The advancements in beam steerable RPA mark the continuous effort dedicated to reduce the profile and weight of the RPA, which is especially critical for applications to small satellite platform. It has been shown that the use of a planar feed source and thin-panel

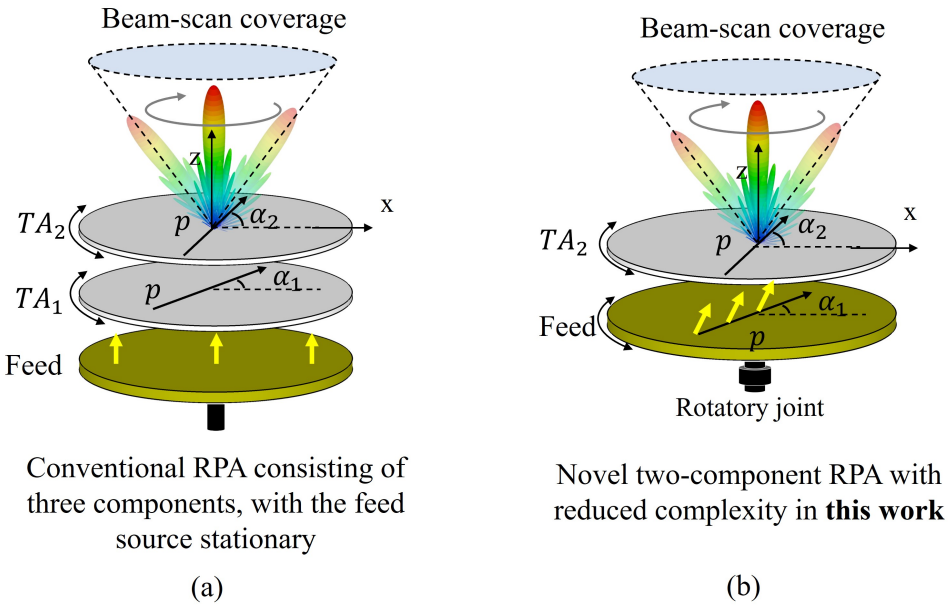

Figure 4.11 (a) The conventional RPA using at least three components, including a stationary feed source with uniform-phase illumination and two mechanically rotatable gradient-phase surfaces. (b) The novel two-component RPA demonstrated in this work with reduced system complexity. It includes a rotatable gradient-phase feed source and a rotatable gradient-phase surface. The feed accepts input from the bottom through a rotatory joint, and rotation of the feed and TA_2 can potentially be realized using motors on edge.

gradient-phase surfaces can significantly shrink the total height of the RPA system to around one or two wavelengths. Recently, metasurfaces [50, 112, 115], transmitarrays [49, 51, 113], lenses [114], and graded-dielectric plates [52] have been proposed as RPA's beam-deflective surfaces, and they largely lowered the weight and profile of the RPA systems. Innovations in low-profile feed sources for RPA (or NFMS antenna) have also been reported in the recent literature, such as resonant cavity antenna [50], radial slot line array [115, 125], radial line continuous transverse stub antenna [114]. Nonetheless, all the reported RPAs utilized at least three components, two of which (TA_1 and TA_2) should be independently rotatable [Fig. 4.11 (a)]. The mechanical implementation of such a multi-element system still involves substantial complexity [52]. Other mechanical steering concepts may require fewer components [126,127], but they involve in-plane translation motion that leads to a significant lateral variation in the antenna profile and requires larger clearance for operation. In [128], the demonstrated concept utilized in-plane rotations of a traveling-wave waveguide and a waveguide-coupled pre-phased array to achieve 2D beam coverage. However, the waveguide involves complex machining and requires two discrete waveguide ports that make it challenging to implement rotations in practice. Therefore, further simplification of RPA configuration is of great interest from a practical point of view, and it becomes the aim of this section.

The discussions in section 4.1 reveal that the summation of two independently rotated gradient phase shifts is sufficient to realize 2D beam steering. This implies the conventional three-component RPA configuration can be further simplified if a feed source radiating with a gradient phase is used. In this case, only one phase-shifting surface (TA_2) is needed on top of the feed [Fig. 4.11(b)]. This new configuration can offer the same 2D beam steering capability but uses only two components. It can help lower the system profile and weight, simplify mechanics, and reduce transmission loss. In particular, we demonstrate the development of the CP gradient-phase transmitarray (GPTA) based on a modified S-ring unit cell that is optimized to reduce power reflected back to the feed panel. For the gradient-phase feed array (GPFA) panel, we propose a novel hybrid-phasing technique that utilizes both element rotation and feed line delay to create the CP phase gradient. This allows us to extend the AR bandwidth of the RPA without using more sophisticated radiating element.

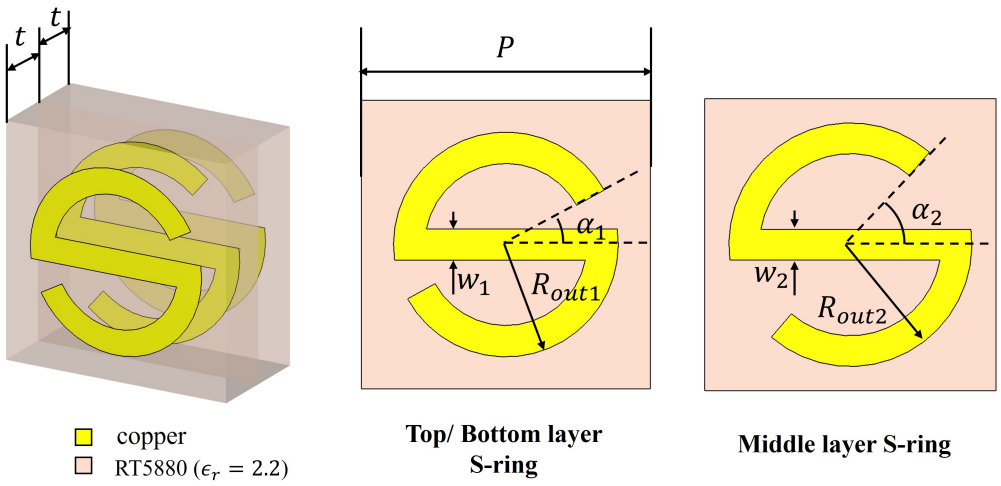

P	R_{out1}	w_1	α_1	R_{out2}	w_2	α_2	t
6.28 mm	2.44 mm	0.68 mm	29.0°	2.62 mm	0.66 mm	49.4°	1.575 mm

Figure 4.12 The modified S-ring unit cell design for the GPTA of the two-component RPA, optimized to reduce reflection in the frequency band of operation. The dimension of the middle-layer S-ring element is made independent of the top and bottom layer S-ring to obtain more degree of freedom for optimization.

4.4 Design of CP Gradient-Phase Transmitarray

4.4.1 Design of the Transmitarray Unit Cell

Since the GPFA panel is placed very close to the GPTA (a wavelength or less spacing), it becomes critical that the reflection from the GPTA should be minimized to avoid multiple reflections between the panels that can degrade the beam quality, and to reduce the power reflected back to the feed port that impacts efficiency and threatens back-end electronics. The 3-layer S-ring CP transmitarray unit cell in section 4.2.1 has demonstrated promising CP transmission phase control ability and transmission bandwidth, making it a candidate unit cell for the GPTA. However, the this unit cell appeared to have limited tunability on the reflected power and thus requires additional degree of freedom in the element optimization.

To overcome this, a modification to the middle layer is introduced to gain more flexi-

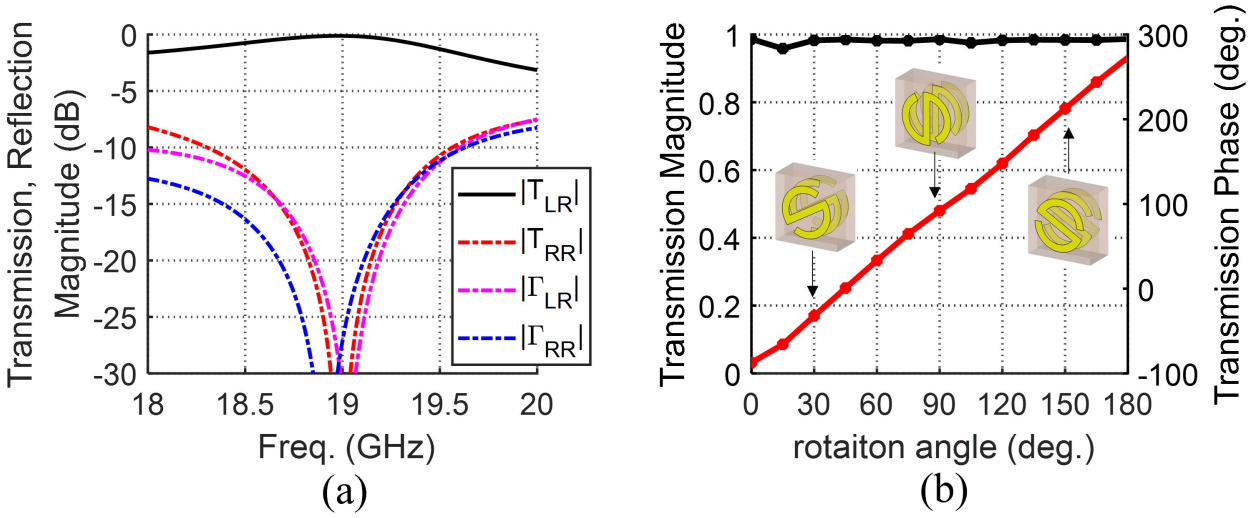

Figure 4.13 Simulated performance of the modified S-ring unit cell. (a) Transmission and reflection magnitude under RHCP excitation. (b) Transmission coefficient magnitude and phase for T_{LR} (the component of interest) versus element rotation angle at 19 GHz.

bility in optimizing the unit cell's reflection and transmission coefficient simultaneously. In particular, the first and third layers of the S-ring element have identical geometry, whereas the parameters of the middle layer S-ring are independent and can be different (parameters in Fig. 4.12). Since the CP component that carries the geometrical phase is orthogonal to the incident wave. Therefore, when the unit cell is designed for RHCP incidence, we aim to maximize the transmitted LHCP component and suppress transmitted RHCP and all reflected components. A lower permittivity substrate also appeared to be helpful in reducing reflections from the unit cell. Therefore, Rogers RT5880 with $\epsilon_r = 2.2$ ($\tan\delta = 0.0009$) was chosen as the new substrate.

The magnitude of transmission coefficient (T_{LR}, T_{RR}) and reflection coefficients (Γ_{LR}, Γ_{RR}) of the unit cell considering RHCP excitation are shown in Fig. 4.13 (a). The desired transmission $|T_{LR}|$ is greater than -1.0 dB for 18.4 - 19.4 GHz, while $|T_{RR}|$, $|\Gamma_{LR}|$, $|\Gamma_{RR}|$ are all below -10 dB for this frequency range. Similar to the previous version, the unit cell provides $0° - 360°$ phase coverage through the rotation of the S-ring element based on the rotation-phase property [108] (the three layers of S-ring in the unit cell rotate simultaneously). The

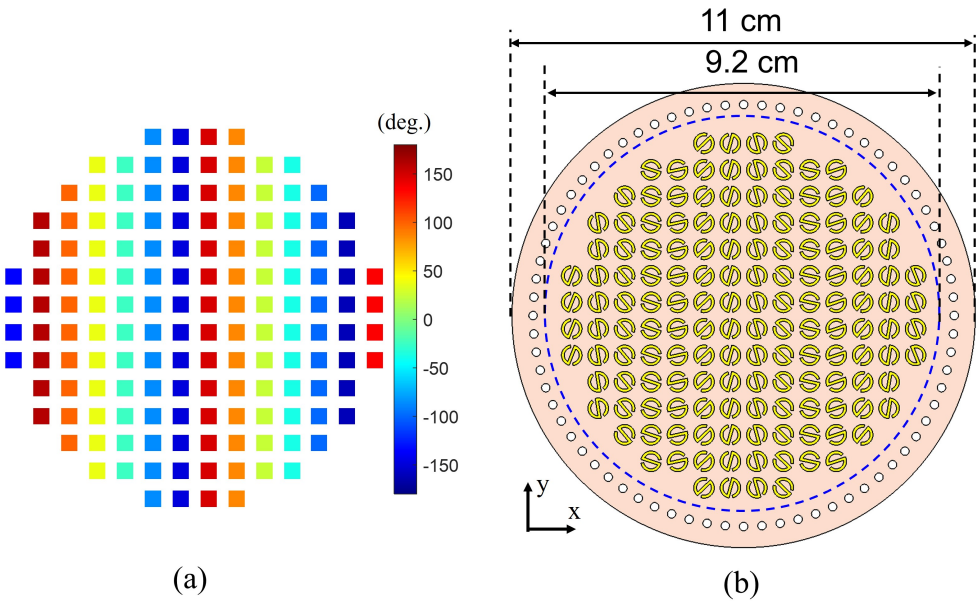

Figure 4.14 (a) The required phase shift by each element to provide the desired phase gradient. (b) The GPTA design with the modified S-ring elements rotated based on the required phase shift. The drill holes along the circumference are used for assembling with the GPFA in measurements.

phase of the transmission coefficient $\angle T_{LR}$ versus element rotation angle is presented in Fig. 4.13(b) for 19 GHz. High transmission is maintained as the element rotates, and good phase linearity can also be observed.

4.4.2 Gradient-Phase Transmitarray Design

The GPTA was designed using the new S-ring unit cell with an aperture diameter of 9.2 cm, which is sufficient to fully cover the 8×8 element GPFA (discussed in section 4.5). The elements in the transmitarray are given proper rotation angles to provide a phase gradient of $p = 0.433k$ along x-direction. For ease of mounting during measurements, the board area is extended to 11 cm diameter to accommodate a ring of 2-mm diameter mounting holes, which are evenly distributed with 5° angular spacing.

4.5 Design of the Gradient-Phase Feed Array

4.5.1 Radiating Element of the Feed Array

In the CP GPFA design, element rotation is involved in creating the CP phase gradient (will be articulated in Section 4.5.2). Considering the need for element rotation, the radiating element is chosen to be a U-slot loaded truncated-corner patch (TCP) [Fig. 4.15(a)]. It offers several advantages in terms of design and implementation compared to the annular-ring loaded TCP used in [118]: the U-slot configuration allows the feeding pointing to be located at the center of each patch, simplifying parametric design of the array. This is because the feed points are fixed and equally spaced regardless of the rotation angle of the patches. In contrast, the normal TCP or annular-ring loaded TCP necessitates an off-center feed point, causing the feed point location to change when the patch rotates. The feed points in the array are thus non-uniformly distributed and the feed network topology has to be re-designed when parameters change [118]. Additionally, the optimized slot width of the U-slot (0.15 mm) in this application appeared to be larger than the slot width of the annular gap [118] loaded TCP (0.1 mm, which is the design constraint), thus offering more tolerance in fabrication.

The U-slot loaded TCP designed for RHCP at 19 GHz is shown in Fig. 4.15(a). The simulation and optimization of the patch were performed under periodic boundary conditions to take into account mutual coupling between the elements. The patch is fed by a 50-ohm stripline on layer 3 through a probe (conductive via) [Fig. 4.15(a)], and the simulated S_{11} and axial ratio (AR) versus frequency are shown in Fig. 4.15(b) and 4.15(c). This design achieves decent matching bandwidth because of the capacitive loading created by the U-slot, whereas the AR bandwidth agrees with what is typically expected for a TCP element [129].

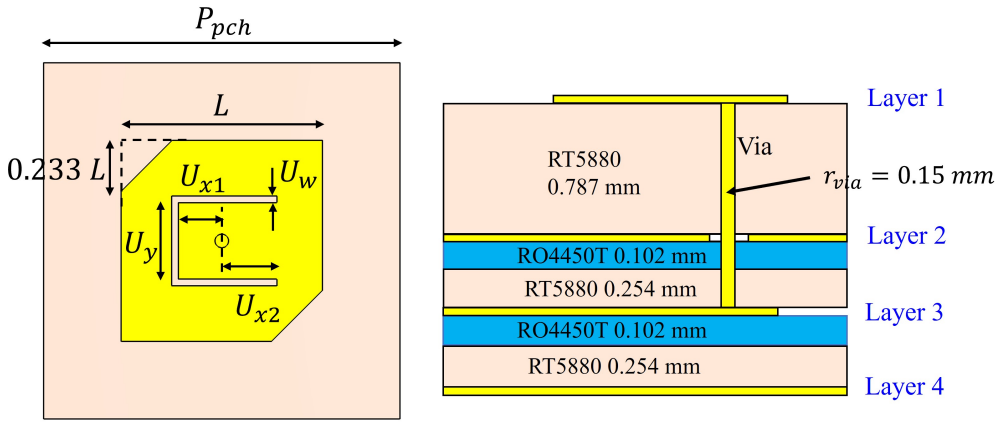

P_{pch}	L	U_{x1}	U_{x2}	U_y	U_w
7.9 mm	4.46 mm	0.97 mm	1.22 mm	1.69 mm	0.15 mm

(a)

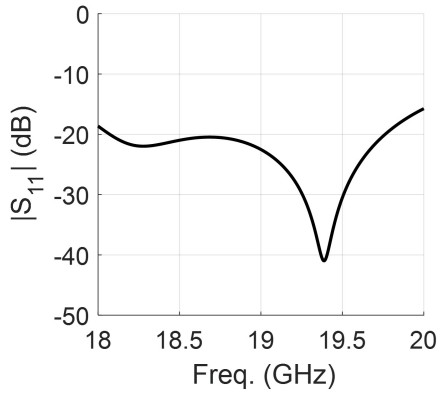

(b)

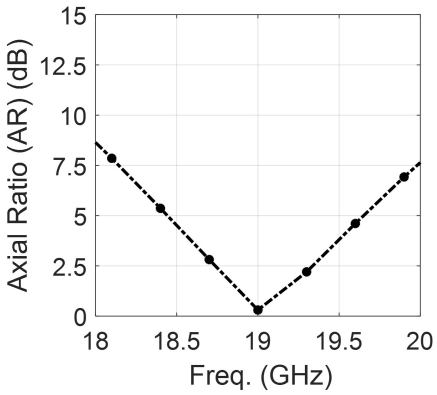

(c)

Figure 4.15 (a) The U-slot loaded truncated-corner patch element for the feed array. (2) Simulated reflection coefficient S_{11} of a single element when fed by a 50-ohm stripline underneath. (3) The axial ratio of a single element.

4.5.2 Hybrid-Phasing Technique for the Feed to Suppress Cross-polarization Lobes

One of the critical challenges of the GPFA design is to make sure the element radiates with the specified phase such that the phase gradient in the aperture can be realized. In CP feed arrays, there are two common approaches to create phase shift to the elements: (1) delay line method and (2) element rotation method. The delay line method uses the length of the feed lines to control the phase at which each element is excited, and is thus independent of the polarization of the radiating element. A limitation of this method is that the delay lines can become too long to be distributed in a tight array environment (half-wavelength spacing). The element rotation method works exclusively in CP and simplifies the design of the feed network because phase shift is purely rotation-dependent and all the elements can be excited simultaneously. In this case, an interesting fact leads to performance concerns in an RPA system. This is because the RHCP and LHCP components always experience the conjugate phase shift in the system because element rotation is the only technique to realize phase shift for both the GPFA and the GPTA. As a result, when the Co-Pol beam of the RPA is scanned to (θ_1, ϕ_1), the X-pol component will also form a beam but at $(-\theta_1, -\phi_1)$. When the feed array element has excessive X-pol, say, at off-center frequencies, the X-pol beam can reach considerable power level and significantly affect the performance of the RPA. This becomes particularly problematic when a broadside beam is desired, in which case both the Co-Pol and X-pol beams are pointed at $(\theta = 0°, \phi = 0°)$, and the AR of the broadside beam gets significantly impacted. This effect is also visually illustrated in Fig. 4.16 (case 1).

To overcome the challenges of delay line method and element rotation method, we propose a "hybrid-phasing" scheme that use the combination of short delay lines and element rotation to create the gradient phase [Fig. 4.16 (case 2)]. It ensures that the GPFA still radiates the Co-Pol component with the desired phase gradient, but the radiated phase of the X-Pol component is perturbed so that a uniform phase will no longer be formed at the exiting aperture of the RPA. This method improves the AR performance of the RPA without the need of more sophisticated radiating element design that complicates the prototyping of the

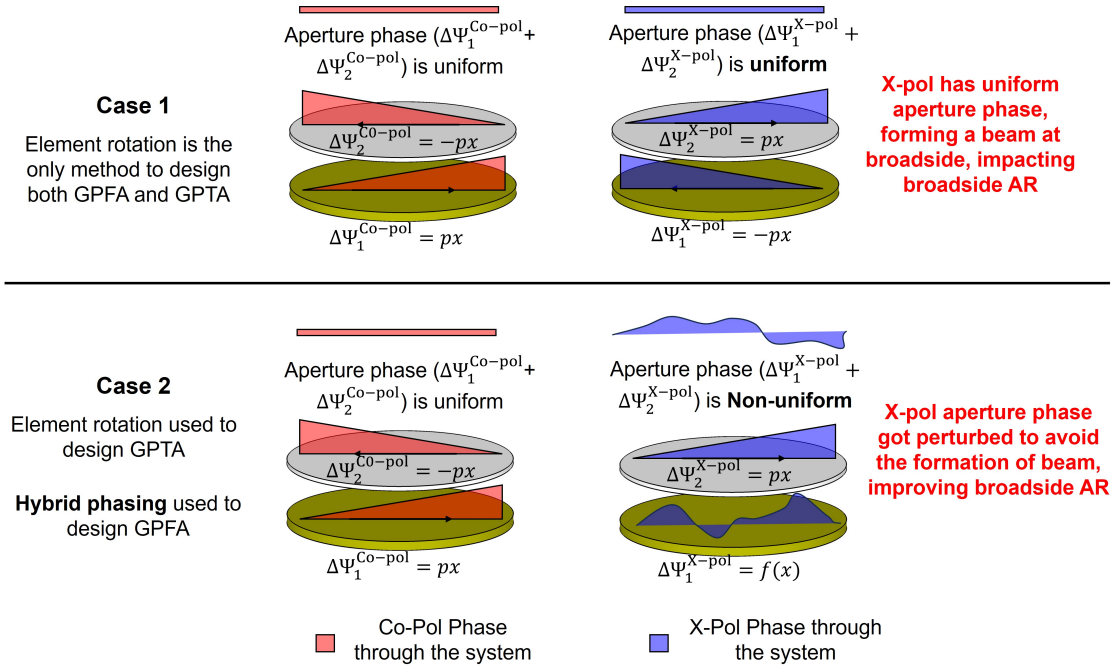

Figure 4.16 Visual illustration of Co-Pol and X-Pol phase behavior in the RPA system when different techniques are used to create the phase gradient for the GPFA and GPTA.

GPFA. The optimization of the rotation angles and delay-line length of each patch element is performed as the following:

1. An 1×8 array along $x-$direction using the U-slot TCP was constructed for full-wave analysis in CST [Fig. 4.17 (a)]. Each element was fed by a segment of stripline terminated by a waveport that provides individual excitation to each element. The length of the striplines are identical and fixed for each element. In total eight waveports were used.

2. Periodic boundary condition was used for the $+y$ and $-y$ boundary, and open boundary condition was used for the rest of the boundaries. This allows the linear array simulation to reasonably represent a full array's performance (i.e., 8×8 array) but with much shorter simulation time.

3. The counter-clockwise rotation angle of each element is denoted as R_i, and the excitation phase at the waveport is denoted as D_i, $(i = 1, 2, \ldots 8)$. It can be inferred

that the radiating phase of each element is $\psi_i^R = R_i + D_i$ for RHCP component, and $\psi_i^L = -R_i + D_i$ for LHCP component.

4. To ensure that the radiating phase of the elements form a gradient for the RHCP component, it is enforced that:

$$\psi_i^R = R_i + D_i = (i-1)pP_{pch} \tag{4.22}$$

with $p = 0.433k$ being the desired RHCP phase gradient, and P_{pch} being the element spacing of the patch elements.

5. The phase delay at the first port is set to be 0 as a reference, and the phase delay D_i $(i = 2, 3, \ldots 8)$ for the rest of the ports are to be optimized. The rotation angles R_i of each element is calculated based on the condition in (4.22). It is also enforced that $-180° \leq D_i \leq 0°$ such that the delay lines can be reasonably short (less than half effective wavelength).

6. In the full-wave simulation of the 1×8 array, the eight waveports were excited simultaneously with the given phase delay D_i. The far-field pattern of the array is capture in $\phi = 0°$ plane. The condition in (4.22) guarantees that an RHCP beam scanned to around $(\theta = 25.7°, \phi = 180°)$ is always obtained, but the level of LHCP depends on the choice of D_i. If no phase delay is applied to the elements ($D_i = 0°$), the LHCP lobe will occur near $(\theta = 25.7°, \phi = 0°)$ because of the conjugate phase gradient [see Fig. 4.17 (b)]. Therefore, the goal of optimization is then set to minimize the LHCP level in the range of $20° \leq \theta \leq 30°$ and $\phi = 0°$.

It is worth noting that, even though the GPTA will be placed in the near field of the GPFA, the far-field pattern of the feed array is a good indication of the radiating phase of the elements. It is also much easier to define the optimization goal based on far-field pattern than on near-field distribution.

The optimized R_i, D_i values are as shown in Table 4.3. The simulated far-field patterns of a element-rotation-only 1×8 array ($D_i = 0$) and the optimized 1×8 array with hybrid

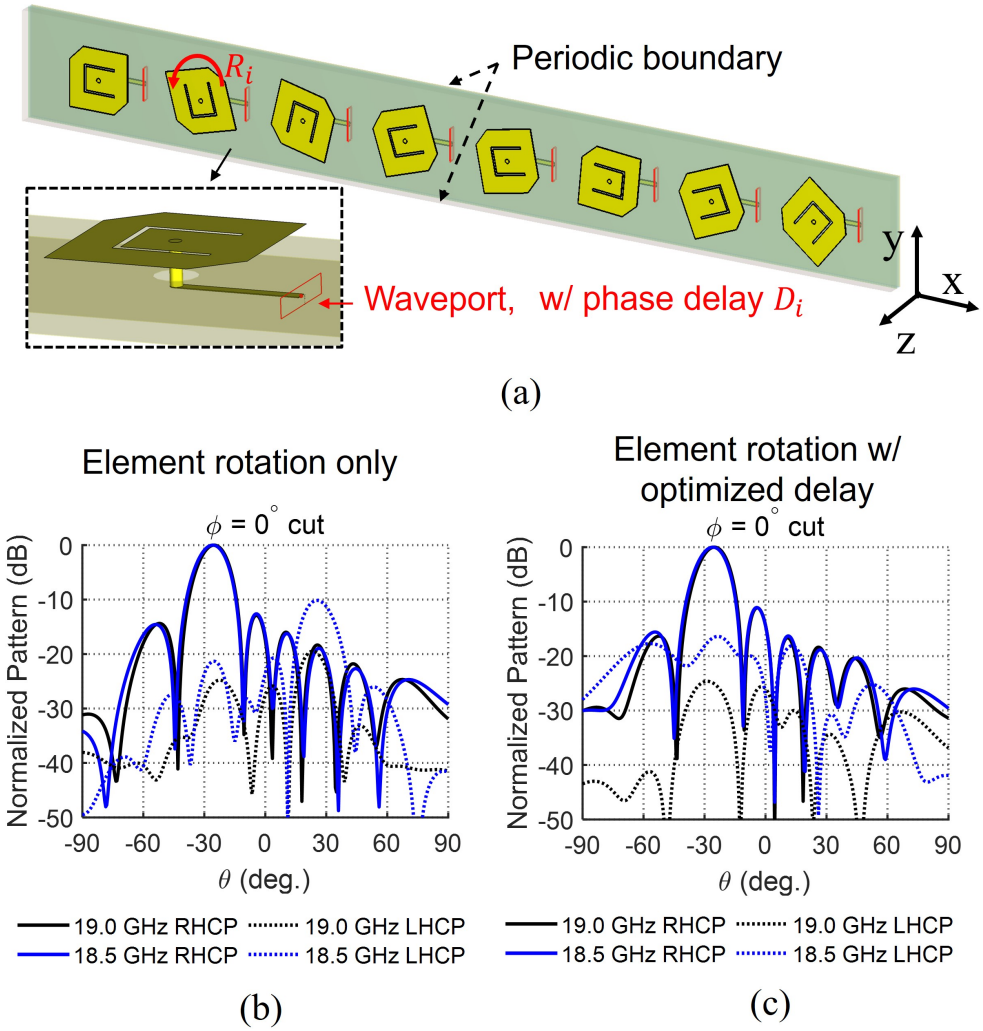

Figure 4.17 (a) The 1×8 TCP array created in full-wave simulations to optimize the rotation angle and line delay. Substrates made transparent to shown the feeding mechanism used for this study. (b) The simulated far-field pattern at 19.0 and 19.5 GHz, of the 1×8 TCP array when only element rotation is used to create the phase gradient. (b) The simulated far-field pattern at 19.0 and 19.5 GHz, of the 1×8 TCP array with the optimized rotation angle and line delay.

Table 4.3: Optimized GPFA element rotation angle (counterclockwise) and phase delay at 19 GHz for eight patches in a row (listed from $-x$ to $+x$)

Element # along $+x$	1	2	3	4	5	6	7	8
Rotation R_i (deg.)	78.1	183.1	334.8	95.7	88.9	252.8	279.5	308.9
Line Delay D_i (deg.)	0	-26.9	-100.5	-143.3	-58.4	-144.2	-92.8	-44.1

phasing are shown in Fig. 4.17 (b) and (c). It is evident that the LHCP lobe level in the $20^\circ \leq \theta \leq 30^\circ$ range got significantly reduced, for both the center frequency (19.0 GHz) and off-center frequency (19.5 GHz). Table 4.3 will be used to design the 8×8 element GPFA in section 4.5.3, with which the effectiveness of the hybrid phasing method will be further demonstrated in the RPA simulation results.

4.5.3 The 8×8 Gradient-Phase Feed Array

The complete GPFA consists of 8×8 U-slot TCP elements, as shown in Fig. 4.18. It radiates dominantly RHCP with a gradient along x direction. It consists of eight identical rows of elements [Fig. 4.18(a)], and the eight elements in each row are rotated by the optimized angles in Table 4.3. The elements are fed by the stripline feeding network underneath [Fig. 4.18(b)]. The length of each branch is distinctly designed to provide the optimized phase delay in Table 4.3 at 19 GHz. The GPFA is fed at the center by a coaxial interface from the back (in reality with a rotatory joint for the feed panel to rotate). The ground plane on layer 4 is cut into the shape as shown in Fig. 4.18(c) to suppress the parallel plate mode (PPM) between the two ground plane layers of the stripline feed network. The cut ground plane still covers the feed network and has negligible impact on the performance of the feed network. However, it is worth noting that, a more common and more effective way to suppress PPM is to use multiple shorting pins between the two ground layers. Making cut outs in the ground plane in this case is a compromise made to simplify the design such that it complies the fabrication capability of PCB manufacturers. The simulated S_{11} is shown in Fig. 4.18(e), which suggest less than -12 dB reflection coefficient in the range of 18 - 20 GHz.

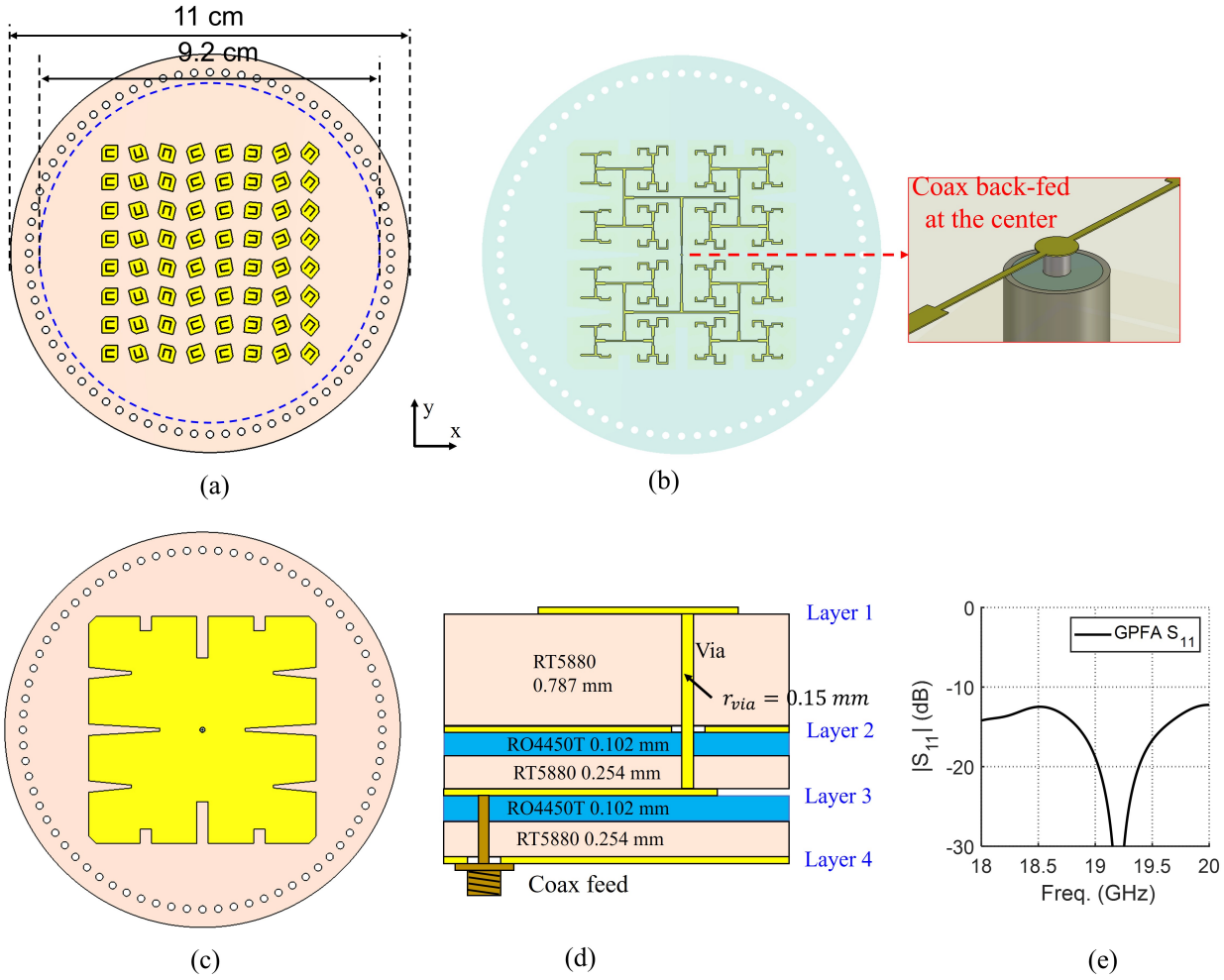

Figure 4.18 The hybrid-phasing GPFA that generates the desired phase gradient for RHCP while perturbing the LHCP phase. (a) Layer 1, rotated U-slot TCP array. (b) Layer 3, feed network with varied delay lines. (c) Layer 4, the shaped ground plane with excessive area cut out to suppress the formation of parallel plate mode between layer 2 and layer 4. (d) Cross section of the board, layer 2 and layer 3 are ground planes. (e) The simulated reflection coefficient S_{11} of the GPFA using a 50-ohm coaxial port from the bottom center.

The 8×8 elements can be completely covered by the 9.2-cm diameter transmitarray, and an additional ring of 2-mm diameter drill holes on the circumference is included only for mounting purposes.

4.6 Fabrication and Measurements of the Two-Component Risley Prism Antenna

Both the GPFA and GPTA were fabricated with Fineline PCB [Fig. 4.19 (a) - (c)]. The GPFA panel weighs 32 g and the GPTA panel weighs 68 g. The assembly of the coaxial connector to the GPFA was performed at UCLA: First, the 0.3-mm diameter pin (Mil-Max 6083) was first inserted to the bottom drill hole until it touched the feeding point of the stripline (verified with DC conduction test). Then, the field replaceable 2.92 mm SMA connector with a 0.3-mm diameter socket (PE45591) was pushed on to the back of the GPFA to mate with the pin. Solder paste was pre-applied to the ground plane, once the SMA connector was in-position, heat gun was used to melt the solder paste and a secured contact between the connector and the GPFA was established after the heat dissipated.

The S_{11} of the GPFA alone was first measured [Fig. 4.19 (d)], and then the GPTA was mounted on top of the GPFA, in the position of broadside beam and 60°-scanned beam, respectively to test the impact of different GPTA orientations on the S_{11} [Fig. 4.19 (e)]. It appears that the existence of the GPTA has negligible influence on the S_{11}, regardless of the GPTA's orientation [Fig. 4.19 (f)]. The dip in the S_{11} appears to be shifted towards lower frequency compared to the simulated result, which is likely due to fabrication tolerances and the potential inaccuracy incurred during the manual assembly of the SMA connector. Nonetheless, the S_{11} remains below -10 dB in the targeted frequency range of 18.5 - 19.5 GHz, and is sufficient for the testing of the RPA.

The GPFA and GPTA were then mounted in the spherical near-field range at UCLA. A customized mounting bracket was 3D-printed to ensure the secure and accurate orientation of the GPFA and GPTA [Fig. 4.19 (g)]. Nylon screws and bolts were used to fasten the GPFA and GPTA together, and nylon spacers were used to maintain their spacing. The

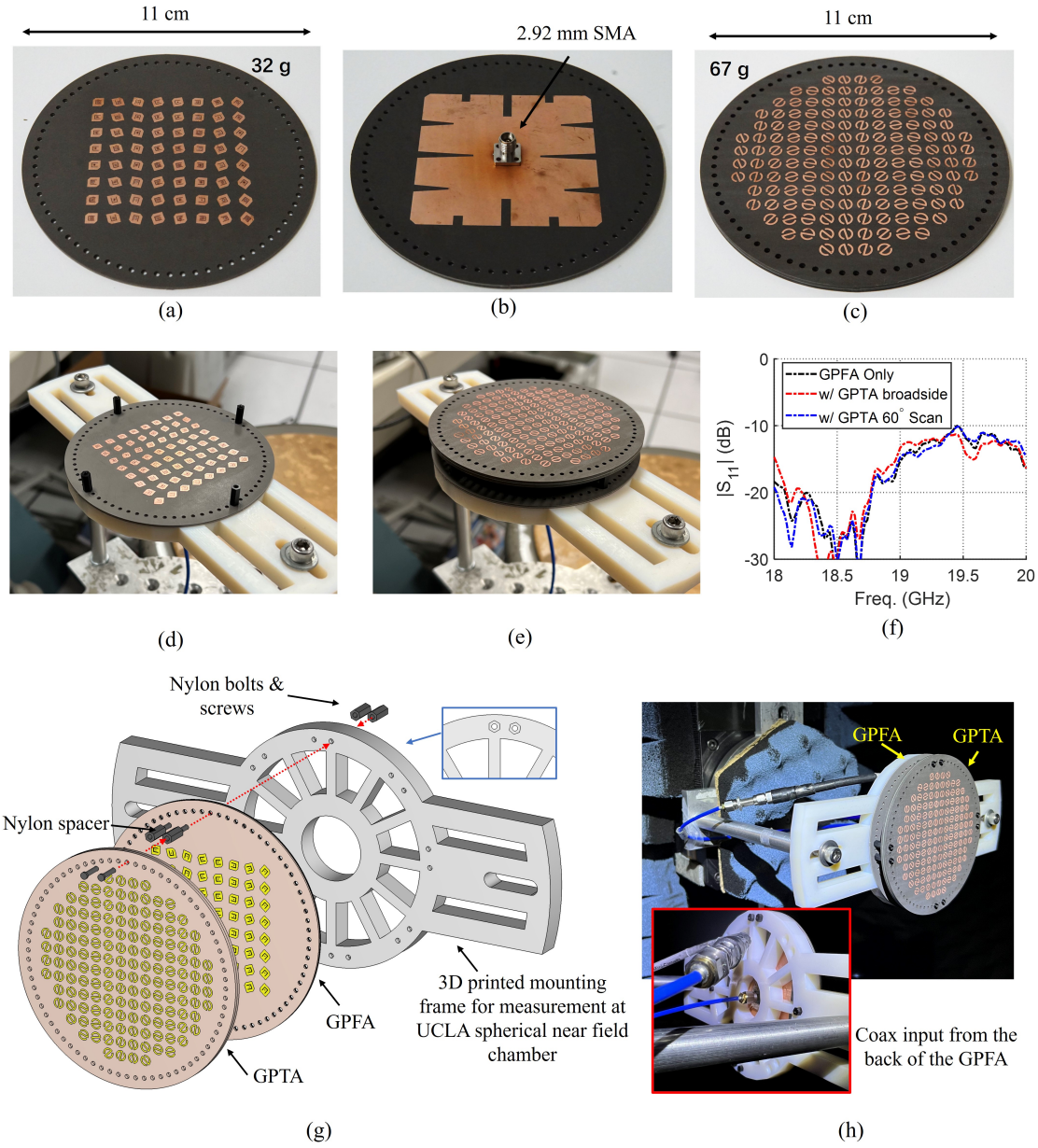

Figure 4.19 The fabricated RPA and measurement setup. (a) Front of the GPFA. (b) Back of the GPFA. (c) The GPTA. (d) Photo of the GPFA being measured for S_{11}. (e) Photo of the complete RPA system being measured for S_{11}. (f) The measured S_{11} of the GPFA alone, and the RPA for different beam pointing directions. (g) Illustration of the assembly mechanism of the RPA system with the customized 3D-printed mounting bracket for antenna measurements. (h) Photo of the RPA being measured in the spherical near-field chamber at UCLA.

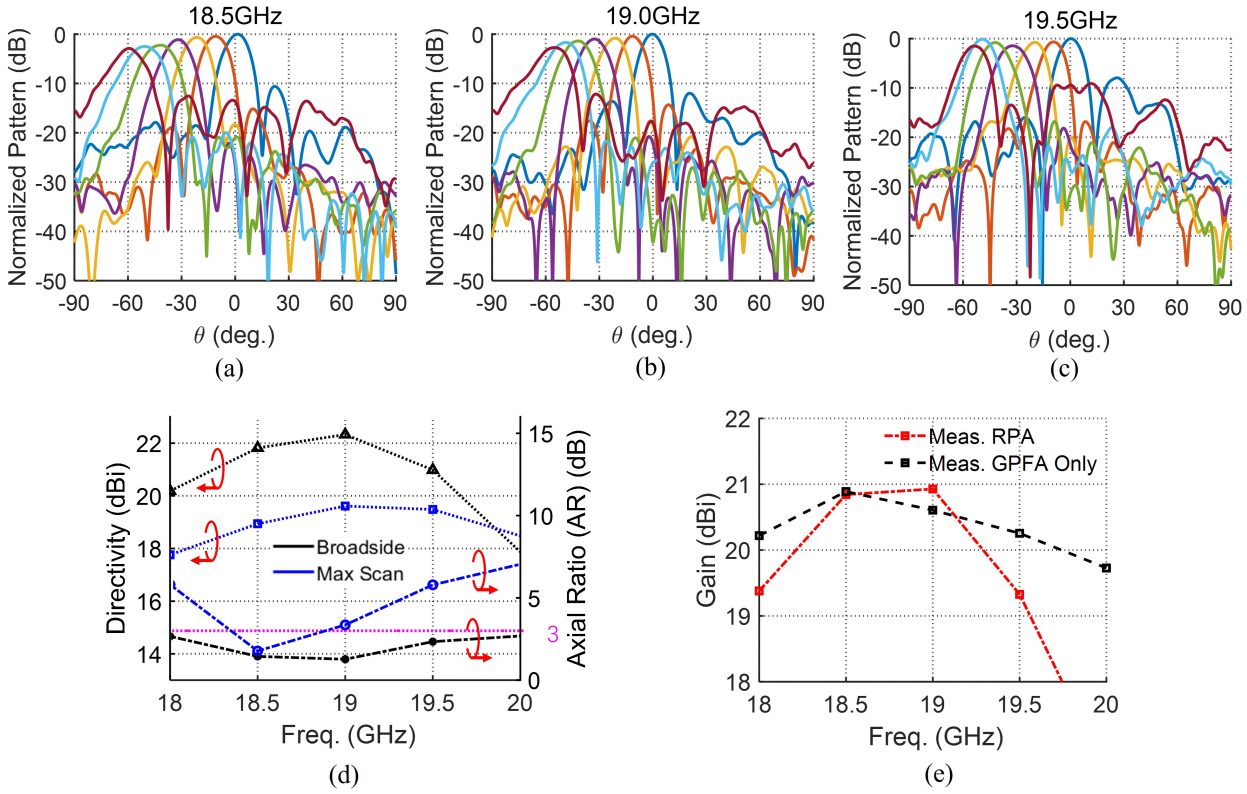

Figure 4.20 Measured results. (a) - (c) Multiple scanned beams created by the RPA in the half-plane of $\phi = 180°$ at 18.5, 19.0, and 19.5 GHz. (d) Measured directivity and AR of the broadside beam and the 60°-scanned beam versus frequency. (e) Measured gain of the GPFA alone, and the broadside beam gain of the RPA.

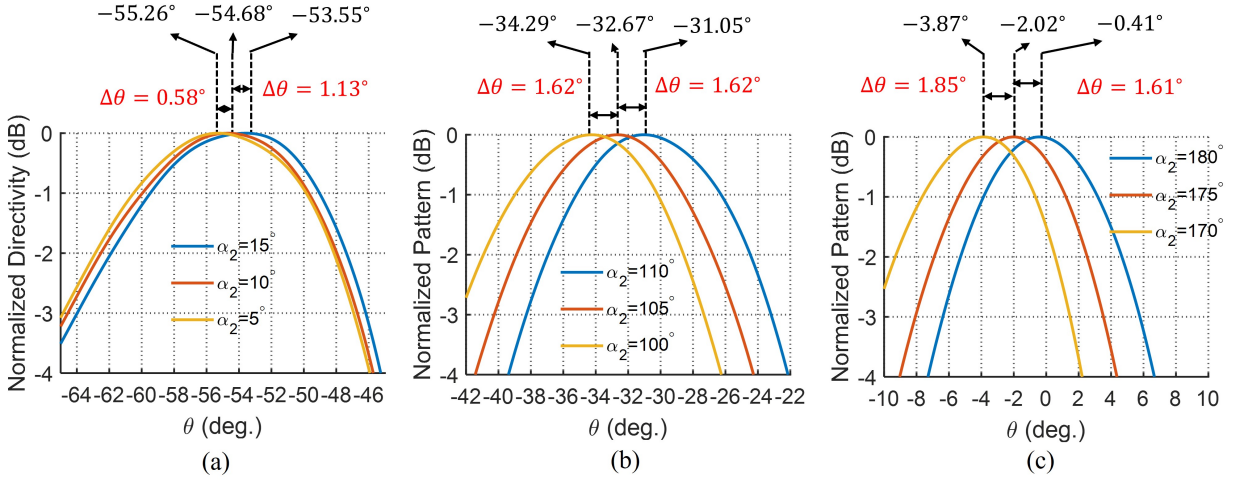

Figure 4.21 The minimum rotation step (5°) is applied to the GPTA to achieve multiple closely spaced beams. (a) - (c) Showing adjacent scanned beams at different elevation range to demonstrate the beam scan resolution of this RPA.

broadside and 60°-scanned beam performances were measured using different spacings between the GPTA and GPFA (from 8 mm to 11 mm). The measured results suggest that a spacing of 11 mm offers the best overall performance including directivity and AR bandwidth. Therefore, 11 mm spacing were used for the rest of the measurements. The total height of the system is thus 15.7 mm (not including SMA connector), which is 0.99λ at 19 GHz.

To demonstrate the beam scan capability, the GPFA and GPTA were rotated by various angles to generate representative beam scans from broadside to 60° in the $\phi = 180°$ half-plane. The obtained beams at 18.5, 19.0, and 19.5 GHz are shown in Fig. 4.20 (a) - (c), marking a very promising scan capability up to 60° in elevation. The scan loss is around 3 dB for the maximum scanned beam, which is close to what is expected from the $\cos(\theta)$ roll-off. While beam scans are demonstrated in a single azimuth cut, this RPA can achieve the same elevation scan in $0 - 360°$ azimuth range by simply rotating both the GPFA and GPTA.

The measured directivity and AR of the broadside beam and 60°-scanned beam are presented in Fig. 4.20 (d). The measured AR of the broadside beam is below 3 dB across the bandwidth captured, thanks to the hybrid-phasing method applied in the GPFA design. The 1-dB directivity and 3-dB AR overlapped bandwidth of the broadside beam is about 1.1 GHz (5.79%), and the 3-dB directivity and 3-dB AR overlapped bandwidth is greater than 1.75 GHz (>9.21%). Within this frequency band, the 60°-scanned beam also manifest a directivity variation less than 3 dB. The AR of the 60°-scanned beam is overall below 5 dB, which is reasonable for CP antennas scanned at such wide angles. The measured gain of the GPFA alone and the RPA are shown in Fig. 4.20 (e). The gain of the RPA at 19 GHz is 20.93 dBi, corresponding to an aperture efficiency around 38.6% (considering a 9.2 cm diameter circular aperture). Several factors affected the efficiency of the RPA: (1) The 8×8-element GPFA provides a square-shaped illumination, which intrinsically under illuminates the circular transmitarray aperture. (2) Limited by the PCB vendor's capability, a compromise was made to implement cut-ground plane instead of shorting pins to stop PPM. The partial ground plane creates slightly more back radiation compared to a full

ground plane with shorting pins. The estimated back radiation loss is around 0.37 dB based on simulations. (3) The fabrication tolerance and manual assembly of the SMA connector causes the measured S_{11} to be higher than designed. The measured -10 dB S_{11} corresponds to around 0.46 dB mismatch loss.

To examine the beam scan resolution, the smallest achievable rotation step of the measurement setup (5°) was applied to the GPTA, resulting in a set of closely spaced beams. The RPA was always aligned such that the plane of beam scan is aligned with the $\phi = 180°$ plane in the measurement. The adjacent three beams at different elevation angle ranges are shown in Fig. 4.21. The measured beam scan resolution appears to be no greater than 2° across the beam scan range. While smaller step of mechanical rotation can achieve even finer beam scan resolution, the current resolution is sufficient to achieve 1-dB beam overlap.

4.7 Potential Mechanical Implementation and Integration with CubeSat Platform

The mechanically steerable two-component RPA demonstrated in this chapter significantly reduces the overall profile of the antenna and brings it a step closer to realistic implementations. While the integration of RPA to CubeSats requires the collective expertise from various fields, a potential scheme for implementing RPA on CubeSats is proposed by the author and is depicted in Fig. 4.22: each panel, i.e., the GPTA and the GPTA, will be held by a pair of supporting plates. Grooves on the panel and the support plates can be used to camp bearing balls (not shown) that allow the panel to rotate freely but not to shift laterally. Each panel can be driven at the edge by a set of Gear and bearing that connects to the step motor packaged in the back of the RPA. Thanks to the light weight of the panels and the low friction ensured by the bearing balls, the step motors can be significantly miniaturized. (Note that the grooves and gear teeth can be manufactured separately and mounted to the panels.) The GPFA is fed from the bottom center by a coaxial cable using a rotatory joint to ensure RF connection while not hindering the rotation of the feed panel. The two-component RPA has a total thickness of 16 mm that occupies less than a quarter of the volume offered by

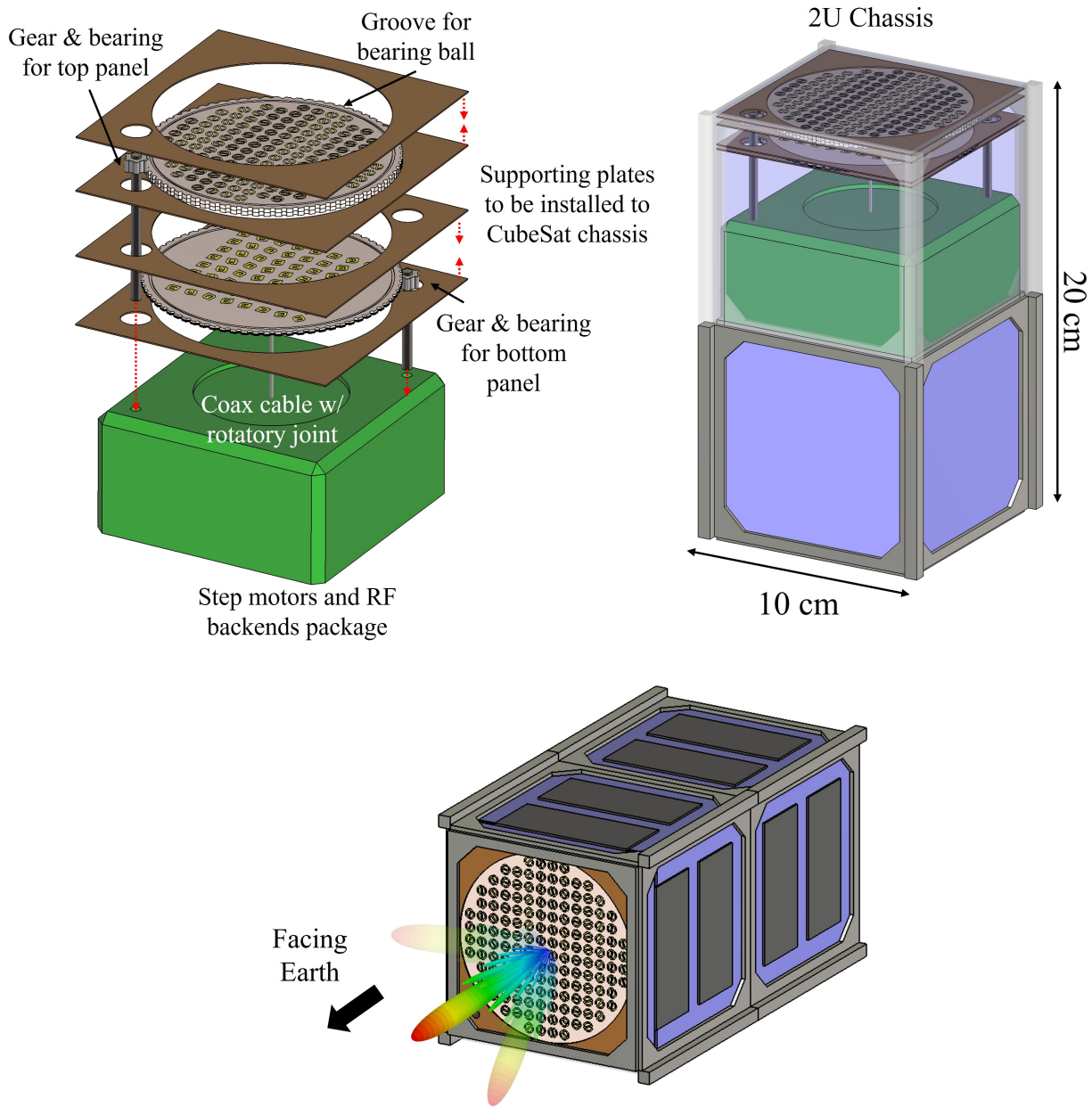

Figure 4.22 Illustrative diagram of a potential mechanical implementation of the RPA and the integration with a 2U CubeSat chassis.

1U CubeSat, thus leaving room for the necessary motors and RF backends to be distributed within the compact CubeSat. Fig. 4.22 illustrates a potential RPA implementation on a 2U CubeSat, and the author looks forward to further contributions from various engineering fields to bring this vision of CubeSat-based beam steerable RPA to reality.

4.8 Summary

Risley prism antenna (RPA) is a unique category of mechanically beam steerable antenna that achieves 2D beam steering capability with merely in-plane rotation motion and without any active RF components, making it very promising for SmallSat and CubeSat applications. Understanding the working principle is not only essential for the implementation of RPAs, but also inspires new antenna configurations that further reduce the system weight, profile, and complexity of RPAs. This chapter started by establishing the mathematical models to explain the working principle of RPAs based on phase-shifting surfaces. Using the proposed phase method, the far-field beam pointing angle was concisely associated with the phase gradient and orientations of the phase-shifting surfaces. The proposed model was verified to have a more accurate prediction of the beam steering angles than the paraxial model used in the existing literature. The proposed model also inspired a novel reduced-complexity RPA configuration that utilizes only two components to realize the same beam steering coverage as traditional RPAs that necessitates three or more components. A K-band CP two-component RPA based on a gradient-phase transmitarray and a gradient-phase feed array was designed, manufactured, and measured. The RPA achieved more than 9.21% 3-dB directivity and 3-dB AR overlapped bandwidth, with beam scan up to 60° in elevation, and demonstrated scan resolution less than 2°. The total height of the antenna is about a wavelength at 19 GHz, with a total weight of 99 g. The presented RPA verified this novel compact RPA configuration with promising beam scan capability, highlighting its potential for CubeSat applications.

CHAPTER 5

Electronically Beam Steerable CP Reflectarray Antennas

The small form factor of CubeSats and limited power onboard challenge the design of compatible antenna systems. Depending on particular mission requirements, mechanically steerable antennas might not always be a suitable option considering the reliability of the mechanical systems in space. Therefore, another direction of CubeSat antenna research is to seek low-cost and power-efficient beam steerable antennas that are operated purely electronically. Electronically beam steerable reflectarrays (or transmitarrays) stand out as potential options because they can offer wide-angle beam scan with a low profile and reasonable cost, and most importantly, with no moving parts involved. They typically incorporate phase-reconfigurable unit cells to correct the phase of the illumination from the feed source to achieve the desired aperture phase distribution. The reconfiguration of the unit cells, as has been discussed in previous chapters, is typically achieved by changing the bias voltage applied to switches or varactors embedded in the element.

While a considerable number of publications can be found on beam steerable reflectarrays and transmitarrays, limited works have demonstrated wideband CP beam steering capability. In [78], an electronically beam steerable CP transmitarray at Ka-Band was presented. The generation of CP was realized through the sequential rotation of four adjacent linearly polarized (LP) elements, with each element providing a 1-bit (2-state) phase resolution. While wide beam scan and promising bandwidth were demonstrated, this transmitarray suffered from low efficiency: the use of LP element led to an intrinsic loss of 3 dB, and the 1-bit phase resolution resulted in another 3 dB quantization loss. Therefore, a true CP unit cell with higher phase resolution is crucial to improve the performance of electronically steerable

reflectarray and transmitarray antennas.

The design of multi-bit CP unit cells becomes even more challenging when large-bandwidth at higher frequencies is desired, and this is a subject that has not been investigated much. A recent 2-bit unit cell reported in [79] claimed to be able to work in CP. The element was a microstrip patch backed by a slot-loaded plane. p-i-n diode switches were used to control the current flow in the slot-loaded plane, thereby realizing different reflection phase. However, the reported technique was proposed in L-band, and its scalability to K-band remains to be tested. Authors in [130] presented the concept of a 2-bit, CP transmitarray unit cell in Ka-band. The unit cell used a receive-transmit configuration, and the transmission phase was reconfigured through p-i-n diode switches. The simulated unit cell demonstrated a 3-dB transmission bandwidth of around 10%. However, such transmitarray unit cells generally consist of multiple layers which increases the cost and complexity of fabrication. Another concept that is considered promising for broadband CP unit cell design, known as the spiraphase element, was introduced in [131]. It took advantage of the geometrical phase property, and electronically creates element rotation by switches to reconfigure the phase of the unit cell. A CP reflectarray [81] based on this concept achieved 6% bandwidth in L-band. The concept was later tested in higher frequency designs [82, 83]. In [83], a Ka-band CP reflectarray unit cell was conceptualized to be reconfigurable through switches to potentially provide 2-bit phase resolution. Static prototypes have demonstrated a reasonable 1-dB directivity bandwidth of nearly 9.6%. However, the manufactured prototypes were built with pre-rotated, single-state unit cells, and thus the performance of the actual multi-state unit cell was not fully demonstrated. Considering the specific requirements imposed by CubeSat IoS, there is still a significant technological gap to be closed in the field of broadband CP beam steerable reflectarrays.

In this chapter, we demonstrate the conceptualization and validations of switch-reconfigurable unit cell designs for K-band CP beam steerable reflectarray antenna. The unit cells utilize different switch combinations to electronically create "rotation" of the element, thereby realizing phase shift that is frequency-independent. An overview of the outline of this chapter is as shown in Fig. 5.1: to start with, we study the impact of unit cell phase quantization

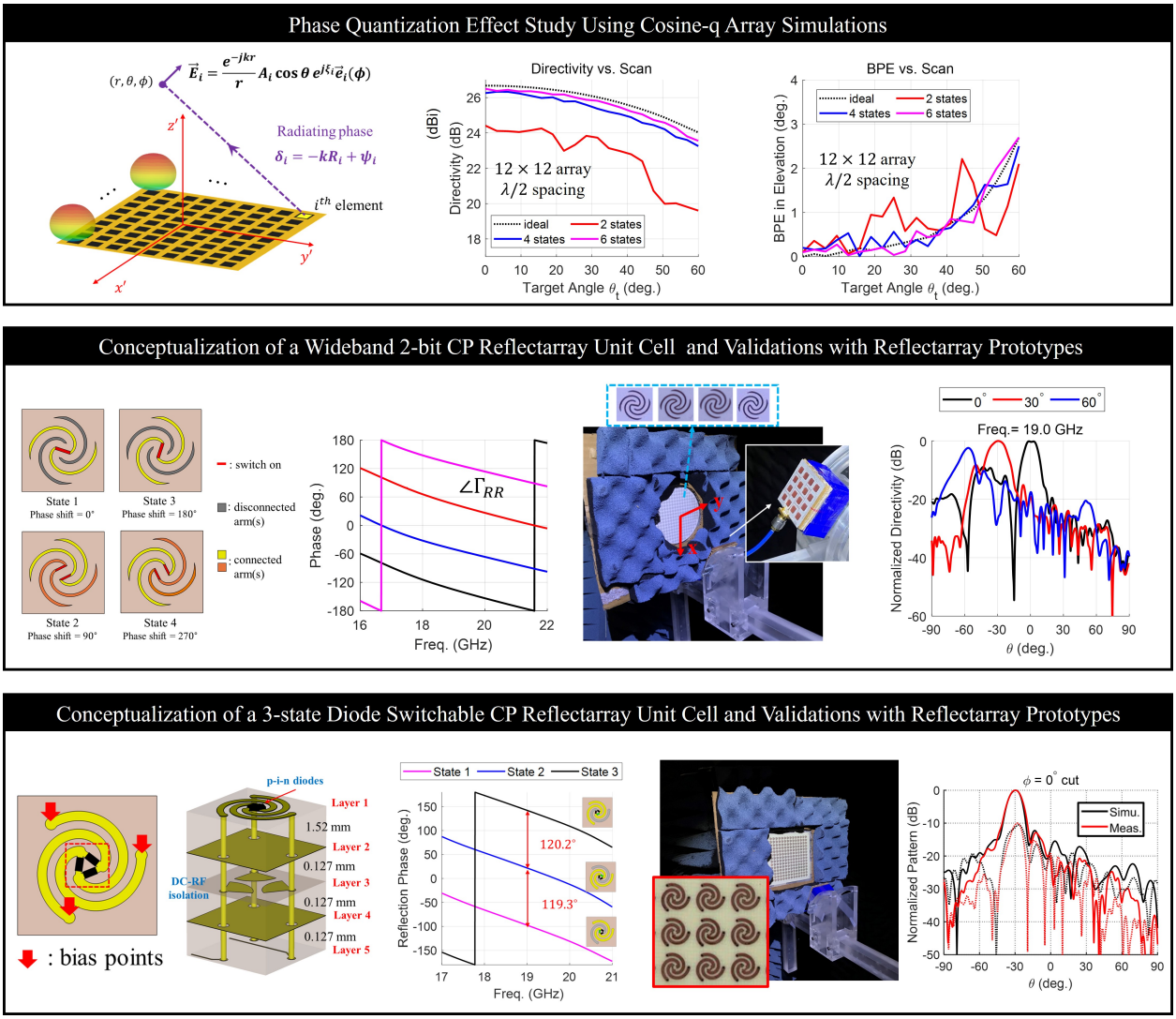

Figure 5.1 Overview of the outline and key contributions of this chapter.

on reflectarrays' quantization loss and beam pointing error using cosine-q array simulations. Then, a 2-bit (4-state) CP reflectarray unit cell based on rotated Archimedean spiral arms is conceptualized and validated for the frequency range of 17.8 - 20.2 GHz, through measurements of reflectarray prototypes. Lastly, a 3-state CP reflectarray considering realistic p-i-n diode switch models, DC-RF isolation, and biasing lines are proposed. Prototypes are fabricated and measured to validate the concept.

5.1 Fundamentals of the CP Beam Steerable Reflectarray

5.1.1 Geometrical Phase Property Facilitating Broadband CP Reconfigurable Unit Cell Design

As has been discussed in depth in previous chapter, the geometrical phase property that exist in CP operations can be exploited in the design of broadband CP reflectarray/transmitarray unit cells. For reflectarray unit cells, the property can be explicitly expressed in a matrix representation:

$$\begin{bmatrix} E_L^r \\ E_R^r \end{bmatrix} = \begin{bmatrix} \Gamma_{LL} e^{-j2\phi_0} & \Gamma_{LR} \\ \Gamma_{RL} & \Gamma_{RR} e^{j2\phi_0} \end{bmatrix} \begin{bmatrix} E_L^i \\ E_R^i \end{bmatrix} \tag{5.1}$$

where E^i, E^r represent incident and reflected fields, while the subscripts denote polarization: "L" for left-hand CP (LHCP) and "R" for right-hand CP (RHCP); $\Gamma_{LL}, \Gamma_{LR}, \Gamma_{RL}, \Gamma_{RR}$ are the corresponding CP reflection coefficients for the unrotated element; ϕ_0 is the angle of element rotation (measured positive counter-clockwisely when looking from the direction of incidence). Because the geometrical dependent phase is frequency-independent, the major band-limiting factor then resides in the reflection magnitude of the unit cell. The unit cell design task thus shifts to maximizing $|\Gamma_{LL}|, |\Gamma_{RR}|$, and simultaneously minimizing $|\Gamma_{LR}|, |\Gamma_{RL}|$. This is done by optimizing the unit cell geometry for the chosen substrate properties.

This property has been applied and validated in many CP reflectarray and transmitarray designs, also known as the variable rotation technique (VRT) [108, 110, 132]. However, most of these antennas were not targeted for beam steering applications, nor were the elements designed for reconfiguration. While mechanically rotating the unit cells appears to be a plausible option for ideal reconfiguration [48], the small spacing between the unit cells ($\simeq$ 5 mm) at K/Ka-band and the weight/power constraints posed by the CubeSats make this rather unfeasible. An ingenious alternative to mechanical rotation is to electrically switch among rotated copies of the element [81]. This allows the reconfiguration of the unit cell phase without any moving parts. In this work, we extend this idea to K-band to conceptualize a reflectarray using electronically switchable unit cells suitable for the CubeSat platform. We also provide an in-depth discussion on the unit cell's operational principles, which to our best

understanding, was not convincingly presented in [81] for an L-band implementation. The size/weight/power constraints imposed by CubeSats as well as the small unit cell size at K-band make this implementation particularly challenging.

5.1.2 Impact of Phase Discretization on Gain and Beam Pointing

The unit cell proposed in this work is conceptualized to use electronic switches to realize phase reconfiguration. Therefore, like any other electronic beam steering technique, it implies a trade-off between unit cell complexity and quantization loss. This is because, the number of switches (or specifically, the number of rotated copies of the element) limits the number of phase states that can be realized. Quantization loss has been extensively studied for phased arrays [133], and some recent works also discussed this subject within the scope of reflectarray antennas [57]. In this section, we provide representative analysis to estimate the gain and beam-pointing degradation due to the quantization of the phase response of individual unit cells.

We employ the $\cos^q(\theta)$ array method for our analysis [134]. It is a rapid numerical analysis that offers a good estimation for the performance of an array, without the need for full-wave simulations on a specific design. In particular, each element is modeled as a point source with a far-field pattern defined as $\cos^q(\theta)$ [134]. In general, each element can have its individual pattern (i.e., q value), amplitude, and phase. The far field of the array is obtained by summing the contributions from each point source in the far field. Assuming the array is in $x' - y'$ plane, and the broadside of each element is aligned along $+z'$ axis (as in Fig. 5.2). The radiated field of an array of N elements in the upper half-space ($0 \leq \theta \leq \pi/2$) can be obtained as:

$$\vec{E}_{ary}(r, \theta, \phi) = \frac{e^{-jkr}}{r} \sum_{i=1}^{N} A_i \cos^{q_i}(\theta) e^{j\xi_i} \vec{e}_i(\phi) \tag{5.2}$$

In (5.2), (r, θ, ϕ) marks the location of the far-field observation point in global coordinates; A_i is the amplitude of i^{th} element; ξ_i is defined as:

$$\xi_i = kx'_i \sin\theta \cos\phi + ky'_i \sin\theta \sin\phi + \delta_i \tag{5.3}$$

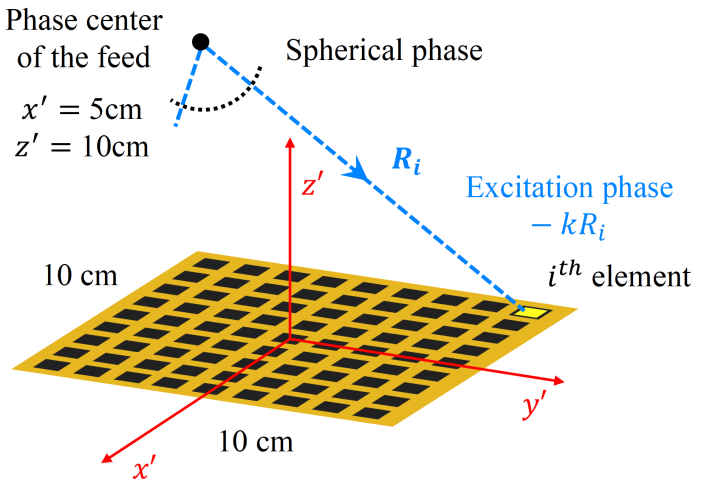

(a)

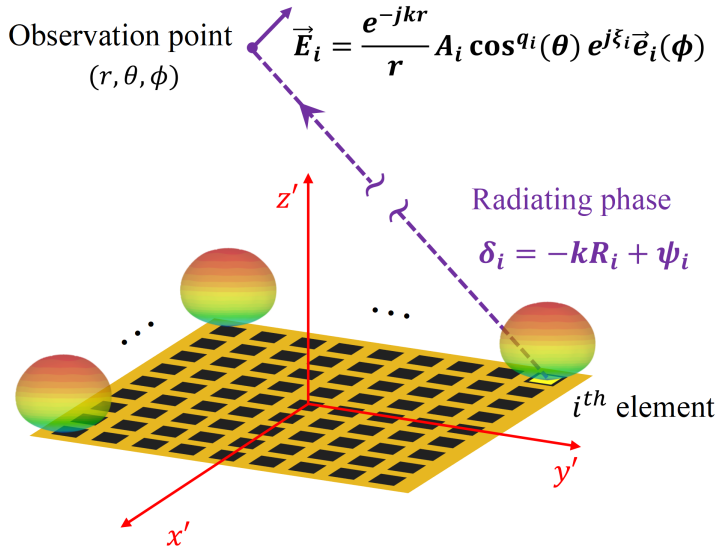

(b)

Figure 5.2 Illustration of the $\cos^q(\theta)$ array analysis. (a) The excitation phase of each element is first determined based on the feed's location and element's location. R_i represents the distance between the feed phase center and the center of i^{th} element. (b) The radiating phase δ_i of each element combines the excitation phase $-kR_i$ and the phase compensation ψ_i provided by the element. The far field of each individual element can be obtained and summed up to give the total far field of the array.

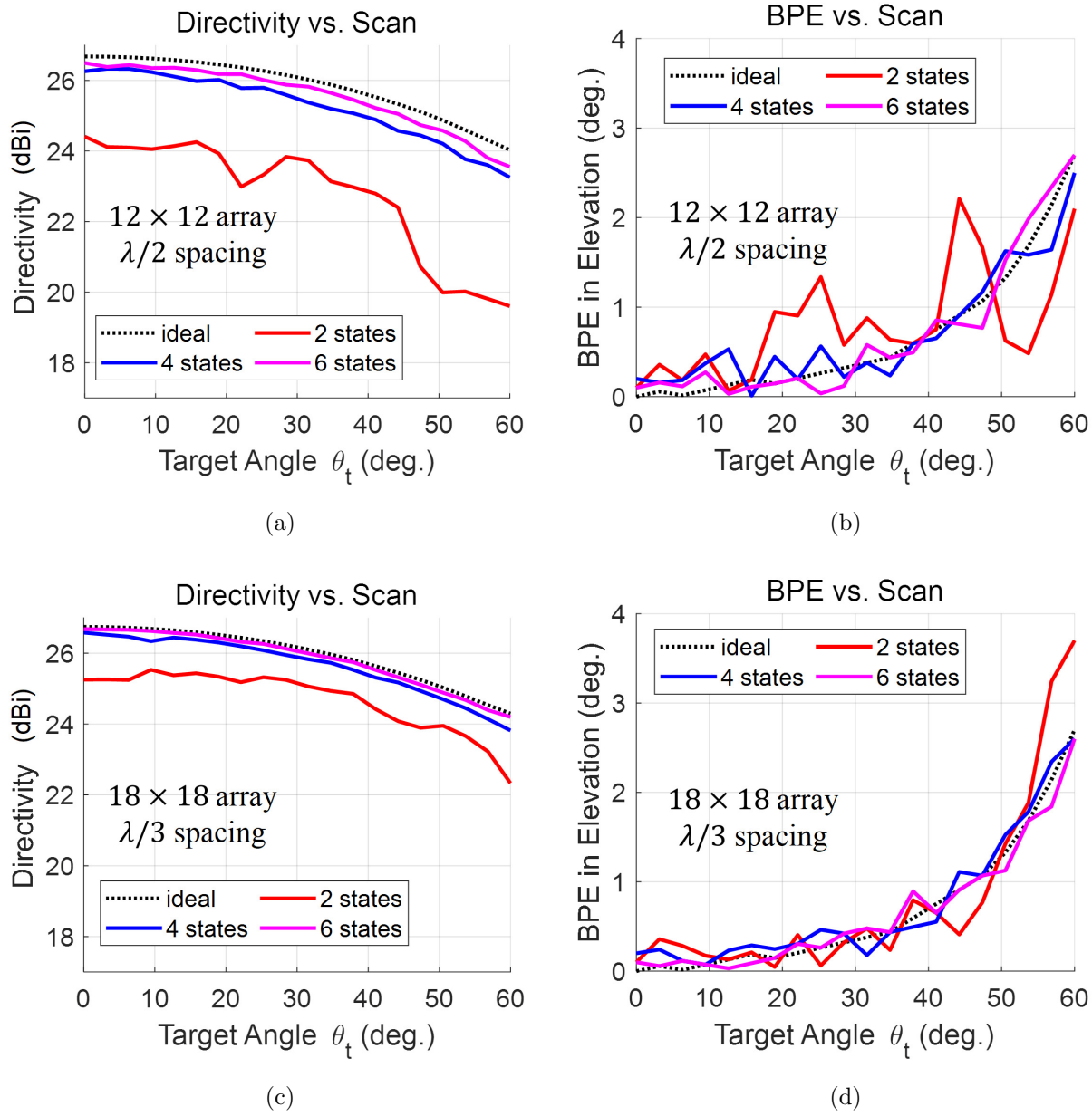

(a) (b) (c) (d)

Figure 5.3 Directivity and beam pointing error (BPE) versus scan angle, for different numbers of states. The results were obtained by $\cos^q(\theta)$ array simulations using $q = 1$. The "ideal" case results were generated by assigning the optimal phase compensation for each element in the array (no quantization). (a) and (b): results for 12×12 array with $\lambda/2$ element spacing; (c) and (d): results for 18×18 array with $\lambda/3$ element spacing. Both arrays have dimensions of 10 cm×10 cm, with the same offset feed location.

where k is the free space wavenumber ($k = 2\pi/\lambda$, with λ being free space wavelength); (x_i', y_i') is the location of the i^{th} element in the array's local coordinate; δ_i is the radiating phase of i^{th} element. The vector component $\vec{e}_i(\phi)$ indicates the polarization of each element, and is determined as [134]:

$$\vec{e}_i(\phi) = \begin{cases} \hat{\theta}\cos\phi - \hat{\phi}\sin\phi & \text{x} - \text{polarized} \\ \hat{\theta}\cos\phi + \hat{\phi}\sin\phi & \text{y} - \text{polarized} \\ e^{-j\phi}(\hat{\theta} - j\hat{\phi}) & \text{RHCP} \\ e^{j\phi}(\hat{\theta} + j\hat{\phi}) & \text{LHCP} \end{cases} \tag{5.4}$$

The radiating phase δ_i of each element can be expressed as (Fig. 5.2(b)):

$$\delta_i = -kR_i + \psi_i \tag{5.5}$$

The first term "$-kR_i$" is the excitation phase due to the feed source (with R_i being the distance between the phase center of the feed and the center of i^{th} element). The second term "ψ_i" is the phase compensation provided by the element. Ideally, ψ_i should be able to take any arbitrary value within $[0°, 360°)$. However, when the element has a limited phase resolution (finite number of states), ψ_i can only take discretized values. Particularly, a unit cell capable of N states can provide N discrete values of ψ_i. Therefore, δ_i will depend on the location of the element, the location of the feed, the phase resolution of the element, and the target beam direction (which determines the choice of ψ_i, as will be discussed in Section 5.3).

The impact of phase quantization depends on many factors such as element spacing, array size, feed location, etc. It is beyond the scope of this chapter to thoroughly address all these factors. We focus on a 10 cm×10 cm aperture dimension with an offset feed and perform the analysis at the center frequency (19 GHz) of our specific application (Fig. 5.2(a)). The feed location is chosen to be F =10 cm above the array, with a lateral offset of 5 cm in x' direction. We investigate inter-element spacings of $\lambda/2$ and $\lambda/3$ for our study. The corresponding number of elements for a 10 cm aperture is thus 12×12 and 18×18, respectively. We assume uniform amplitude over the array ($A_i = 1$), and $q_i = 1$ for the pattern of every element.

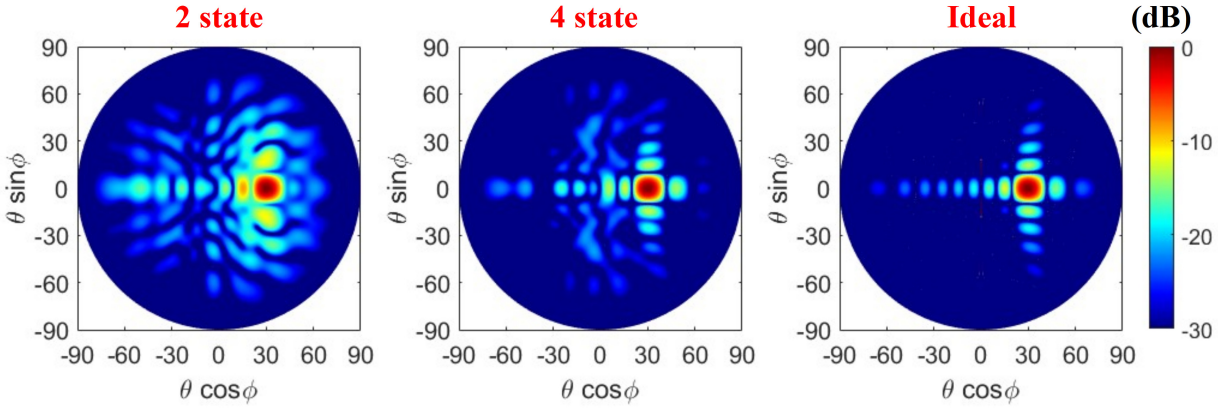

(a)

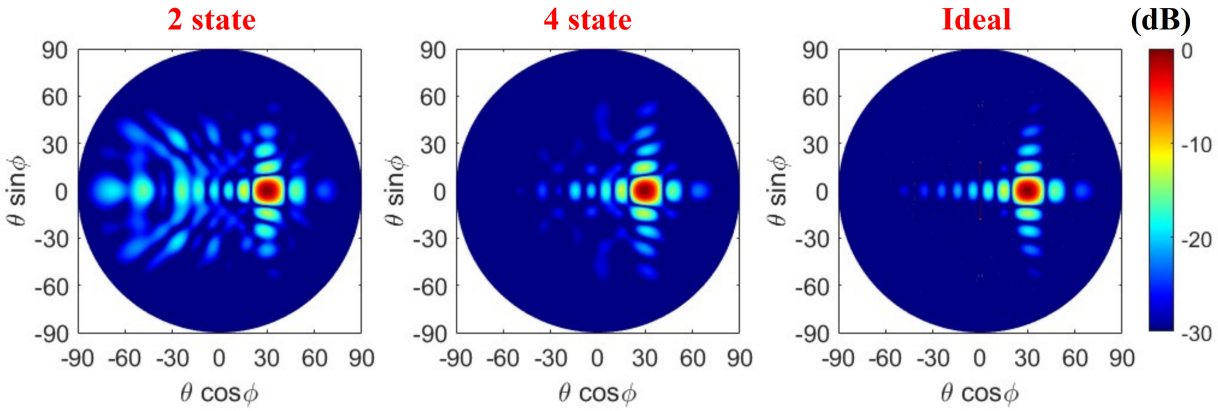

(b)

Figure 5.4 The normalized far-field patterns for 10 cm$\times$ 10 cm $\cos^q(\theta)$ ($q = 1$) arrays obtained with different element phase resolutions, when target scan angle is set to $\theta_t = 30°$, $\phi_t = 0°$. (a) Results for 12×12 array ($\lambda/2$ element spacing); (b) results for 18×18 array ($\lambda/3$ element spacing).

The two arrays were analyzed using different element phase resolutions to reveal the impact of quantization. The results of directivity and beam pointing error (BPE) versus different target scan angle θ_t (assuming $\phi_t = 0°$) are shown in Fig. 5.3. The "ideal" case refers to results obtained via assigning each element the ideal phase compensation (without any quantization). The directivity curves are plotted in Fig. 5.3(a) and 5.3(c). The "ideal" curves manifest a $\cos^n(\theta)$-like roll-off as expected [133] (In this formula, θ is the scan angle from broadside, n describes the rate of the directivity roll-off versus scan. The "ideal" case results in Fig. 5.3(a) and 5.3(c) are close the to curve of $n = 1$). It is evident that increasing phase resolution from two states to four states reduces the quantization loss to < 1 dB for both the 12×12 element and the 18×18 element array. However, it is also noted that the impact of quantization loss for the 18×18 element array is less severe than the 12×12 element array, implying that a densely packed array can be favorable to reduce quantization loss. To visually illustrate the effect of phase quantization, representative far-field patterns of the two $\cos^q(\theta)$ arrays for $\theta_t = 30°$, $\phi_t = 0°$ are presented in Fig. 5.4. It is evident that when the element has lower phase resolution, the sidelobe levels increase, causing degradation in beam quality and array directivity.

The average quantization loss for each array size and each number of states are tabulated in Table 5.1. For each case, the values presented in the table is the average of the quantization loss for all target scan directions (as shown in Fig. 5.3(a), 5.3(c)). As a reference, the equations established for phased arrays are also used to estimate the quantization loss [133]:

$$D/D_0 = \frac{1}{1 + \bar{\Phi}^2} \tag{5.6}$$

where D/D_0 is the loss in directivity; $\bar{\Phi}^2$ is the phase error variance in radians squared. For array elements with P bits, $\bar{\Phi}^2$ is calculated as [133]:

$$\bar{\Phi}^2 = \frac{\pi^2}{3 \cdot 2^{2P}} \tag{5.7}$$

The quantization loss estimated using (5.6) for different phase resolutions is also presented in Table 5.1. It is evident that the equations do not predict the quantization loss's dependency on different inter-element spacings, which is observed in $\cos^q(\theta)$ array analysis. The

Table 5.1: Quantization loss calculated based on (5.6), (5.7) and using numerical results obtained with $\cos^q(\theta)$ ($q = 1$) analysis.

Number of States	Calculated with (5.6), (5.7)	Numerical result of 12×12, $\lambda/2$ spacing $\cos^q(\theta)$ array	Numerical result of 18×18, $\lambda/3$ spacing $\cos^q(\theta)$ array
2-state(1-bit)	-2.6 dB	-3.1 dB	-1.2 dB
4-state(2-bit)	-0.8 dB	-0.6 dB	-0.3 dB
6-state(2.6-bit)	-0.4 dB	-0.3 dB	-0.1 dB

main reason for this discrepancy is attributed to the existence of the feed source used for reflectarrays. In standard phased arrays, the phase of each element is quantized to 2^P states (for which case (5.7) was derived). In contrast, for reflectarrays the radiating phase of each element is the summation of both the quantized phase shift and the excitation phase due to the feed, as represented by (5.5). This additional excitation phase is different for each element because of the different path lengths from the feed phase center to the reflectarray elements. The excitation phase constitutes an additional phase variation (also referred to as pseudorandom phase in [57]) in the aperture that could result in difference in array pattern and directivity. Since the excitation phase has a close relation with elements' location and feed location, the quantization loss also manifest dependency on these factors. In fact, when assuming the excitation phase to be uniform, both the 12×12 and the 18×18 $\cos^q(\theta)$ arrays provide similar quantization loss.

BPE is calculated by taking the absolute difference between the target scan angle θ_t and the beam-peak angle of the calculated array pattern. The BPE curves (in Fig. 5.3(b) and 5.3(d)) do not demonstrate an obvious relationship with phase resolution or array density. In general, the BPE of all the arrays follow a similar trend of increasing with the target scan angle. We remark that even the "ideal" array shows an increasing BPE. This is attributed to the non-isotropic pattern used for each element (which is $\cos(\theta)$ in our case) [57].

While the BPE can reach 3° when $\theta_t = 60°$ is desired, this error can be mitigated through calibrations in practice.

An exhaustive search using $\cos^q(\theta)$ array simulation was then performed to estimate the beam pointing resolution (BPR): all realizable beam directions were first discovered, and the BPR was calculated by taking the average of the angular gaps between adjacent beams. The results suggest that using a 2-state element phase resolution for the 12×12 array can achieve a BPR around 0.22° in elevation, and 0.19° in azimuth. The resolution is further improved when higher phase resolution and/or a denser array is used: Assuming an 18×18 array with a 4-state element phase resolution, the achievable BPR is approximately 0.06° in elevation and 0.10° azimuth. Considering that the broadside beamwidth is approximately 10° for our aperture, even 2-state phase resolution can provide reasonably continuous beam coverage after proper calibration. However, as previously noted, increasing the number of states and employing a denser array can reduce the directivity loss due to quantization. Thus, element with higher phase resolution is still advantageous and will be investigated in following sections.

These numerical simulations suggest that a higher phase resolution and a denser array help mitigate the impact of phase quantization. Nonetheless, in practice, higher phase resolution and tighter element spacing can increase the design complexity significantly. Therefore, a balance between implementation complexity and array performance should be carefully considered.

5.2 Conceptualization of the Broadband CP Phase Reconfigurable Reflectarray Unit Cell

5.2.1 Broadband CP Unit Cell with Phase Reconfigurability

The geometry of the proposed unit cell using the Archimedean spiral element is illustrated in Fig. 5.5. This design inherently supports broadband CP radiation and the phase response of the unit cell can be reconfigured by changing the connections between the arms using

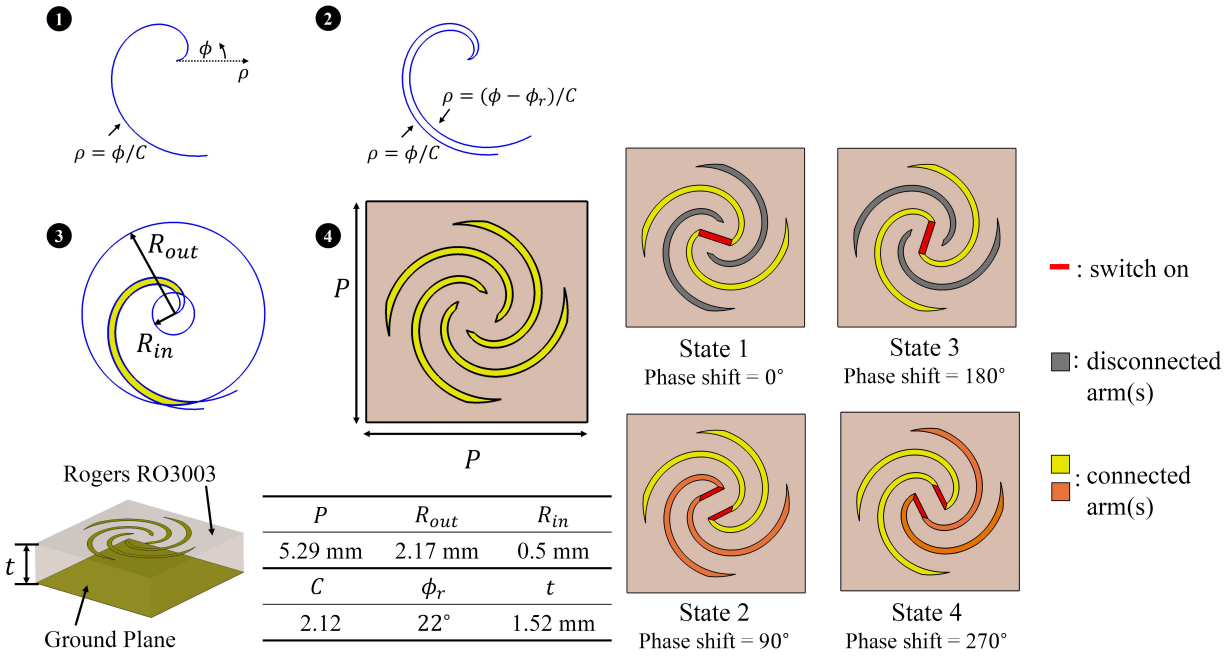

P	R_{out}	R_{in}
5.29 mm	2.17 mm	0.5 mm
C	ϕ_r	t
2.12	22°	1.52 mm

(a) (b)

Figure 5.5 (a) Proposed unit cell consisting of four rotated copies of Archimedean spiral arms and the details of its design process and parameters. (b) Demonstration of the four states of phase shift and their corresponding schemes of switching.

switches. The Archimedean profiles facilitate the packing of multiple spirals in the same unit cell. Increasing the number of spirals enables higher phase resolution, thereby reducing quantization loss. However, higher phase resolution also leads to complex switching network design that complicates its implementation on CubeSats. To achieve a good balance between the implementation complexity and unit cell phase resolution, we select four spiral arms per unit cell.

The unit cell period is $P = 5.29$ mm, which corresponds to $0.34\lambda_0$ (λ_0: the free-space wavelength at 19 GHz). As illustrated sequentially in Fig. 5.5(a), each spiral arm is formed by a pair of Archimedean spiral curves with a relative rotation angle ϕ_r about the center. The spiral takes the analytical form of $\rho = \phi/C$ in polar coordinates, where C is a constant that controls the length of the arm. The arms are bounded by a circular margin whose radius is R_{out}= 2.17 mm. The central area of the element has a circular clearance ($R_{in} = 0.5$ mm) for incorporation of switching units, e.g., p-i-n diodes. Standard Rogers RO3003 laminate (ϵ_r=3, $\tan\delta = 0.001$) with a thickness of 1.52 mm ($\approx 0.17\lambda_g$, λ_g: wavelength in the medium at 19 GHz) is used as substrate.

The phase reconfiguration is realized by switching the connections between the arms in the center, as shown in Fig. 5.5(b): by connecting the opposite arms alternatively, one effectively rotates the element pattern by 90°, creating two phase states (state 1 and state 3) that have a relative phase shift of 180°. Similarly, by switching the connections between two adjacent spirals, one can create two more states (state 2 and state 4) that have a relative phase shift of 180°. As articulated in the Appendix A, state 1 and state 2 (as well as state 3 and state 4) manifest a near 90° phase difference. Therefore, by addressing a total of six switching locations in the center, one can create four phase states with a relative step of 90°.

The reason behind the four-arm configuration providing four phase states, and especially why state 1 and state 2 manifest a 90° phase shift, was not convincingly presented in the L-band implementation of this concept in [81], to our best understanding. In this work, we provide an explanation by analyzing the radiating phase of the currents. For the brevity and continuity of this section, an in-depth discussion of the working principles is provided in Appendix A. However, the operation principle can be briefly summarized as the follow-

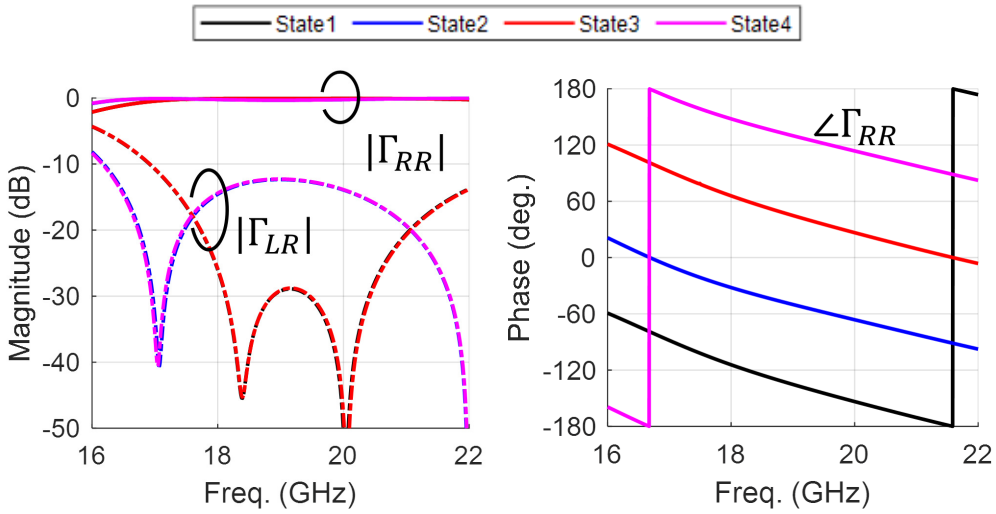

(a) (b)

Figure 5.6 Simulated reflection coefficient of the unit cell with idealized elements under RHCP excitation. The results for all four states are shown: (a) Magnitude of Γ_{RR} and Γ_{LR}; (b) phase of Γ_{RR}. Γ_{RR} and Γ_{LR} are the reflection coefficients for the reflected RCHP (Co-Pol) and LHCP (X-Pol) components respectively.

ing: Take the RHCP incidence case as an example, the incident wave induces current with clockwise sequential phase in the four arms. The switch connections allow the exchange of currents (carrying the excited phase) in the connected pair(s) of arms, making the four arms radiate with a counter-clockwise sequential phase and contribute dominantly to RHCP radiation that constitutes the reflection of the unit cell. By using different connections among the arms, one essentially controls the relative phase of the radiating current in the arms, thereby creating different CP phase shift.

5.2.2 Simulated Performance of the Reflectarray Unit Cell

The proposed unit cell can provide four phase states $(0°, 90°, 180°, 270°)$ depending on the connection between the arms, as shown conceptually in Fig. 5.5(b). As a proof of concept, the unit cells with ideal open- and short-circuit were simulated: i.e., the switches that are turned on (highlighted red in Fig. 5.5(b)) are represented by direct metallic connection, and the switches that are turned off are simply left open. With these idealizations made to the unit cell, simulations were conducted in CST Studio using periodic boundary conditions.

The simulated reflection coefficients of unit cells for four different states under RHCP excitation are shown in Fig. 5.6. We achieved LHCP (X-Pol) reflection lower than -10 dB and RHCP (Co-Pol) reflection near 0 dB over the range of 17.8 - 20.2 GHz, for all four states (Fig. 5.6(a)). Furthermore, it can be observed from Fig. 5.6(b) that the phase curves maintain a relative spacing close to 90° over the entire frequency range as was expected. Similar results can be obtained for LHCP excitations as well. These results verify the unit cell's broadband CP characteristic and phase reconfigurability, which enable the constituent reflectarray to meet the stringent RF requirements set by CubeSat IoS.

The unit cell's performance under different angle of incidence θ_{inc} was also studied and shown in Fig. 5.7. Two representative states, state 1 and state 2, were excited by RHCP wave with θ_{inc} varied from 0° to 40°. For both states, the X-pol level increases as θ_{inc} increases (Fig. 5.7(a), 5.7(c)). In the frequency band of 17.8 - 20.2 GHz, the Co-Pol level of both states remain better than -0.5 dB when $\theta_{inc} \leq 20°$, and overall better than -1 dB for $\theta_{inc} \leq 30°$. More importantly, the phase of the Co-Pol component remains stable as θ_{inc} increases, with only a slight shift near the edges of the desired frequency band (Fig. 5.7(b), 5.7(d)). In our proposed reflectarray architecture, the majority of the unit cells experience angle of incidence less than 30°. Therefore, the degradation of the unit cell's X-Pol as a function of θ_{inc} is not a major concern for reflectarray performance.

5.3 Design and Validation of the Reflectarray Prototypes

5.3.1 Design of the Reflectarray with the Multi-Archimedean spiral Unit Cell

To further validate our concept, we employ the idealized unit cells introduced in Section 5.2 to design multiple reflectarray prototypes to demonstrate reconfigurability in CP beam-scan angle. The reflectarray prototypes are designed for an RHCP feed and produce RHCP beams under an offset feeding configuration with $F/D = 1$ (Fig. 5.8(a)). Each reflectarray has a circular aperture with a diameter of 10 cm ($\approx 6.3\lambda_0$), and provides a distinct beam-scan direction. The design methodology for the reflectarrays is as follows: for a desired scan

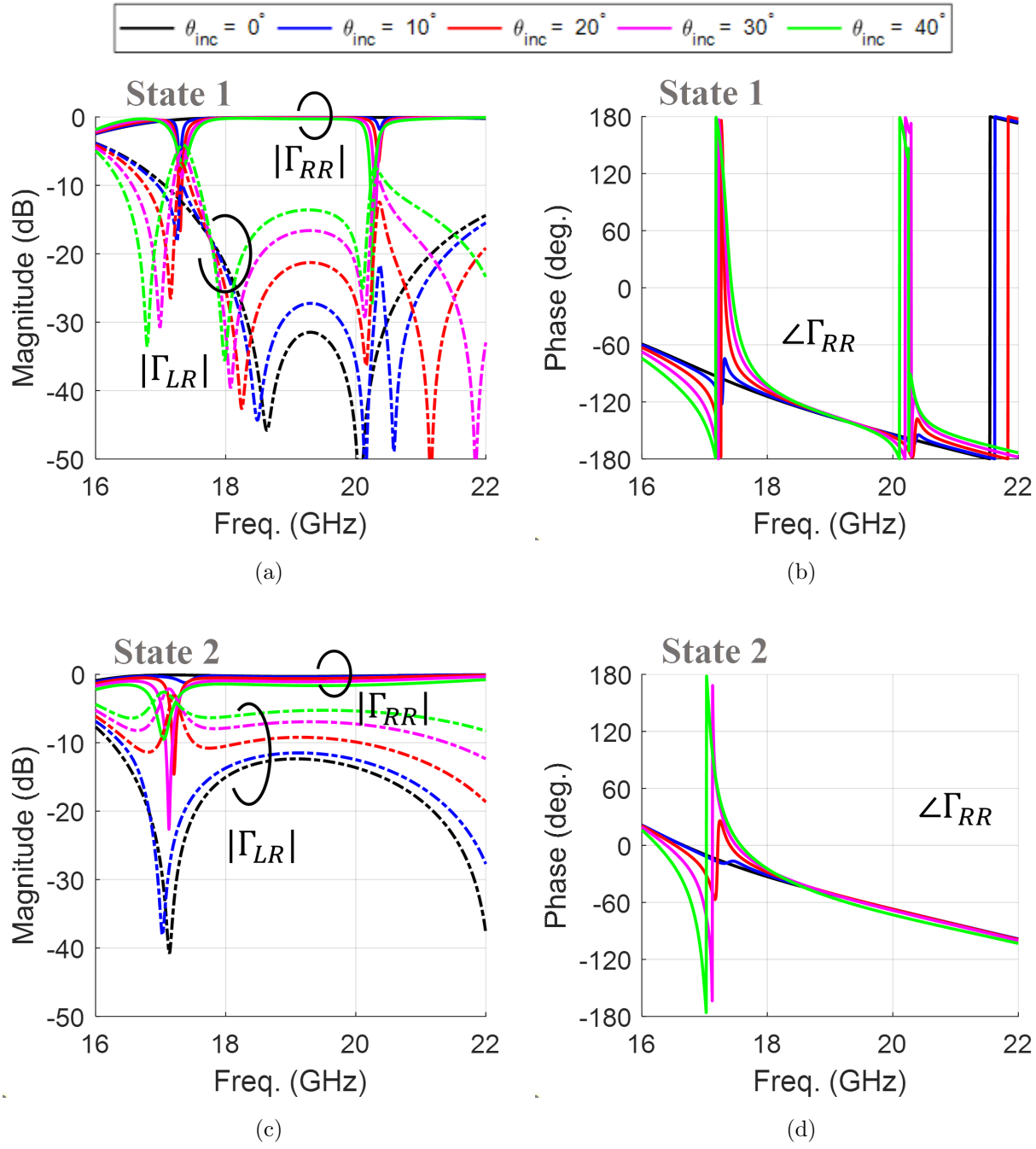

Figure 5.7 Simulated reflection coefficient of the unit cell versus incident angle under RHCP excitation. (a) State 1, reflection magnitude; (b) State 1, reflection phase; (c) State 2, reflection magnitude; (b) State 2, reflection phase.

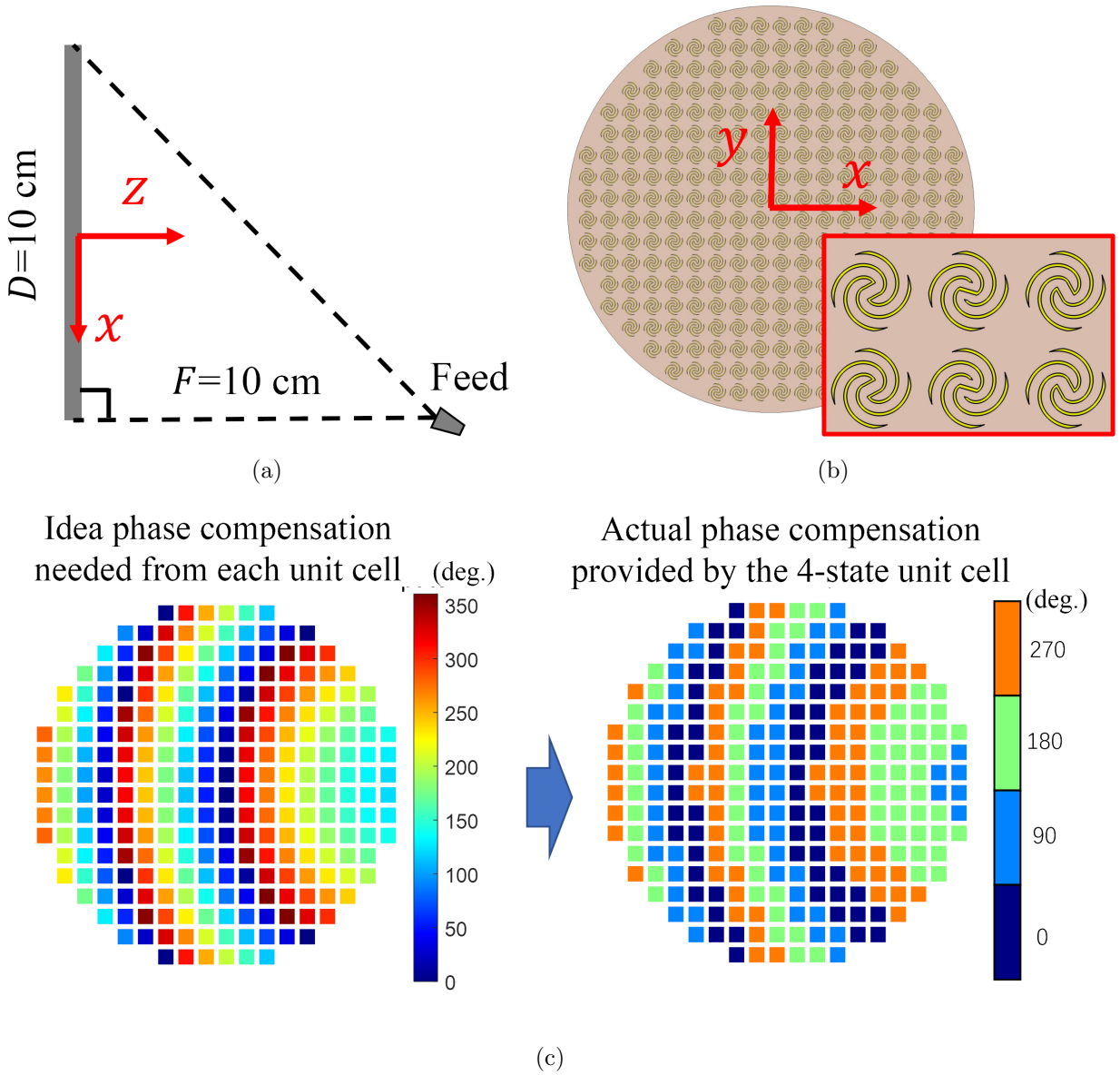

Figure 5.8 (a) The offset feeding configuration of the reflectarray antenna system. (b) Representative reflectarray prototypes designed and simulated in CST Studio. (c) Illustration of the design process of the reflectarray (shown for the case generating broadside beam). Left: the ideal phase compensation required for each element calculated by (5.8). Right: the actual phase compensation that can be provided by the 4-state phase resolution unit cells. The states of each unit cell is determined based on the criterion in (5.9).

angle (θ_t, ϕ_t), the ideal phase correction ψ over the aperture is first determined by:

$$\psi(x', y') = -k\left[x' \cos\phi_t \sin\theta_t + y' \sin\phi_t \sin\theta_t - R(x', y')\right] \tag{5.8}$$

where k is the free space wavenumber, (x', y') is an arbitrary point in the reflectarray aperture and $R(x', y')$ is the distance between the phase center of the feed and the point (x', y'). This continuous phase compensation in (5.8) is then approximated by discrete unit cells with four states of phase shift. In particular, for the i^{th} unit cell in the array, the optimal state number N_i is assigned based on the criterion below:

$$N_i = \begin{cases} 1 \text{ (cell phase } 0^\circ) & \psi_i \in (-45^\circ, 45^\circ] \\ 2 \text{ (cell phase } 90^\circ) & \psi_i \in (45^\circ, 135^\circ] \\ 3 \text{ (cell phase } 180^\circ) & \psi_i \in (135^\circ, 225^\circ] \\ 4 \text{ (cell phase } 270^\circ) & \psi_i \in (225^\circ, 315^\circ] \end{cases} \text{ when} \tag{5.9}$$

where $\psi_i = \psi(x'_i, y'_i)$ with (x'_i, y'_i) being the centroid of the i^{th} unit cell. This discretization process is illustrated in Fig. 5.8(c). It is evident that the reflectarrays for different scan directions (θ_t, ϕ_t) should have distinct unit cell arrangements (since the idealized elements are static). Therefore, multiple versions of the reflectarray with distinct element states need to be fabricated to evaluate the scan capability. In particular, we designed three reflectarray prototypes to generate a beam that points to broadside, 30° and 60° (scanned in the plane of offset) respectively. Note that such an effort of building multiple reflectarrays is only needed for the current stage of proof-of-concept because of the use of the idealized elements with open/short connections. Once switching capability is incorporated into the reflectarray elements, a single reflectarray will be capable of generating multiple beam scan directions as needed. While we demonstrate only three representative scan angles in $\phi = 0^\circ$ plane with our prototypes, the reflectarray has the capability to scan to in other cuts with much finer resolutions. As per our studies in Section 5.1, the realizable BPR in θ and ϕ can be around 0.1° on such an array.

The reflectarray prototypes were first simulated in CST Studio. An RCHP feed source with a $\cos^q(\theta)$ pattern ($q = 14.54$) was used to illuminate the reflectarrays with an average edge taper of −10 dB. The pattern of the feed is defined by $\cos^q(\theta)\vec{e}(\phi)$, where θ and ϕ are

defined in the feed's local coordinates, and $\vec{e}(\phi)$ being defined as:

$$\vec{e}(\phi) = e^{-j\phi}(\hat{\theta} - j\hat{\phi}) \tag{5.10}$$

The value for q is calculated by letting:

$$20\log\left[\cos^q(\delta_s/2)\right] = -10 \text{ dB} \tag{5.11}$$

with δ_s being the subtended angle of the feed, which is 45° for our geometry (Fig. 5.8(a)).

The simulated results showing multiple scanned beams at 17.8, 19.0, and 20.2 GHz are shown in Fig. 5.9. The simulation results verify that the designed reflectarrays are able to scan an RHCP beam from broadside to 60° across the frequency band of interest. The reflectarray maintains its performance over the target frequency band 17.8 - 20.2 GHz. The maximum directivity variation across the entire band is about 2 dB, corresponding to a 12.6% 2-dB directivity bandwidth. The broadside axial ratio (AR) remains below 1.5 dB for the target 12.6% bandwidth, as can be observed Fig. 5.9(d).

The maximum directivity of this aperture size at 19 GHz is 26 dBi (based on $4\pi A/\lambda^2$), whereas the simulated directivity at 19 GHz is 23.5 dBi. The major factors contributing to the aperture efficiency of the reflectarray can be estimated with the simulated patterns with this ideal $\cos^{14.54}(\theta)$ feed. This allows us to isolate the impact of the imperfect feeding condition and focus on only the performance of the reflectarray. Within the −2.5 dB total loss, the spillover loss and the loss due to X-pol can be estimated by analyzing the radiation pattern of the full-wave simulated reflectarray. The illumination (taper) loss is estimated using the $\cos^q(\theta)$ array analysis tool introduced in Section 5.1.2. These three items collectively account for −1.9 dB of loss, and the residual −0.6 dB is attributed to the use of the 2-bit unit cell. These major factors impacting directivity and the estimated values at 19 GHz are tabulated in Table 5.2.

In order to validate the quantization loss, two simulations were further considered: (1) Reflectarray using only the state-1 element, but rotating each element so that the elements provide ideal 'continuous' phase compensation (this array works just like a normal reflectarray using variable rotation technique); (2) Reflectarray using only the state-1 element,

Table 5.2: Factors impacting reflectarray directivity and their estimated values at 19 GHz

Factors	Value
Spillover	-0.7 dB
Illumination (taper)	-0.4 dB
Cross-polarization	-0.8 dB
Use of 2-bit Unit Cell	-0.6 dB
Total	-2.5 dB

but with four discrete rotation states (by step of 45°). This emulates the case of using 2-bit unit cell. Comparing these two cases provides another perspective to estimate the effect of quantization, and the results suggest a quantization loss around -0.4 dB, which is very close to the -0.6 dB loss estimated based on the simulations of the actual 2-bit reflectarray.

With these promising simulation results, the reflectarray prototypes for different beam scanning angles were then fabricated. The fabrication was performed with Advanced Circuits under a standard printed circuit board (PCB) process.

5.3.2 Design of a CP Patch Array Feed at 19 GHz

The choice of feed source is critical in performing measurements. The feed source must also function in the target frequency band of 17.8 - 20.2 GHz. However, the design of a proper feed for this reflectarray antenna system should consider not only the RF requirements such as polarization and bandwidth, but also the mechanical constraints posed by CubeSats such as the mass and profile of the feed. Microstrip patch antenna has the advantages of being low-profile and lightweight, and emerging works have achieved promising CP bandwidth for microstrip patch arrays [135]. Such designs typically incorporate complex multi-layer feeding networks to achieve the desired CP bandwidth. However, implementing multi-layer designs becomes expensive and challenging at K-band due to associated tolerances. While a CP feed that suits our specific application is under development, we begin with a simplified CP patch array design to evaluate the reflectarrays' performance. In particular, as shown in Fig. 5.10, the initial feed design incorporates a 4×4 truncated-corner patch array (TCPA) which was

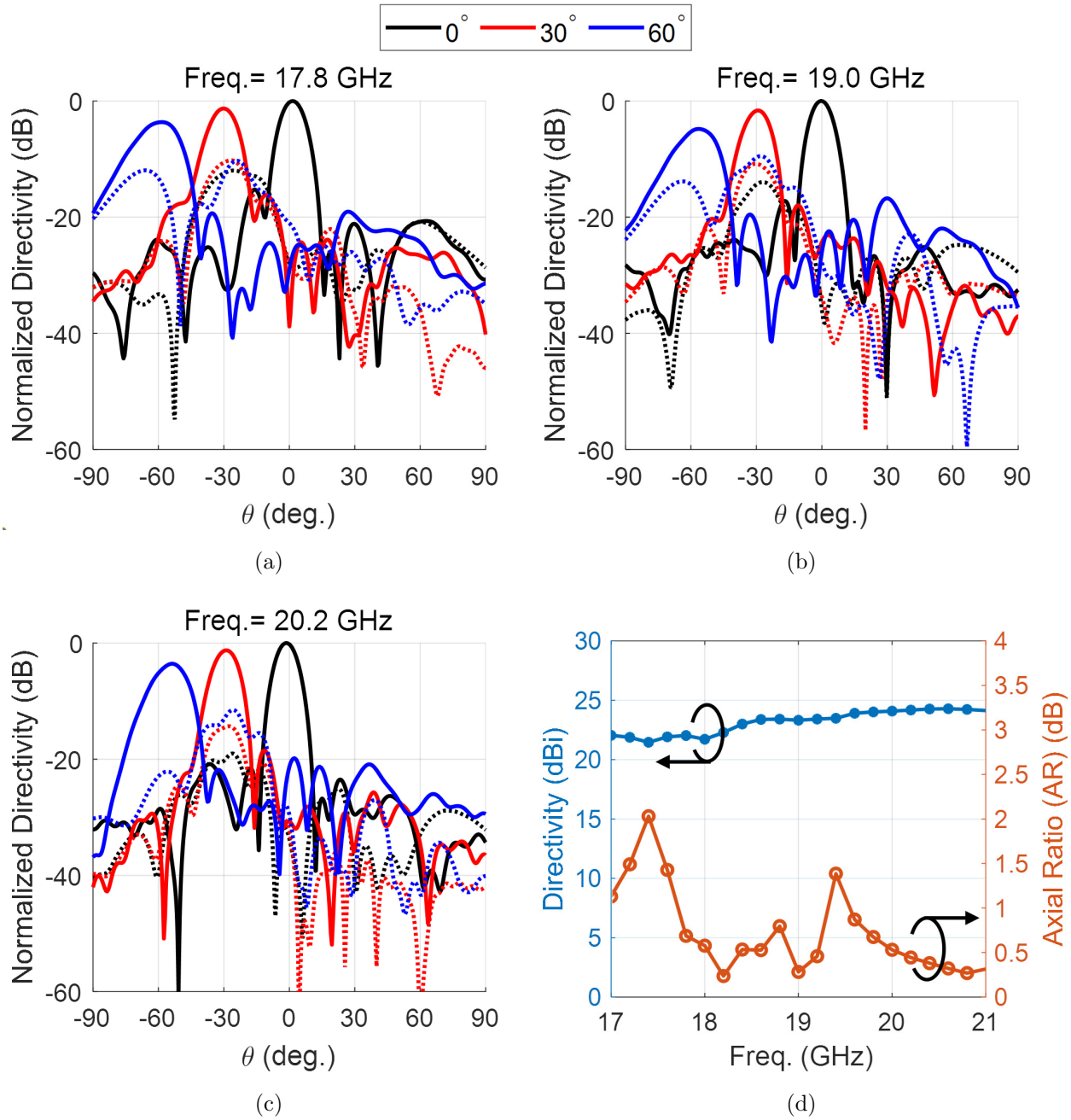

Figure 5.9 Simulated results of the reflectarrays. Normalized patterns of representative scanned beams are presented at (a) 17.8 GHz, (b) 19.0 GHz and (c) 20.2 GHz (Solid curve: RHCP (Co-Pol), dashed curve: LHCP (X-Pol)). The patterns at each frequency are normalized to the corresponding broadside beam directivity: 22.5 dBi, 23.5 dBi and 24.4 dBi. (d) The simulated broadside directivity and axial ratio versus frequency.

optimized for 19 GHz (the center frequency of target band). The feed lines are distributed on the same layer as the patches and are designed for edge-feeding. This single-layer design allows us to easily fabricate the CP feed and perform early-stage tests of the reflectarrays, even though it does not cover the entire target bandwidth.

The details of the CP-TCPA design are presented in Fig. 5.10(a). Each patch is formed by truncating the diagonal corners from a square to generate RHCP radiation [135]. Microstrip lines with a characteristic impedance of 150 ohms are used to directly feed each patch. The feeding network is matched to 50 ohms at the edge of the board, where a coaxial connector can be mounted. Limited by the space between the patches, the feed network does not include any matching section at each T-branch, but only uses a tapered section at the edge to match the 150-ohm line to 50 ohms. These efforts are made to maintain the $0.5\lambda_0$ element spacing at 19 GHz (which determines feed taper) while having the patches and feed network on the same layer. Despite the simplicity of the feed network, a good impedance match ($S_{11} < -15$ dB) was achieved. The broadside AR of the simulated CP-TCPA is 0.8 dB. The substrate of the feed array is Rogers RT5880 ($\epsilon_r = 2.2, \tan\delta = 0.0009$) with a standard thickness of 0.508 mm.

This CP-TCPA was then fabricated at UCLA's Center for High-Frequency Electronics and measured in the spherical near-field range at UCLA (Fig. 5.10(b)). The measured S_{11} and radiation patterns are presented and compared to the simulated results in Fig. 5.10(c) and 5.10(d) respectively. It is evident that a reasonable match between the measured and simulated S_{11} was achieved at 19 GHz. As far as the main beam region is concerned, the measured pattern agrees reasonably well with simulation, indicating that this feed can provide an acceptable illumination to the reflectarray. The measured pattern manifests slightly higher sidelobes and an overall higher X-Pol level. This is likely due to the fabrication tolerance and the interactions with the connector which was not modeled in simulations.

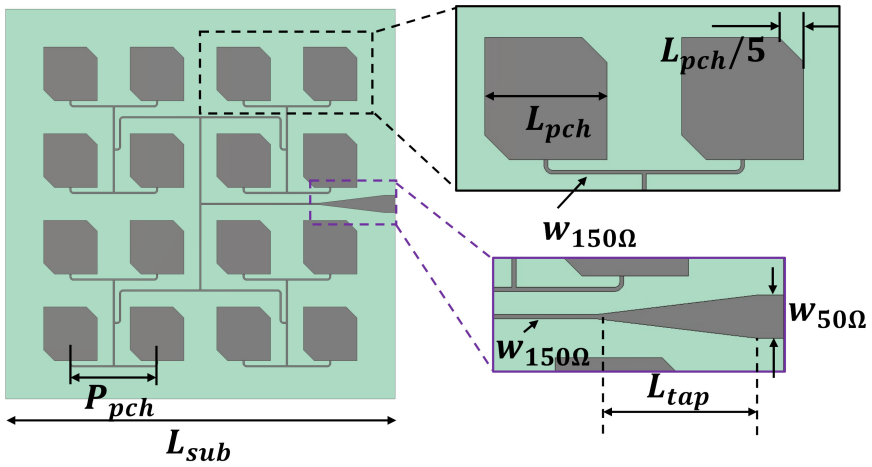

Unit: [mm]

L_{sub}	P_{pch}	L_{pch}
35.55	7.90	4.90

L_{tap}	$w_{150\Omega}$	$w_{50\Omega}$
6.50	0.15	1.58

Substrate thickness: 0.508 mm

(a)

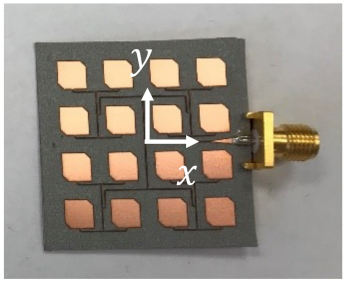

(b)

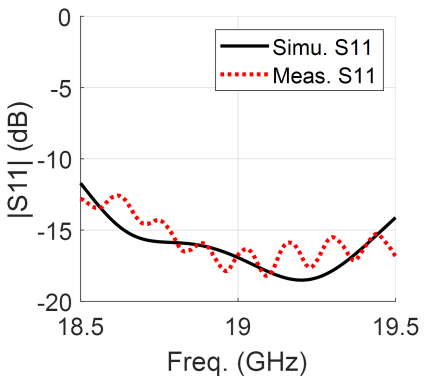

(c)

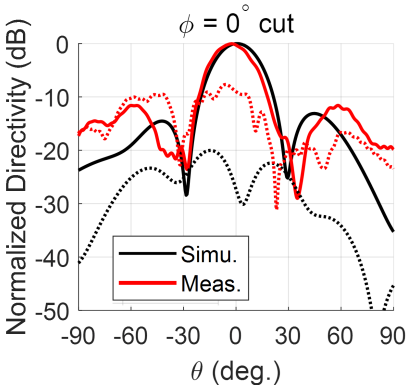

(d)

Figure 5.10 (a) The geometry of the CP-TCPA and values of corresponding design parameters. (b) Photo of the fabricated CP-TCPA. (c) The measured vs. simulated reflection magnitude $|S_{11}|$. (d) The measured vs. simulated far field pattern of the feed at 19 GHz. The solid lines represent the RHCP (Co-Pol) patterns and the dash lines represent the LHCP (X-Pol) patterns.

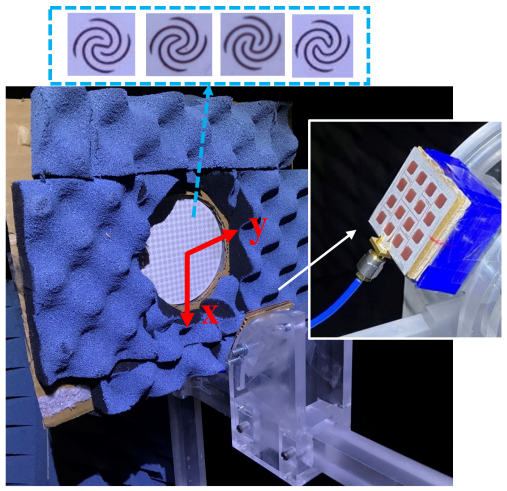

(a)

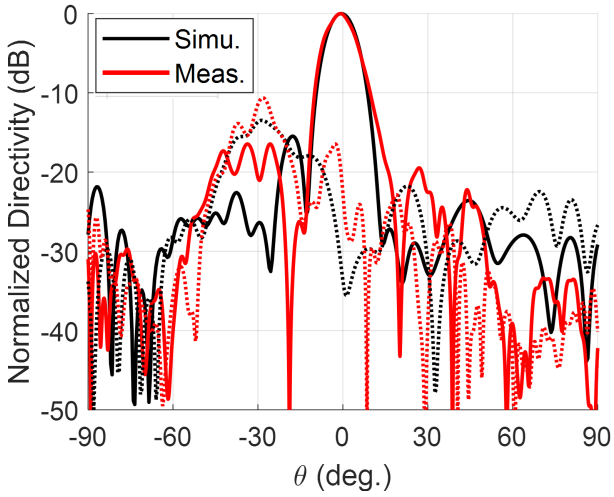

(b)

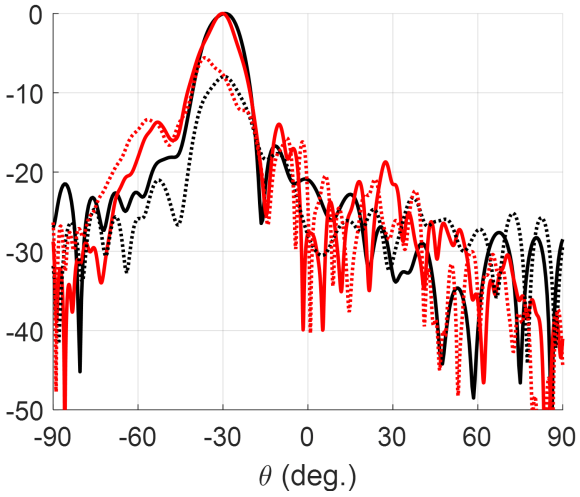

(c)

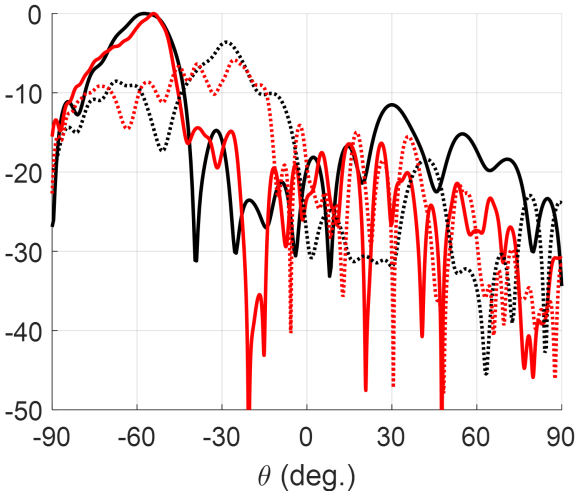

(d)

Figure 5.11 (a) Photo of the the reflectarray prototype being measured with the CP-TCPA feed. (b) - (d): Measured vs. simulated normalized patterns in $\phi = 0°$ plane (plane of offset) at 19.0 GHz for broadside, 30° and 60° scanned reflectarrays using CP-TCPA feed. The measured RHCP directivities are 23.0 dBi, 20.1 dBi and 17.9 dBi for each case, respectively.

5.3.3 Reflectarray Measurement with the CP-TCPA Feed

The fabricated CP-TCPA was then used to feed the reflectarray prototypes (Fig. 5.11(a)). Absorber was used to cover the metallic mounting plate to prevent its reflection of the high sidelobes of the CP-TCPA feed. The measured patterns (in the plane of offset) are presented in Fig. 5.11(b), 5.11(c), 5.11(d) and compared with the simulated patterns. For all three cases, we observed a reasonable match between measurement and simulation. The measured broadside directivity is 23.0 dBi at 19 GHz, corresponding to an aperture efficiency of 50.4%. We observed a -0.5 dB extra directivity loss compared with the estimation in Table. 5.2, and this is attributed to the use of the CP-TCPA.

It's worth noting that, the high X-pol level in Fig. 5.11(b), 5.11(c), and 5.11(d) is attributed to the specular reflection, which is a well-known phenomenon with reflectarrays. As can be noticed, the majority of the X-Pol occurs in the specular reflection direction: around 30° away from the feed, which agrees with the 26.5° tilt angle of the feed. Since the specular reflection is strongly related to the feed source, its level and direction are relatively insensitive to beam scan directions. On the other hand, the directivity of the Co-Pol beam will decrease as it scans, thus, the X-pol level appears higher when the beam is scanned more from broadside. This matches with what can be observed from Fig. 5.11. While this can be potentially improved using a larger aperture, our current demonstration focuses on a 10-cm aperture to comply with the dimensions of 1U of CubeSat. In reality, the aperture size can be enlarged if higher directivity is desired and an extended CubeSat platform is available (e.g., 2U, 3U).

These results validate our reflectarray design and support our ongoing efforts on the design of a compact, low-cost and broadband, CP microstrip patch feed that covers the entire frequency band of 17.8 - 20.2 GHz.

Table 5.3: Measured RHCP (Co-Pol) directivity of the reflectarrays using LP horn feed.

	17.8 GHz	19.0 GHz	20.2 GHz
Broadside	19.4 dBi	19.4 dBi	19.5 dBi
30° scanned	19.8 dBi	19.5 dBi	20.5 dBi
60° scanned	15.8 dBi	17.1 dBi	17.2 dBi

5.3.4 Evaluating the bandwidth of the Reflectarray Prototypes using a Linearly-Polarized Horn

To evaluate the bandwidth performance of the reflectarrays, we used a standard LP horn (NARDA-638) as an alternative feed source. It is well-known the LP radiation from the feed can be treated as a superposition of an RHCP and an LHCP wave of equal amplitude and phase. Our designed reflectarray will correct the phase of the RHCP component and thus result in a collimated RHCP beam. On the other hand, the LHCP component will experience a conjugate phase shift (according to the phase property discussed in Section 5.1.1) and will not result in a definitive main beam in the far field. Therefore, one should still expect a directive RHCP (Co-Pol) beam in the far-field pattern of the reflectarray, regardless of the LHCP (X-Pol) pattern. Further, the LP horn covers the target frequency band and provides the optimal amplitude taper. Thus using an LP horn can effectively validate the bandwidth of our reflectarray.

The measurement was performed in the spherical near-field range at UCLA (Fig. 5.12(a)). The reflectarray prototypes for different scan angles were measured at three representative frequencies and the RHCP patterns are shown in Fig. 5.12. The LHCP (X-Pol) patterns are omitted since they do not reveal the actual X-Pol performance of the reflectarray because of the use of the LP source. At each frequency, the measured patterns demonstrated beam scan up to 60° and thereby verifying the reflectarrays' performance over the interested frequency band. The measured directivity of each beam is listed in Table. 5.3. Despite the overall 3 dB loss in directivity due to the use of LP feed horn, the directivity remains stable over the frequency band for each beam angle.

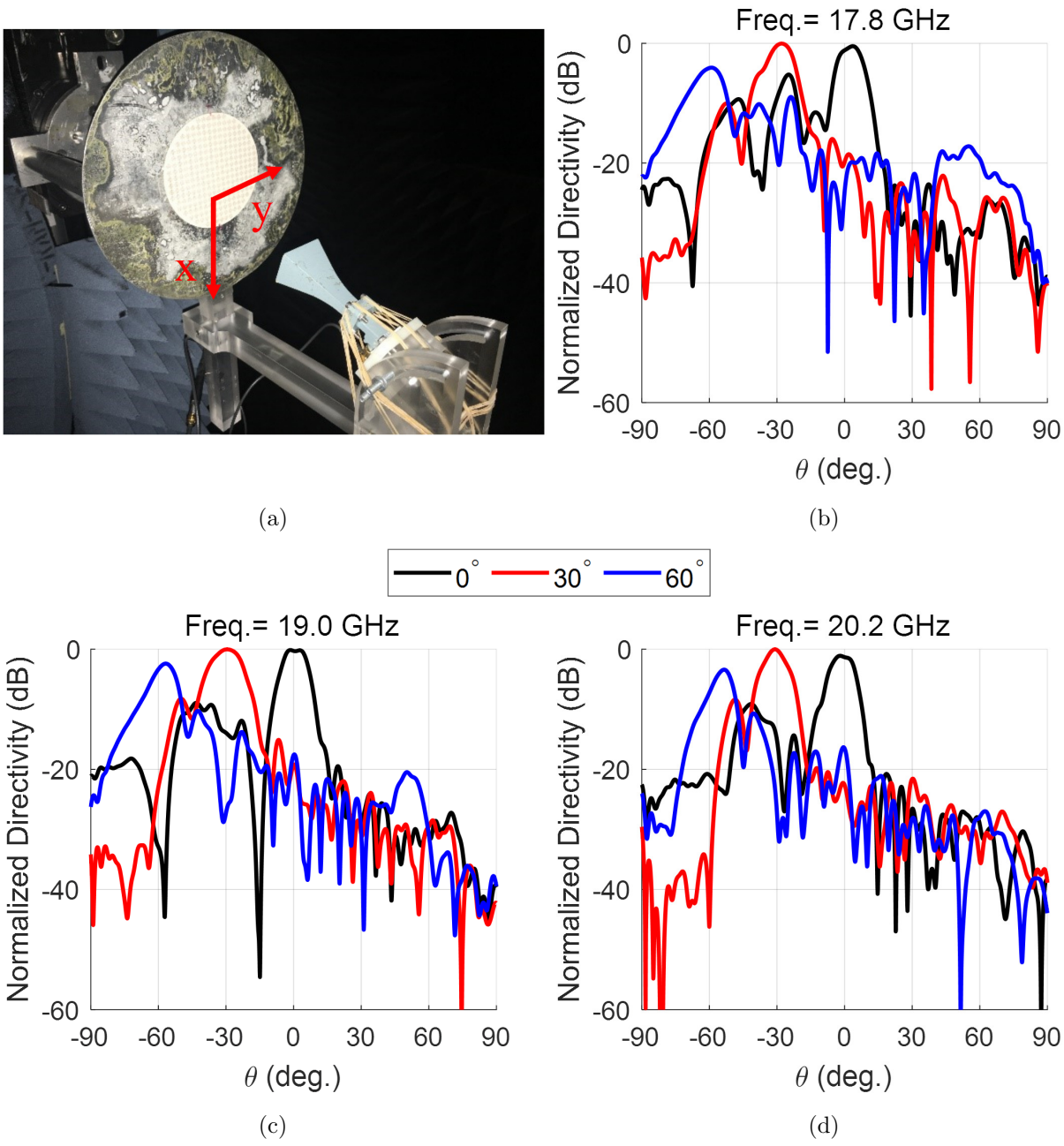

Figure 5.12 (a) Photo of the reflectarray measurement setup using a LP horn (NARDA-638) as feed. The metal plate behind the reflectarray was used for mounting purpose. (b) - (d): Measured reflectarray patterns showing multiple scanned beams in $\phi = 0°$ plane (plane of offset) at 17.8, 19.0 and 20.2 GHz for the reflectarray prototypes using LP horn feed. The measured RHCP (Co-Pol) directivities are tabulated in Table 5.3.

It's interesting to point out that the measured directivities of the broadside beams are slightly lower than the 30° scanned beams. This is because the broadside beam suffered from more feed blockage than the 30° scanned beam, which was scanned away from the feed. As for the 60° scanned beam, the scan loss dominates. For reference, the estimated scan loss using the $\cos(\theta)$ roll-off model is -0.6 dB for a 30° scanned beam, and -3.0 dB for a 60° scanned beam. These results validate our reflectarray design in terms of bandwidth and the potential of dynamic beam steering in the band.

5.4 Conceptualization of a 3-State Reconfigurable Unit Cell Tailored for PIN Diode Switch Implementation

The successful validation of the 2-bit unit cell in section 5.2 justified the promising CP bandwidth potential of unit cells based on switch-reconfigured multi-Archidemedean spiral arms. However, the 2-bit unit cell require at least six switches per unit cell to perform reconfiguration, which incurs substantial cost and complexity for prototyping. On the other hand, it can be shown through cosine-q array studies that even a 3-state phase resolution (120° phase step) can substantially reduce the quantization loss to less than 1.5 dB. Therefore, a 3-arm Archimedean spiral unit cell using less number of switches but not compromising CP bandwidth thus become a reasonable trade-off between quantization loss and implementation complexity. This section presents such a 3-state unit cell design for 17.8 - 20.2 GHz, which is tailored for practical implementation with p-i-n diode switches. The unit cell includes the necessary features for p-i-n diode mounting, DC biasing and DC-RF isolation.

The key features of the unit cell are shown in Fig. 5.13. The 3-arm Archimedean spiral element is located on the top layer. Each arm is built from a spiral curve defined by $\rho = \phi/2.276$ and truncated by an inner circle and an outer circle. The three arms are relatively rotated by 120° about the center. On the central terminations of the arms, mounting pads are designed based on the footprints of the p-i-n diode MA4GP907. On the outer rim, each arm is terminated with a via pad, which connects with a through-via that conducts the DC bias. As shown in the stacked view (Fig. 5.13), the spiral element on layer 1 is backed by

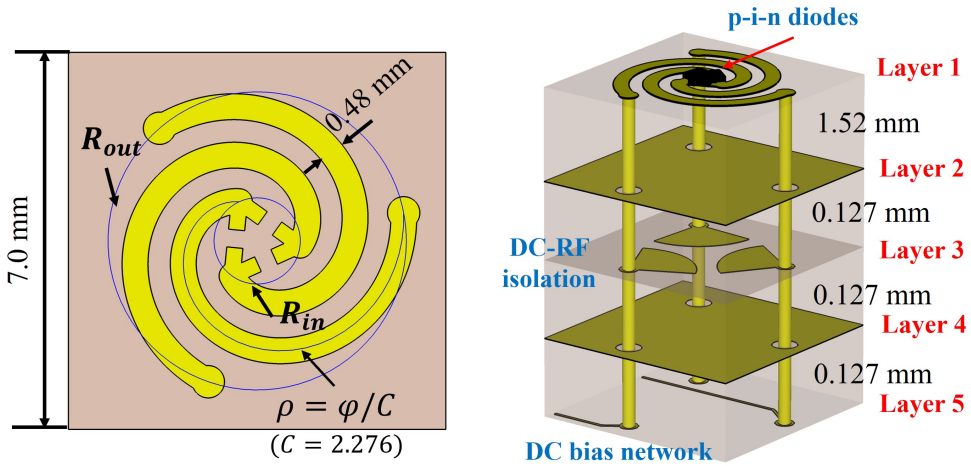

Substrate: Rogers RO3035

Unit: [mm]

P	R_{out}	R_{in}	w	R_{pad}	t_1	t_2
7.0	2.77	0.8	0.48	0.3	1.52	0.127

Figure 5.13 The key design parameters of the 3-state reflectarray unit cell tailored for p-i-n diode switch implementations.

ground plane on layer 2. The vias penetrate the ground plane (with clearance) and connect with the radial stubs (layer 3) that are used for DC-RF isolation. It's worth noting that, radial stubs creates a broadband short-circuit condition at the center of the sector, thus it is typically paired with an additional quarter-wavelength transmission line to create the broadband open-circuit condition for the RF signal. In this particular design, the space is very limited for the distribution of additional transmission lines along with the radial stubs. Instead, we remove the quarter-wavelength lines and connect the radial stubs directly to the vias, and optimize the entire structure simultaneously. This is effectively merging the quarter-wavelength lines as part of the spiral arms, and is possible due to unique wire-like spiral arms element used in this design.

Another ground plane is assigned on layer 4, it serves as a ground for DC bias and also provides better shielding between the radial stubs and the DC supply network on layer 5. Based on this unit cell, the total thickness of the reflectarray will be 1.90 mm, or $0.12\lambda_0$ (λ_0: free space wavelength at 19 GHz).

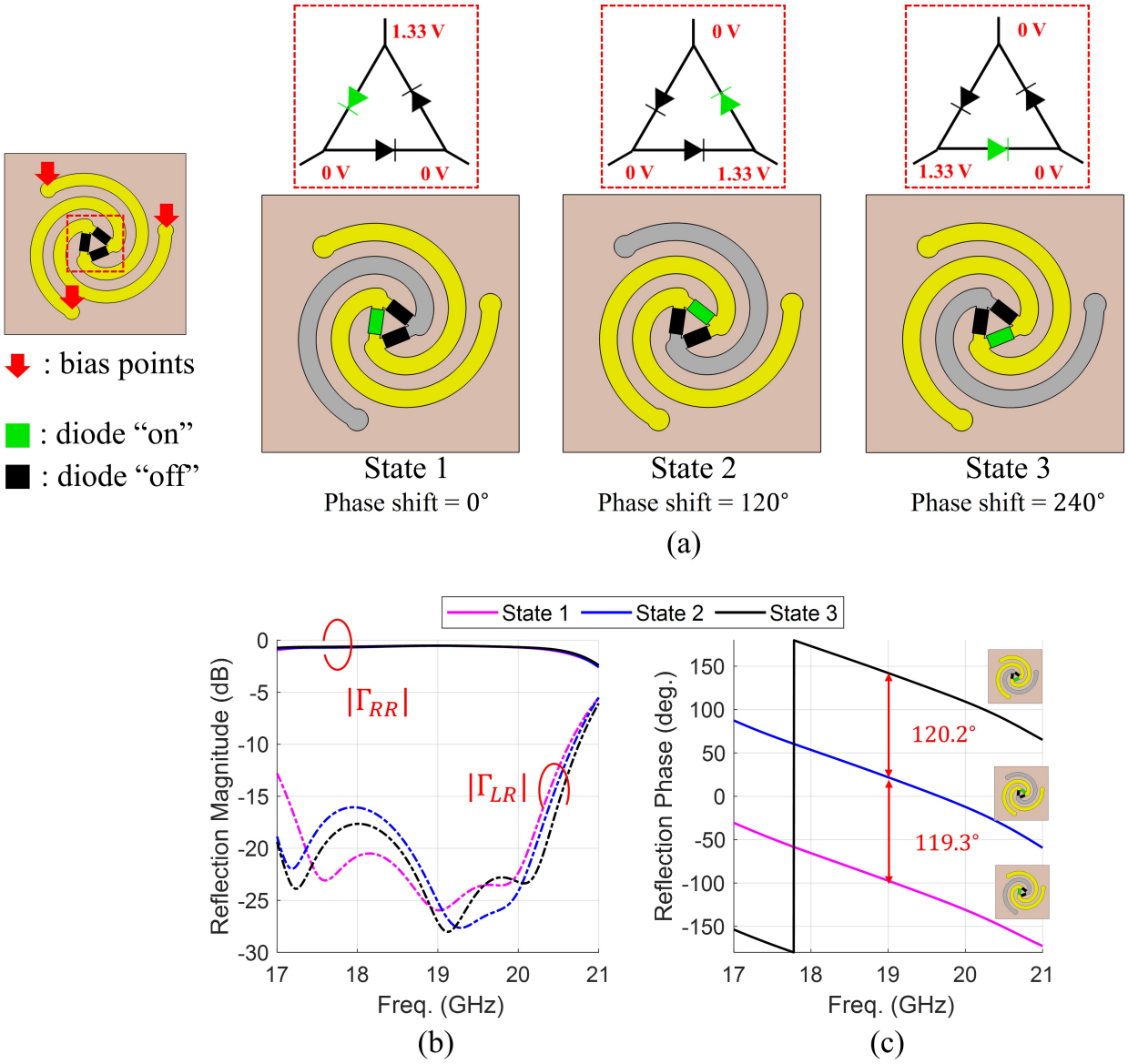

Figure 5.14 (a) The biasing scheme to realize 3-state phase reconfiguration of the unit cell. (b) The simulated reflection coefficient magnitude of the unit cell. (c) The simulated reflection phase of the unit cell.

The three diodes assembled in the center of the element form a triangular-type circuit [Fig. 5.14 (a)]. The metallic element will conduct the DC bias voltage from the three bias points to the diodes. Each two adjacent diodes share the same biasing voltage from one of the bias points. By turning one of the diodes on at a time, one creates three different types of connection in the center, which effectively rotates the element by a step of 120°. According to (5.1), the corresponding CP phase shift (consider RHCP incidence) is twice the rotation angle: i.e., $0°, 240°$ and 480°. Considering phase wrap of 360°, the three states can also be interpreted as $0°, 240°$ and 120°, which are equivalent to three phase states with 120° spacing [referred to as State 1, 2, 3 in Fig. 5.14 (a)].

The unit cells for all three states were simulated in CST Studios. The "on" diode was modeled as a resistor (5.2 Ω) and an inductor (30 pH) in series, and the "off" diodes were modeled as a capacitor (25 fF) and an inductor (30 nH) in series (values from MA4GP907 datasheet). In the frequency band of interest (17.8 GHz - 20.2 GHz): the cross-polarized magnitude $|\Gamma_{LR}|$ is suppressed below -16 dB [Fig. 5.14(b)]. The co-polarized magnitude $|\Gamma_{RR}|$ is maximized, and the overall -0.5 dB magnitude drop is mainly due to the loss in diodes. The phase curves of the reflected co-polarized component $\angle\Gamma_{RR}$) have a relative spacing of 120° and is stable versus frequency [Fig. 5.14 (c)], which validates the 3-state phase reconfiguration capability of the unit cell. By altering the length and using different loading for the bias lines, it was shown that the RF performance of the unit cell did not change, thus justifying the effectiveness of the DC-RF isolation.

5.5 Validations of the 3-State Reflectarray Unit Cell with Reflectarray Simulations and Prototype Measurements

5.5.1 Reflectarray Simulations with PIN Diodes Modeled

A 14×14 reflectarray was then designed using the proposed unit cell [Fig. 5.15 (a)]. The diodes in each unit cell were considered and modeled as equivalent lumped elements as done for the unit cell simulations. The reflectarray was simulated with a RHCP $\cos^{14.5}\theta$

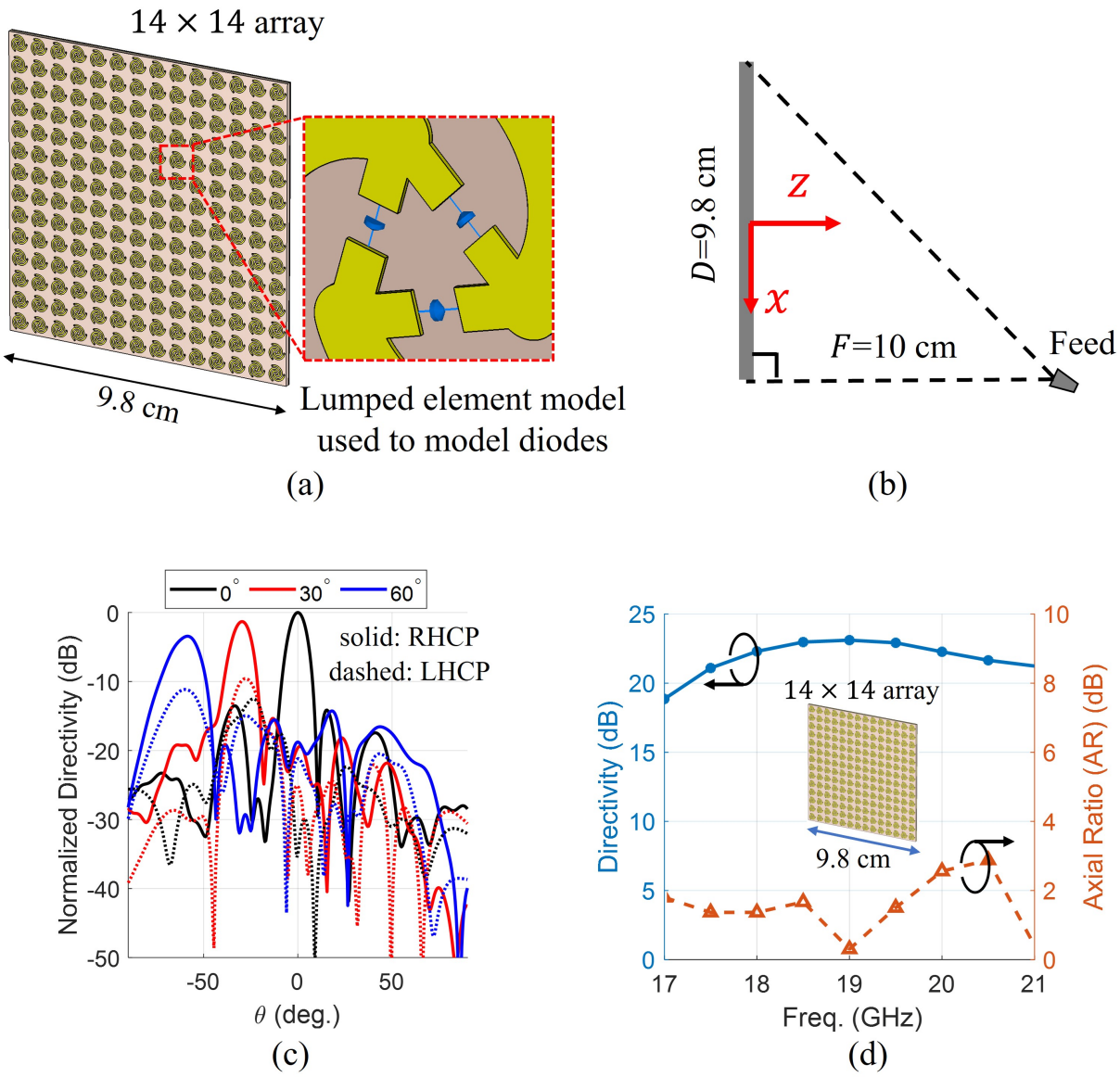

Figure 5.15 (a) The simulated 14 × 14 reflectarray with p-i-n diodes in each element modeled with corresponding lumped element model. (b) The offset feeding configuration of the reflectarray. (c) The simulated pattern of the reflectarray showing multiple scanned beams from broadside to 60° at 19 GHz. (d) The simulated directivity and AR of the reflectarray over frequency.

feed in an offset configuration as shown in Fig. 5.15. Simulated patterns of representative scanned beams are presented in Fig. 5.15 (c). The peak directivity of 23.2 dBi was achieved at 19 GHz, corresponding to an aperture efficiency of 43.2% (including quantization loss), which is a competitive number for electronically steerable reflectarrays. Across the band of 17.8 - 20.2 GHz (12.6% bandwidth), the simulated broadside directivity variation is around 1 dB and the axial ratio remains below 3 dB [Fig. 5.15 (d)]. These results support the anticipated performance of the proposed unit cell.

5.5.2 A Potential Architecture for the DC Bias Control Board and its Assembly with the Reflectarray Board

One of the limitations of most reconfigurable reflectarrays and transmitarray antennas reported in the literature is that the DC bias lines of all the elements have to be wired to the edge of the boards to connect with multi-pin connectors. This causes the DC bias lines to be very densely distributed, largely limiting the number of bias lines that can be accommodated on the board, and consequently limiting the scalability of the design. Therefore, we propose an architecture as shown in Fig. 5.16 to distribute the bias lines locally and utilize board-to-board (B2B) connectors (Female: Molex 5054130610, Male: Molex 5052740612) to connect the reflectarray board and the PCB board delivering DC bias voltage. The DC bias voltage can be delivered to each biasing point through a series input signal with cascaded shift registers [Model used for demonstration: SN74HCS164QBQARQ1, Fig. 5.16 (c)]. With this architecture, the size of the array is no longer limited by the bias lines, and the reflectarray boards can even be manufactured as modular panels to achieve the scalability of the antenna aperture. This architecture can also be realized with the ball grid array (BGA) packing technique to avoid the assembly of B2B connectors.

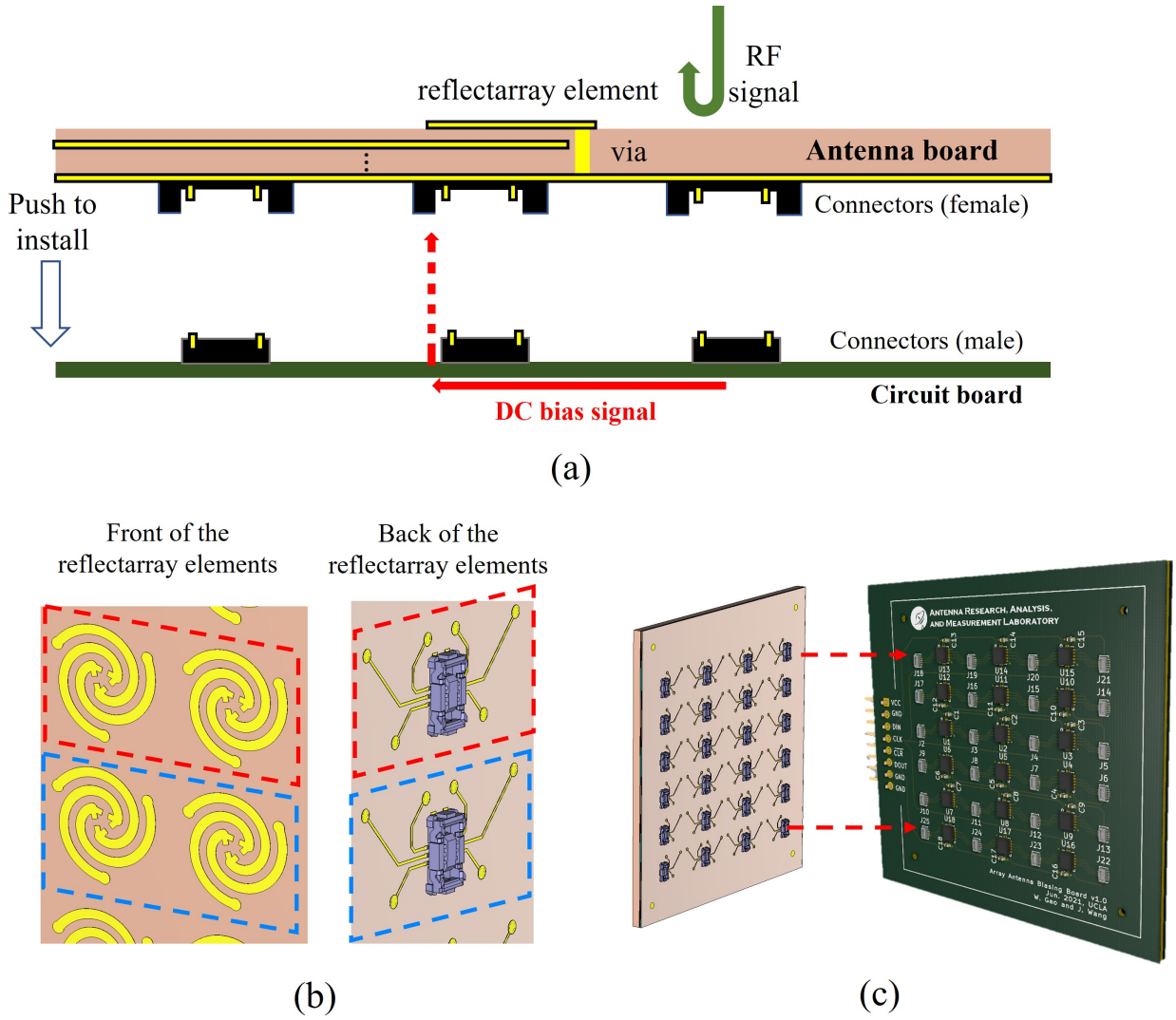

Figure 5.16 (a) A potential architecture that connects the reflectarray board with a DC bias control PCB board using B2B connectors. (b) The grouping of the elements. Each two elements are assigned to an 8-pin B2B connector (with 2 pins left dummy). (c) An illustration of the reflectarray board being assembled to the PCB control board. (showing 6×6 element array as an example).

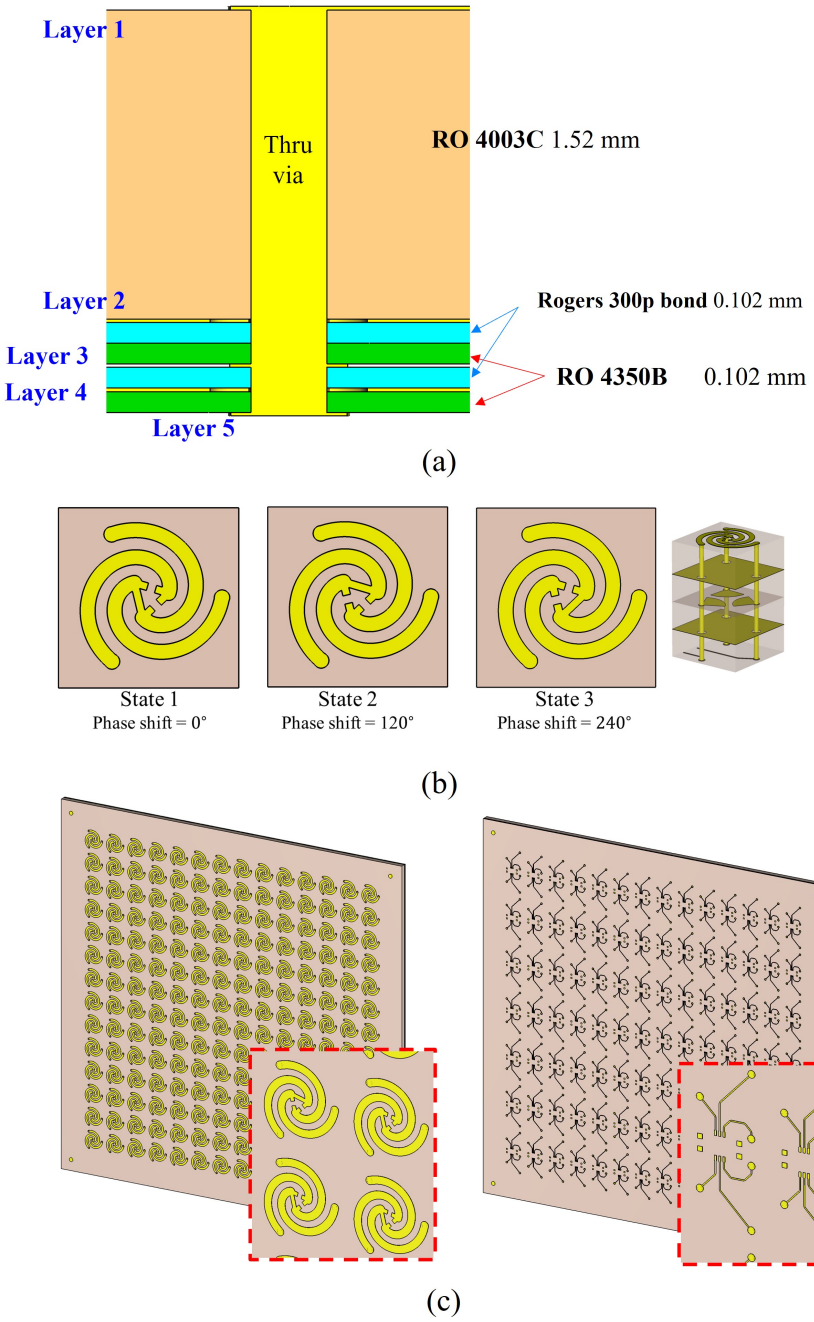

Figure 5.17 (a) The board stack-up view for the prototyping of the reflectarray boards. (b) The idealized elements using ideal open/short connections to model the switches. (c) The front and back of the 14 × 14 reflectarray panels for prototyping, showing the reflectarray elements and the bias lines.

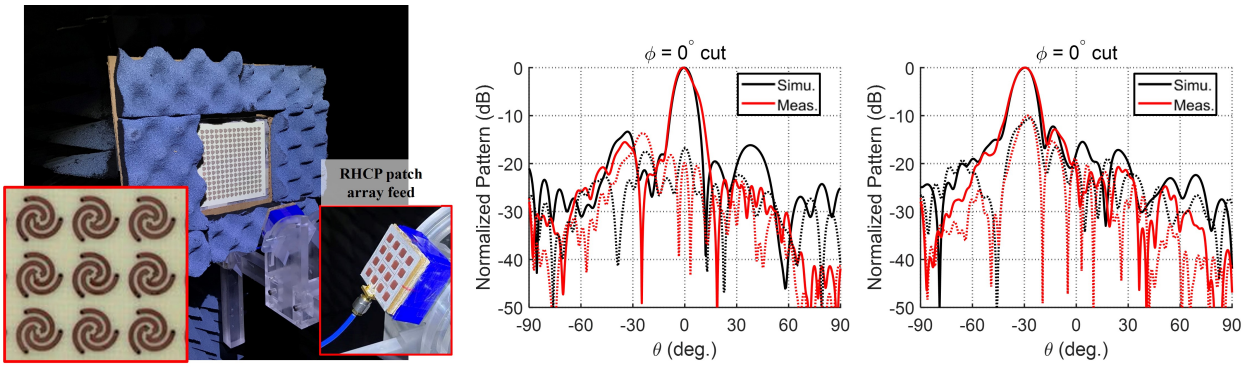

(a) (b) (c)

Figure 5.18 (a) Photo of the reflectarray prototypes being measured in the spherical near-field range at UCLA. (b) - (c) Measured versus simulated patterns of the reflectarrays for broadside beam and 30°−scanned beam at 19 GHz. (Solid lines: RHCP pattern, dashed lines: LHCP pattern.)

5.5.3 Reflectarray Prototypes Validating the 3-State Unit Cell and Multi-layer Configuration

Reflectarray prototypes were then manufactured to validate the concept of the 3-state unit cell and to verify this multi-layer configuration. For proof of concept, ideal open/short circuit conditions were considered to represent the switches (Fig. 5.17). However, all the rest of the structures in the design were maintained. The stack-up view of the antenna board is shown in Fig. 5.17 (a). Two reflectarray instances, designed for broadside beam and 30°−scanned beam, are fabricated. The fabrication was performed by Fast Turn PCB.

The reflectarray prototypes were then measured for radiation pattern in the spherical near-field chamber [Fig. 5.18 (a)]. The measured patterns manifest a good match with the simulation results [Fig. 5.18 (b)]. The measured directivity for the broadside beam is 23.7 dBi, corresponding to an aperture efficiency of 46.5% at 19 GHz when considering a 10 cm square aperture. The measured directivity of the 30°−scanned beam is 22.3 dBi at 19 GHz, corresponding to a 1.4 dB scan loss that is close to that estimated from $\cos(\theta)$ roll-off. These measurements verified the effectiveness of the 3-state unit cell as a candidate for CP beam steerable reflectarrays. The effectiveness of the DC-RF isolation was also verified with the presence of DC bias lines.

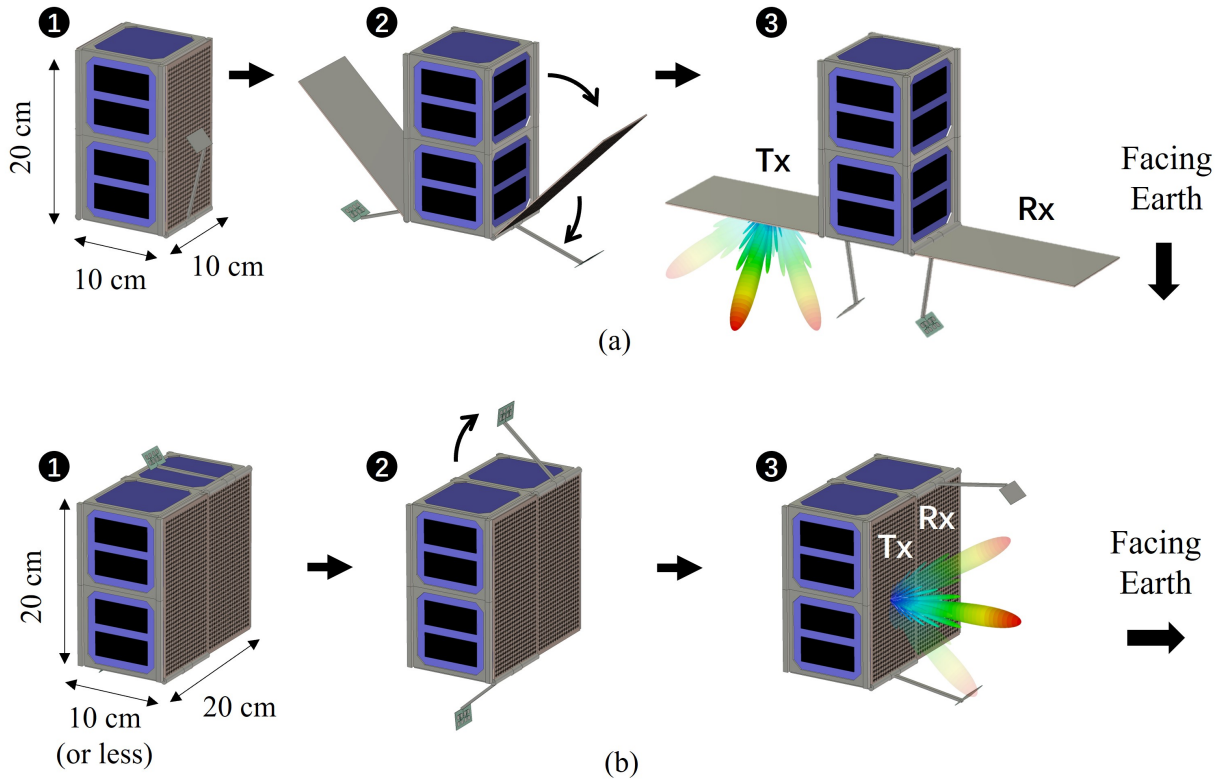

Figure 5.19 Illustrative diagrams showing potential implementation of the reflectarrays on CubeSat platforms. (a) On a 2U CubeSat, the Tx and Rx reflectarrays as well as the corresponding feeds are folded to the side of the CubeSats when stowed, and deployed when in orbit. (b) On a 4U CubeSat, the Tx and Rx reflectarrays are attached to the side wall of the CubeSat and only feeds are deployed.

5.6 Potential Implementation on CubeSat Platforms

The thin-panel profile of the electronically steerable reflectarray antennas offers various options for CubeSat integration. A possible solution for deploying reflectarrays on CubeSats, as has been demonstrated in [11, 13] for fixed beam designs, is to fold and unfold the reflectarray panel while having the feed source mounted on the chassis of the CubeSat. The advantage of such a configuration is that the feed stays stationary and is close to the RF utilities, ensuring stable distribution of RF power and avoiding additional loss. However, for beam steerable reflectarrays, this configuration has several disadvantages: (1) the body of the CubeSat presents a considerable blockage and limits the scanning range of the antenna; (2) the folding and deployment of the reflectarray can be more challenging considering the

existence of additional circuits and wires for DC bias control. Alternatively, two potential schemes for implementing beam steerable reflectarrays on CubeSats are depicted by the author in Fig. 5.19, where both schemes offer sufficient clearance for beam scan. For this illustration, 10 cm by 20 cm rectangular reflectarray panels are considered. Fig. 5.19 (a) demonstrates the deployment sequence of a Tx and an Rx reflectarray along with their feeds, using a 2U CubeSat. Both the reflectarray panel and feed can be stowed to the side of the CubeSat and deploy when in orbit. Fig. 5.19 (b) shows another possible mechanism to integrate the reflectarray panels to the chassis of a 4U CubeSat. Only the feeds need to be deployed and the reflectarray remains stationary. Fig. 5.19 presents only representative methods for implementing beam steerable reflectarray on CubeSats, and the realization of these concepts requires collaborative efforts from all engineering aspects that the author looks forward to.

5.7 Future Directions

The reflectarray prototypes in this chapter have successfully validated the CP bandwidth potential and phase reconfigurability of the proposed multi-Archimedean spiral arm unit cell. The multi-layer configuration for p-i-n diode switch implementations has also been verified through measurements of the 3-state unit cell reflectarray prototypes. The full beam scanning capability relies on the incorporation of actual switches in the unit cell, which raises several technical challenges that requires continuing research input:

(a) The availability of low-capacitance switches (preferably less than 25 fF for good off-state isolation) is critical for the implementation of the switch-reconfigured beam steerable reflectarrays in K-band. While commercial p-i-n diodes such as MA4AGFCP910 have a rated frequency range of up to 40 GHz and a rated capacitance around 25 fF [136], measurements of such p-i-n diodes at X-band have suggested higher-than-rated capacitance values [137]. This causes the switches to be less effective in "shutting" the RF current, especially at higher frequencies, leading to significant deterioration in the fabricated unit cell's performance (i.e., rise in X-pol and shift in frequency). This

necessitates extensive characterization of the p-i-n diodes' performance and potential adjustments to the unit cell design based on the measured switch parameters. With the increasing interest in RF switch implementation in wireless devices, it is also anticipated that the switch manufacturing industry can be advanced to enable even lower capacitance and lower loss switches such that the reconfigurable unit cell design can enjoy more tolerance. Other switch technologies, such as MEMS switch, graphene and VO2 material may also offer appealing possibilities.

(b) Due to the uncertainty observed in the current p-i-n diode switches' performance, experimental validation of the unit cell's performance also becomes a necessary step before the fabrication of a full array. A commonly used method for reconfigurable unit cell characterization is the waveguide simulator approach [138, 139]. However, the limitations in waveguide simulation are that it only measures the unit cell's performance under oblique incidence [140], and it enforces a PEC boundary condition around the unit cell that does not necessarily represent the unit cell's actual working condition. Simulations have shown that the waveguide simulator fails at measuring the multi-Archimedean unit cell's performance as it significantly altered the field distribution at the unit cell boundary. Another potential method is the free space characterization of a smaller array sample, which measures the reflection/transmission performance of the partial array through free space [141]. However, this method still requires the construction of an array of considerable size (8×8 in [141]) that makes the characterization of the unit cell expensive. As such, low-cost and effective unit cell characterization techniques are also worth further investigation.

5.8 Summary

Electronically beam steerable reflectarray antenna is another promising architecture for CubeSat applications considering its advantages of being low-profile, lightweight, and having no moving parts. Meeting the challenging antenna requirements of CubeSat IoS with beam steerable reflectarrays necessitates innovative unit cell designs. In this chapter, switch-

reconfigured CP unit cells targeted for the 17.8 - 20.2 GHz band was conceptualized and validated. To achieve wideband CP reconfiguration, the unit cells exploit the geometrical phase property, and utilize switches to control the connection among multiple rotated Archimedean spiral arms to electronically create element rotation. Two unit cells have been presented based on this concept: First, a 2-bit four-arm Archimedean spiral unit cell was designed and validated. Several proof-of-concept 10-cm-diameter reflectarray prototypes incorporating idealized elements were designed, fabricated, and measured. Measurement results demonstrated RHCP beam scan up to 60° in the plane of offset at representative frequencies across the target band of 17.8 - 20.2 GHz. Then, a 3-state three-arm Archimedean spiral unit cell tailored for p-i-n diode switch implementation was designed and validated. The unit cell has multiple layers to distribute DC-RF isolation structures and bias lines underneath each element. A unique B2B connection mechanism was proposed to connect the reflectarray board and potential bias-controlling PCB board. This configuration allows localized distribution of the bias lines and enhances the scalability of beam steerable reflectarrays. Reflectarray prototypes with ideal switch connections were fabricated and measured for representative beam scan directions. The measured results demonstrated excellent agreement with simulations for broadside and scanned beams. These encouraging results have demonstrated the CP bandwidth potentials of electronically steerable reflectarray antennas as new options for IoS CubeSats antennas.

CHAPTER 6

Maximizing Unit Cell Phase Resolution in Switch-Reconfigured Antennas: Pixelated Topology Design with Binary Particle Swarm Optimizations

The next-generation millimeter-wave wireless communication relies heavily on low-cost, low-profile, and power-efficient beam steering devices that can be deployed in mass [142, 143]. These requirements motivated extensive research in reconfigurable reflectarray/transmitarray antennas, reconfigurable intelligent surfaces (RIS), and metasurfaces. For these technologies, reconfigurable unit cells are the key building blocks as they enable the array to dynamically change the aperture phase (and even amplitude) to realize beam steering and even beam forming. Unit cell phase reconfiguration is typically realized through switching of p-i-n diode, MEMS switch, or tuning with varactors, liquid crystals, etc [40, 41, 111]. Particularly, the switch reconfiguration method has attracted great interest for its fast reconfiguration speed, simple binary bias control, and lower power consumption. However, the binary nature of switches also limits the number of phase states that can be achieved by the unit cells. The constructed arrays thus suffer more from the phase quantization effect, which is manifested as higher quantization lobes, distorted pattern, and higher gain loss [57]. For reflectarray/transmitarray applications, it has been shown that 1-bit (2-state) phase resolution can lead to over 2 dB loss in array directivity, and 2-bit (4-state) phase resolution can effectively limit the quantization loss to around 0.5 dB [57].

Achieving a higher phase resolution typically accompanies more switches per unit cell. The majority of the relevant literature reported 1-bit unit cells, and single switch [71, 74, 144] or two switches [72, 76, 145] per unit cell appear to be popular strategies. For 2-bit unit

cells, the complexity in design increases significantly, and exotic element configurations have been proposed to realize 2-bit phase resolution while complying with other requirements such as bandwidth and polarization. Four or more switches per unit cell appeared to be typical in these designs [130, 146, 147]. The drastically increased complexity and cost to implement the switches can diminish the benefit of higher-phase-resolution unit cells. This, however, is because most of the existing works have not exploited all the possible binary combinations of the switches to realize the maximum number of phase states. For a unit cell with N independently controlled switches, there are 2^N possible "on/off" combinations of the switches that can realize 2^N different current distributions. If designed properly, a 4-state unit cell can be realized using only two switches, which is then considered very attractive for practical implementations.

Very limited works have targeted 2-bit switch-reconfigured unit cells (SRUC) using only two switches, and the reported works are all limited to linear polarization (LP) scenarios. In [148], a 2-bit Ku-band reflectarray unit cell using two MEMS switches was conceptualized. It contains a square patch loaded by a double-slot conductor plane. Each slot is crossed by a MEMS switch, the location of which was optimized such that a near-2-bit phase can be generated. In [149], the 11.8 GHz reflectarray unit cell combined the phase delay from two branches of delay lines distributed on the bottom layer to create four different phase states. A p-i-n diode was inserted in each delay line to control the electric length of the line being connected, thereby changing the phase delay provided by each branch. In [150], the 5.8 GHz reflectarray unit cell utilized a similar dual-layer configuration to realize four phase states with only two p-i-n diodes. In [151], a 4-state 275 GHz unit cell was conceptualized for potential millimeter-wave/terahertz reflective surface applications. The unit cell contains a square patch element, which is connected to two delay lines distributed on the same layer. Each delay line is terminated with a graphene-actuated phase shifter. Depending on the switch state, each branch can provide two different phase shifts, and the combined current from the two delay lines results in four different phase states. This type of unit cells require multiple delay lines that have to either occupy a larger footprint or necessitate an additional layer. The capability of achieving even phase separation while maintaining efficiency also

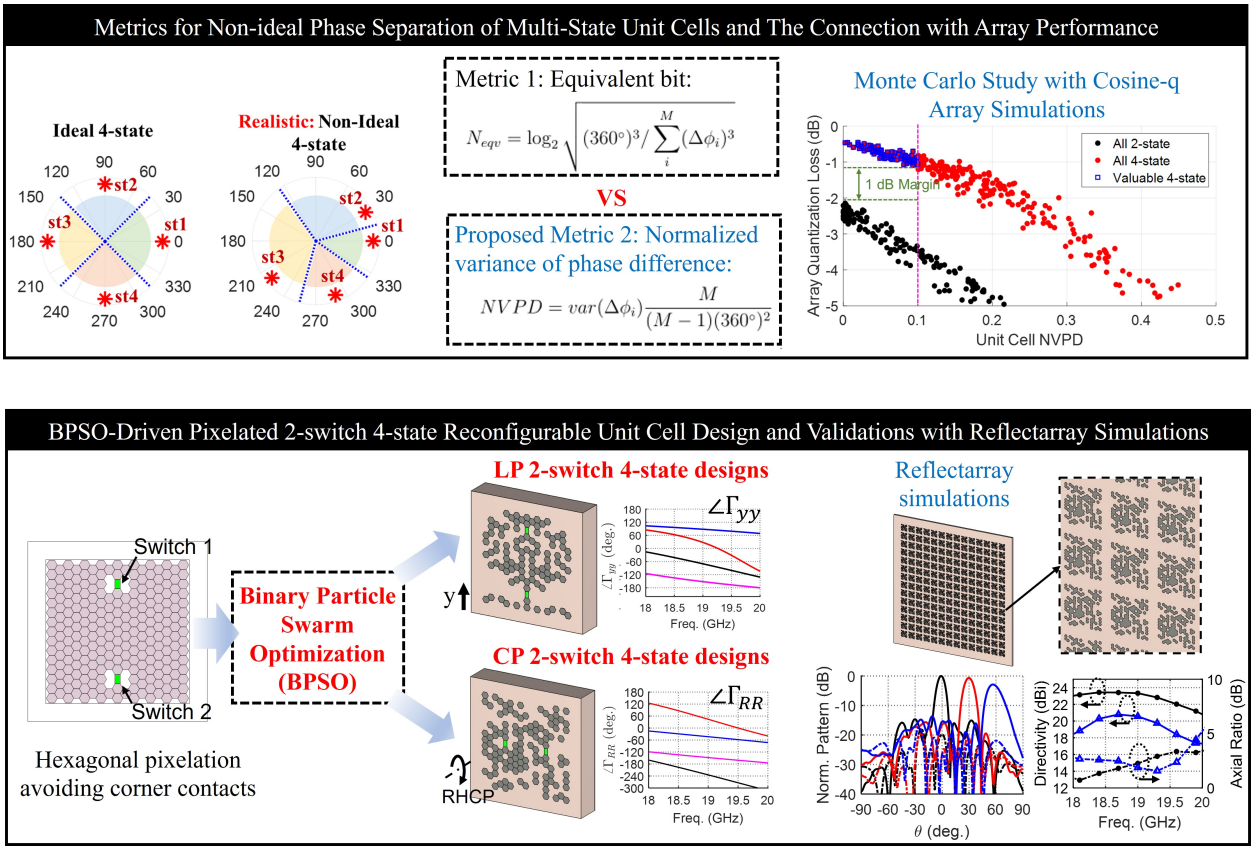

Figure 6.1 Overview of the outline and key contributions of this chapter.

appeared to be challenging. Further, none of these designs have discussed circular polarization (CP) applications, which is critical for applications such as satellite communications. Nonetheless, the existing works have demonstrated the growing interest in fully utilizing the switch combinations in SRUC to maximize the unit cell phase resolution and array performance. A generalized unit cell design methodology for LP and CP applications is worthy of further investigation.

In this chapter, we propose a topology optimization approach to design unit cell element geometry that can achieve four phase states (nearly 2-bit) with two switches, for both LP and CP. This is accomplished by performing binary particle swarm optimization (BPSO) [152,153] on the pixelated element area, with pre-assigned switch locations and orientations considered (Fig. 6.2). The optimization searches for the optimal distribution of the conductive pixels to realize four evenly-spaced phase states. The outline of this chapter is as summarized in Fig. 6.1: We first discuss quantitative metrics that can gauge the non-ideal

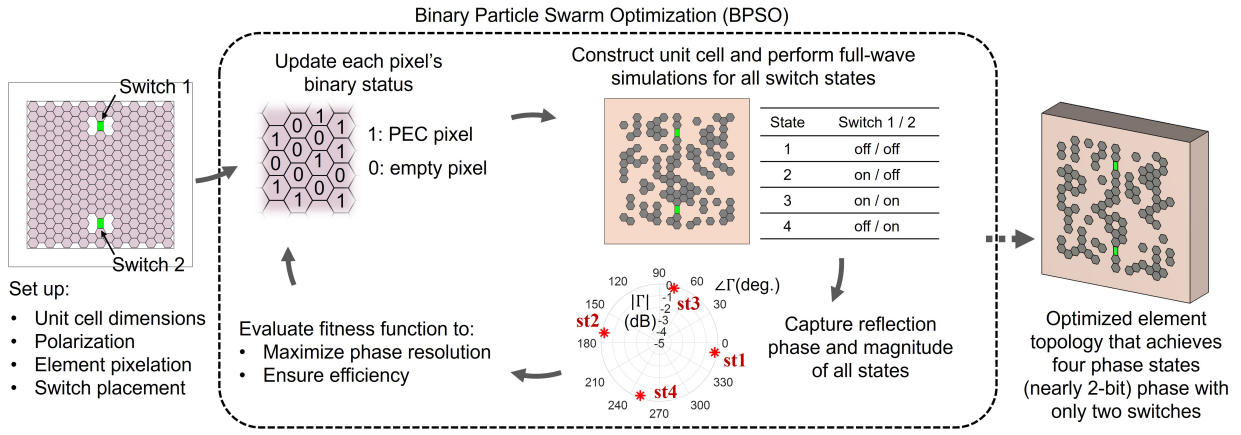

Figure 6.2 Overview of the proposed workflow to design switch-reconfigured reflectarray unit cells that achieves 4-state (nearly 2-bit) phase resolution with only two switches per unit cell.

phase quantization of SRUCs, and establish a connection between these unit cell metrics with expected array performance. Then, K-band beam steerable reflectarray unit cells are considered as design examples. Unique SRUC designs have been achieved, including the first CP 2-switch 4-state SRUC reported in the literature. The performance of the designed SRUCs is validated in beam steerable reflectarray simulations. Critical observations and design insights are also provided. This work was performed in collaboration with Botian Zhang from UCLA Antenna Lab, who was responsible for implementing the BPSO algorithm.

6.1 Metrics for SRUC Design and Their Connection with Array Performance

Ideally, a M-state SRUC should provide M different phase shifts with a spacing of $360°/M$. However, in a particular SRUC design, the M phase states are usually not spaced evenly. This deviation from the ideal phase distribution has an impact on the array performance, and the number of phase states M becomes insufficient to characterize this effect. Additional metrics that quantitatively measure the uneven phase distribution of an SRUC thus become necessary, especially for defining the optimization goal. This section begins with an overview of the reflectarray design process using phase-quantized unit cells. Then, the normalized

variance of phase difference is introduced as a metric that characterizes the evenness an SRUC's inter-state phase separation. The notion of equivalent bit [154] is also discussed as an alternative metric. Finally, the connection between the unit cell's metrics and the performance of the reflectarray is investigated by a Monte Carlo study using array simulations with cosine-q element patterns.

6.1.1 Design of Reflectarrays with Phase-Quantized Unit Cells

In a reflectarray, the required phase compensation at each unit cell can vary continuously from 0° to 360° based on the incident phase and the target aperture phase [155]. An ideal M-state unit cell provides only discrete states of phase compensation with a spacing of $360°/M$. Typically, the state of each unit cell is chosen such that the provided phase shift is closest to the required value. For example, for an ideal 2-state unit cell, this state selection criterion can be visualized in the polar plots [Fig. 6.3(a)]: the two black dots correspond to the phase compensation provided by the 2-state unit cell (0° and 180°), and each dot lies in a 180°-sector with a distinct color. In a reflectarray, the required phase compensation at each unit cell will fall in either of the sectors, and the corresponding state will be assigned to the unit cell. For the reflectarray to scan the beam, different phase compensation for the unit cells is calculated and the state assignment process is performed by the same rule. For designs with ideal 4-state unit cells, the 360° phase range is divided into four sectors [Fig. 6.3(d)], and similar state assignment rules apply. The resulted phase error at each unit cell falls in the range of $[-180°/M, 180°/M]$. The phase error across the reflectarray aperture deteriorates the array pattern and results in quantization loss. Higher phase resolution (larger M) leads to smaller phase error in the aperture and reduces quantization loss.

6.1.2 Characterization of Uneven Phase Quantization

Evenly separated phase states considered in Section 6.1.1 [Fig. 6.3(a), 6.3(d)] are usually unattainable in practical unit cell designs (especially for 2-bit unit cells using only two switches [148–151]). When the M states are not evenly spaced [as shown in Fig. 6.3(b), 6.3(e)],

larger phase error can occur in the reflectarray, which eventually impacts the reflectarray performance. In the worst-case scenarios [Fig. 6.3(c), 6.3(f)], all the M states provide the same phase shift, and the reflectarray can no longer compensate for the spherical incident phase radiated from a feed to generate a directive beam. These observations suggest that merely the number of phase states is insufficient to characterize a reconfigurable unit cell. Additional metrics should be used to measure how evenly spaced the M states are.

In [154], the notion of equivalent bit (N_{eqv}) was proposed as a measure of non-ideal unit cell phase separation. The equivalent bit of a unit cell can be calculated as [154]:

$$N_{eqv} = \log_2 \sqrt{(360^\circ)^3 / \sum_{i}^{M} (\Delta\phi_i)^3} \tag{6.1}$$

where $\Delta\phi_i$ are the phase different between the M states. When the M states are equally spaced, $\Delta\phi_i = 360^\circ/M$ and the equivalent bit $N_{eqv} = \log_2(M)$, which agrees with the conventional "bit" definition. When the M states are not ideally spaced, N_{eqv} becomes smaller than $\log_2(M)$, implying a degradation in phase resolution. However, this equation does not carry a clear mathematical meaning and its connection with the performance of the array has not been clearly discussed either.

In this section, we propose to use the variance of the phase difference between adjacent states to measure the evenness the inter-state phase separation. For an $M-$state reflectarray unit cell, the calculation is as the following:

Suppose the unit cell reflection coefficients of the M states are denoted as $\Gamma_1, \Gamma_2, ..., \Gamma_M$, which are sorted based on their phase ($\angle\Gamma_i$) from low to high. Then, the phase differences $\Delta\phi_i$ of adjacent states can then be calculated as:

$$\begin{aligned} \Delta\phi_i &= \angle\Gamma_{i+1} - \angle\Gamma_i, \quad i = 1, 2, ..., M-1 \\ \Delta\phi_M &= \angle\Gamma_1 + 360^\circ - \angle\Gamma_M \end{aligned} \tag{6.2}$$

from which it becomes clear that the mean of $\Delta\phi_i$ is:

$$mean(\Delta\phi_i) = 360^\circ/M, \quad i = 1, 2, ..., M \tag{6.3}$$

The variance of phase difference (VPD) $\Delta\phi_i$ is then:

$$var(\Delta\phi_i) = \sum_{i=1}^{M}(\Delta\phi_i - 360^\circ/M)^2 \tag{6.4}$$

Note that for an ideal M-state phase resolution, the M phase states are equally spaced and $\Delta\phi_i = 360^\circ/M$ for $i = 1, 2, ..., M$. Therefore, (6.4) implies that the variance of $\Delta\phi_i$ essentially measures how much the phase differences between adjacent states deviate from the ideal phase spacing. The variance $var(\Delta\phi_i)$ equals 0 in the case of an ideal M-state phase resolution and becomes greater than 0 when the M phase states are not equally spaced. The variance has a maximum value when the unit cell has the worst-case phase resolution, i.e., the phase of all M states are the same [as shown in Fig. 6.3(c) for 2-state case and Fig. 6.3(f) for 4-state case]. In such worst cases, according to (6.2), $\Delta\phi_1 = \Delta\phi_2 = ...\Delta\phi_{M-1} = 0$, $\Delta\phi_M = 360^\circ$, and:

$$var(\Delta\phi_i)_{\max} = \frac{M-1}{M}(360^\circ)^2 \tag{6.5}$$

We further normalize $var(\Delta\phi_i)$ by its max value and obtain the normalized variance of phase difference (NVPD):

$$NVPD = var(\Delta\phi_i)\frac{M}{(M-1)(360^\circ)^2} \tag{6.6}$$

NVPD is a value in the range of $[0, 1]$ for any M values chosen, making it easier to compare SRUC of different number of states. NVPD equals 0 in the case of an ideal M-state unit cell and becomes greater than 0 when the M phase states are not equally spaced.

6.1.3 Uneven Phase Quantization and its Impact on Reflectarray Performance

Equivalent bit and NVPD discussed in section 6.1.2 measure the uniformity of the unit cell's phase quantization, but their connection with the reflectarray performance remains to be clarified. The goal of this section is to address the following questions:

a) How is the NVPD (or N_{eqv}) of a unit cell related to the performance of the array constructed with this unit cell?

b) How to decide if a 4-state unit cell design prevail over a 2-state design?

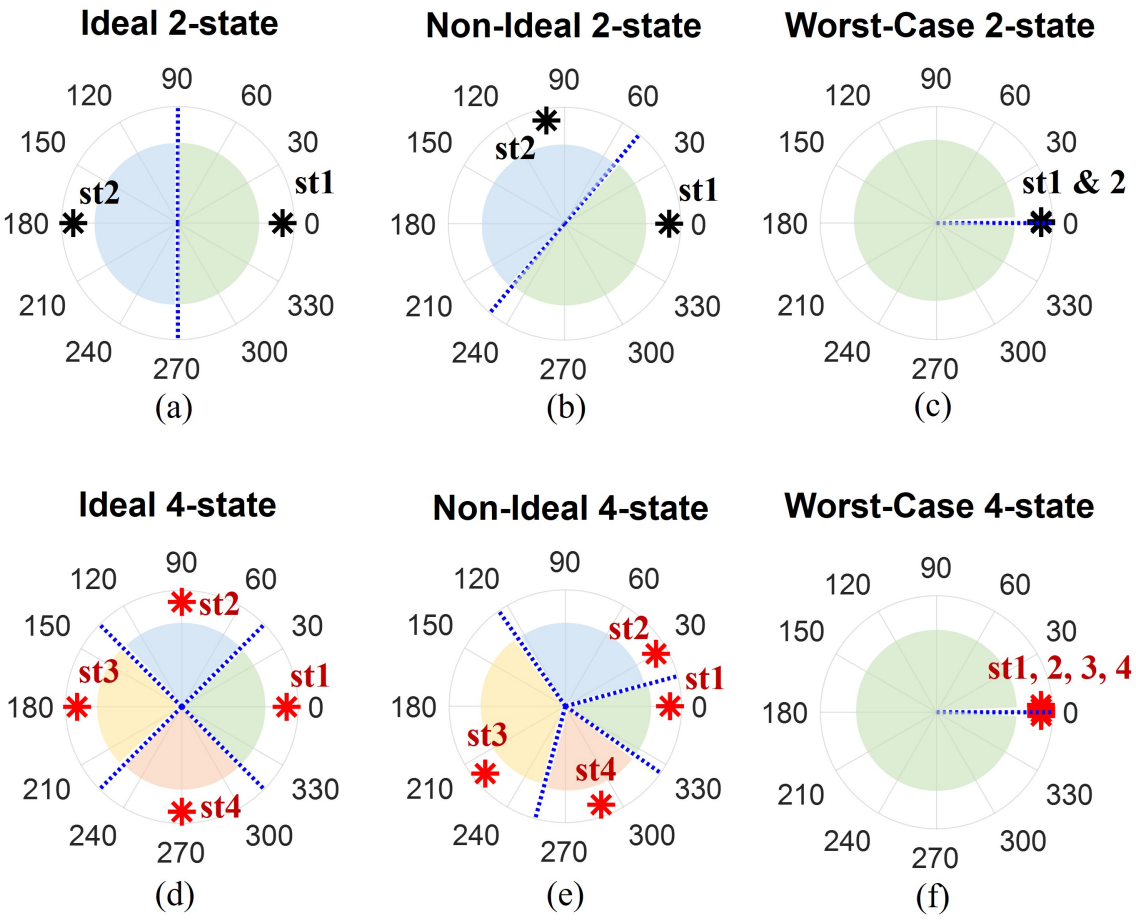

Figure 6.3 (a) - (c) Examples of the possible phase states of a 2-state unit cell presented on a polar plot, showing the ideal case, a non-ideal case, and the worst-case scenario. (e) - (f) Examples of the possible phase states of a 4-state unit cell plotted on a polar plot, showing the ideal case, a non-ideal case, and the worst-case scenario. The colored sectors mark the angular range of required phase compensation in which the corresponding state provides the minimum phase error.

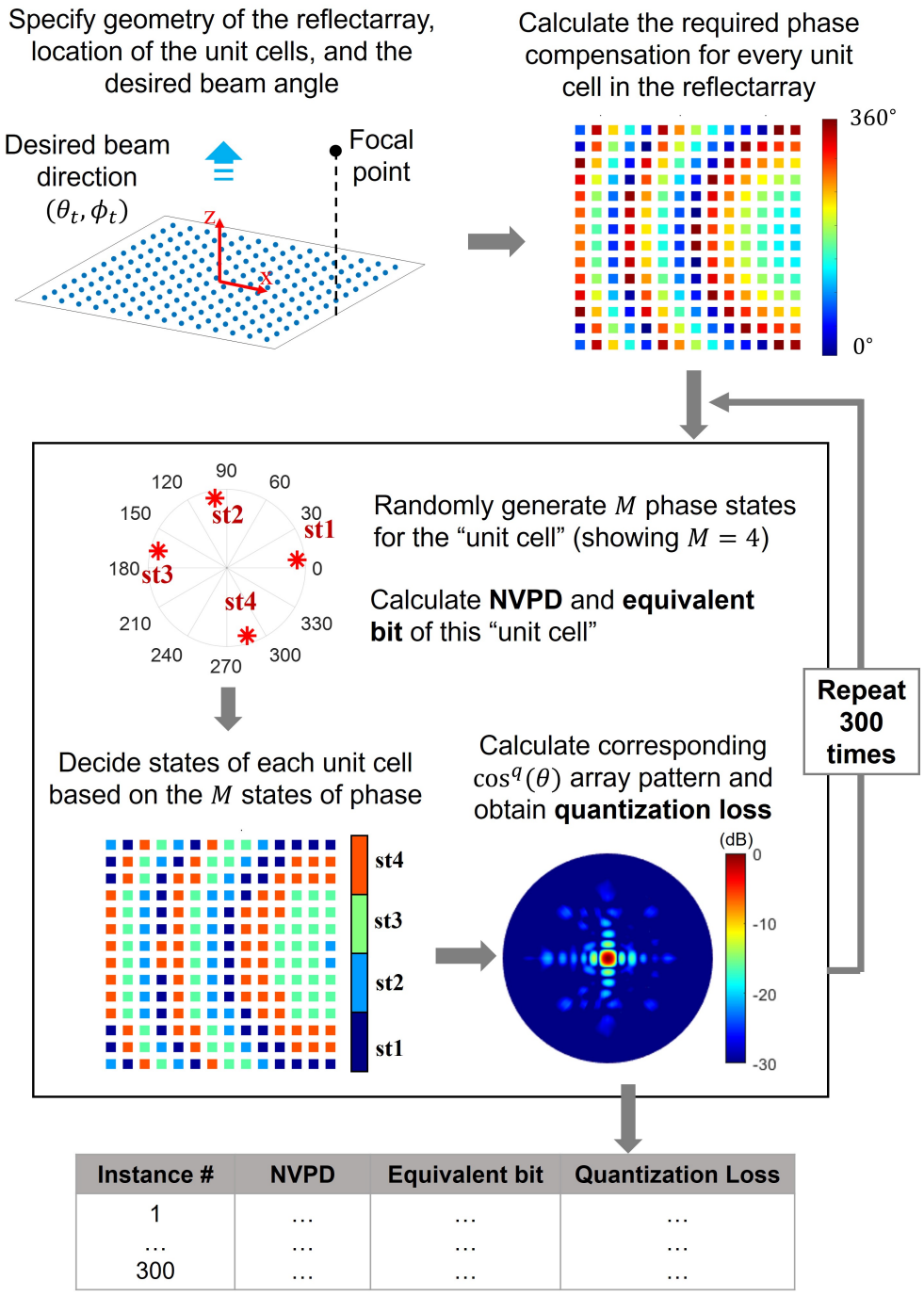

Figure 6.4 Illustration of the Monte Carlo study applied to reveal the relationship between unit cell's NVPD (or equivalent bit) value and the resulted array quantization loss.

The performance of a reflectarray is subject to the influence of various factors, and here we focus on the impact of the phase quantization of the unit cells. One of the most critical impacts of phase quantization is directivity loss in the array. To investigate the relationship between the unit cell's metrics and the quantization loss of the array, we performed a Monte Carlo study using the cosine-q array simulations [134, 147]. The process is summarized in the following and visualized in Fig. 6.4:

0) To begin with, we fix the basic geometries of the reflectarray, including array size, element spacing, focal point locations, as well as the desired beam direction. With these parameters, the ideal phase compensation required at each unit cell is calculated.

1) In each instance, we generate M random phase values within $[0°, 360°)$ to represent the reflection phase of a non-ideal M-state unit cell. The corresponding NVPD and equivalent bit values are calculated using (6.6) and (6.1).

2) This particular set of M-state phases is used to quantize the required phase compensation, resulting in a "map" that specifies the state assigned to each unit cell, as well as the unit cell's corresponding location and phase compensation (Fig. 6.4). This process is the same as that in designing reflectarrays with actual SRUCs [147].

3) The cosine-q array pattern [147] is calculated based on each unit cell's phase compensation obtained in step 2. The far-field pattern and the directivity of this array are evaluated. The directivity loss is the difference from the maximum directivity of the array when ideal (non-quantized) phase compensation is used for each unit cell.

4) This process is repeated 300 times to consider a reasonable amount of possible M-state phase combinations. Eventually, a diagram of directivity loss versus NVPD (or equivalent-bit) value is obtained.

This study was performed by considering both 2-state and 4-state unit cell phase resolution. A 14×14 $\cos^q(\theta)$ array ($q = 1$) with $0.5\lambda_0$ spacing (λ_0: free space wavelength) element spacing was considered. A typical offset feed configuration was used, the focal point

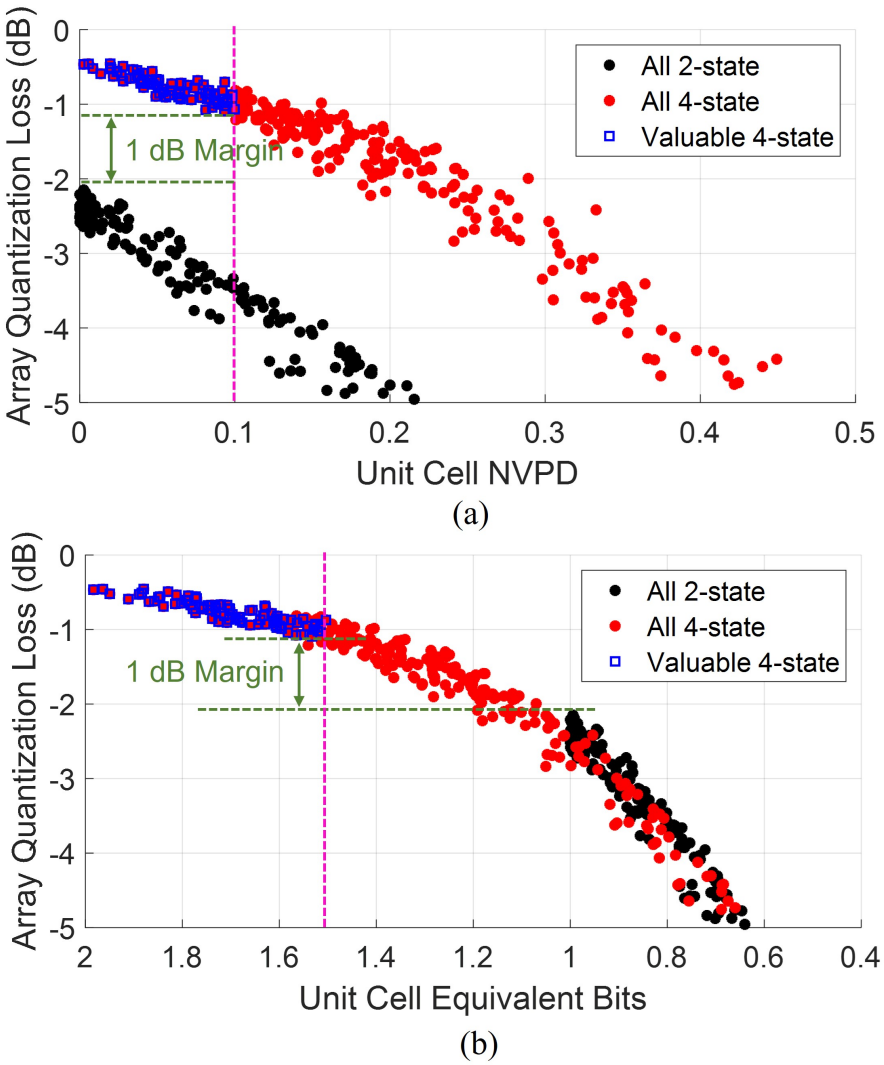

Figure 6.5 The result of the Monte Carlo study using cosine-q array simulations. Each data point corresponds to the quantization loss of a broadside cosine-q array designed using a particular set of M-state unit cell phase ($M = 2$ or 4). The array size studied is 14×14, with $0.5\lambda_0$ spacing. (a) Quantization Loss using 2-state and 4-state unit cells versus NVPD. (b) The same data set presented using equivalent bit as the horizontal axis.

is $z = 7\lambda_0$ ($F/D = 1.0$) above and $x = 3.5\lambda_0$ offset from the center of the array. The arrays were designed to generate a broadside beam. A diagram showing the array directivity loss versus the unit cell's NVPD value was obtained from the Monte Carlo study [Fig. 6.5(a)]. For either 2-state or 4-state phase resolution, the trend of the data points shows that the array's quantization loss increases as the NVPD value increases, and the lowest quantization loss is achieved when NVPD= 0 (e.g. when the phase states have equal spacings).

For a 4-state unit cell to be considered substantially beneficial over a 2-state unit cell, a threshold for the NVPD value can be determined. A potential criterion can be the 1 dB quantization loss margin: as can be observed from Fig. 6.5(a), any 4-state unit cell with NVPD$<$ 0.1 can offer at least 1 dB better quantization loss than the best 2-state (1-bit) unit cell. By this criterion, 4-state unit cells with NVPD $<$ 0.1 can be considered "valuable", and the data points that fall in this range are highlighted blue in Fig. 6.5(a). The same set of data points are also presented versus equivalent bit in Fig. 6.5(b). It is observed that the directivity loss now appears to be more monotonically dependent on equivalent bit. The highlighted data points (corresponding to NVPD $<$ 0.1) now distribute in the range of equivalent bit $>$ 1.5 bit. This comparison shows that both NVPD and equivalent bit of the unit cell are closely related to the quantization loss of the array. While they might be used interchangeably to guide the multi-state unit cell design, we adopt NVPD in the rest of this chapter as its definition carries more clear mathematical meaning.

This Monte Carlo analysis using cosine-q array simulations provides insights into the relationship between the unit cell's uneven phase separation and the associated impact on array performance. This study may also be applied for other applications (e.g., RIS) that involve multi-state unit cells with generally uneven phase separations, and provide helpful design guidelines. The NVPD defined in this section will also be used to construct the fitness function of the BPSO algorithm, which is articulated in Section 6.2.3.

6.2 Topology Design of Switch-Reconfigurable Unit Cells using Binary Optimization

In this section, we introduce the procedures to design switch-reconfigurable unit cells that achieve the maximum number of phase states for the given number of switches. Efforts are devoted to optimizing the topology of the unit cell element, which is most critical to the electromagnetic performance (i.e., operating frequency, bandwidth, polarization, etc.) of the unit cell. To accomplish this, binary particle swarm optimization (BPSO) is implemented to design the pixelated element area with reasonable switch locations and orientations considered. In particular, we focus mainly on 4-state (ideally 2-bit) reflectarray unit cells that use only two switches because they provide a good balance between implementation complexity, cost, and quantization loss. For demonstration purposes, we focus on the design of K-band reflectarrays operating at a center frequency of 19 GHz, but the method is anticipated to be scalable to other frequencies with slight modifications.

6.2.1 Element Pixelation Suggesting Hexagons over Squares

The basic geometry of the reflectarray unit cell is as shown in Fig. 6.6(a). The unit cell consists of an element layer on top and a ground plane layer on the bottom. The two layers are spaced by Rogers RO4003C laminate ($\epsilon_r = 3.55$, $\tan\delta = 0.0027$) of 1.52 mm standard thickness. The unit cell has a length and width of 7 mm ($0.44\lambda_0$, λ_0: free space wavelength at 19 GHz). We limit the unit cell element to reside within a 5.6×5.6 mm^2 square area in the center (80% of the unit cell length and width). Our goal is then to design the element topology within this area such that four phase states can be created based on the four "on/off" switch combinations.

A proper pixelation scheme for the element area is necessitated. While square pixel [153] is adopted in most pixelated antenna designs due to the easy implementation, it has the drawback of resulting in corner contacts if no special constraints are applied [Fig. 6.6(b)]. These point contacts at the corner are not fabrication-friendly and can create unpredictable connection problems. Hexagonal pixelation, on the other hand, naturally avoids this prob-

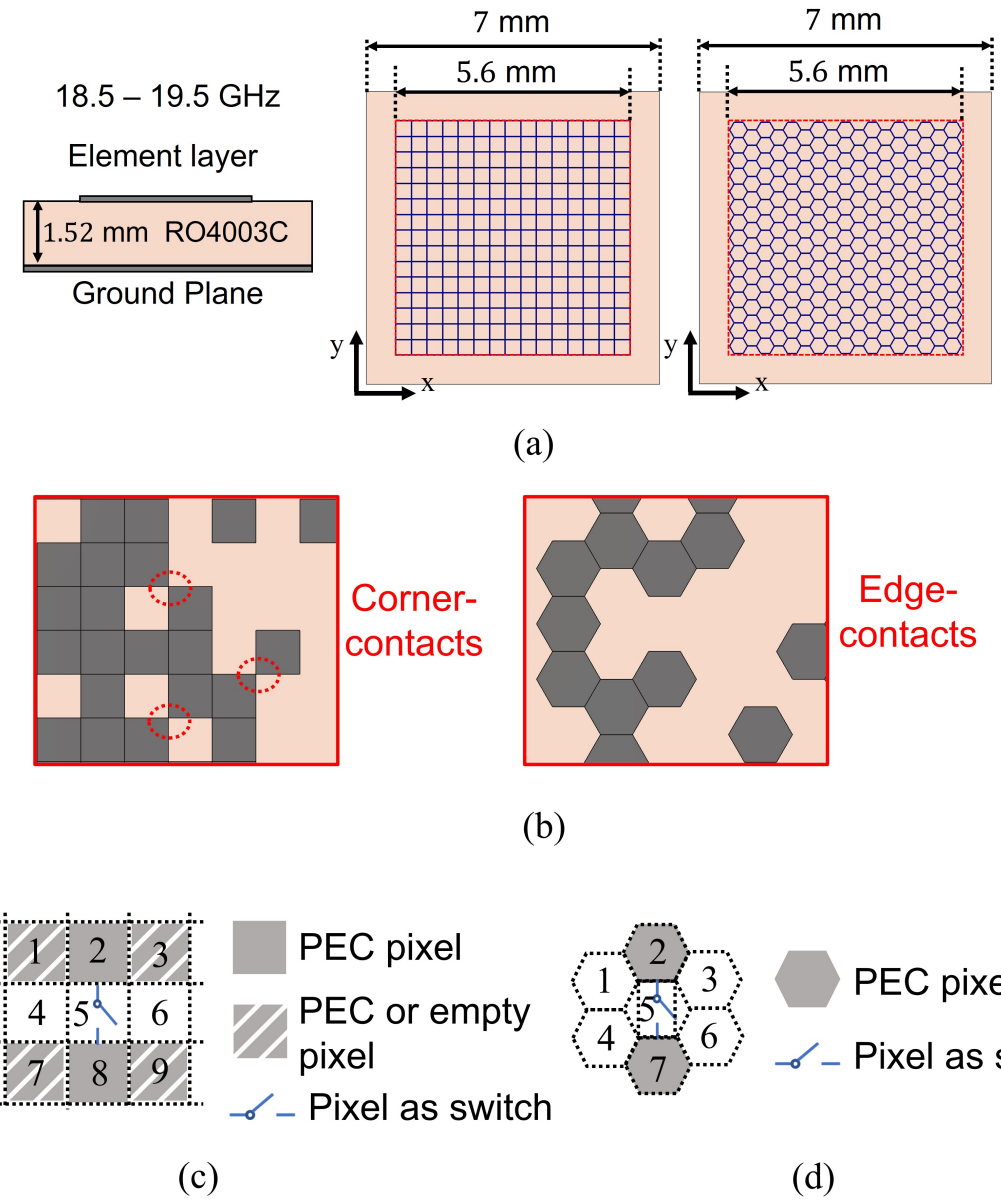

Figure 6.6 (a) Basic geometry of the reflectarray unit cell, and the square- and hexagonal-pixelation scheme for the element area. (b) An illustration of the corner-contact issue with square pixels. In comparison, hexagonal pixelation naturally avoids corner-contact problem. (c) Illustration of the idealization made to model on/off switches using short/open circuit of a single pixel. Showing the special rules enforced for pixels around the "switch" to ensure meaningful switch connections.

lem and only edge-contacts exist between adjacent pixels [Fig. 6.6(b)]. For the purpose of validating the optimization design process, we adopt both pixelation schemes in this chapter and compare their corresponding unit cell designs.

With the square pixelation, the element area is divided into 15×15 pixelated regions, and each pixel can be filled with metal (in this case we consider PEC) or be empty. The size of a single pixel is 0.37 mm $\times$ 0.37 mm. With the hexagonal pixelation, the element area is divided into 247 pixels as shown in Fig. 6.6(a). The side length of each hexagon pixel is 0.21 mm, and the center distance between adjacent pixels is thus 0.36 mm. Next, we discuss the modeling and placement of the switches.

6.2.2 Switch Modeling, Placement, and Constraints

The switches are the key components for the unit cell to generate different phase compensations. Since the goal of this work is to demonstrate the topology optimization method and validate its effectiveness, we use ideal open/short conditions to represent the state of switches. Additionally, considering that the size of a single pixel is comparable to the footprint of an RF switch at this frequency (e.g., MACOM MA4GP907), we further simplify the problem by using a single pixel to represent the switch. Applying these simplifications, an on-state switch is represented by a PEC pixel (short-circuit), and an off-state switch is represented by removing this pixel (open-circuit). Note that non-ideal switches can be considered as part of the design process if suitable lumped element models for particular switches are used [148, 149], but this is beyond the scope of this work and will not be considered here.

In general, the on/off state of the switches is expected to alter the current flow in the element so that a substantial difference in the unit cell's phase response can be realized. To ensure realistic connections for the switches, constraints must be applied for the pixels in the vicinity of the switches. In particular, this is done by applying the rules as depicted in Fig. 6.6(c) and 6.6(d) for square- and hexagonal-pixelation, respectively: (1) the two terminals of the switch must be PEC pixels to ensure current conduction; (2) the pixels on both sides across the switch must be empty to ensure enough clearance and avoid unrealistic

conduction. The locations and orientations of the switches can be determined based on prior knowledge, or be considered as part of the design problem.

The rest of the pixels in the unit cell are given full freedom and can be either PEC or empty, which is to be determined in the following BPSO process. The goal of the unit cell design is then to optimize the pixelated element pattern such that four phase states can be realized when using the four switching combinations of the two switches. Meanwhile, the NVPD of the unit cell should be as small as possible. Determination of the states of each pixel (be PEC or removed) constitutes a binary optimization problem, which suits very well the capability of the BPSO algorithm [153]. Next, we elaborate on the BPSO implementation.

6.2.3 BPSO Designing the Pixelated Element

Here we expand on the optimization process using the example of a 2-switch, 4-state, y-polarized reflectarray unit cell using hexagonal pixels. The band of operation is set to cover at least a 1 GHz bandwidth, from 18.5 to 19.5 GHz. The process is introduced as the following:

1. The element area is divided into 247 hexagonal pixel regions. Since the unit cell is expected to accept y-polarized excitation and reflect y-polarized wave, the switches are also aligned along y. In this instance, we assign the two switches on the axis of symmetry of the element as shown in Fig. 6.7(a).

2. The two pixels on the terminals of each switch are enforced to be PEC, and the two pixels on both sides of the switch are enforced to be empty [Fig. 6.7(a)]. The status of the rest 233 pixels is left to be determined.

3. The parameter to be optimized is a 1×233 binary vector $\boldsymbol{x}$ consisting of '0' and '1'. Each element in the vector defines the status of a corresponding pixel, with '1' indicating that the pixel is filled with PEC and '0' indicating that the pixel is empty.

4. For each solution sample, the corresponding unit cell is created in CST Studio based on the "pixel map" $\boldsymbol{x}$. Then, four independent unit cell simulations are performed,

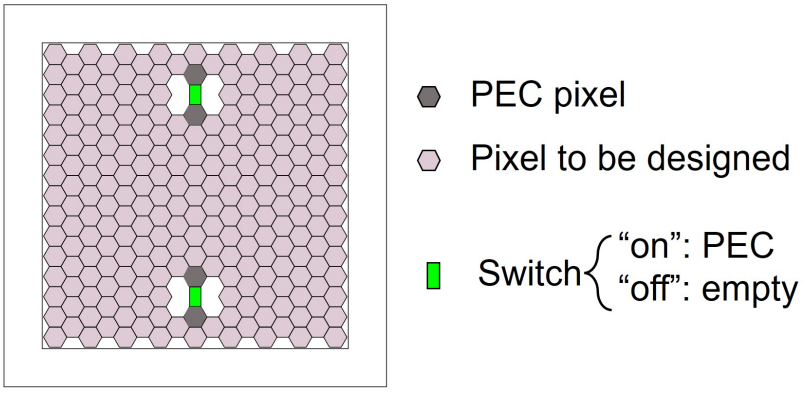

(a)

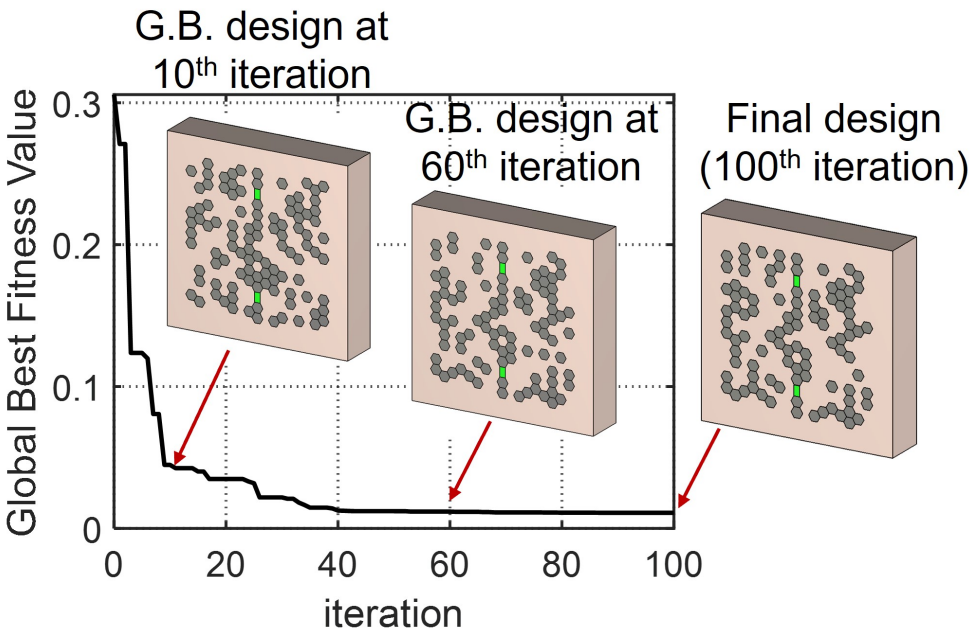

(b)

Figure 6.7 (a) A representative pixelation and switch placement scheme used for designing a 2-switch 4-state LP unit cell. (b) The corresponding BPSO convergence plot showing the global best fitness value versus the number of iterations. Unit cell element corresponding to the global best at different iterations are shown to demonstrate the evolution of the pixel distribution.

each considering one of the four switch combinations ("off-off", "on-off", "on-on", "off-on"). The reflection coefficients for each case are captured for evaluation of the fitness function.

5. The phase of the Co-Pol reflection coefficients at three representative frequencies across the band (18.5 GHz, 19.0 GHz, and 19.5 GHz) are used to evaluate the fitness function. At each frequency, the NVPD of the unit cell is calculated using (6.6). Then, the fitness function takes the maximum of the NVPD values of all frequencies:

$$f(\boldsymbol{x}) = \max(NVPD^{\{18.5GHz,19.0GHz,19.5GHz\}}) \tag{6.7}$$

   To ensure the efficiency of the unit cell, we enforce that the magnitude of the Co-Pol reflection coefficients is greater than -1 dB for all cases ($|\Gamma^{yy}| \geq -1$ dB). If $|\Gamma^{yy}| < -1$ dB for any switch state, at any frequency point, the fitness function will be given a penalty value of 10^8.

6. A BPSO algorithm updates the binary sequence states of the pixels. The BPSO algorithm is shown as Algorithm 1. Reference [156] introduced the concept of velocity in binary space and developed the binary-PSO from continuous PSO. Continuous PSO updates the velocity of a particle according to the distance from the particle's current position to its personal optimum (PBEST), and the distance from the current position to a global optimum (GBEST). BPSO inherits the continuous PSO's velocity update scheme.

   The algorithm that update the particle's position marks a difference between BPSO and continuous PSO. In BPSO, the velocity of the n^{th} bit of the m^{th} particle at t^{th} iteration, $v_{mn,t}$, determines the possibility that the binary position, $x_{mn,t}$, takes a value of 1 or 0. To map the continuous-valued velocity $v_{mn,t}$ and the binary position $x_{nm,t}$, an intermediate variable $S(v_{mn,t})$ is first defined via the *sigmoid limiting transformation* of $v_{mn,t}$ [153]:

$$S(v_{mn,t}) = \frac{1}{1 + \exp(-v_{mn,t})} \tag{6.8}$$

   A random continuous number with a uniform distribution in $(0, 1)$, $r_{mn,t}$, is then generated and compared with $S(v_{mn,t]})$. The n^{th} bit of the m^{th} particle, $x_{mn,t}$, is updated

by:

$$x_{mn,t} = \begin{cases} 0, & r_{mn,t} < S(v_{mn,t}) \\ 1, & r_{mn,t} > S(v_{mn,t}) \end{cases} \tag{6.9}$$

Algorithm 1 Binary PSO Algorithm: $c_1 = 1,\ c_2 = 1,\ V_{max} = 6,\ N_{dim} = 233,\ N_{swarm} = 50,\ T = 100$

Require: : $V_0 \leftarrow rand([-V_{max}, V_{max}], N_{dim}, N_{swarm})$

$S_0 \leftarrow 1/(1 + \exp(-V_0))$

$X_0 \leftarrow rand([0, 1], N_{dim}, N_{swarm}) < S_0$

Evaluate $\boldsymbol{f}(X_0)$

$PBEST_0 \leftarrow X_0,\ GBEST_0 \leftarrow \boldsymbol{x_0}(min(\boldsymbol{f}(X_0)))$

$t \leftarrow 0$

while $t \leq T$ **do**

$t \leftarrow t + 1$

$V_t \leftarrow V_{t-1} + c_1(PBEST_{t-1} - X_{t-1}) + c_2(GBEST_{t-1} - X_{t-1})$

$S_t \leftarrow 1/(1 + \exp(-V_t))$

$X_t \leftarrow rand([0, 1], N_{dim}, N_{swarm}) < S_t$

Evaluate $\boldsymbol{f}(X_t)$

Update $PBEST_t$ and $GBEST_t$

end while

return $GBEST_t$

In our study, the BPSO algorithm in MATLAB updates the particles' velocities and positions, while CST Studio Suite launches full-wave simulations on unit cells to get magnitudes and phases of reflection coefficients. Like most cases of antenna optimization, a time-consuming part of the optimization is evaluating fitness functions that involve full-wave simulations. As stated in 4), one fitness function evaluation requires four full-wave simulations for a 4-state unit cell design. Since the four simulations are with the same solver settings and almost the same structures except the difference in switches' states, the required computational resources and time are almost the same for the four simulations. The four simulations were thus performed in parallel to accelerate the optimization.

Another feature we implemented to accelerate binary optimization is solution storage. The program keeps a record of the unique binary position $\boldsymbol{x}_{m,t}$ and the corresponding fitness function value $f_{m,t}$ through the iterations. Each new position $\boldsymbol{x}_{m,t}$ is checked against the stored solution sets for duplicates: if $\boldsymbol{x}_{m,t}$ matches any of the items in the storage, the program skips the full-wave simulations and directly load the corresponding fitness function value from the storage; if no match is found in the storage, full-wave simulations are launched and the solution storage records this new set of binary position and fitness function value. This feature reduces simulation time significantly in the final stage of BPSO because it avoids repeated simulations on duplicated solutions, which occur frequently in the final stages of BPSO when particles tend to converge in a limited range of solution space.

The BPSO runs on a desktop computer with a 32-core AMD CPU and 256GB Memory. The complete evaluation of a single solution, including four full-wave simulations in parallel and the calculation of fitness value, costs around 1 min. Each iteration of BPSO involves 50 independent evaluations (50 particles used), which translates to 50 min per iteration time consumption. For 100 iterations, the maximum time consumption to obtain an SRUC design is thus around 5000 min. However, thanks to the use of solution storage and duplicate check, the total time consumption for a 100-iteration optimization can be reduced to 3000-4000 min. Further time reduction could be achieved by a particle-level parallelization that simultaneously evaluates multiple particles in an iteration.

The optimization typically reaches convergence around 60 - 80 iterations, and we terminate the optimization after iteration 100. To visualize the evolution of the pixel distribution, we present the element corresponding to the global best parameter $\boldsymbol{x}$ at different iterations in Fig. 6.7(b). It is interesting to observe that element geometry experiences considerable variation since the early stage (10^{th} vs. 60^{th} iteration), but only minor modifications were made since the fitness value stabilizes (60^{th} vs. 100^{th} iteration). These help justify that the proposed design methodology is capable of exploring the solution space at the early stages and exploiting the local solution space during the final stages of the optimization. The detailed analysis of the optimized unit cells will be presented next in Section 6.3.

6.3 Design Results of Linearly-Polarized (LP), 2-switch 4-state Unit Cells

In this section, several LP unit cells for y-polarization operation are designed by considering different pixelation and switch placement schemes. The simulated reflection coefficient of the unit cells and their phase resolution are analyzed. Reflectarrays constructed using each of these unit cell designs are studied in full-wave simulations to verify the beam scan capability. The benefit of enforcing symmetry in the unit cell geometry is also addressed and verified.

6.3.1 Unit Cell Design Results

Six independent reconfigurable unit cells designed for y-polarization, each optimized after 100 iterations, are shown in Fig. 6.8. The four states and their corresponding switches' status are marked in the parenthesis as "(top switch status, bottom switch status)". Design #1 and #2 considered vertically aligned switches on the center axis of the unit cell, and are based on square and hexagonal pixelations, respectively [Fig. 6.8(a), 6.8(b)]. To show the effect of different switch placement, design #3 and #4 considered vertically aligned switches on the diagonal line of the unit cell [Fig. 6.8(c), 6.8(d)]. Design #5 and #6 are designed by enforcing left-right symmetry in the unit cell, as an effort to demonstrate the improvement of X-Pol suppression for $y-$polarization (Fig. 6.8e, 6.8f).

The simulated reflection coefficients of each unit cell design (using floquet boundary in CST Studio), for all the four phase states under normal incidence are presented. All six designs achieved near-unity reflection magnitude for the Co-Pol component ($|\Gamma_{yy}|$) and better than -10 dB X-Pol ($|\Gamma_{xy}|$) suppression in the considered bandwidth of 18.5 - 19.5 GHz. Notably, designs #5 and #6 achieved outstanding X-Pol suppression. This is because the left-right symmetry enforces the x-components of the induced current in the left- and right-half of the element to be always equal in amplitude and opposite in direction [see current plots in Fig. 6.9(b)]. Consequently, the E-field resulted from the x-components of the current cancel out in the reflected wave.

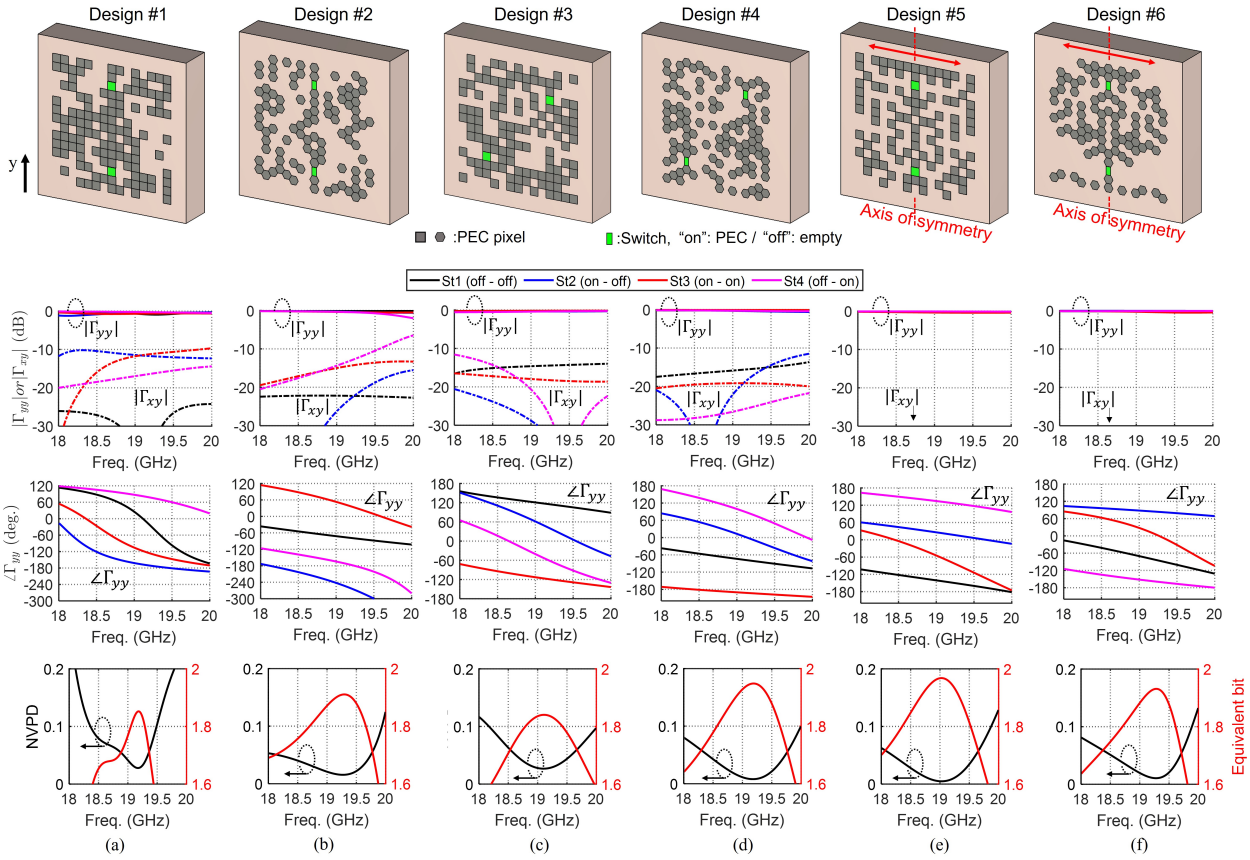

Figure 6.8 LP, 2-switch, 4-state reflectarray unit cells designed for $y-$polarization. Design #1 - #6 are independent designs with different pixelation and switch placement schemes: (a), (b) switches placed vertically on the center-axis, using square and hexagon pixels, respectively; (c), (d) switches placed vertically on the diagonal line, using square and hexagon pixels, respectively; (e), (f) left-right symmetry enforced and switches placed vertically on the center-axis, using square and hexagon pixels, respectively. From top to bottom showing the optimized unit cell geometry, simulated reflection coefficients (Co-Pol, X-Pol magnitudes, and Co-Pol phase), and the NVPD and equivalent bit values over frequency.

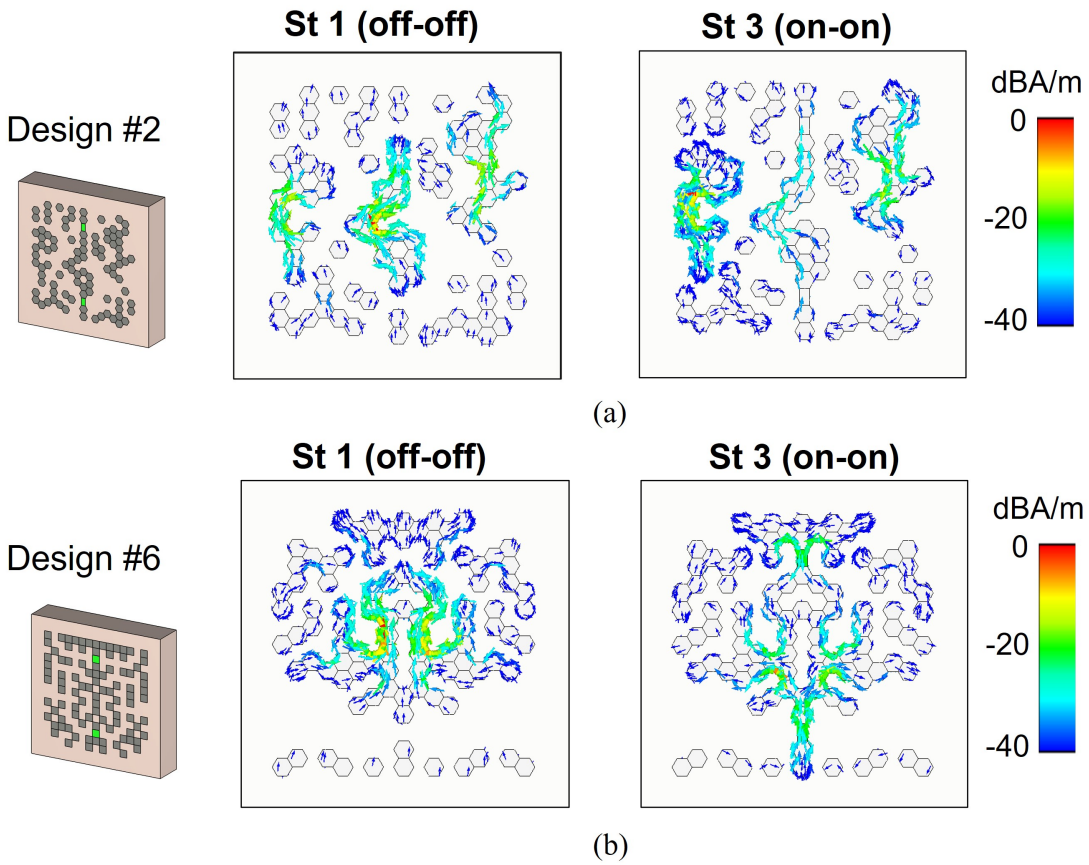

Figure 6.9 Representative simulated element surface currents under $y-$polarized normal incidence for unit cell #2 and #6. Showing the currents of two switching states: state 1 and state 3, respectively for each case.

The reflection phase ($\angle\Gamma_{yy}$) for the four states demonstrate good separation for all designs. NVPD and equivalent bit over frequency are also calculated using (6.6) and (6.1), serving as quantitative evaluation of the unit cells' phase performance. As shown in Fig. 6.8, all the designs achieve NVPD$\leq$ 0.09 and equivalent bit$\geq$ 1.6 bit in the band of 18.5 - 19.5 GHz. At 19 GHz, the equivalent bit of designs #2 to #5 all exceed 1.8 bit. These results verified the effectiveness of the algorithm in obtaining suitable unit cell designs that meet the desired unit cell performance, i.e., creating a 4-state phase resolution with only two switches. We next test these unit cells by studying beam steerable reflectarray performance in full-wave simulations.

6.3.2 K-band Beam Steerable Reflectarray Design and Simulations

To further evaluate the unit cells' performance, LP reflectarrays with representative beam scan angles were created using each of the six unit cell designs. The reflectarrays consist of 14×14 elements, with an offset focal point as shown in Fig. 6.10. The required ideal phase compensation at each unit cell can be calculated as [147]:

$$\Psi(x_i, y_i) = -k(x_i \sin\theta_t \cos\phi_t + y_i \sin\theta_t \sin\phi_t - R_i) \tag{6.10}$$

where (x_i, y_i) is the location of the i^{th} unit cell in the reflectarray; k is the free space wave number; R_i is the path length between the focal point and the i^{th} unit cell; (θ_t, ϕ_t) are the desired far-field direction of the beam. Three representative target beam directions: (1) $\theta_t = 0°$, $\phi_t = 0°$ (broadside); (2) $\theta_t = 30°$, $\phi_t = 0°$; (3) $\theta_t = 60°$, $\phi_t = 0°$ (scanned towards feed), are considered in each case.

Referring to this required phase compensation $\Psi(x_i, y_i)$, the simulated reflection phase at the center frequency was used to properly determine the state to be assigned for each unit cell. For a particular unit cell design, suppose the reflection phase of the four states at 19 GHz are represented by $\angle\Gamma_{yy}^m$, $m = 1, 2, 3, 4$, then, the state m that leads to the smallest value of:

$$\cos[\Psi(x_i, y_i) - \angle\Gamma_{yy}^m] \tag{6.11}$$

will be assigned to the i^{th} unit cell of the reflectarray. While this chapter demonstrates square-aperture reflectarrays as examples, same procedures apply for arrays with different aperture shape, size, or feed locations as well.

Using this method, we created reflectarrays for each unit cell design (from #1 to #6) and performed full-wave simulations in CST to obtain the far-field pattern. Fig. 6.11 shows the example of a broadside-beam reflectarray designed using unit cell #2. Ideal open/short condition of the switch was used for the reflectarray simulations as well. In other words, all the elements are identical except that the switch pixels are either PEC or empty, depending on the assigned state (see the close-up view in Fig. 6.11). A $y-$polarized cosine-q feed source [134] with $q = 9.3$ (providing around -10 dB edge taper) was used to illuminate the

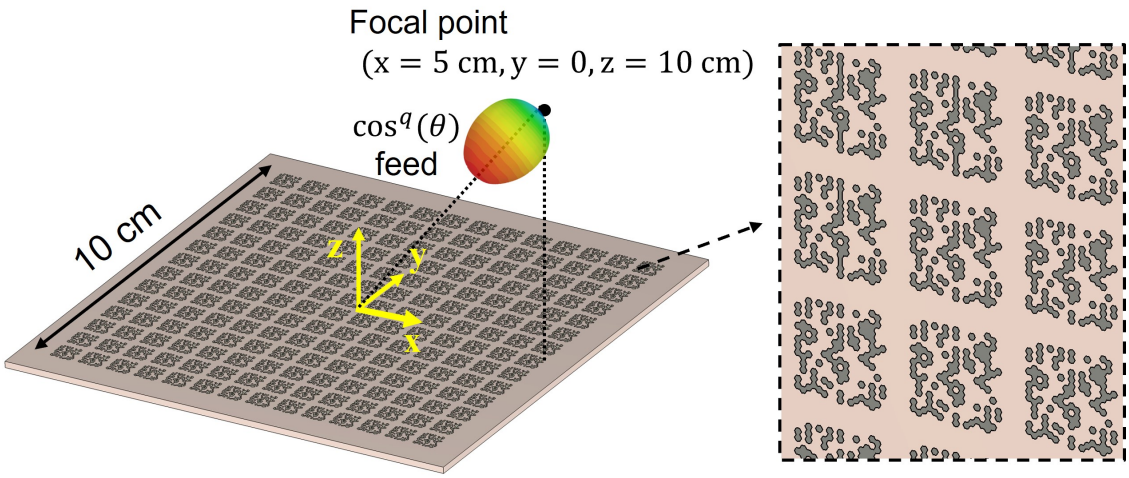

Figure 6.10 The 14 × 14 reflectarray configuration for testing the array performance of the unit cells. Ideal open/short conditions are considered for the switches. This example shows a broadside beam reflectarray using unit cell design #2. The array size and the offset focal point location are identical across all instances studied in this chapter.

reflectarrays. Note that the cosine-q feed was used only as a representative feed source to validate the reflectarrays, and was not intended to maximize efficiency (because the cosine-q feed provides a circular illumination pattern that under-illuminates the corners of the square-aperture reflectarrays).

The simulated reflectarray patterns at 19 GHz in the plane of offset are presented in Fig. 6.11 to demonstrate the beam scan capability. Beam scan up to 60° has been successfully achieved with all six unit cell designs, justifying their effectiveness in creating various phase compensations through different switch states. The directivity bandwidth for the broadside and 60°-scanned beams of each case are also presented in Fig. 6.11. All designs achieved 3-dB directivity bandwidth covering 18.5 - 19.5 GHz, verifying the promising bandwidth potential of the designed unit cells. The reflectarray based on unit cell #2 achieved the highest broadside directivity, 24.31 dBi, corresponding to 53.5% aperture efficiency at 19 GHz (considering a 10 cm by 10 cm square element area size; spillover and illumination efficiency included), which is considered very competitive for reflectarrays using 4-state SRUC.

It should be noted that the X-pol performance of the scanned beams (especially for the 60°-scanned beam) varies by design. Particularly for design #1, the X-Pol level near the main

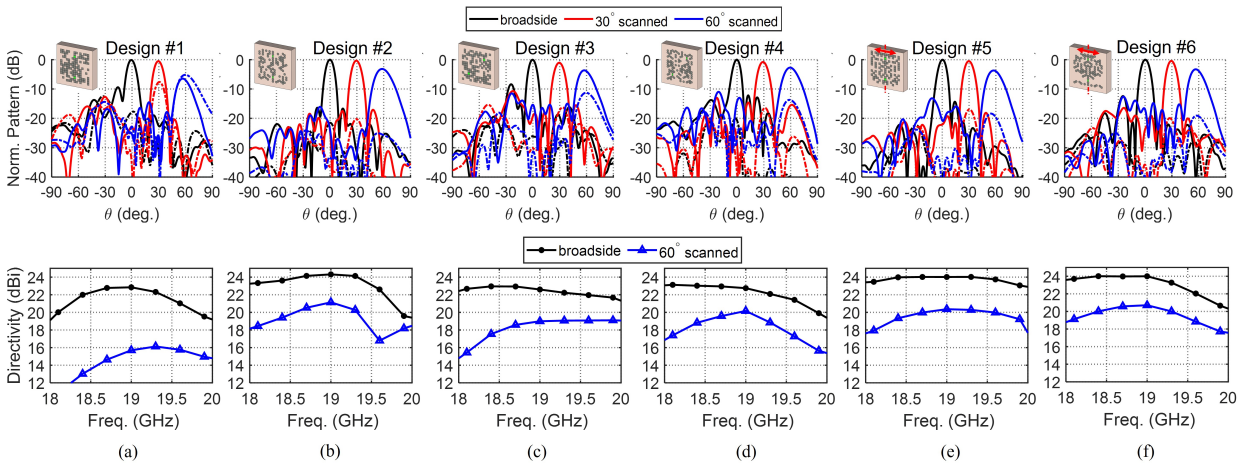

Figure 6.11 Simulated LP reflectarray patterns showing representative scanned beams at 19 GHz and corresponding directivity bandwidth. (a) - (f) correspond to the reflectarrays designed individually with unit cell # 1 - # 6 as shown in Fig. 6.8. The reflectarray patterns are normalized to the broadside directivity of each case, with solid lines being the Co-Pol (Ludwig 3rd vertical) patterns and dashed lines representing the X-pol (Ludwig 3rd horizontal) patterns.

beam region increases dramatically as the beam scans and becomes even higher than the Co-Pol main beam for the 60°-scanned case. Unit cells #3 and #4 also demonstrate a noticeable X-Pol lobe for the 60°-scanned beam. Recall that the far-field pattern of the reflectarray can be treated as the product of the unit cell pattern and the array factor. This excessive X-pol for scanned beams is thus likely originated from the unit cells' high X-Pol radiation near $\theta = 60°$, which was not captured in the unit cell simulations considering normal incidence. Because, based on the floquet theory [157], the unit cell's reflection coefficient under a certain incident angle represents only the unit cell's radiation components in the specular direction of the incident wave. A potential remedy is thus to optimize the unit cell for both normal and oblique incidence (e.g., 60° incidence) during the design. However, considering additional incident angles during the optimization accompanies additional full-wave simulations, which can considerably extend the optimization time (to be discussed with examples in Section 6.4).

An alternative method to improve the X-pol performance, as suggested by the reflectarray patterns corresponding to design #5 and #6, is to impose left-right symmetry in the unit cell element. Although unit cells #5 and #6 were optimized only for normal incidence, the

symmetry in the current causes the radiations in x-direction (i.e., X-Pol) to cancel, and the X-pol level is significantly reduced. It is worth pointing out that design #2 also achieved low X-Pol in the reflectarray pattern. While no symmetry was enforced during its design, the element of design #2 indeed demonstrates better left-right symmetry compared to design #1, #3, and #4. Further, the current in unit cell #2 also appears to be dominantly along $y-$direction [Fig. 6.9(a)], which also helps to limit radiation in $x-$direction. The current direction in design #2 is largely determined by the geometry of the element, which consists of three separated narrow sections along y.

These observations suggest that for LP unit cell designs, enforcing element symmetry in the direction orthogonal to the polarization is a simple and effective method to suppress X-pol. The switches are thus desired to be distributed on the axis of symmetry and oriented along the direction of polarization. It may also be helpful to apply additional constraints during the topology design to foster the currents to distribute along the desired polarization direction (e.g., by cutting slots along the polarization direction), which is beyond the scope of this work. These encouraging SRUC and beam steerable reflectarray simulation results validated the proposed SRUC design process using pixelated element and BPSO algorithm. It also demonstrates that both square and hexagon pixels can be effective in the design, though hexagonal pixelation naturally avoids corner contact and can be potentially more favorable for fabrications. The presented 2-switch 4-state SRUCs use single-layer elements and demonstrate no sacrifice in performance compared with other LP SRUCs that used multiple layers (Table 6.1). We then implement this workflow to address a more challenging design problem: CP SRUC that uses two switches to generate four states.

6.4 Design Results of Circularly-Polarized (CP), 2-switch 4-state Unit Cells

The design of CP phase reconfigurable unit cells has been a challenging yet intriguing topic [111]. So far, there has been no reported CP SRUC that utilizes two switches to realize four phase states, to the best of the authors' knowledge. In this section, we implement the

BPSO algorithm to design 2-switch 4-state SRUCs for CP reflectarray applications.

6.4.1 Unit Cell Design Results

For this CP design, the same unit cell geometry and pixelation method as used for LP designs were adopted [Fig. 6.6(a)]. The design goal for optimization was evaluated based on the CP reflection magnitude and phase. In particular, we consider the unit cell receiving right-hand CP (RHCP) excitation and reflecting dominantly RHCP wave. The Co-Pol reflection coefficient is thus now represented by Γ_{RR} and the X-Pol reflection coefficient is Γ_{LR}. The optimization is expected to minimize NVPD evaluated using $\angle\Gamma_{RR}$ at 18.5, 19.0, and 19.5 GHz. Likewise, we enforce $|\Gamma_{RR}| > -1$ dB at normal incidence to ensure the efficiency of the unit cell. Only hexagonal pixelation and one representative scheme of switch placement are considered for this demonstration.

The unit cell #7 was optimized by considering only normal incidence performance, and the resulting design is as shown in Fig. 6.12 (a). The unit cell demonstrated reasonable X-pol suppression and a good phase separation among the four states (NVPD= 0.005, N_{eqv} = 1.97 bit at 19 GHz). Three reflectarray instances were designed based on unit cell #7 and simulated. The same 14×14 array size and offset feed configuration as used for LP (Fig. 6.10) was adopted for these CP reflectarrays. The feed source used is now an RHCP cosine-q feed source with $q = 9.3$, which provides around -10 dB edge taper illumination. Representative beam scan patterns in the plane of offset are shown in Fig. 6.13 (b). The issue of high X-Pol level for the 60°-scanned beam is also observed in this case. The axial ratio (AR) performance over frequency also suggested this limitation over the 18.5 - 19.5 GHz bandwidth. Next, we discuss the methods to improve the AR performance of the reflectarray.

6.4.2 Improving the X-pol Suppression at Large Scan Angles

The discussion on LP SRUC designs in Section 6.3 demonstrated that enforcing symmetry in the element can effectively suppress X-Pol. For CP SRUC, elements with sequentially rotated features [147] have been proven effective to achieve low X-Pol (low AR) CP performance.

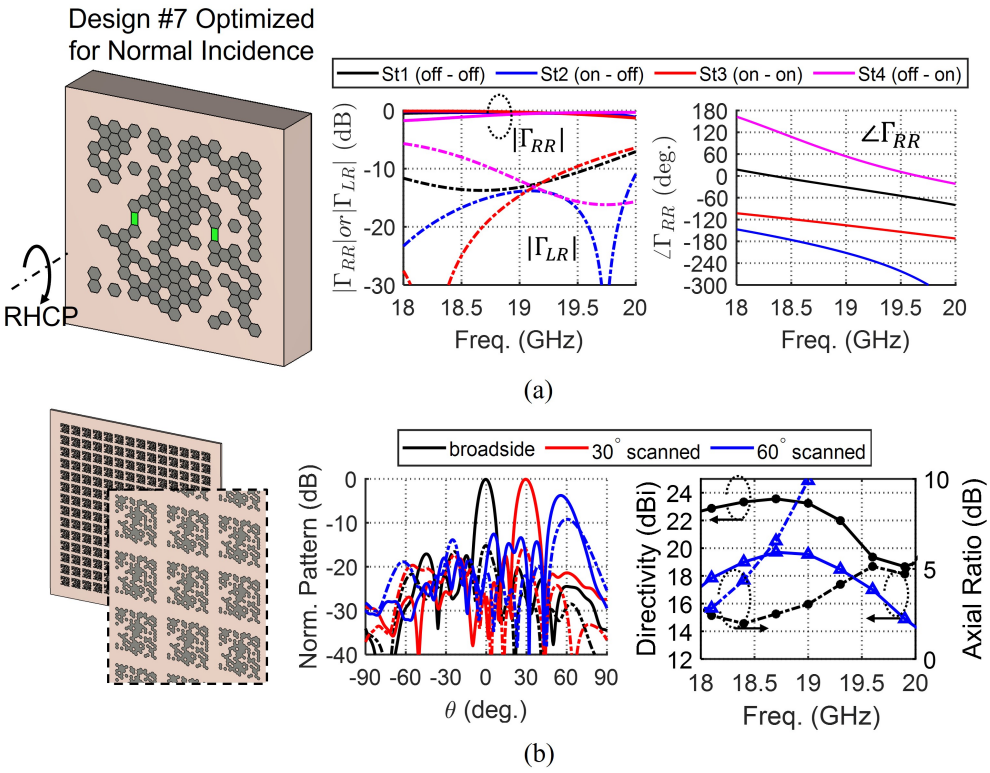

Figure 6.12 The CP 2-switch, 4-state reflectarray unit cell #7 designed for RHCP, optimized by only considering normal incidence. (a) Showing geometry and unit cell performance under normal incidence. (b) Showing simulated reflectarray patterns along with directivity and AR over frequency. Solid lines correspond to Co-Pol (RHCP) pattern, and dashed lines correspond to X-Pol (LHCP) pattern.

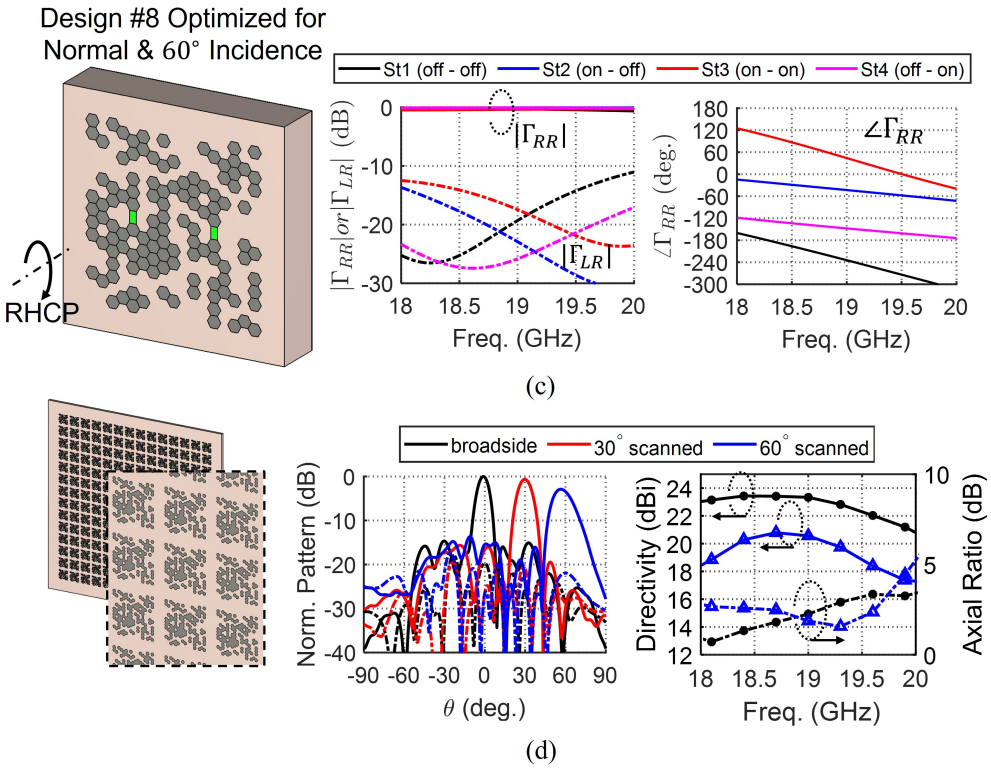

Figure 6.13 The CP 2-switch, 4-state reflectarray unit cell #8 designed for RHCP, optimized for both normal and 60° incidence. (a) Showing geometry and unit cell performance under normal incidence. (b) Showing simulated reflectarray patterns along with directivity and AR over frequency. Solid lines correspond to Co-Pol (RHCP) pattern, and dashed lines correspond to X-Pol (LHCP) pattern.

However, the unique phase reconfiguration mechanism of this type of elements necessitates more than two switches to realize four states, which does not meet the design goal of this work.

Since the X-Pol level of the array pattern is closely related to the X-Pol of the element pattern at this angle, another effective method is to optimize the unit cell performance for both normal and oblique incidence. This is done by modifying the definition of the fitness function: in addition to minimizing NVPD value under normal incidence and enforcing magnitude $|\Gamma_{RR}^{Inc=0^\circ}| > -1$ dB, we further enforce that the reflection magnitude at 60° incidence must satisfy $|\Gamma_{RR}^{Inc=60^\circ}| > -2$ dB. This additional constraint will ensure the optimized design must have good X-Pol suppression at 60°. During the optimization process, each unit cell instance in each round will be evaluated for both normal and 60° incidence. Consequently, the time needed for optimization was nearly doubled compared to previous designs optimized for only normal incidence.

The optimized 2-switch, 4-state CP unit cell (design #8) based on this new fitness function is shown in Fig. 6.13 (a) along with its reflection coefficients under normal incidence. The X-pol level remains below −14 dB for 18.5 - 19.5 GHz. The phase of the four states also achieved good separation over frequency, with NVPD= 0.003, $N_{eqv} = 1.98$ bit at 19 GHz.

The simulated scanned patterns and the bandwidth performance of the reflectarrays based on unit cell #8 are presented in Fig. 6.13 (b). A significant improvement in the X-Pol level and AR can be observed for both the broadside beam and the 60°-scanned beam. The directivity variation within the targeted frequency range (18.5 - 19.5 GHz) is less than 2 dB for both broadside and 60°-scanned beam. The broadside directivity is 23.33 dBi, corresponding to 42.7% aperture efficiency at 19 GHz. The 3-dB directivity bandwidth of the broadside beam spans beyond the 2 GHz (10.5%) bandwidth captured. The axial ratio of both the broadside and the 60°-scanned beam are overall below 3 dB within the targeted 5.3% bandwidth, which suggests very promising bandwidth potential.

These results proved the benefit of considering multiple incident angles during the CP SRUC optimization process. Note that similar adjustment in fitness function can be adopted

Table 6.1: Summary and comparison among reported 2-switch 4-state SRUCs with representative designs in this work

Ref.	Polarization	Num. of RF layers	Freq. (GHz)	N_{eqv} @ center freq.	NVPD @ center freq.
[148]	LP	2 + GND	12.5	1.86 bit	0.0235
[149]	LP	3	11.8	1.89 bit	0.0177
[150]	LP	2 + GND	5.8	1.89 bit	0.0177
[151]	LP	1 + GND	275	1.69 bit	0.0597
SRUC#6 this work	LP	1 + GND	19	1.88 bit	0.0197
SRUC#8 this work	CP	1 + GND	19	1.98 bit	0.0031

when designing low-X-Pol LP SRUC as well (as an alternative or addition to enforcing element symmetry), but the results will not be repeated here due to the page limitation. This section demonstrates the proposed BPSO + pixelation design process can be configured to achieve unconventional CP 2-switch 4-state SRUC designs that have not been reported before. A summary of the 2-switch 4-state SRUC designs in the literature is provided in Table 6.1 and compared to representative designs in this work.

6.5 Fabrication and Measurements of Reflectarray Prototypes

To validate the pixelated SRUC design, three K-band CP reflectarray instances based on CP SRUC #8 were designed and fabricated [Fig. 6.14(a)]. For concept validation, the three reflectarrays considers ideal open/short condition for the switches, and were designed to create a broadside beam, $30°-$, and $60°-$scanned beams (scanned away from the feed to avoid blockage). The reflectarrays were fabricated by Fast Turn PCB, and were measured using the CP septum horn as feed (discussed in chapter 7) in the spherical near-field range at UCLA

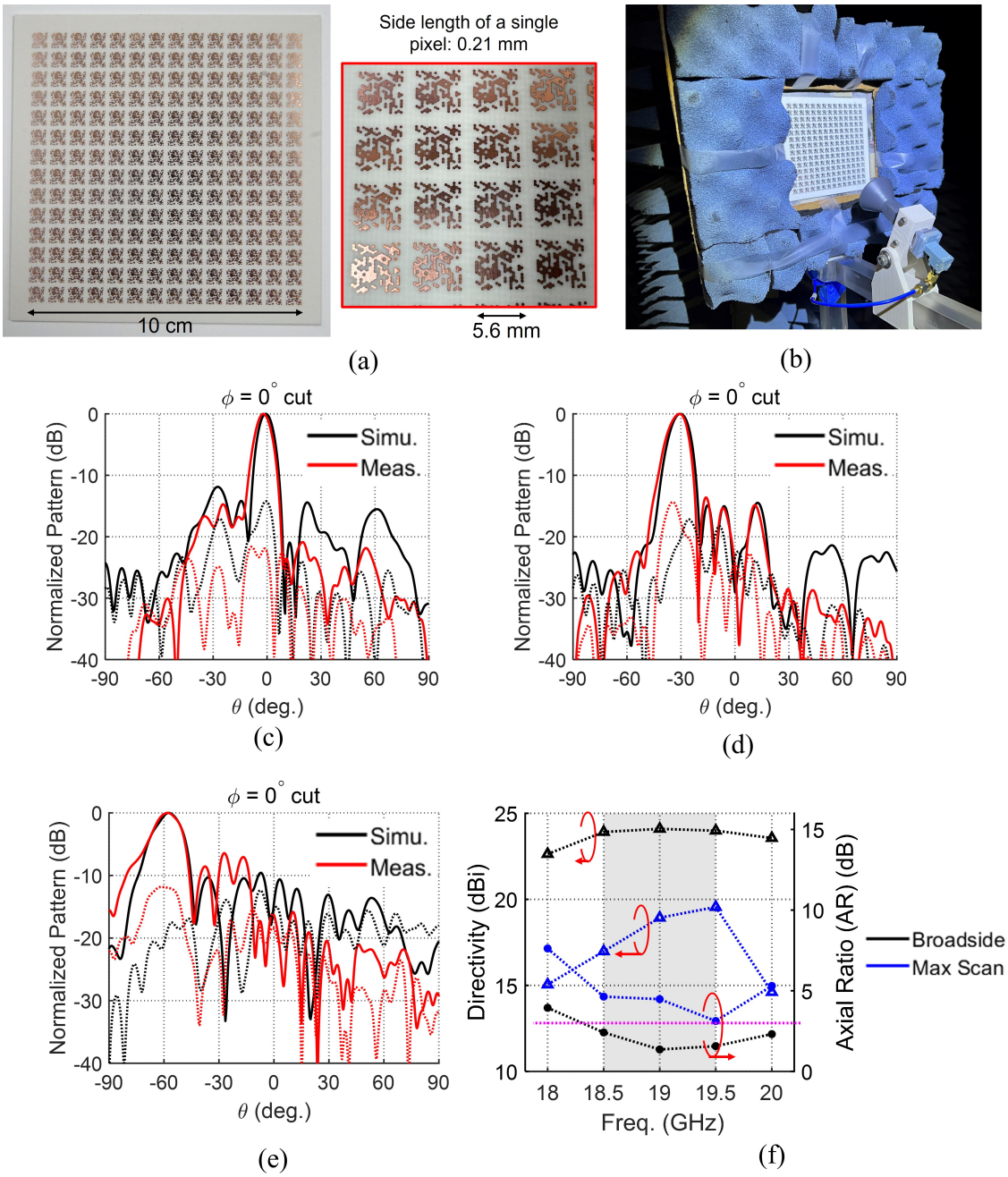

Figure 6.14 (a) Photo of the fabricated reflectarray prototype (showing instance for broadside beam), and the close-up photo of the pixels. (b) Photo of the reflectarray being measured in the spherical near-field chamber at UCLA. The CP septum horn was used as feed to cover the bandwidth. (c) - (e): Measured vs. simulated reflectarray patterns in the plane of beam scan. (solid lines: RHCP, dashed lines: LHCP). The measured directivity for broadside beam, 30°−, and 60°−scanned beams are 24.10 dBi, 23.53 dBi, and 18.93 dBi, respectively. (f) The measured directivity and axial ratio versus frequency, for both the broadside and 60°-scanned beam.

[Fig. 6.14(b)]. Good agreement between measurements and simulations have been achieved for all three cases. Beam scan up to 60° was also successfully demonstrated [Fig. 6.14(c) - (e)]. The measured broadside directivity is 24.10 dBi, and the 60°−scanned beam directivity is 18.93 dBi. Note that the use of a CP feed horn presents a physical blockage in the aperture of the reflector, and it caused the slight discrepancy between simulations and measurements. The measured reflectarrays also achieved promising CP directivity and axial ratio bandwidth, as shown in Fig. 6.14(f). These measurement results successfully validated the fabrication feasibility of hexagonal pixelation, the CP phase reconfigurability of the proposed 4-state SRUC (using only two switch pixels), and the bandwidth potential of the design method.

6.6 Future Directions

The purpose of this work is to introduce and validate a novel design process for SRUCs to fully utilize the switch combinations to achieve the highest possible phase resolution. While the demonstrations were made mainly for 2-switch 4-state SRUC for reflectarrays at 19 GHz, the methodology holds relevance for various potential applications: e.g., transmitarrays and RIS in different frequency bands, Dual-polarization reconfigurable arrays, polarization conversion arrays, etc. It is anticipated that tailoring to the unit cell geometry, pixelation size, and switch(es) location and size can become necessary to adopt this BPSO design process under particular design constraints. The use of more realistic switch models, such as lumped element model for p-i-n diode switches [74], can also be included in the optimization process. The BPSO process and the generated data also have the potential to be integrated with machine learning algorithms for other applications such as generative design of SRUCs based on given specifications.

6.7 Summary

Switch-reconfigured unit cell (SRUC) is one of the key enabling technologies of low-cost beam steerable reflectarrays, transmitarrays, and reconfigurable intelligent surfaces (RIS). SRUC

with ≥2-bit (4-state) phase resolution is critical to ensure the efficiency of these devices. Although two switches can be sufficient to create four different states, most reported 4-state SRUCs require four or more switches, which incurs excessive complexity and cost. Therefore, designing 2-switch 4-state SRUCs can substantially benefit the deployment of these reconfigurable arrays, but it has been a topic rarely touched upon. This chapter addresses this critical and challenging problem by implementing binary particle swarm optimization (BPSO) to design the topology of the pixelated unit cell element, so that four phase states can be realized with only two switches. To guide the optimizations, normalized variance of phase difference (NVPD) was introduced as an alternative metric of equivalent bit to characterize the uneven inter-state phase separation of SRUCs. The connection between NVPD and the array quantization loss was also investigated. Additionally, hexagonal pixelation was introduced to overcome the corner contact problem of square pixelation, eliminating potential weak connections among pixels and benefiting practical implementation.

Enabled by the unique methodology, we obtained several novel designs of 2-switch 4-state SRUCs for LP and CP reflectarrays in 18.5 - 19.5 GHz. The CP unit cell presented in this chapter marks the first CP 2-switch 4-state SRUC reported in the literature, to the best of the authors' knowledge. The performance of the SRUCs was extensively evaluated with both unit cell and reflectarray simulations. LP and CP reflectarrays with representative beam scans of up to 60° and competitive bandwidth performance in 18.5 - 19.5 GHz were achieved. Moreover, several design insights have been highlighted. It was shown that enforcing symmetry in the LP unit cell element is effective in suppressing the X-pol of the reflectarray. Whereas for CP unit cells, significant X-Pol suppression and AR improvement were achieved by considering multiple incident angles during the unit cell optimization. Reflectarrays were prototyped and measured to demonstrate up to 60° RHCP beam scan, thus further validating the feasibility of using pixelated unit cells to achieve 2-switch 4-state phase reconfiguration. The proposed design process in this chapter relied on minimum prior knowledge of SRUC design and reveals unconventional SRUC configurations that should provide new possibilities in the implementation of beam steerable arrays and RIS for next-generation wireless applications.

CHAPTER 7

Novel Additive Manufacturing Enabling Ultra-lightweight Antennas: Application of the Charge-Programmed Multi-Material 3D Printing

Weight reduction is an antenna research topic that attracts significant attention in the emerging applications of small satellites and CubeSats [9]. The increasing demand for high gain and beam steerable satellite antennas further amplifies the significance of lightweight antenna technologies because of the increased electrical and mechanical complexity associated with beam steering. Through decades, innovations in lightweight satellite antennas have been demonstrated in various forms, including novel antenna concepts, use of advanced materials, optimization on structures, etc [9]. Recently, the possibilities in lightweight antenna design have been further expanded thanks to the emergence and maturation of diverse additive manufacturing (AM) techniques that allow researchers to more accurately control the distribution of material in an antenna, realize exotic structures, and remove excessive mass.

However, most existing AM technologies are only suitable for printing either dielectric or metallic material exclusively, thus limiting the types of antenna that can be developed. While the combination of multiple processes is possible (such as stereolithography followed by electroless plating), it lacks precise control of the distribution of conductive material and is suitable only for certain groups of antennas. In comparison, the recently reported charge-programmed multi-material (CPMM) 3D printing [158] technique demonstrated unmatched advantages in developing complex 3D electronics. Enabled by two major steps, i.e., the multi-material stereolithography (SLA) and the selective metal deposition, CPMM printing renders accurate control over the volumetric distribution of conductive and non-conductive

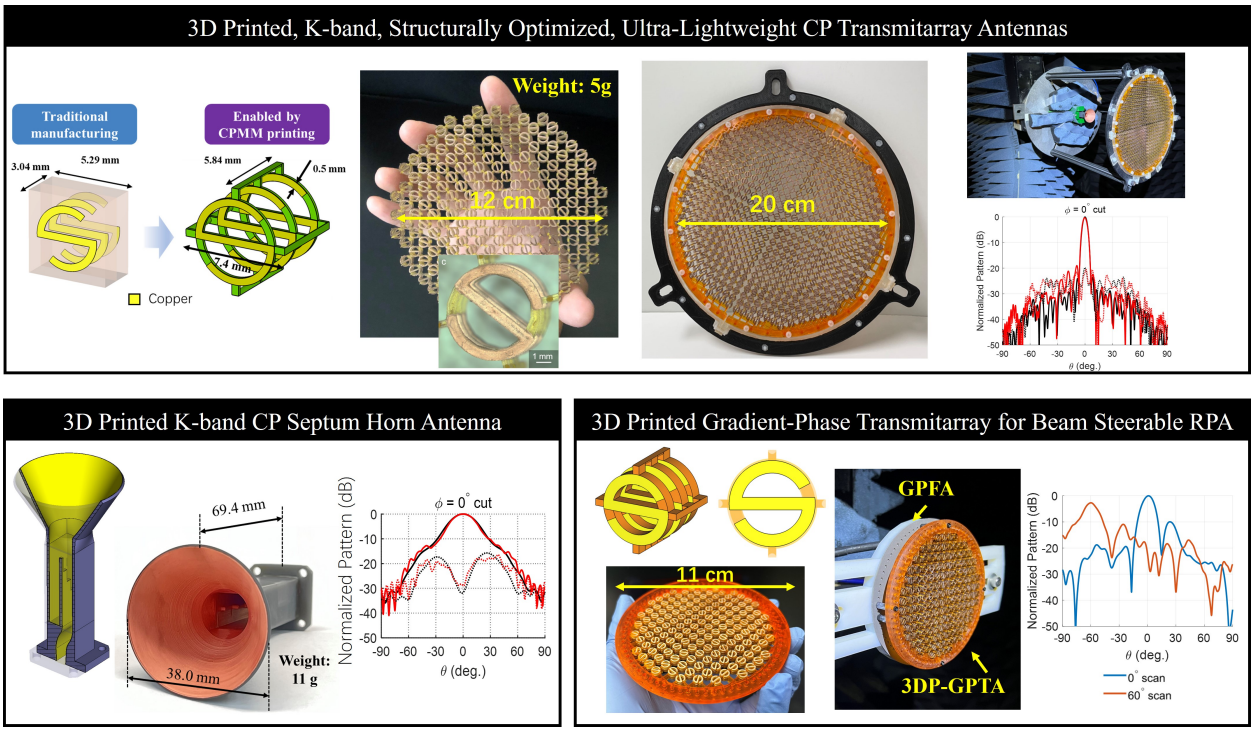

Figure 7.1 Overview of the outline and key contributions of this chapter.

material in a monolithic development. As illustrated in Fig. 7.2, the micro-SLA develops the polymer structure with a programmable charged surface area, and the selective metal deposition that forms metallization on the charged surface area. The micro-SLA process yield a resolution of 50 μm in xy direction and $25-100$ μm in z direction [159]. The metallization thickness is typically in the order of hundreds of nanometers to several micrometers. The resulting structure can have complex inter-penetrated metal and dielectric material [158]. This novel technique can potentially manufacture a broad category of antennas that are otherwise difficult or impossible to build using other AM methods.

In this chapter, we exploit this unique advantage of CPMM printing and demonstrate the design, development, and measurement of several ultra-lightweight antennas. In particular, the chapter will be divided into three major sections (Fig. 7.1) that cover (1) K-band ultra-lightweight CP transmitarrays using structurally-optimized S-ring unit cells; (2) a K-band CP horn antenna with built-in septum polarizer and meandered waveguide; (3) a 3D-printed lightweight version of the GPTA panel for beam steerable RPA. This chapter marks a fruitful

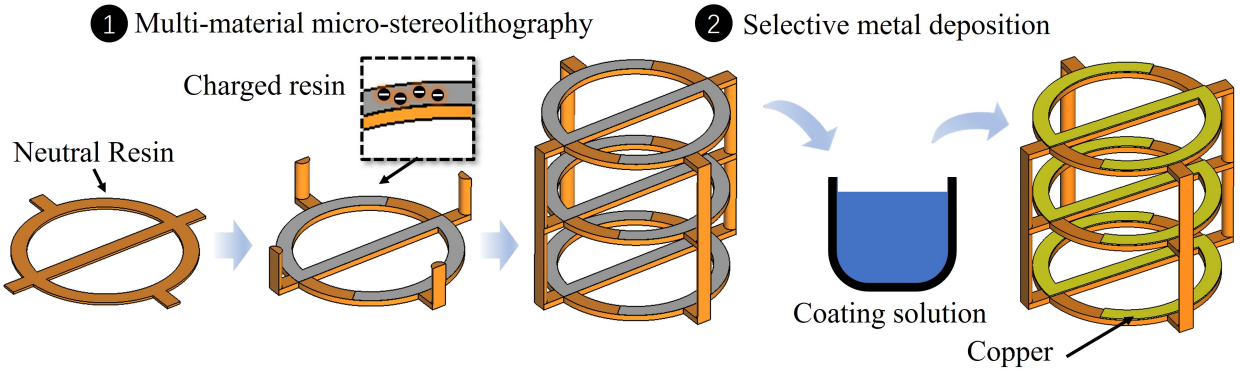

Figure 7.2 An illustrative diagram showing the two major processes of the CPMM 3D printing technique. A single S-ring transmitarray unit cell is used as a representative 3D structure consisting of dielectric and multiple layers of selectively deposited conductor material.

collaboration with Prof. Xiaoyu Zheng's research laboratory based at the University of California, Berkeley. Prof. Zheng's students, Dr. Ryan Hensleigh, Dr. Zhenpeng Xu, and post-doctoral researcher, Dr. Zhen Wang, were responsible for all the AM fabrication work of the antennas in this chapter.

7.1 3D Printed Ultra-Lightweight CP Transmitarray Antennas at 19 GHz

Transmitarray antennas are known for their advantages of high-gain, low-profile, and free of feed blockage. A transmitarray typically consists of multiple layers of metallic patterns, which are essential for the transmitarray unit cells to achieve the desired transmission magnitude and phase. The manufacturing of a transmitarray traditionally employs the printed circuit board (PCB) process (Fig. 7.3 left): the metallic patterns are made by removing the excessive copper from a complete piece of copper-plated laminates; multiple pieces of such boards with copper patterns are then bonded or air-spaced to build the transmitarray. The dielectric laminate, though important to the electromagnetic property of the antenna, in many cases is not necessary but rather for supporting purposes. Excessive dielectric accounts for the majority portion of antenna weight and dielectric loss, and this is inevitable

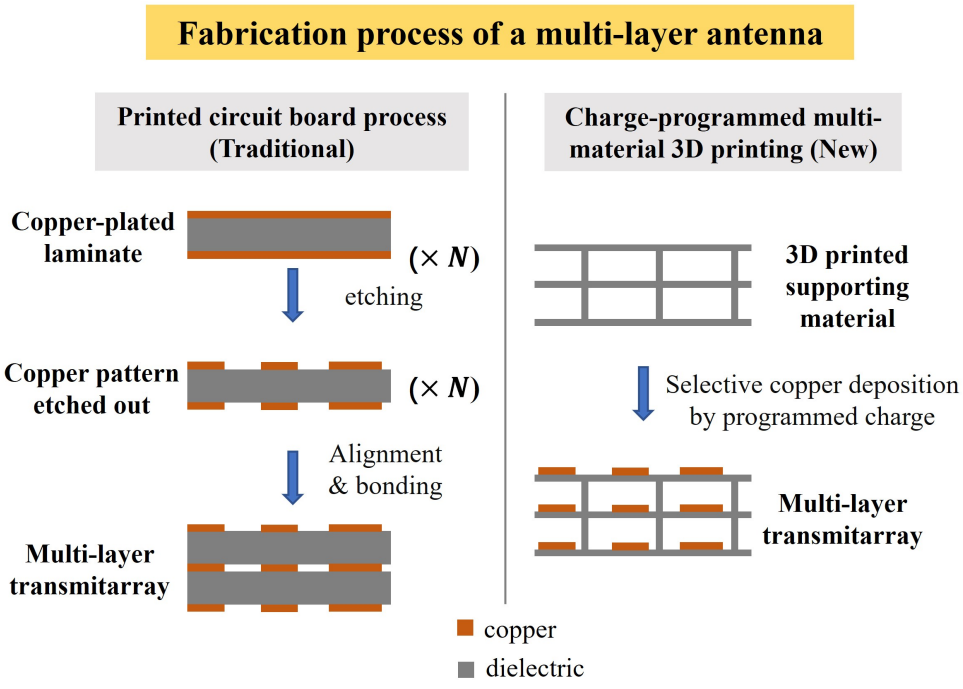

Figure 7.3 Comparison of traditional PCB process (left) and the novel charge-programmed 3D printing (right) in manufacturing of multi-layer antenna.

with the traditional manufacturing process. Therefore, to further reduce the mass of such a multi-layer antenna, innovative manufacturing techniques are necessitated.

The CPMM printing technique becomes very suitable for the development of multi-layer antennas such as transmitarrays. As will be shown in this section, since CPMM offers new degree of freedom to engineer the structure of the antenna, significant weight reduction can be achieved by optimizing the structure of the transmitarray unit cell. Next, we present the design, fabrication, and measurement of several CP, ultra-lightweight transmitarrays developed using CPMM printing for K-band operations.

7.1.1 Design and Fabrication of the Transmitarray

The unit cell designed at 19 GHz consists of three copper layers with identical "S-ring" shaped pattern [yellow part in Fig. 7.4(a)]. Minimum dielectric structures (green part in Fig. 7.4, $\epsilon_r \approx 3.6$) are included merely for supporting the metallic pattern and maintaining

the necessary spacing between layers and between adjacent unit cells. The unit cell is carried over from the previous S-ring unit cell designs, and it also works by the geometrical property: the various CP phase shift through rotation of the S-ring element. The transmission matrix representation of this property is as follows:

$$\begin{bmatrix} E_L^t \\ E_R^t \end{bmatrix} = \begin{bmatrix} T_{LL}^{\phi_0=0} & T_{LR}^{\phi_0=0} e^{j2\phi_0} \\ T_{RL}^{\phi_0=0} e^{-j2\phi_0} & T_{RR}^{\phi_0=0} \end{bmatrix} \begin{bmatrix} E_L^i \\ E_R^i \end{bmatrix} \tag{7.1}$$

where E_L^i, E_R^i and E_L^t, E_R^t are the LHCP and RHCP components in the incident and transmitted wave; ϕ_0 is the angle of rotation; $T_{**}^{\phi_0=0}$ are the corresponding CP transmission coefficients before the rotation of the element. To utilize the rotation-phase, the unit cell was optimized to achieve high transmission for the cross-handed polarization component. The simulated transmission coefficient T_{LR} versus ϕ_0 at 19 GHz is shown in Fig. 7.4(b), high transmission (> 0.9) and 360° phase coverage with good linearity can be observed.

The transmitarray has a diameter of 12 cm with a focal length of 14.5 cm [$F/D = 1.2$, as shown in Fig. 7.4(c), 7.4(d)]. The rotation angle of each element is properly determined such that the spherical phase from the feed is converted to a uniform phase at the exiting aperture. It is designed to work with a RHCP feed and generates a LHCP broadside beam. The transmitarray was fabricated with the charge-programmed 3D printing process as in [158]. The selective deposition scheme uses surface charge between 3D-printed substrate and deposition materials. We utilized two UV-curable resins (negatively charged and neutral resin), and a commercially available large-area stereolithography system (Anycubic). The dielectric sections are printed with neutral resin, while the "S-ring" region was patterned with the negative resin. We paused and switched materials based on the part's digital design [160]. Once printed, the transmitarray was subsequently soaked in positive palladium catalyst solution (4mM), a dimethylamino borane reduction solution (10mM), and finally a copper electroless deposition solution, leaving behind metallic copper on the charged resin after several minutes. The fabricated transmitarray is shown in Fig. 7.5(a).

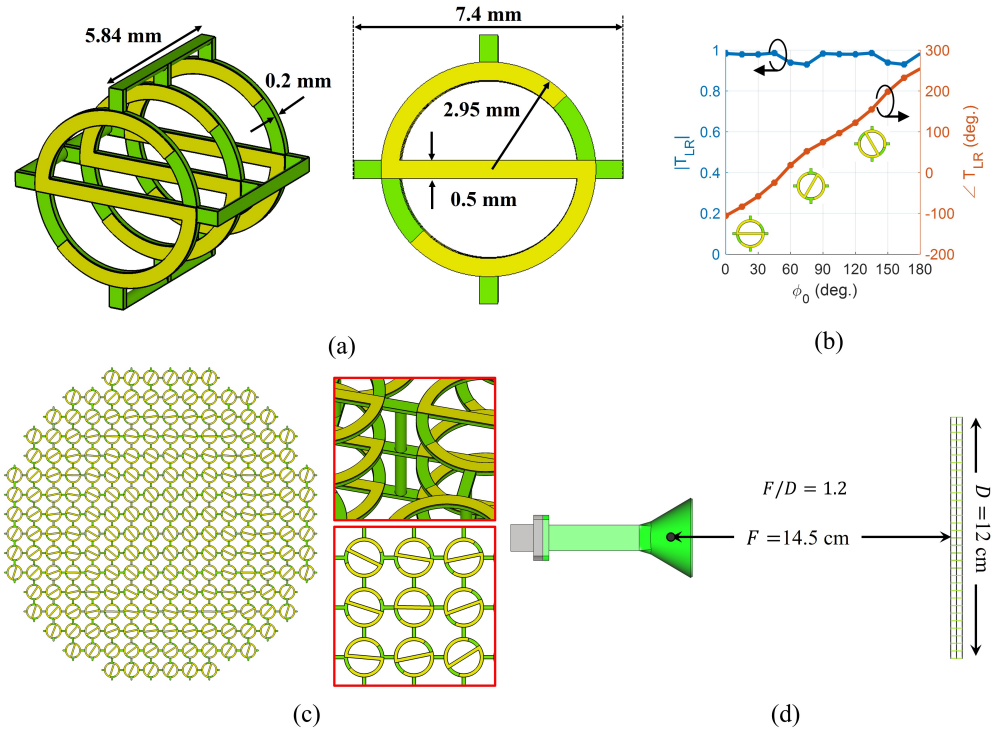

Figure 7.4 (a) The S-ring unit cell design and the key dimensions. (b) The simulated transmission coefficient (T_{LR}) versus different element rotation angle phi_0 at 19 GHz. (c) The transmitarray design based on S-ring unit cell. (d) Side-view of the transmitarray system configuration that was used for simulations and measurements. The feed horn is the RHCP septum horn antenna that will be introduced in details in section 7.2.

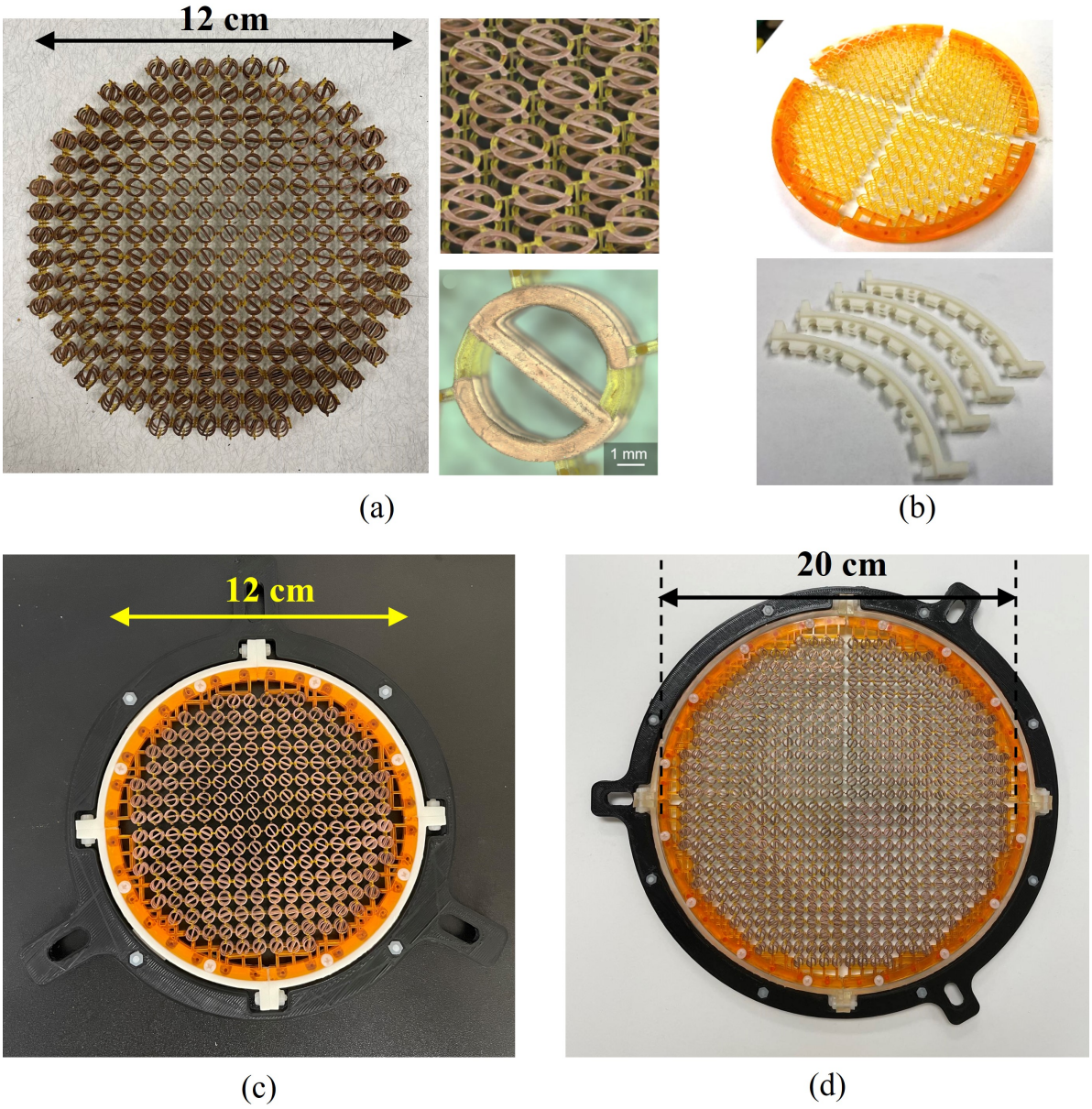

Figure 7.5 Photo of the fabricated transmitarrays. The dielectric structure appears as light yellow color, and copper trace appears as brown color. Note that dielectric structure also exists under the copper traces. (a) The one-piece 12-cm diameter transmitarray. (b) The four quadrants of the transmitarray (before metal deposition) and the locking frames for assembling. (c) The tiled 12-cm diameter transmitarray. (d) The tiled 20-cm diameter transmitarray.

7.1.2 Aperture-Tiling Mechanism Bypassing the Limitations of 3D Printer Size

One of the limitations that exists for all AM techniques is that the size of the printed object is limited by the 3D printer. This limits the achievable antenna aperture size, and consequently the attainable directivity/gain of the printed antenna. The CPMM facility applied in this work has a footprint size of around 12 cm by 12 cm. While expansion to the printing facility is possible, it incurs additional costs and requires the reconstruction of a new system. Instead, we proposed an aperture tiling mechanism (designed by Dr. Zhenpeng Xu) that first prints the transmitarray as segments and then assembles them into the full transmitarray with properly designed inter-segment locking frame [Fig. 7.5(b)]. This allows us to achieve transmitarray aperture sizes that are beyond the current facility limitation to achieve more directive radiation. Using the aperture tiling mechanism, we re-fabricated the 12-cm diameter transmitarray [Fig. 7.5(c)] and also fabricated a 20-cm diameter transmitarray [Fig. 7.5(d)]. Both designs were first printed as four quadrants and then assembled. The aperture-tiled 12-cm diameter transmitarray served as a comparison with the one-piece design in Fig. 7.5 (a) to reveal any performance impacts caused by aperture tiling. The 20-cm transmitarray, however, was only attainable with the tiling method.

7.1.3 Measurement of the Transmitarrays

The fabricated transmitarray prototype was then measured in the spherical near-field range at UCLA [Fig. 7.6 (a) - (c)]. The RHCP septum horn (that will be introduced next in section 7.2) was used as the feed source. The 19.0 GHz radiation pattern of all three cases are plotted against the simulated patterns in Fig. 7.6 (d), 7.6 (e), 7.6 (f). Good agreement between measurement and simulation can be observed for all three cases, suggesting good printing accuracy. Compared with the pattern of the one-piece 12-cm transmitarray [Fig. 7.6 (d)], the tiled version [Fig. 7.6 (e)] demonstrated slight degradation in the broadside X-pol level, which indicates the errors in alignment and assembly of the tiles. Overall, the tiled 12-cm transmitarray maintains the radiation pattern reasonably well. It's worth noting that, the one-piece 12-cm diameter transmitarray weighed only 5 g, whereas a 3-later transmitarray of

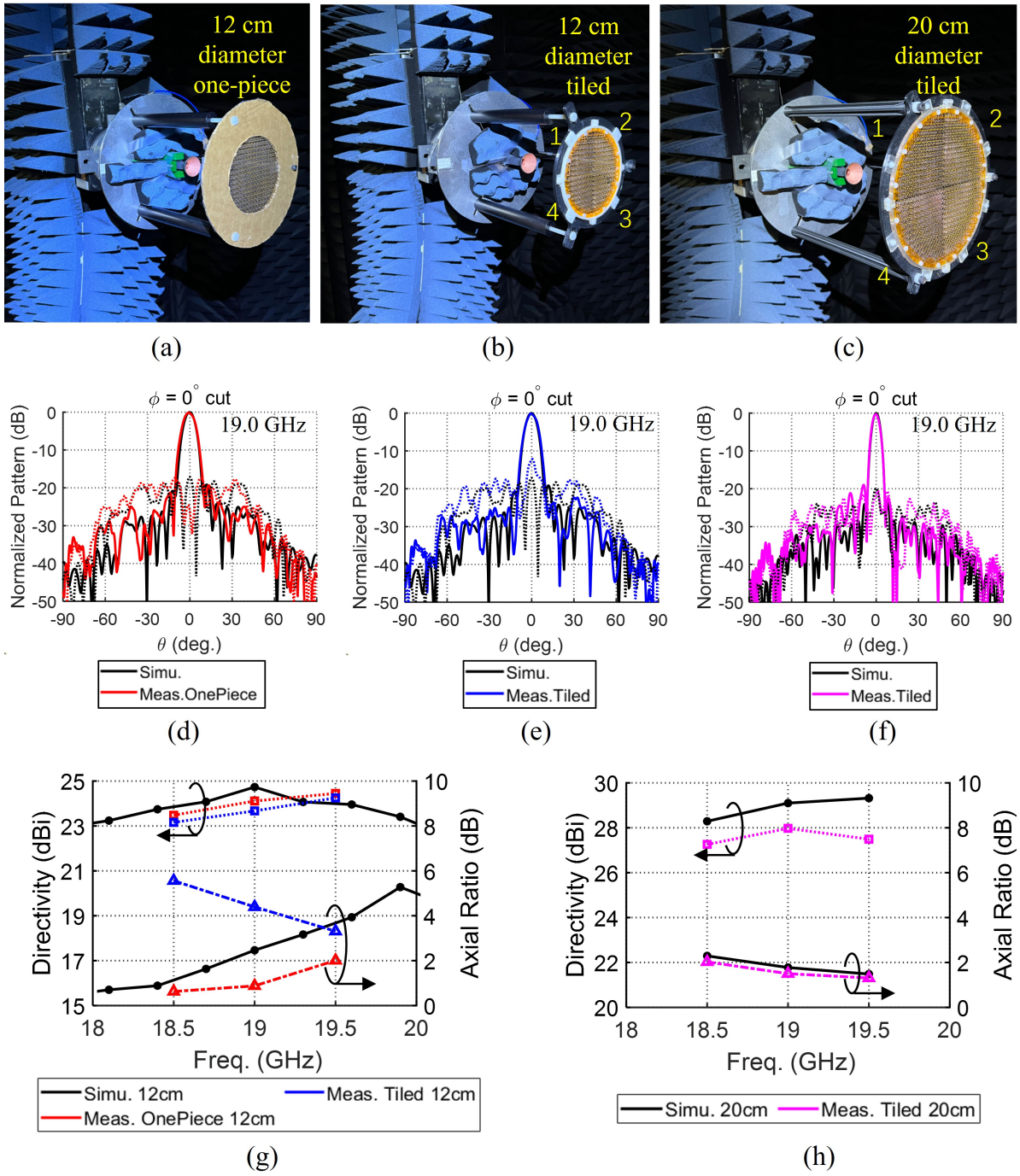

Figure 7.6 (a) - (c) Photos of the transmitarrays being measured in the spherical near-field range at UCLA. (d) - (f) The simulated and measured patterns of the transmitarrays at 19 GHz. (Solid lines: LHCP patterns; dashed lines: RHCP patterns.) (g) - (h) The simulated and measured directivity and AR of the transmitarrays at representative frequencies.

the same aperture size but based on standard Rogers laminates (RO3003) can weigh about 70 g. This marks an order-of-magnitude weight reduction thanks to the unique unit cell structure enabled exclusively by CPMM printing.

The measured directivity and AR of the transmitarrays at representative frequencies are shown in Fig. 7.6 (g) for the 12-cm transmitarrays, and in Fig. 7.6 (h) for the 20-cm transmitarray. All the designs demonstrated promising bandwidth potentials. The discrepancy observed between the simulated and measured curves can be attributed to the measurement uncertainty, potential scattering by the mounting structures, and potential variation in the electric property of the 3D printed resin (which was not designed for RF applications). These results validated the encouraging ultra-lightweight transmitarray developments enabled by CPMM printing. Such a significant antenna weight reduction can bring huge merit for many applications such as satellite and CubeSat planetary missions, where the mass of the antenna system is critical [9].

7.2 Monolithically 3D Printed CP Septum Horn Antenna at K-Band

Horn antennas are reliable, extensively studied, and widely applied in communications systems. Horn antennas can be designed to achieve competitive performance (polarization, bandwidth, cross-polarization suppression, etc.) through the incorporation of sophisticated features, such as spline profiles, corrugations, ridges, septums, etc. These complex geometrical features, while leveraging antenna performance, are very challenging to manufacture with traditional techniques such as computer numerical control (CNC) machining. The cost and accuracy of these traditional manufacturing methods get further challenged in higher frequencies such as millimeter-wave and beyond, where the geometrical features can be in the order of hundreds of microns or less. The advancement in additive manufacturing (AM) techniques have offered new low-cost approaches for the manufacturing of advanced horn antennas with exotic geometrical features [161].

The AM techniques demonstrated for antenna manufacturing can be divided into two

major categories, depending on whether metal is the only material involved. Selective Laser Melting (SLM) and Direct Metal Laser Sintering (DMLS) are the metal-printing AM methods that have been used for fabricating horn antennas [162–165]. The advantage of this category is that the horn with complex geometries can be monolithically printed in metal and does not require additional processing. These methods yield good printing accuracy (tens of microns) and has been used for horn antennas from microwave up to terahertz ranges [162–165].

The other category of techniques fabricates the horn by first 3D-printing the body using polymer and then performing surface metallization [166–172]. This leads to significantly lighter antennas compared to their traditional all-metal version. Therefore, these techniques show promise for emerging small satellite and CubeSat applications where the weight of the antenna becomes critical [9, 169]. Typically, these processes utilize Fused Deposition Modeling (FDM) or Stereolithography (SLA) to first construct a lightweight polymer body of the horn, and then perform plating to establish the conductive surface of the horn. Several plating methods have been reported in the literature. One of the methods is to apply conductive spray to the surface of the SLA-printed components [169], but it requires a "split-block" design so that the internal structures of the horn/waveguide are exposed for thorough coating. This method raises the concern for tolerances because of the assembling process involved. Electroless plating is another technique that has become popular for the metallization of complex devices as it makes it possible to perform plating in monolithic structures with complex internal features (Fig. 7.7). Electroless plating first uses chemical treatment to activate the surface of the SLA-printed component, and then submerge the component in the coating solution. The conductive coating should have a thickness of at least three skin depths [170, 171] to avoid RF leakage. Electroplating can be used to improve the plating thickness once a surface metallization is formed. Waveguides and horns fabricated by such "polymer + metallization" processes have also been demonstrated from tens to hundreds of GHz [169–172].

In contrast, the CPMM printing technique demonstrates appealing advantages in terms of advanced horn antenna fabrications because the charged surface is already monolithically

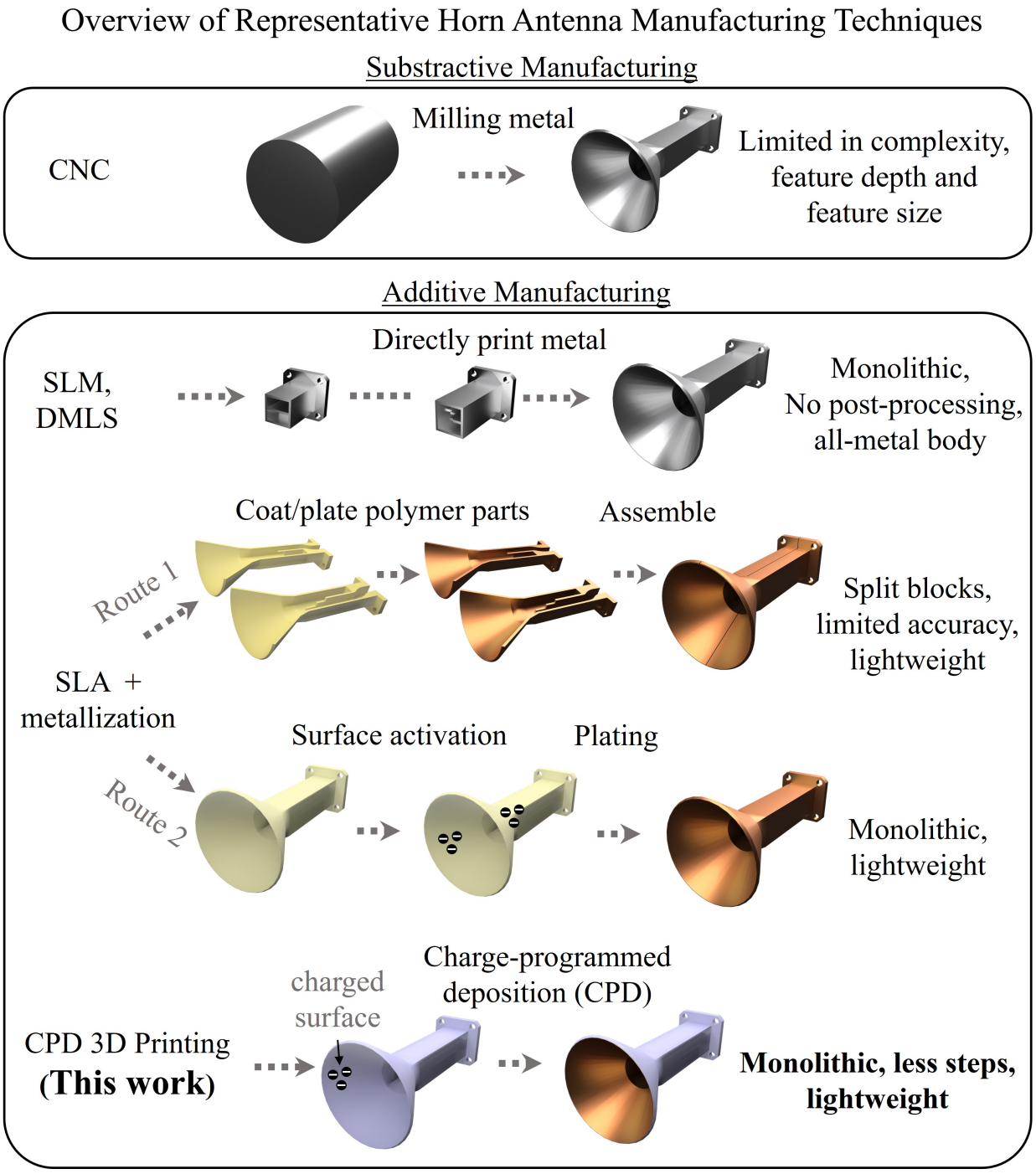

Figure 7.7 Overview of the representative horn manufacturing techniques and a comparison of their key characteristics.

built into the polymer body of the horn and surface activation is no longer required. The time and procedures involved in the antenna fabrication are thus considerably reduced. Such a one-step process with customizable free-form factors and individually addressable 3D interfaces is not achievable in other approaches. Since the plating of the horn's idoes not require selectivity (full surface is to be coated), thus a more accurate description for the method used for this horn development is charge-programmed deposition (CPD). In this section, we for the first time introduce the CPD process to the monolithic fabrication of advanced horn antennas. In particular, we demonstrate the development of a lightweight, circularly polarized (CP) K-band horn antenna. The horn has intricate internal features including a stepped septum polarizer, a meandered waveguide transition, and a square-to-circular waveguide adapter. The horn is monolithically manufactured without the need of assembling split blocks.

7.2.1 Design of the Circularly-Polarized Horn with Septum Polarizer

The horn in this work is designed for K-band at the center frequency of 19 GHz. Although the horn will be built in one piece with a monolithic body, the three segments of the horn considering their functionality are presented as separated parts in Fig. 7.8 for illustrative purposes. The three segments are: (1) the circular horn with a rectangular-to-circular waveguide adapter; (2) the polarizer consisting of a square waveguide and a stepped septum; (3) the meandered waveguide transition from a WR-42 interface to one port of the polarizer. The horn is designed to be compatible with a commercially available coax-to-WR-42 adapter that will be used for excitation. The detailed designed parameters are shown in Fig. 7.8.

The septum polarizer (segment 2) is the key section for the wideband CP performance of the horn. Septum polarizer is a widely applied structure in waveguide devices and horn antennas to generate high-purity circular polarization in a wide bandwidth [173]. The stepped septum is the most common configuration, while smooth septums with optimized profiles have also been proposed to improve the power handling capability [174]. In this work, a 5-stage stepped septum is employed and the dimensions of the stages are optimized (with par-

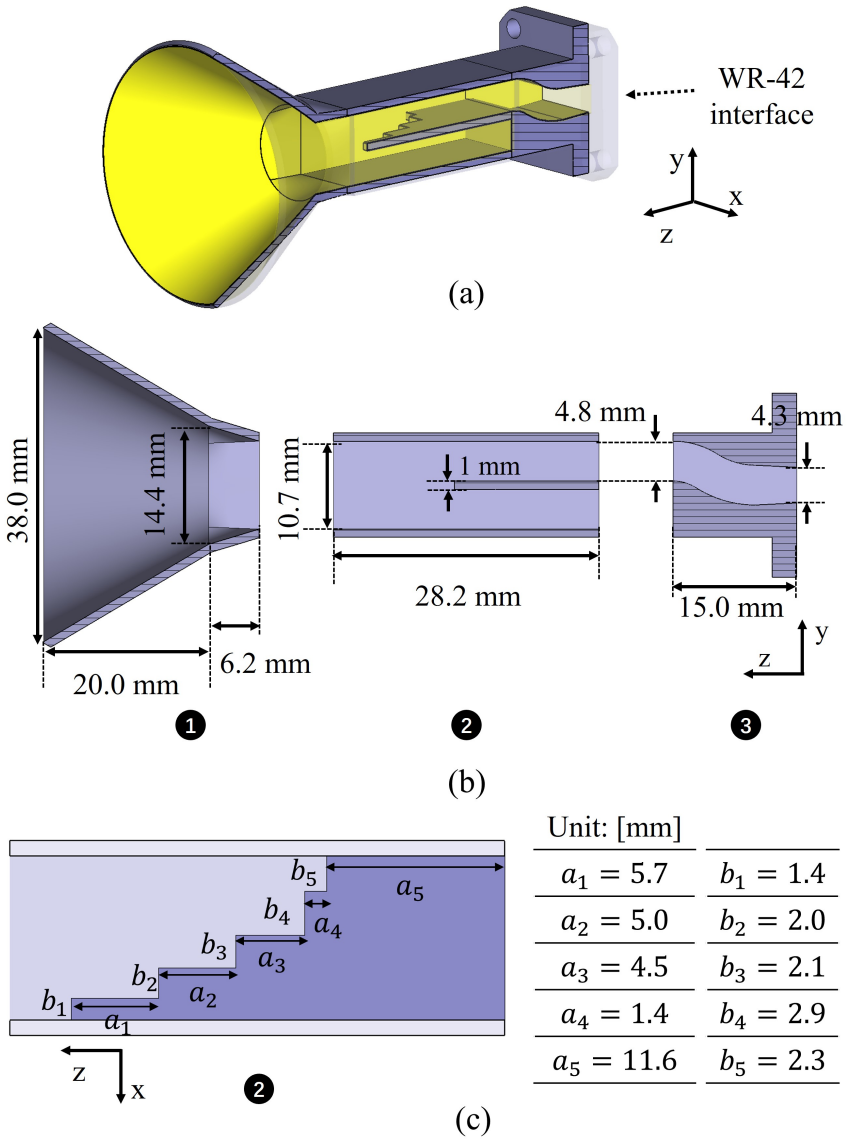

Unit: [mm]	
$a_1 = 5.7$	$b_1 = 1.4$
$a_2 = 5.0$	$b_2 = 2.0$
$a_3 = 4.5$	$b_3 = 2.1$
$a_4 = 1.4$	$b_4 = 2.9$
$a_5 = 11.6$	$b_5 = 2.3$

Figure 7.8 The CP septum horn designed to be manufactured using the CPD process. (a) Overview of the horn design with a monolithic polymer body and copper coating on the interior surface. (b) The cross-section of the horn in the $y - z$ plane. The three segments are separated for a better illustration of the design. (b) The septum polarizer section shown in the $x - z$ plane and the parameters of the stepped septum.

ticle swarm optimization [152]) based on the initial geometry suggested in [173] [Fig. 7.8(c)]. The width of the square waveguide is chosen to match the longer dimension of the WR-42 waveguide to minimize mismatch.

The typical working condition of a septum polarizer is to excite one port of the septum polarizer with the other port terminated with a matched load [163, 175]. While this allows the horn to radiate dual CP, it also increases the profile and weight of the horn, which may not be favorable in certain scenarios. When a septum polarizer is optimized, the two ports usually have good isolation such that terminating one port of the polarizer with a closed cavity does not impact the performance of the polarizer [162, 176]. Adopting such a design allows the horn to have a single excitation port and makes the horn more compact. However, this also makes the feeding port to be offset from the center axis of the horn (as in [162,176]). To make the horn easier to align, we introduce the meandered waveguide transition (segment 3) to align the center of the waveguide port onto the center axis of the horn. Segment 3 also provides a smooth transition that matches the polarizer port with the WR-42 interface that has slightly different dimensions.

It is also worth noting that the three segments can potentially be manufactured as modularized parts to enable a polarization reconfigurable design: by simply changing the orientation of segment 3, one can switch the polarizer port being excited and realize either right-hand CP (RHCP) or left-hand CP (LHCP) radiation. For the monolithic horn demonstrated in this work, the excited port is chosen such that RHCP radiation is generated.

7.2.2 Fabrication of the Horn with Charge-Programmed Deposition 3D Printing

The body of the horn was 3D printed by a commercial printer, Anycubic Photon Mono X (Anycubic Inc.). The printer was equipped with a high-resolution LCD screen to selectively cure the resin with predefined areas and build the 3D structures layer by layer [Fig. 7.9(a)]. The resin was composed of a commercial rigid resin (Formlabs tough 2k, Formlabs Inc.) and bis(2-(methacrylooyloxy)ethyl))phosphate (PDD, Sigma-Aldrich Inc.) in a 90:10 mass

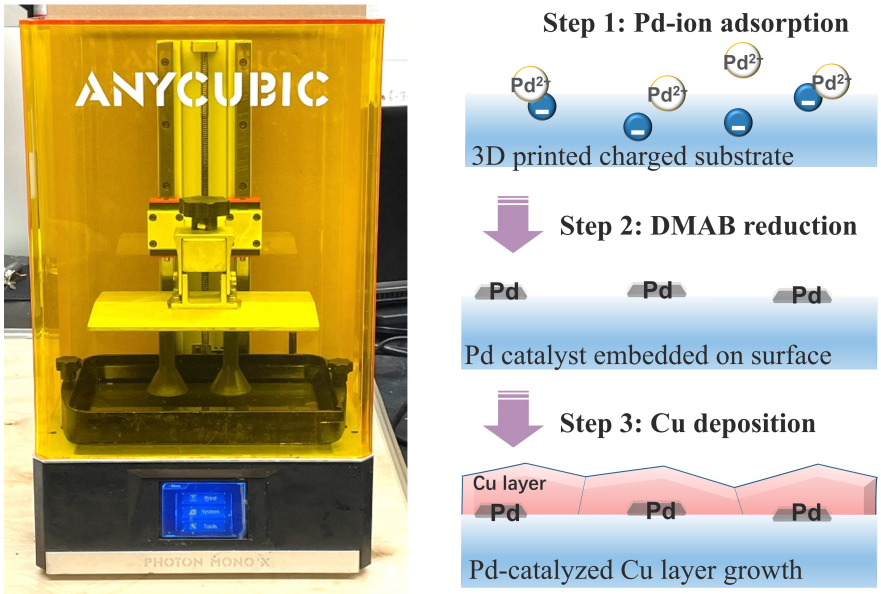

(a) (b)

Figure 7.9 (a) The polymer body of the horn being printed in the printer. (b) The schematic illustration of the Cu-deposition procedure.

ratio. The commercial rigid resin served as the matrix for the structure. PDD provided the negatively charged site to immobilize the Pd ion for catalyzing the following metal deposition.

After the body of the horn was printed, an aqueous solution of tetraamminepalladium(II) chloride monohydrate (Sigma-Aldrich Inc.) of 1.4 mg/mL was added fully into the inner chamber of the horn. In 2-5 minutes, the Pd ions were anchored by PDD to the interior surface of the horn's chamber. After rinsing the horn with deionized water and drying with compressed air, an aqueous solution of borane dimethylamine complex (DMAB, Sigma-Aldrich Inc.) of 0.7 mg/mL was filled into the chamber and kept for 5 min to reduce the immobilized Pd ions into Pd nanoparticles with catalytic activity. Finally, a Cu electroless plating solution (1:1 mixture of parts A and B of the electroless Cu kit from Caswell Inc.) filled up the horn and plated Cu under the catalysis by Pd. This process lasted 3 hours to meet the metallization thickness requirement (greater than three skin depths, skin depth at 19 GHz is 0.473 μm). This procedure of copper deposition is illustrated in Fig. 7.9(b).

After rinsing, drying, and polishing the bottom, the horn was obtained as shown in

Fig. 7.10. The entire manufacturing process, including printing, plating, and post-processing, can be completed in a day at a low material cost. The weight of the horn is only 11 g, which is around 80% of weight reduction compared to a traditionally manufactured all-metal horn of similar size at this frequency (referring to standard gain horn Narda 638). The copper coating has a thickness around 1.8 μm (more than three times skin depth for this frequency range) according to the scanning electron microscope (SEM) image of a representative sample of the horn [Fig. 7.10 (b)].

7.2.3 Measurement Results of the Horn Antenna

The fabricated horn was assembled with a coax-to-WR-42 waveguide adapter from Narda. To be consistent with the measurement setup, in simulations, the CAD model of a representative adapter was assembled with the horn. The horn was then excited from the 50-ohm coax port of the adapter. While the WR-42 waveguide is rated for 18.0 - 26.5 GHz, its cut-off frequency is about 14.1 GHz and thus we performed the simulation in the frequency range of 17.0 to 21.0 GHz. The simulated and measured reflection coefficients (S_{11}) are shown in Fig. 7.11(a). Limited by the frequency range of the vector network analyzer, the S_{11} was only measured up to 20.0 GHz. Nonetheless, the measured S_{11} is below -10 dB in the frequency range considered and agrees well with the simulated result. The minor differences can be attributed to fabrication tolerances, measurement uncertainties, and slight variations between the simulated adapter and the actual part used. In simulations there appeared to be a resonance near 19.36 GHz, causing a hump in the S_{11} and a slight degradation in axial ratio (AR) and directivity [Fig. 7.11(b)]. This is related to a resonance in the septum polarizer section and it is caused by the reflection at the circular-to-square adapter (segment 1). While using a longer circular-to-square transition section can help reduce the reflection, it will also increase the total length of the horn. The current horn design still well satisfies our objective to demonstrate the CPD process's capability in manufacturing complex horn antennas.

The radiation pattern of the horn was then measured in the spherical near-field range

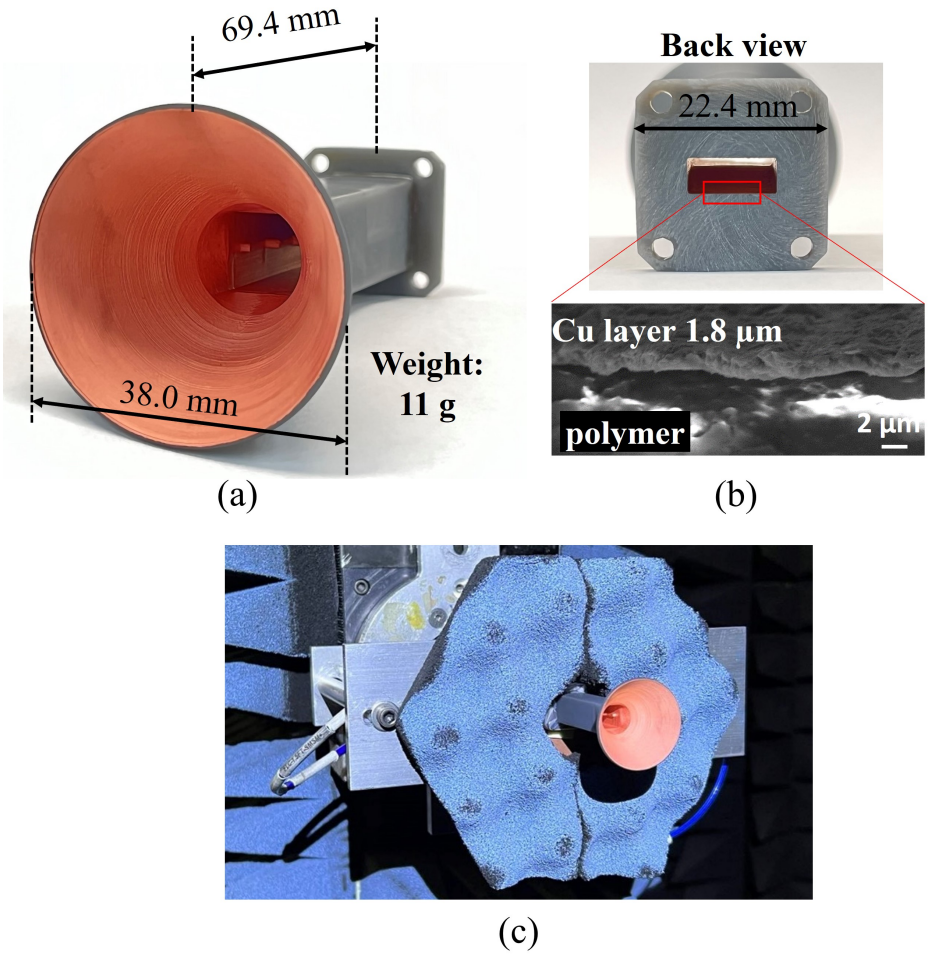

Figure 7.10 Photos of the fabricated horn and antenna measurement setup. (a) The completed horn after copper deposition. (b) The rectangular waveguide interface of the horn and the scanning electron microscope (SEM) image showing the plating thickness. (c) The horn being measured for its radiation pattern in the spherical near-field range at UCLA.

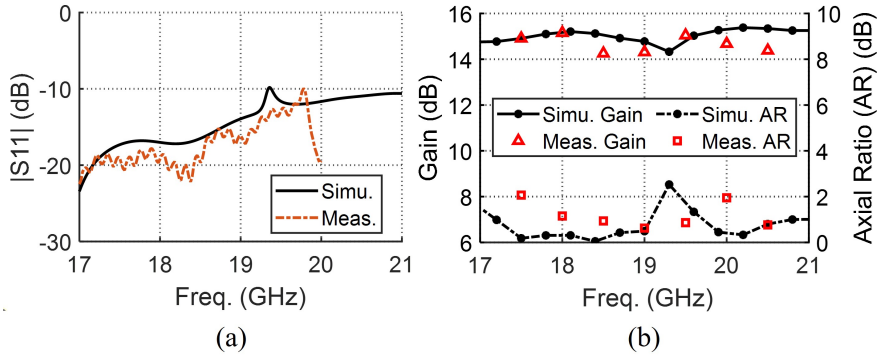

Figure 7.11 (a) Simulated and measured reflection coefficient $|S_{11}|$ of the horn when excited using a coax-to-WR-42 waveguide adapter. (b) Simulated versus measured gain and axial ratio (AR) of the horn.

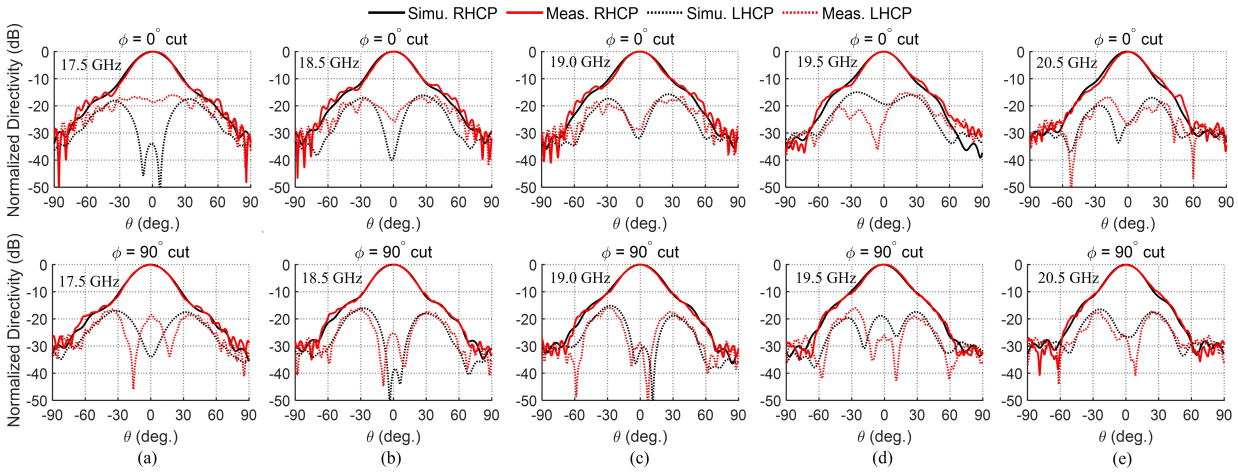

Figure 7.12 (a)-(c) Measured versus simulated RCHP and LHCP radiation patterns of the horn in two orthogonal cuts, at representative frequencies from 17.5 to 20.5 GHz. The measured RHCP directivity for the presented frequencies are 15.05 dBi, 15.26 dBi, 15.29 dBi, 15.37 dBi, and 15.97 dBi, respectively.

at UCLA [Fig. 7.10(c)]. The measured CP patterns in the two orthogonal cuts of the horn are presented in Fig. 7.12 for representative frequencies from 17.5 to 20.5 GHz. Excellent agreement with the simulated patterns can be observed for most of the frequency samples, justifying that all the features of the horn were manufactured with good accuracy. The measured RHCP directivity for 17.5, 19.0, and 20.5 GHz are 15.05 dBi, 15.29 dBi, and 15.97 dBi, respectively. The measured broadside AR across the frequency band is well below 2.5 dB [Fig. 7.11(b)]. The slight differences compared to the simulations can be due to the fabrication tolerances and measurement uncertainties that can not be fully represented in simulations.

The gain of the fabricated horn is measured via the substitution method by referencing a Narda 638 standard gain horn. Overall, the measured gain appeared to be slightly lower than the simulated gain [Fig. 7.11(b)]. This can be attributed to the fact that the simulation model assumed an ideal copper coating with a smooth surface, whereas in reality, the layering effect of SLA can increase the surface roughness of the coated metal, leading to increased ohmic loss [172]. At the center frequency 19 GHz, the measured gain is 14.31 dB, corresponding to a measured gain loss of 0.98 dB. The measured return loss based on the measured S_{11} (-16 dB) is around 0.11 dB, and the residual of the loss (0.87 dB) is attributed mainly to the ohmic loss in the copper coating. This value is also comparable to the loss that has been reported in the literature for horn antennas built using other "SLA + metallization" processes [170–172]. However, it is anticipated that improvement in the ohmic loss can be achieved by improved metal deposition, e.g., through additional electroplating processes.

The lightweight and low-cost horn antenna with a monolithic body can largely benefit applications with critical requirements on mass, e.g., for small satellites and CubeSats. While demonstrated at 19 GHz, it is anticipated that this technology can be applicable for horn antennas in the millimeter-wave range as well. This demonstration marks the first successful development of an advanced horn antenna using the novel CPD process and opens up appealing design and fabrication possibilities for horn antennas and other advanced waveguide devices.

7.3 3D Printed Gradient-Phase Transmitarray for Beam Steerable RPA

In chapter 4, it has been shown that a two-component RPA consisting of a GPFA and a GPTA can achieve promising 2D beam steering capability with merely in-plane rotation motion. In this section, we implement CPMM printing for the manufacturing of the GPTA panel to achieve further weight reduction for the system. This fabricated transmitarray weighs less than 50% of the GPTA built with the Rogers RT5880 substrate.

7.3.1 Design of the Transmitarray Unit Cell

The transmitarray unit cell design for the 3D-printable GPTA (3DP-GPTA) is carried over from the design for the Rogers laminate-based GPTA. However, we tailored the unit cell to exploit the advantages of the novel CPMM 3D printing technique. It utilizes a dielectric skeleton instead of bulk laminate to support the copper S-ring element, thereby removing the excessive weight. The 3D-printable unit cell design and the parameters are shown in Fig. 7.13. The first and third layers of the S-ring element have identical geometry, whereas the parameters of the middle layer S-ring are slightly different (parameters in Fig. 7.13). This modification to the middle layer introduces an additional degree of freedom to minimize the reflection and maximize transmission at the same time. The 3D-printed resin has a dielectric constant around $\epsilon_r = 3.6$. For transmitting VRT unit cells, the CP component that carries the geometrical phase is orthogonal to the incident wave. Therefore, when the unit cell is designed for RHCP incidence, we aim to maximize the transmitted LHCP component.

The magnitude of transmission coefficient (T_{LR}, T_{RR}) and reflection coefficients (Γ_{LR}, Γ_{RR}) of the unit cell considering RHCP excitation are shown in Fig. 7.14 (a). The T_{LR} is greater than -1 dB for 18.6 - 19.4 GHz, while T_{RR}, Γ_{LR}, Γ_{RR} are all below -10 dB for this frequency range. The unit cell provides $0° - 360°$ phase coverage through the rotation of the S-ring element based on the rotation-phase property (the three layers of S-ring in the unit cell rotate simultaneously). The transmission coefficient T_{LR} versus element rotation angle ϕ_0 are presented in Fig. 7.14(b) for 19 GHz. High transmission is maintained as the element

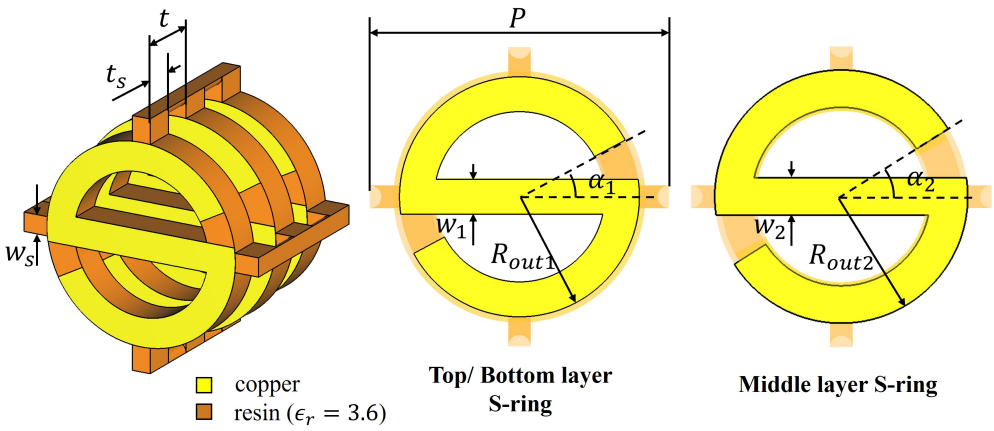

P	R_{out1}	w_1	α_1	R_{out2}	w_2	α_2	t	t_s	w_s
6.60 mm	2.65 mm	0.77 mm	28.2°	2.78 mm	0.82 mm	32.3°	1.75 mm	1.0 mm	0.50 mm

Figure 7.13 The unit cell design for 3D-printable gradient-phase transmitarray.

rotates, and good phase linearity can also be observed.

7.3.2 3D-Printable Gradient-Phase Transmitarray

The 3DP-GPTA is then constructed using the S-ring unit cell [Fig. 7.15 (a)]. The elements span a circular area of 9.2 cm diameter, which is sufficient to fully cover the 8×8 GPFA (presented in section 4.5). The elements in the transmitarray are given proper rotation angles to provide a phase gradient of $p = 0.433k$ along x-direction. A frame supporting the elements is included for mounting. The 3DP-GPTA was then fabricated through the CPMM printing process at UCLA. The entire GPTA including the mounting frame was built all-in-one, without the need for alignment and bonding of different layers. The total weight of the 3DP-GPTA (including the bulk frame) is 28 g, whereas the same-size 3-layer GPTA based on RT5880 substrate weighs 68 g. Therefore, a more than 50% weight reduction is achieved using the CPMM-printed GPTA. Such a weight reduction becomes very attractive for platforms where antenna weight is of important concern, e.g., CubeSats.

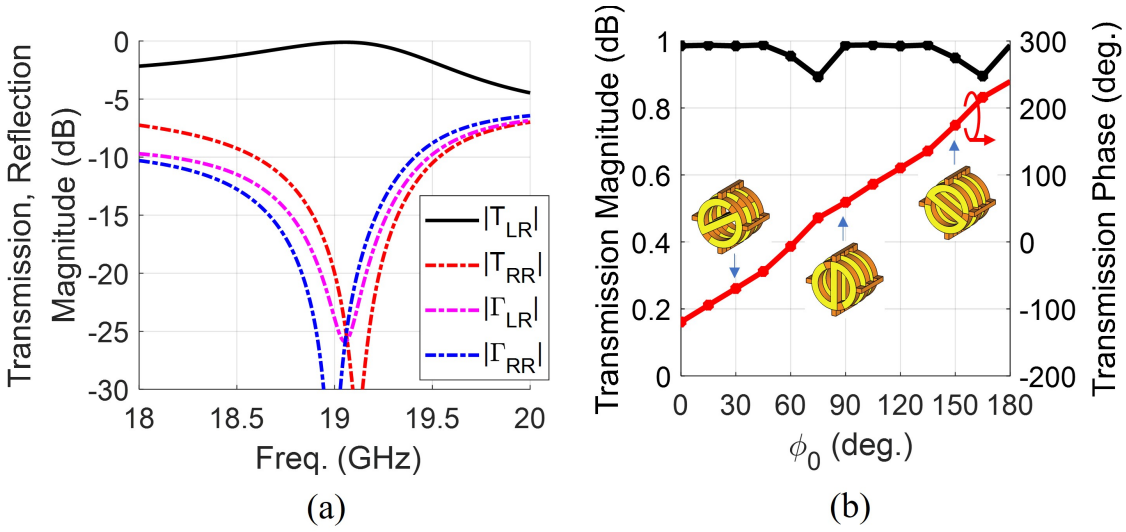

Figure 7.14 Simulated performance of the S-ring unit cell. (a) Transmission and reflection magnitude under RHCP excitation. (b) Transmission coefficient magnitude and phase for T_{LR} (The component of interest) versus element rotation angle ϕ_0 at 19 GHz.

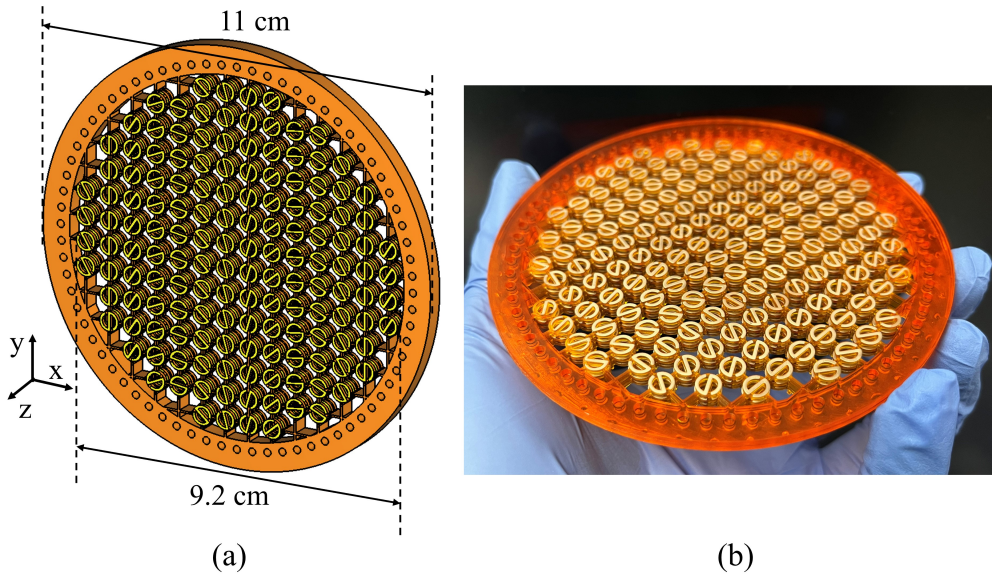

Figure 7.15 (a) The 3DP-GPTA design and some key dimensions. The elements are differently rotated to provide a phase gradient along x-direction. (b) The Photo of the 3DP-GPTA fabricated through the novel CPMM printing technique at UCLA. The entire 3-layer transmitarray was fabricated in a single process, without the need for aligning and bonding.

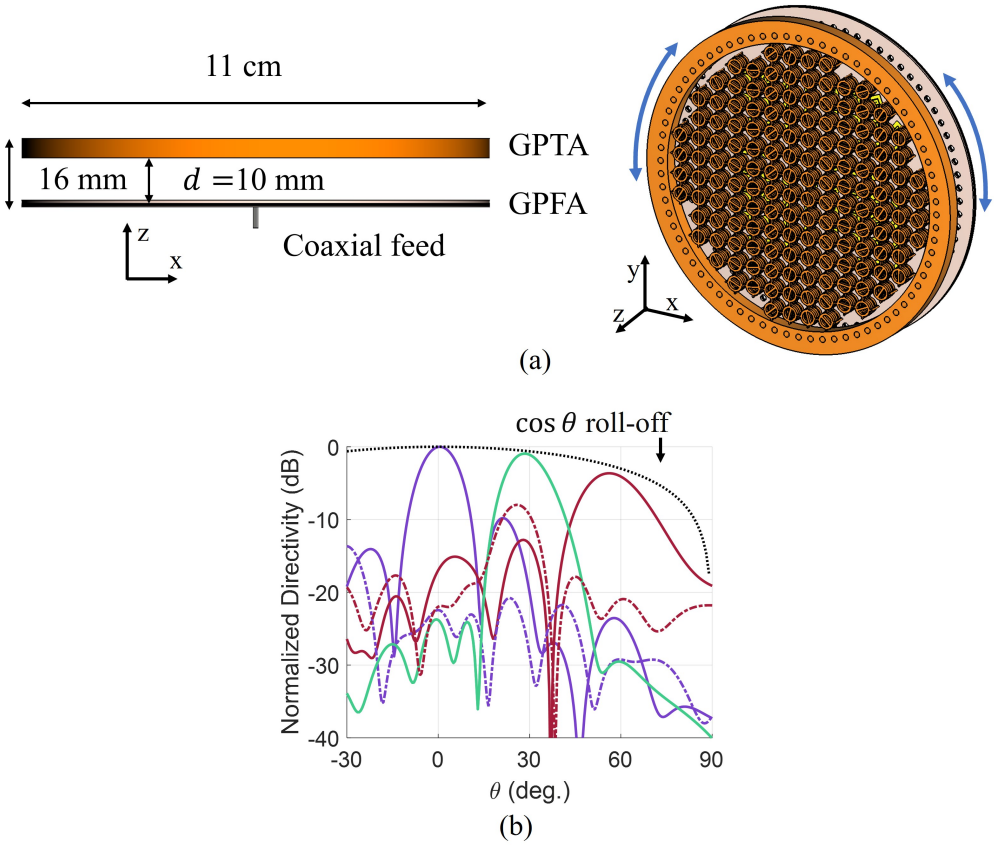

Figure 7.16 (a) The GPFA and GPTA forming an RPA system in simulations. (b) Representative simulated pattern at 19 GHz showing beam scan up to 56° in elevation. [solid lines: LHCP (Co-Pol); dashed lines: RCHP (X-Pol)]

7.3.3 Simulation and Measurements of the Beam Steerable RPA based on 3D Printed Gradient-Phase Transmitarray

The RPA system was first evaluated with full-wave simulations in CST Studio. The 3DP-GPTA and GPFA were placed in parallel with a spacing d, and with their axes aligned [Fig. 7.16(a)]. Considering the complicated near-field effect between GPTA and GPFA, a suitable value for d needs to be determined through full-wave simulations of the RPA using different d. By evaluating the RPA directivity and bandwidth, $d = 10$ mm was chosen for the rest of the simulations. The total height of the system is thus 16 mm, or 1.01 wavelength at 19 GHz.

Representative scanned beams at 19 GHz in $\phi = 0°$ cut are demonstrated in Fig. 7.16(b).

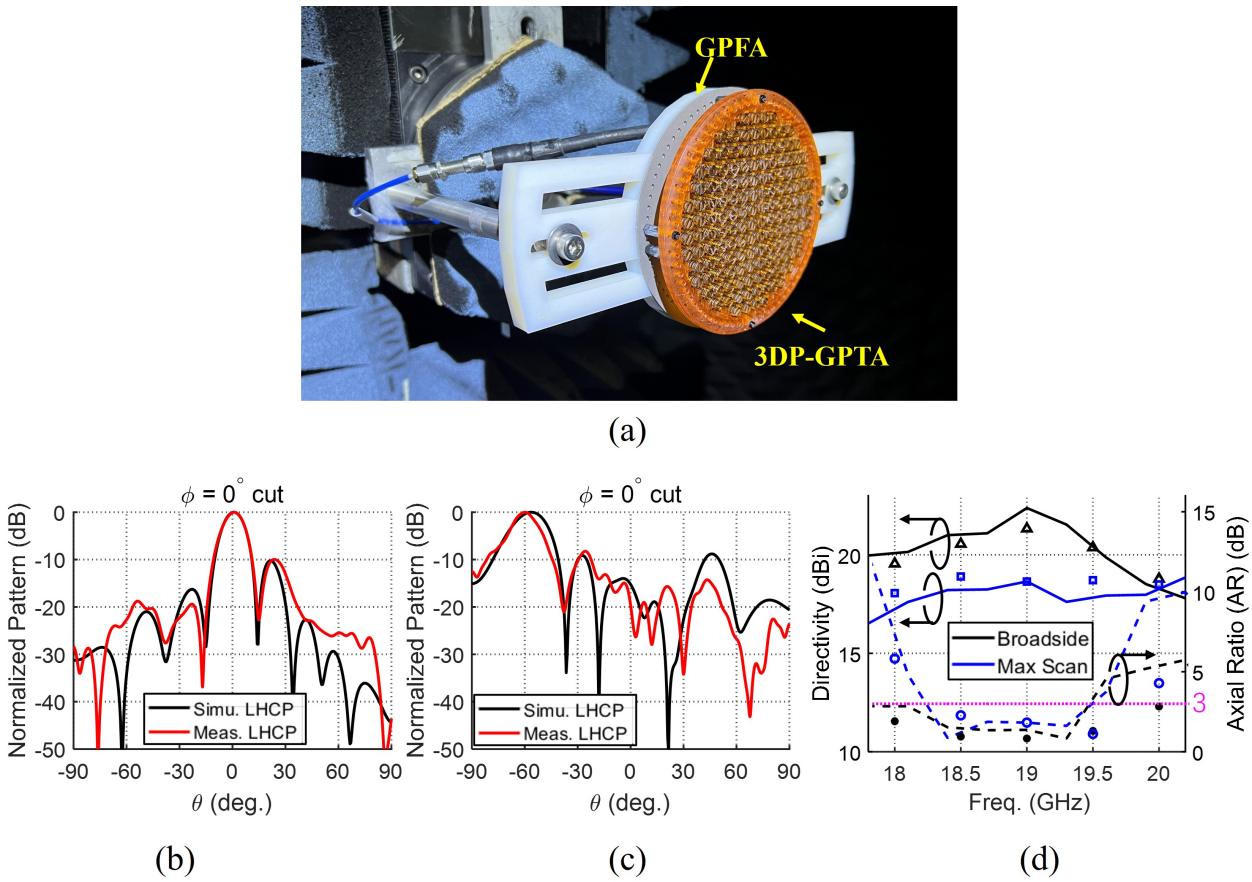

Figure 7.17 (a)Photo of the RPA system assembled by the GPFA and the 3DP-GPTA being measured at the spherical near-field range at UCLA. (b) Measured versus simulated LHCP pattern of the broadside beam. (c) Measured versus simulated pattern of the 60° scanned beam. (d) Measured versus simulated directivity and AR over frequency, for the broadside beam and maximally-scanned beam. (dashed lines represent simulated data, dots represent measured data points.)

The Co-Pol beam is now LHCP since the GPTA flips the handedness as discussed in section 7.3.1. The broadside directivity is 22.7 dBi, corresponding to an aperture efficiency of 55.6% at 19 GHz considering a 9.2 cm diameter aperture area. The maximally scanned beam is pointed at 56.1° with a directivity of 19.2 dBi, corresponding to a scan loss of -3.5 dB (close to what is expected from the $\cos(\theta)$ roll-off). While only several scanned beams are demonstrated in one far-field cut, this RPA can scan to the same elevation angle in $0-360°$ azimuth range by simply rotating both the GPFA and the 3DP-GPTA. The resolution of beam scan in elevation and azimuth is about half of the angular step of the mechanical rotation [118], which depends on the actual implemented mechanics.

The RPA was then measured for its radiation pattern in the spherical near-field range at UCLA. Representative patterns at 19.0 GHz are shown in Fig. 7.17 (b), 7.17 (c) for the broadside beam and 60°-scanned beam, respectively. Good agreement with simulated patterns can be observed. The measured directivity and AR of the RPA are also presented against the simulated data in Fig. 7.17 (d). The RPA demonstrated promising bandwidth potential: the 3-dB AR bandwidth for both the broadside and maximally-scanned cases are greater than the 18.5 - 19.5 GHz range (>5.3%). The 3-dB directivity bandwidth for both cases is beyond 9%, and completely covers the 3 dB AR bandwidth. These results mark the successful development of the 3DP-GPTA and highlighted the potential of CPMM printing in enabling lightweight beam steerable antenna systems.

7.4 Future Directions

While this chapter demonstrated several CPMM-printed antennas targeting significant weight reductions, the potential applications of CPMM in antenna design and manufacturing extend beyond. For instance, introducing mechanical meta-lattice [177] can further improve the structural strength of antennas while maintaining the low mass. The incorporation of flexible materials can also enable a range of wearable, deployable, and conformal antenna developments. The unprecedented freedom in controlling the conductive and non-conductive material distribution in a 3D volume may also reveal new areas in antenna design for ex-

traordinary performances.

7.5 Summary

The CPMM 3D printing is a novel AM technology that can unlock new possibilities for designing and manufacturing advanced antennas. CPMM printing's accurate control over the metalized area in complex 3D volume significantly enhances the freedom in the structural design of antennas. One of the benefits of unique antenna structures is significant weight reduction in the antenna, which is the main objective of the developments demonstrated in this chapter. Several antennas designed for and manufactured by CPMM printing have been covered: (1) In the first part, we demonstrate K-band ultra-lightweight CP transmitarray antennas that utilize an optimized dielectric skeleton to support three layers of conductive S-ring element. The unique unit cell structure minimizes the use of material and resulted in an order-of-magnitude weight reduction compared to traditionally fabricated transmitarrays. We further proposed an aperture tiling mechanism that allows the development of large-aperture antennas that exceeds the footprint of the 3D printer. (2) In the second part, we developed a K-band CP horn antenna with CPMM printing, which is a monolithic design with a meandered waveguide transition, a stepped-septum polarizer, and a circular horn adapted to a square waveguide. The horn has a polymer body and copper-plated interior surface, thus achieving considerable weight reduction compared to all-metal versions. (3) In the third part, a CPMM-printed GPTA panel was developed as part of a two-component beam steerable RPA. The RPA can achieve 2D beam coverage with demonstrated beam scan to nearly 60° in elevation and the ability of full azimuth beam coverage. All the antennas have been validated in simulations and measurements. The encouraging results highlighted the potential of CPMM printing in enabling low-cost, lightweight, and beam steerable antennas for CubeSat applications and beyond. It is also expected that more advanced antenna topology and configurations enabled by CPMM printing can be developed to achieve unprecedented electromagnetic and mechanical performances in the future.

CHAPTER 8

Conclusions

The growing demand for wideband, low-profile, and low-cost beam steerable antennas for CubeSats and other next-generation applications has motivated continuing innovations in the design and manufacturing of modern antennas. The most crucial requirement for beam steerable antennas is the ability to dynamically control the aperture phase. Therefore, both reflectarray and transmitarray become appealing candidates for these scenarios considering their outstanding control of the phase front of the reflected/transmitted wave. The combination of reflectarray/transmitarray with other devices (e.g., feed arrays) can unlock even more unique possibilities for beam steerable antennas. This dissertation presented novel synthesis methods and implementations for reflectarrays and transmitarrays to enable low-profile circularly-polarized (CP) beam steerable antennas that can potentially be integrated with CubeSats. Following a comprehensive literature review on beam steerable antennas in chapter 2, and a revisit of the enabling fundamental properties in chapter 3, the major contribution of this work is embodied by: (1) a novel mechanically steerable transmitarray-based Risley-prism antenna (RPA) architecture in chapter 4; (2) a unique electronically beam steerable reflectarray architecture in chapter 5; (3) a generalized reconfigurable unit cell design methodology in chapter 6; (4) the implementation of novel additive manufacturing (AM) technique in achieving innovative antenna structures in chapter 7.

In chapter 4, the working principles of a general category of RPAs based on phase-shifting surfaces were clarified by considering the phase gradient in the aperture. It was shown that the rotation of two gradient-phase surfaces controls the phase gradient at the exiting aperture of the system, which eventually steers the beam in a 3D conical volume. A new mathematical model was thus established to more accurately associate the beam pointing angle and the

orientation of the surfaces. It was also shown that when the steered angle is small, the new model can reduce to the paraxial model that was traditionally used for optical Risley prisms and even RF RPAs. Based on the understanding of the RPA's working principle, a novel RPA architecture that uses only two components was proposed and validated. The new architecture achieves the same 2D beam coverage as the traditional architectures, which typically necessitate three or more components in the system. To validate this concept, a K-band RPA based on a gradient-phase feed array (GPFA) and a gradient-phase transmitarray (GPTA) were designed and manufactured. The GPFA used a hybrid-phasing method that combines element rotation and varied delay lines to create the Co-Pol phase gradient while perturbing the X-Pol phase gradient, which significantly improves the axial ratio (AR) of the RPA. The GPTA utilized an S-ring unit cell to achieve high transmission and low reflection. The fabricated K-band RPA demonstrated beam scan from broadside to nearly 60°, with over 9.2% 3-dB directivity and 3-dB AR bandwidth. The beam scan resolution is better than 2° when implementing a 5° mechanical rotation step.

In chapter 5, novel switch-reconfigured multi-Archimedean spiral unit cells were proposed for beam steerable reflectarrays to meet the wideband CP requirement of CubeSats. By properly addressing the switches (with DC bias), the connection among the spiral arms can be reconfigured, which allows one to exploit the geometrical phase caused by element rotation without any moving parts. To validate the concept, a 4-arm Archimedean spiral unit cell for K-band CP beam steerable reflectarray antenna working across 17.8 - 20.2 GHz was designed. In the target 12.6% bandwidth, the simulated reflectarray achieved an overall directivity variation less than 2 dB and AR less than 1.5 dB for the broadside beam. Several proof-of-concept 10-cm-diameter reflectarray prototypes incorporating idealized elements were designed, fabricated, and measured. Measurement results demonstrated RHCP beam scan up to 60° in the plane of offset at representative frequencies across the target band of 17.8 - 20.2 GHz. Then, a 3-arm Archimedean spiral unit cell tailored specifically for p-i-n diode switch implementation was designed. The unit cell takes a multi-layer layout to accommodate the necessary DC-RF isolation structures and DC bias lines within a tight, half-wavelength footprint. Reflectarray simulations also demonstrated 3-dB directivity and

AR bandwidth covering 17.8 - 20.2 GHz. The 3-state unit cell was validated with reflectarray prototype measurements, highlighting the potential of this reflectarray to meet the stringent technical requirements of IoS CubeSats.

In chapter 6, a generalized design methodology for switch-reconfigurable unit cells (SRUC) has been proposed. The chapter starts with a discussion of non-ideal unit cell phase separation, which is a realistic problem that exists in multi-state unit cell designs. Quantitative metrics to gauge the phase non-uniformity of an SRUC, i.e., equivalent bit used in a few literatures and the normalized variance of phase difference proposed in this work, are compared. A Monte Carlo study based on the cosine-q array simulation was presented to connect the unit cell metrics with expected array performance, and to further guide the design of SRUCs. Then, a BPSO-driven pixelated topology design workflow was established to design 2-switch 4-state SRUC. Multiple reflectarray SRUC designs for linear-polarization (LP) and CP operations have been obtained, including the first 2-switch 4-state CP SRUC reported in the literature. The performance of the SRUCs was comprehensively evaluated using reflectarray simulations to demonstrate beam scan capability and bandwidth performance. Several critical design insights were also provided to obtain SRUC with better X-Pol performance. Representative reflectarray prototypes based on the pixelated unit cells have been successfully fabricated and measured to show RHCP beam scan up to 60°. The proposed design process relied on minimum prior knowledge of SRUC design and reveals unconventional SRUC configurations that should provide new possibilities in the implementation of beam steerable arrays and reconfigurable intelligent surfaces for next-generation wireless applications.

In chapter 7, CPMM 3D printing technique was implemented to enable several lightweight antennas with uniquely designed structures. In contrast to other AM techniques, CPMM printing allows one to develop complex 3D structures with accurately controlled distribution of metal and dielectric material. Exploiting this feature, the first example was a set of 19-GHz ultra-lightweight transmitarray antennas based on structurally optimized S-ring unit cells, which were designed to minimize the use of dielectric material and significantly reduce weight. An aperture tiling mechanism was also introduced to achieve antenna apertures that

are beyond the printer size limit. The second example was a K-band CP horn antenna with monolithically built-in septum polarizer and meandered waveguide. The horn has a polymer body with a fully-coated interior surface, thus weighing much lower than horn antennas traditionally built with metal. The third example is a lightweight 3D printed GPTA designed to be assembled with the GPFA in chapter 4 to form a beam steerable RPA system. All the 3D-printed antennas were validated through extensive measurements to demonstrate the reliability of the CPMM printing technique. These lightweight antenna concepts enabled by CPMM printing reveal new possibilities in antenna design and manufacturing, and can significantly benefit mass-critical applications such as CubeSat communications and sensing.

APPENDIX A

Further Discussions on the Working Principle of the Multi-Archimedean Spiral Unit Cell

To provide a better understanding of the working principle of the proposed unit cell in chapter 5 and to explain the 90° phase shift between state 1 and state 2 (also between state 3 and state 4), we herein present a graphical explanation by analyzing the induced currents in the spiral elements. Before we begin the detailed explanation, we reiterate the following facts:

(a) When a radiating object is rotated counter-clockwise by ϕ_0, the radiated RHCP component will manifest a phase shift of $e^{j\phi_0}$, and the radiated LHCP field will manifest a phase shift of $e^{-j\phi_0}$. This has been proved in detail in chapter 3.

(b) The spiral arm used in our unit cell is a right-hand spiral (looking from center to edge from the front of the unit cell). When such a right-hand spiral arm is well matched on both ends, current traveling outward from center to the edge radiates RHCP dominantly, whereas current traveling inward radiates LHCP dominantly. Such a traveling current behavior has been observed and discussed in many spiral-like antenna designs [107, 178]. Moreover, it can also be shown in simulations that, when such a right-hand spiral is illuminated by an RHCP wave, the induced current travels inward from the edge to the center of the spiral, while the induced current by LHCP wave will travel outward along the spiral. When such a spiral is terminated with open-circuits on both ends and is used as a scatterer (as in the proposed reflectarray unit cell), generally there can exist both inward and outward traveling currents because of reflection.

We start with the unit cell with no connections in the center to introduce how the induced

current with sequential phase contributes to CP radiation. As shown in Fig. A.1(a), the four arms are labeled from 1 to 4 and are highlighted with distinct colors. The currents originally being excited in each arm are represented with arrows of the corresponding color. As we later trace down the current in each branch, the color of the arrows is maintained for one to easily distinguish the origin of those currents.

Suppose the unit cell in Fig. A.1(a) is excited by an RHCP wave, the induced currents will be traveling inward (as just mentioned in item (b)). Since the four arms are identical and are sequentially rotated by 90°, the induced currents will manifest a sequential phase with $-\pi/2$ phase difference in the clockwise direction (follows the clockwise rotation of the electric field vector of the incident RHCP wave). The induced currents will travel inward and get reflected back at the center of the unit cell because all the arms are terminated with open-circuits. The reflected currents then travel outward along the arms and radiate dominantly RHCP wave, as shown in Fig. A.1(b). The radiated RHCP field will carry the sequential phase due to excitation, as labeled in Fig. A.1(b). Additionally, because the four spiral arms are physically rotated by a step of 90°, from (3.5) we know that the radiated RHCP field from the four arms will intrinsically bear a relative phase shift. Taking arm 1 as a reference, the radiated RHCP field from arm 2 will have an additional $-\pi/2$ phase shift because it is rotated clockwise by 90° from arm 1. Similarly, the radiated RHCP field from arm 3 and arm 4 will have intrinsic phase shift of $-\pi$ and $-3\pi/2$ respectively. Therefore, the radiated RHCP field from each arm will carry both the phase of the current and the phase shift because of physical rotation.

Using arm-1 as reference, and ignoring the CP field amplitude for simplicity, the radiated RHCP field $\vec{e_i^r}$ from the four arms can be written as:

$$\vec{e_1^r} = (\hat{x} - j\hat{y})e^{j(0+0)} \tag{A.1}$$

$$\vec{e_2^r} = (\hat{x} - j\hat{y})e^{j(-\pi/2-\pi/2)} \tag{A.2}$$

$$\vec{e_3^r} = (\hat{x} - j\hat{y})e^{j(-\pi-\pi)} \tag{A.3}$$

$$\vec{e_4^r} = (\hat{x} - j\hat{y})e^{j(-3\pi/2-3\pi/2)} \tag{A.4}$$

The phase term of $\vec{e_i^r}$ consists of two parts: one originates from the geometrical rotation

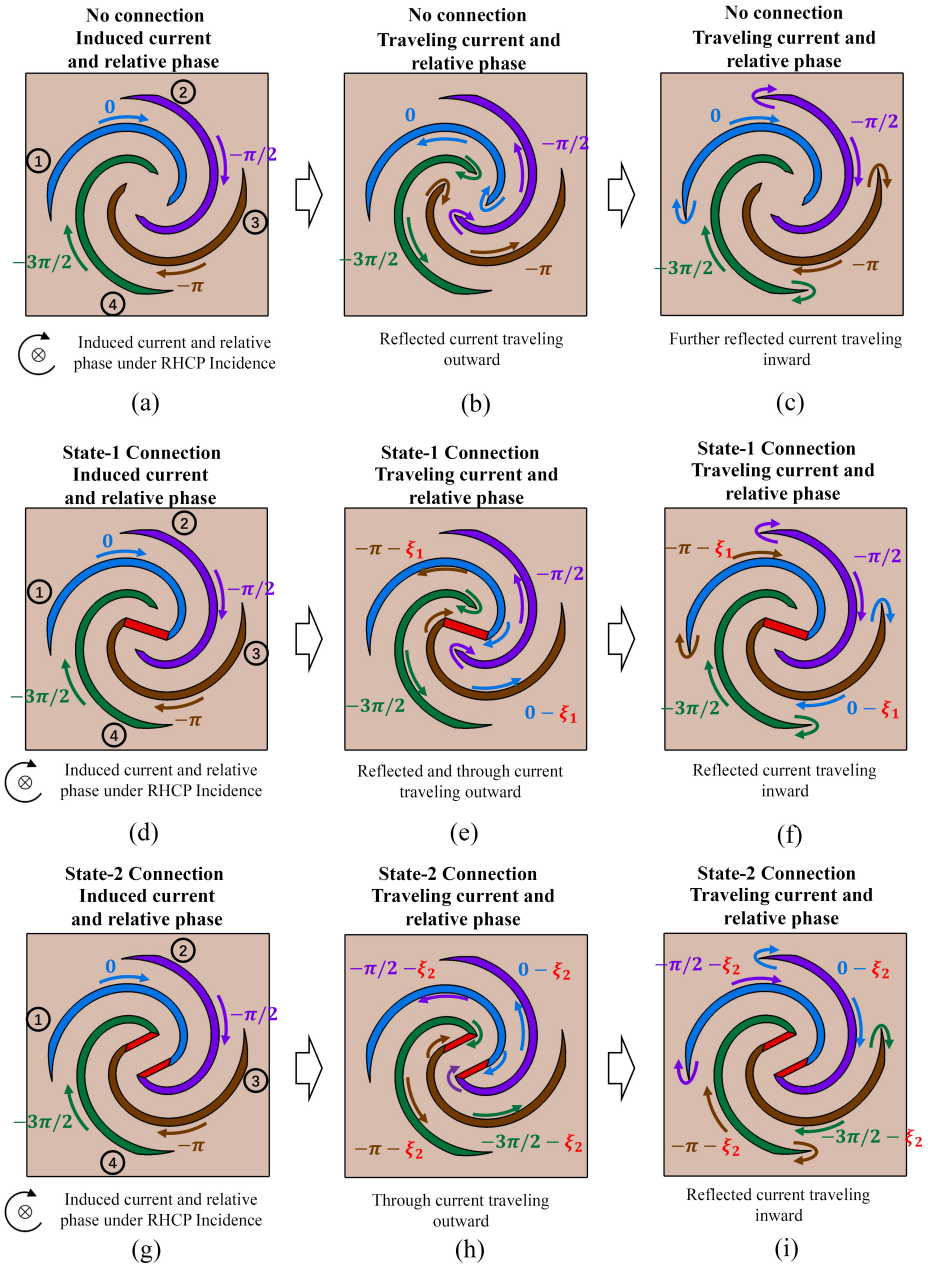

Figure A.1 A graphical illustration explaining the working principle of the proposed unit cell under RHCP excitation. (a)-(c) The induced current and traveling currents in each arm when no switch connection is made in the unit cell. (d)-(f) The induced current and traveling currents in each arm when state 1 connection is established. (g)-(i) The induced current and traveling currents in each arm when state 2 connection is established. The relative phase of the currents are marked in the graphs.

among the arms, and the second is the relative phase of the currents due to the incident RHCP excitation. The total field is the summation of the radiation by each arm:

$$\vec{E}_{tot}^{R} = \sum_{i=1}^{4} \vec{e_i^r} = 0 \tag{A.5}$$

which means the RHCP radiation will completely cancel out.

Since the spiral arm is not long enough to let the outward current radiate completely, the current is not zero as it meets the outer terminals of the arm. Further reflection causes the current to travel inward as shown in Fig. A.1c. The inward traveling current radiates LHCP wave dominantly, and the radiated field from the four arms can be written as:

$$\vec{e_1^l} = \alpha(\hat{x} + j\hat{y})e^{j(0+0)} \tag{A.6}$$

$$\vec{e_2^l} = \alpha(\hat{x} + j\hat{y})e^{j(\pi/2-\pi/2)} \tag{A.7}$$

$$\vec{e_3^l} = \alpha(\hat{x} + j\hat{y})e^{j(\pi-\pi)} \tag{A.8}$$

$$\vec{e_4^l} = \alpha(\hat{x} + j\hat{y})e^{j(3\pi/2-3\pi/2)} \tag{A.9}$$

Note that in the phase term, the phase shift due to physical rotation has the opposite sign of the RHCP case, as indicated in (3.5). We use the coefficient α to indicate the relative decrease in current amplitude in the remaining current. The total field is:

$$\vec{E}_{tot}^{L} = \sum_{i=1}^{4} \vec{e_i^l} = 4\alpha(\hat{x} + j\hat{y}) \tag{A.10}$$

This means the LHCP radiation will add up in phase. This is intuitive since the phase shift due to the sequential rotation of the arms cancels the phase shift due to the incident RHCP field. Any further reflections of the current are assumed to be negligible. The equations above indicate that the reflected wave should be dominantly LHCP, and this is actually observed in unit cell simulations when no connection is made.

With this example of the unit cell using no connections in the center, we then move on to illustrate the current flows in state 1 of the unit cell, as shown in Fig. A.1(d). Under RHCP excitation, the induced current will travel inward with relative phase as labeled in Fig. A.1(d). In this case, arm 1 and arm 3 are connected by the on-switch highlighted red.

The current excited in arm 1, instead of being reflected, will go through the switch and travel outwards in arm 3. Similarly, the induced current in arm 3 will propagate through the switch and travel outwards in arm 1. The current in arm 2 and arm 4 will be reflected and travel outwards along each arm. The relative phase between the outward traveling current can be easily determined as in Fig. A.1(e). Note that the current in arm 1 and arm 3 undergo a slightly longer traveling distance because of the switch, leading to an extra phase delay denoted by ξ_1. Following the analysis method used for the all-open unit cell, the radiated field of the outward-traveling current in each arm can be written as the following:

$$\vec{e_1^r} = (\hat{x} - j\hat{y})e^{j(0-\pi-\xi_1)} \tag{A.11}$$

$$\vec{e_2^r} = (\hat{x} - j\hat{y})e^{j(-\pi/2-\pi/2)} \tag{A.12}$$

$$\vec{e_3^r} = (\hat{x} - j\hat{y})e^{j(-\pi-\xi_1)} \tag{A.13}$$

$$\vec{e_4^r} = (\hat{x} - j\hat{y})e^{j(-3\pi/2-3\pi/2)} \tag{A.14}$$

which leads to:

$$\begin{aligned}\vec{E}^R_{tot}(\text{State1}) &= \sum_{i=1}^{4} \vec{e_i^r} = -(2 + 2e^{-j\xi_1})(\hat{x} - j\hat{y}) \\ &= -4\cos\frac{\xi_1}{2}e^{-j\xi_1/2}(\hat{x} - j\hat{y})\end{aligned} \tag{A.15}$$

The remaining current will be reflected back at the outer terminals of each arm and travel inward along the arms, contributing majorly to LHCP radiation. Similar to the previous case, the total radiation can be obtained as:

$$\vec{E}^L_{tot}(\text{State1}) = \sum_{i=1}^{4} \vec{e_i^l} = 4\alpha \sin\frac{\xi_1}{2}e^{j(\pi/2-\xi_1/2)}(\hat{x} + j\hat{y}) \tag{A.16}$$

Since the switch (red part in figures) has a small electrical length compared with the wavelength in the medium, ξ_1 is a small value. Therefore, $\cos(\xi_1/2)$ is close to 1 and $\sin(\xi_1/2)$ is close to 0, and the amplitude of the RHCP field in (A.15) is much greater than that of LHCP field in (A.16). This essentially implies that the majority of the reflected field is in RHCP when the excitation is RHCP. Additionally, this analysis reveals the phase delay ξ_1 due to the switch can cause the X-Pol of the unit cell to be higher.

Then, we move on to the unit cell in state 2, where arm 1 and arm 2 are connected, and arm 3 and arm 4 are also connected, as shown in Fig. A.1(g). Tracing the current one can tell that the induced current in each arm will travel to its paired arm and propagate outwards along the arms. The relative phase of the traveling current can be easily obtained as shown in Fig. A.1(h). Note that the current in all arms undergo the same extra traveling distance in the switch, and the extra phase delay is denoted as ξ_2. The total radiated field of the outward-traveling current can be obtained as:

$$\vec{E}^R_{tot}(\text{State2}) = \sum_{i=1}^{4} \vec{e^r_i} = -4e^{j(\pi/2-\xi_2)}(\hat{x} - j\hat{y}) \tag{A.17}$$

The remaining current reflected back at the outer terminals of each arm travels inward and contribute majorly to LHCP radiation. The total radiated field is:

$$\vec{E}^L_{tot}(\text{State2}) = \sum_{i=1}^{4} \vec{e^l_i} = 0 \tag{A.18}$$

These indicate that the majority of the radiated field is in RHCP, and ideally the LHCP component vanishes. However, in reality, many other factors can contribute to the LHCP, and eventually raise the X-Pol level in the reflected component of the unit cell as explained subsequently.

More importantly, referring to (A.15) and (A.17), the phase difference between the radiated RHCP field of state 1 and state 2 can be obtained as:

$$\angle\vec{E}^R_{tot}(\text{state2}) - \angle\vec{E}^R_{tot}(\text{state1}) = \frac{\pi}{2} + \frac{\xi_1}{2} - \xi_2 \tag{A.19}$$

Ideally, if the extra phase delay ξ_1 and ξ_2 in the switches are negligible, state 2 has a $\pi/2$ (or 90°) phase shift compared with state 1. In reality, ξ_1 and ξ_2 are small, and the value of $\xi_1/2 - \xi_2$ becomes even smaller. This implies that the phase difference between state 1 and state 2 will only slightly deviate from 90°. This can also be observed in the unit cell's reflection phase in Fig. 5.6(b), where the phase difference between state 1 and state 2 at 19 GHz is about 85°, which is very close to 90°. The working principle and relative phase shift for state 3 and state 4 can be understood in a similar manner by tracing the traveling current and their relative phase, and thus will not be repeated here.

We note here that the analysis above considers only the dominant handedness components radiated by the outward and inward traveling currents. Take the outward traveling current as an example, while they contribute dominantly to RHCP radiation, there can still be a small portion of LHCP radiation that contributes to the X-Pol of the unit cell. It can be observed that shortening the spiral arms worsens the polarization purity. This creates a lower limit of the working frequency of the element. Further, the terms ξ_1 and ξ_2 also place a potential upper limit of the working frequency of the element. This is because, at a higher frequency, the values of ξ_1 and ξ_2 become more significant and can noticeably impact the Co-Pol level and raise the X-Pol level. It can also be observed that longer spiral arms can be beneficial when larger bandwidth of X-Pol suppression is desired. The reason behind this is twofold: (1) as the spirals become longer, the traveling current radiates with better polarization purity. (2) As the spirals become longer, the currents travel longer distances, and the energy carried in the traveling currents gets effectively radiated. Therefore, less current will be reflected (α reduces) thereby resulting in lower X-Pol.

The analysis method presented here does not take into account the mutual coupling between the arms and among adjacent unit cells. Even with the idealizations, our theory predicts the reflection handedness and the phase shift between different states. While these provide general guidelines, the actual unit cell design still needs to be carefully carried out with full-wave simulations to account for all the factors that can impact the phase of the traveling currents. The details of the unit cell optimized for our targeted frequency range 17.8 - 20.2 GHz are presented in section 5.2 of the dissertation.

REFERENCES

[1] M. M. Group, *Internet World Stats*, 2020. [Online]. Available: https://www.internetworldstats.com/stats.htm

[2] T. Lee, "Global internet access from space for humanitarian applications," in *2016 IEEE International Frequency Control Symposium (IFCS)*, 2016, pp. 1–3.

[3] Z. Qu, G. Zhang, H. Cao, and J. Xie, "LEO Satellite Constellation for Internet of Things," *IEEE Access*, vol. 5, pp. 18 391–18 401, 2017.

[4] I. F. Akyildiz and A. Kak, "The Internet of Space Things / CubeSats," pp. 1–7, 2019.

[5] H. Zhou, L. Liu, and H. Ma, "Coverage and Capacity Analysis of LEO Satellite Network Supporting Internet of Things," in *ICC 2019 - 2019 IEEE International Conference on Communications (ICC)*. IEEE, 2019, pp. 1–6.

[6] SpaceX, *Starlink*, 2020. [Online]. Available: https://www.starlink.com/

[7] OneWeb, *OneWeb Satellite Constellation*, 2020. [Online]. Available: https://onewebsatellites.com/

[8] A. Gregorio and F. Alimenti, "Cubesats for future science and internet of space: Challenges and opportunities," in *2018 25th IEEE International Conference on Electronics, Circuits and Systems (ICECS)*, 2018, pp. 169–172.

[9] Y. Rahmat-Samii, V. Manohar, and J. M. Kovitz, "For satellites, think small, dream big: A review of recent antenna developments for cubesats." *IEEE Antennas Propag. Mag.*, vol. 59, no. 2, pp. 22–30, April 2017.

[10] F. E. Tubbal, R. Raad, and K. W. Chin, "A survey and study of planar antennas for pico-satellites," *IEEE Access*, vol. 3, pp. 2590–2612, 2015.

[11] R. E. Hodges, M. J. Radway, A. Toorian, D. J. Hoppe, B. Shah, and A. E. Kalman, "ISARA - Integrated Solar Array and Reflectarray CubeSat deployable Ka-band antenna," *IEEE Antennas and Propagation Society, AP-S International Symposium (Digest)*, vol. 2015-October, pp. 2141–2142, 2015.

[12] S. Gao, Y. Rahmat-Samii, R. E. Hodges, and X. Yang, "Advanced antennas for small satellites," *Proceedings of the IEEE*, vol. 106, pp. 391–403, 2018.

[13] R. E. Hodges, N. Chahat, D. J. Hoppe, and J. D. Vacchione, "A Deployable High-Gain Antenna Bound for Mars," *IEEE Antennas & Propagation Magazine*, no. April, pp. 39–49, 2017.

[14] Ramon Martinez Rodriguez-Osorio and Enrique Fueyo Ramírez, "A Hands-On Education Project: Antenna Design for Inter-CubeSat Communications [Education Column]," *IEEE Antennas and Propagation Magazine*, vol. 54, no. 5, pp. 211–224, oct 2012. [Online]. Available: http://ieeexplore.ieee.org/document/6348155/

[15] Y. Rahmat-Samii, V. Manohar, and J. M. Kovitz, "Novel antenna concepts and developments for cubesats," in *Developments in Antenna Analysis and Synthesis*, R. Mittra, Ed. IET, 2018.

[16] A. H. Lokman, P. J. Soh, S. N. Azemi, H. Lago, S. K. Podilchak, S. Chalermwisutkul, M. F. Jamlos, A. A. Al-Hadi, P. Akkaraekthalin, and S. Gao, "A Review of Antennas for Picosatellite Applications," *International Journal of Antennas and Propagation*, vol. 2017, 2017.

[17] N. Chahat, R. E. Hodges, J. Sauder, M. Thomson, E. Peral, and Y. Rahmat-Samii, "Cubesat deployable ka-band mesh reflector antenna development for earth science missions," *IEEE Trans. Antennas Propag.*, vol. 64, no. 6, pp. 2083–2093, June 2016.

[18] N. Chahat, R. E. Hodges, J. Sauder, M. Thomson, and Y. Rahmat-Samii, "The deep-space network telecommunication cubesat antenna: Using the deployable ka-band mesh reflector antenna." *IEEE Antennas and Propagation Magazine*, vol. 59, no. 2, pp. 31–38, April 2017.

[19] Y. Rahmat-Samii, V. Manohar, J. M. Kovitz, R. E. Hodges, G. Freebury, and E. Peral, "Development of highly constrained 1 m ka-band mesh deployable offset reflector antenna for next generation cubesat radars," *IEEE Trans. Antennas Propag.*, vol. 67, no. 10, pp. 6254–6266, Oct 2019.

[20] N. Chahat, E. Decrossas, D. Gonzalez-Ovejero, O. Yurduseven, M. J. Radway, R. E. Hodges, P. Estabrook, J. D. Baker, D. J. Bell, T. A. Cwik, and G. Chattopadhyay, "Advanced cubesat antennas for deep space and earth science missions: A review," *IEEE Antennas and Propagation Magazine*, vol. 61, no. 5, pp. 37–46, Oct 2019.

[21] N. Chahat, J. Sauder, M. Mitchell, N. Beidleman, and G. Freebury, "One-meter deployable mesh reflector for deep-space network telecommunication at X -band and ka -band," *IEEE Trans. Antennas Propag.*, vol. 68, no. 2, pp. 727–735, Feb 2020.

[22] J. F. Sauder, M. Arya, N. Chahat, E. Thiel, S. Dunphy, M. Shi, G. Agnes, and T. Cwik, "Deployment mechanisms for high packing efficiency one-meter reflectarray antenna (omera)," in *AIAA Scitech 2019 Forum*. [Online]. Available: https://arc.aiaa.org/doi/abs/10.2514/6.2019-0755

[23] D. Krejci and P. Lozano, "Space propulsion technology for small spacecraft," *Proceedings of the IEEE*, vol. 106, no. 3, pp. 362–378, 2018.

[24] Y. Miyazaki, "Deployable techniques for small satellites," *Proceedings of the IEEE*, vol. 106, no. 3, pp. 471–483, 2018.

[25] G.-P. Liu and S. Zhang, "A survey on formation control of small satellites," *Proceedings of the IEEE*, vol. 106, no. 3, pp. 440–457, 2018.

[26] "Tech giants race to build orbital internet [News]," *IEEE Spectrum*, vol. 55, no. 6, pp. 10–11, 2018.

[27] E. C. C. (ECC), "The use of the frequency bands 27.5-30.0 ghz and 17.3-20.2 ghz by satellite networks," Gothenburg, Tech. Rep., 2010.

[28] K. Y. Kapusuz, O. A. Civi, and A. G. Yarovoy, "A dual-band wide-angle scanning phased array antenna in K/Ka bands for satellite-on-the-move applications," in *2017 11th European Conference on Antennas and Propagation, EUCAP 2017*. IEEE, mar 2017, pp. 1898–1902. [Online]. Available: http://ieeexplore.ieee.org/document/7928682/

[29] A. Cuttin, F. Alimenti, F. Coromina, E. De Fazio, F. Dogo, M. Fragiacomo, P. Gervasoni, G. Gotti, A. Gregorio, P. Mezzanotte, E. Pagana, V. Palazzi, F. Pelusi, P. Petrini, L. Roselli, and R. V. Gatti, "A Ka-Band Transceiver for CubeSat Satellites: Feasibility Study and Prototype Development," *2018 48th European Microwave Conference, EuMC 2018*, pp. 930–933, 2018.

[30] A. Clemente, L. D. Palma, F. Diaby, L. Dussopt, K. Pham, and R. Sauleau, "Electronically-Steerable Transmitarray Antennas for Ka-Band," *13th European Conference on Antennas and Propagation, EuCAP 2019*, vol. 2, no. EuCAP, pp. 1–4, 2019.

[31] J. M. Kovitz and Y. Rahmat-Samii, "Novelties of spectral domain analysis in antenna characterizations: Concept, formulation, and applications," in *Advanced Computational Electromagnetics Methods and Applications*, A. Elsherbeni, W. Li, Y. Rahmat-Samii, and W. Yu, Eds. Artech House, 2015.

[32] Y. Rahmat-Samii and R. Haupt, "Reflector antenna developments: A perspective on the past, present and future," *IEEE Antennas and Propagation Magazine*, vol. 57, no. 2, pp. 85–95, April 2015.

[33] Y. Rahmat-Samii, "Reflector antennas," in *Antenna handbook*, Y. Lo and S. Lee, Eds. New York: Van nostrand reinhold, 1993, ch. 15.

[34] "Physical oceanography distrubited active archive center, nasa jet propsultion laboratory," https://podaac.jpl.nasa.gov/QuikSCAT, accessed: 01-18-2019.

[35] W. Hong, Z. H. Jiang, C. Yu, J. Zhou, P. Chen, Z. Yu, H. Zhang, B. Yang, X. Pang, M. Jiang, Y. Cheng, M. K. Al-Nuaimi, Y. Zhang, J. Chen, and S. He, "Multibeam Antenna Technologies for 5G Wireless Communications," *IEEE Trans. Antennas Propag.*, vol. 65, no. 12, pp. 6231–6249, 2017.

[36] G. Buttazzoni, M. Comisso, A. Cuttin, M. Fragiacomo, R. Vescovo, and R. Vincenti Gatti, "Reconfigurable phased antenna array for extending cubesat operations to Ka-band: Design and feasibility," *Acta Astronautica*, vol. 137, pp. 114–121, Aug 2017.

[37] J. Budhu and Y. Rahmat-Samii, "A novel and systematic approach to inhomogeneous dielectric lens design based on curved ray geometrical optics and particle swarm optimization," *IEEE Trans. Antennas Propag.*, vol. 67, no. 6, pp. 3657–3669, June 2019.

[38] J. Budhu, Y. Rahmat-Samii, R. E. Hodges, D. C. Hofmann, D. F. Ruffatto, and K. C. Carpenter, "Three-dimensionally printed, shaped, engineered material inhomogeneous lens antennas for next-generation spaceborne weather radar systems," *IEEE Antennas and Wireless Propag. Lett.*, vol. 17, no. 11, pp. 2080–2084, 2018.

[39] A. Papathanasopoulos, Y. Rahmat-Samii, N. C. Garcia, and J. D. Chisum, "A novel collapsible flat-layered metamaterial gradient-refractive-index lens antenna," *IEEE Trans. Antennas Propag.*, vol. 68, no. 3, pp. 1312–1321, March 2020.

[40] P. Nayeri, F. Yang, and A. Z. Elsherbeni, "Beam-scanning reflectarray antennas: A technical overview and state of the art," *IEEE Antennas Propag. Mag.*, vol. 57, no. 4, pp. 32–47, 2015.

[41] S. V. Hum and J. Perruisseau-Carrier, "Reconfigurable Reflectarrays and Array Lenses for Dynamic Antenna Beam Control: A Review," *IEEE Trans. Antennas Propag.*, vol. 62, no. 1, pp. 183–198, Jan 2014. [Online]. Available: http://ieeexplore.ieee.org/document/6648436/

[42] J. R. Reis, M. Vala, and R. F. S. Caldeirinha, "Review Paper on Transmitarray Antennas," *IEEE Access*, vol. 7, pp. 94 171–94 188, 2019.

[43] J. P. Gianvittorio and Y. Rahmat-Samii, "Reconfigurable patch antennas for steerable reflectarray applications," *IEEE Trans. Antennas Propag.*, vol. 54, no. 5, pp. 1388–1392, 2006.

[44] X. Yang, S. Xu, F. Yang, M. Li, H. Fang, Y. Hou, S. Jiang, and L. Liu, "A Mechanically Reconfigurable Reflectarray with Slotted Patches of Tunable Height," *IEEE Antennas Wirel. Propag. Lett.*, vol. 17, no. 4, pp. 555–558, 2018.

[45] C. Li, S. Xu, F. Yang, and M. Li, "Design and Optimization of a Mechanically Reconfigurable Reflectarray Antenna with Pixel Patch Elements Using Genetic Algorithm," *2019 IEEE MTT-S International Wireless Symposium (IWS)*, vol. 1, pp. 1–3, 2019.

[46] P. Naseri, S. A. Matos, J. R. Costa, and C. A. Fernandes, "Phase-Delay Versus Phase-Rotation Cells for Circular Polarization Transmit Arrays Application to Satellite Ka-Band Beam Steering," *IEEE Trans. Antennas Propag.*, vol. 66, no. 3, pp. 1236–1247, mar 2018. [Online]. Available: http://ieeexplore.ieee.org/document/8240664/

[47] L. Zhang, S. Gao, Q. Luo, W. Li, Y. He, and Q. Li, "Single-Layer Wideband Circularly Polarized Satellite Communications," vol. 65, no. 9, pp. 4529–4538, 2017.

[48] X. Yang, S. Xu, F. Yang, M. Li, Y. Hou, S. Jiang, and L. Liu, "A Broadband High-Efficiency Reconfigurable Reflectarray Antenna Using Mechanically Rotational Elements," *IEEE Trans. Antennas Propag.*, vol. 65, no. 8, pp. 3959–3966, 2017.

[49] N. Gagnon and A. Petosa, "Using rotatable planar phase shifting surfaces to steer a high-gain beam," *IEEE Trans. Antennas and Propag.*, vol. 61, no. 6, pp. 3086–3092, 2013.

[50] M. U. Afzal and K. P. Esselle, "Steering the Beam of Medium-to-High Gain Antennas Using Near-Field Phase Transformation," *IEEE Trans. Antennas Propag.*, vol. 65, no. 4, pp. 1680–1690, apr 2017. [Online]. Available: http://ieeexplore.ieee.org/document/7857713/

[51] T. Lou, X.-X. Yang, H. Qiu, Z. Yin, and S. Gao, "Compact Dual-Polarized Continuous Transverse Stub Array with Two-Dimension Beam Scanning," *IEEE Trans. Antennas Propag.*, vol. PP, no. c, pp. 1–1, 2019.

[52] M. U. Afzal, A. Lalbakhsh, and K. P. Esselle, "Electromagnetic-wave beam-scanning antenna using near-field rotatable graded-dielectric plates," *Journal of Applied Physics*, vol. 124, no. 23, 2018.

[53] "Antenna beam steering technique using dielectric wedges," *IEEE Proceed. Microw., Antennas Propag.*, vol. 136, no. 2, p. 126, 1989. [Online]. Available: http://digital-library.theiet.org/content/journals/10.1049/ip-h-2.1989.0023

[54] E. B. Lima, S. A. Matos, J. R. Costa, C. A. Fernandes, and N. J. Fonseca, "Circular Polarization Wide-Angle Beam Steering at Ka-Band by In-Plane Translation of a Plate Lens Antenna," *IEEE Trans. Antennas Propag.*, vol. 63, no. 12, pp. 5443–5455, 2015.

[55] S. R. Rengarajan, "Scanning and defocusing characteristics of microstrip reflectarrays," *IEEE Antennas Wirel. Propag. Lett.*, vol. 9, pp. 163–166, 2010.

[56] G. B. Wu, S. W. Qu, and S. Yang, "Wide-Angle Beam-Scanning Reflectarray with Mechanical Steering," *IEEE Trans. Antennas Propag.*, vol. 66, no. 1, pp. 172–181, 2018.

[57] H. Yang, F. Yang, S. Xu, M. Li, X. Cao, J. Gao, and Y. Zheng, "A Study of Phase Quantization Effects for Reconfigurable Reflectarray Antennas," *IEEE Antennas Wireless Propag. Lett.*, vol. 16, pp. 302–305, 2017.

[58] S. V. Hum, M. Okoniewski, and R. J. Davies, "Modeling and design of electronically tunable reflectarrays," *IEEE Trans. Antennas Propag.*, vol. 55, no. 8, pp. 2200–2210, 2007.

[59] J. Y. Lau and S. V. Hum, "A planar reconfigurable aperture with lens and reflectarray modes of operation," *IEEE Transactions on Microwave Theory and Techniques*, vol. 58, no. 12 PART 1, pp. 3547–3555, 2010.

[60] P. Padilla, A. Muñoz-Acevedo, M. Sierra-Castañer, and M. Sierra-Pérez, "Electronically reconfigurable transmitarray at Ku band for microwave applications," *IEEE Trans. Antennas Propag.*, vol. 58, no. 8, pp. 2571–2579, 2010.

[61] C. Huang, W. Pan, X. Ma, B. Zhao, J. Cui, and X. Luo, "Using Reconfigurable Transmitarray to Achieve Beam-Steering and Polarization Manipulation Applications," *IEEE Trans. Antennas Propag.*, vol. 63, no. 11, pp. 4801–4810, 2015.

[62] T. Jiang, Z. Wang, D. Li, J. Pan, B. Zhang, J. Huangfu, Y. Salamin, C. Li, and L. Ran, "Low-DC voltage-controlled steering-antenna radome utilizing tunable active metamaterial," *IEEE Transactions on Microwave Theory and Techniques*, vol. 60, no. 1, pp. 170–178, 2012.

[63] J. R. Reis, R. F. Caldeirinha, A. Hammoudeh, and N. Copner, "Electronically Reconfigurable FSS-Inspired Transmitarray for 2-D Beamsteering," *IEEE Trans. Antennas Propag.*, vol. 65, no. 9, pp. 4880–4885, 2017.

[64] M. Frank, F. Lurz, R. Weigel, and A. Koelpin, "Electronically Reconfigurable 6 x 6 Element Transmitarray at K-Band Based on Unit Cells With Continuous Phase Range," *IEEE Antennas Wirel. Propag. Lett.*, vol. 18, no. 4, pp. 796–800, 2019.

[65] C. Liu and S. V. Hum, "An electronically tunable single-layer reflectarray antenna element with improved bandwidth," *IEEE Antennas Wirel. Propag. Lett.*, vol. 9, pp. 1241–1244, 2010.

[66] G. Liu, H. Wang, F. Xue, D. Zhu, and X. Dong, "A wideband reconfigurable reflectarray antenna using single-layer varactor-loaded split patch elements," *IET Conference Publications*, vol. 2018, no. CP741, pp. 13–16, 2018.

[67] C. Huang, W. Pan, and X. Luo, "Low-Loss Circularly Polarized Transmitarray for Beam Steering Application," *IEEE Trans. Antennas Propag.*, vol. 64, no. 10, pp. 4471–4476, 2016.

[68] Y. Wang, S. Xu, F. Yang, and M. Li, "Design of a 1-bit Reconfigurable Transmitarray Element Using an Equivalent Magnetic Dipole," *2018 IEEE Antennas and Propagation Society International Symposium and USNC/URSI National Radio Science Meeting, APSURSI 2018 - Proceedings*, pp. 481–482, 2018.

[69] Y. Zhong, H. Luyen, and N. Behdad, "Electronically Reconfigurable Reflectarray Antenna," *2019 13th European Conference on Antennas and Propagation (EuCAP)*, no. EuCAP, pp. 1–3, 2019.

[70] J. Han, L. Li, G. Liu, Z. Wu, and S. Yan, "A Wideband 1-Bit 12 x 12 Reconfigurable Beam-Scanning Reflectarray: Design, Fabrication, and Measurement," *IEEE Antennas Wirel. Propag. Lett.*, vol. 18, no. 6, pp. 1–1, 2019.

[71] H. Kamoda, T. Iwasaki, J. Tsumochi, and T. Kuki, "60-GHz Electronically Reconfigurable Large Reflectarray Using Single-Bit Phase Shifters," *IEEE Trans. Antennas Propag.*, vol. 59, no. 7, pp. 2524–2531, 2011.

[72] A. Clemente, L. Dussopt, R. Sauleau, P. Potier, and P. Pouliguen, "Wideband 400-element electronically reconfigurable transmitarray in X band," *IEEE Trans. Antennas Propag.*, vol. 61, no. 10, pp. 5017–5027, 2013.

[73] H. Yang, F. Yang, S. Xu, Y. Mao, M. Li, X. Cao, and J. Gao, "A 1-Bit 10 x 10 Reconfigurable Reflectarray Antenna: Design, Optimization, and Experiment," *IEEE Trans. Antennas Propag.*, vol. 64, no. 6, pp. 2246–2254, 2016.

[74] H. Yang, F. Yang, X. Cao, S. Xu, J. Gao, X. Chen, M. Li, and T. Li, "A 1600-element dual-frequency electronically reconfigurable reflectarray at X/Ku-band," *IEEE Trans. Antennas Propag.*, vol. 65, no. 6, pp. 3024–3032, 2017.

[75] M. Wang, S. Xu, F. Yang, and M. Li, "Design and Measurement of a 1-bit Reconfigurable Transmitarray with Subwavelength H-Shaped Coupling Slot Elements," *IEEE Trans. Antennas Propag.*, vol. 67, no. 5, pp. 3500–3504, 2019.

[76] ——, "A 1-Bit Bidirectional Reconfigurable Transmit-Reflect-Array Antenna Using a Single-Layer Slot Element with PIN Diodes," *IEEE Trans. Antennas Propag.*, vol. 67, no. 9, pp. 1–1, 2019.

[77] B. D. Nguyen and C. Pichot, "Unit-Cell Loaded with PIN Diodes for 1-Bit Linearly Polarized Reconfigurable Transmitarrays," *IEEE Antennas Wirel. Propag. Lett.*, vol. 18, no. 1, pp. 98–102, 2019.

[78] L. Dussopt, L. Di Palma, P. Pouliguen, A. Clemente, P. Potier, and R. Sauleau, "Circularly-Polarized Reconfigurable Transmitarray in Ka-Band With Beam Scanning and Polarization Switching Capabilities," *IEEE Trans. Antennas Propag.*, vol. 65, no. 2, pp. 529–540, 2016.

[79] X. Yang, S. Xu, F. Yang, and M. Li, "A novel 2-bit reconfigurable reflectarray element for both linear and circular polarizations," *2017 IEEE Antennas and Propagation Society International Symposium, Proceedings*, vol. 2017-Janua, pp. 2083–2084, 2017.

[80] F. Diaby, A. Clemente, L. Di Palma, L. Dussopt, K. Pham, E. Fourn, and R. Sauleau, "Design of a 2-bit unit-cell for electronically reconfigurable transmitarrays at Ka-band," in *European Microwave Week 2017: "A Prime Year for a Prime Event", EuMW 2017 - Conference Proceedings; 47th European Microwave Conference, EuMC 2017*, vol. 2017-Janua. IEEE, oct 2017, pp. 1321–1324. [Online]. Available: http://ieeexplore.ieee.org/document/8231095/

[81] H. R. Phelan, "L-band Spiraphase reflectarray," *Microw. J.*, vol. 20, pp. 47–50, Jan 1977.

[82] J. Rodriguez-Zamudio, J. I. Martinez-Lopez, J. Rodriguez-Cuevas, and A. E. Martynyuk, "Reconfigurable reflectarrays based on optimized spiraphase-type elements," *IEEE Trans. Antennas Propag.*, vol. 60, no. 4, pp. 1821–1830, 2012.

[83] J. Silva-Montero, J. I. Martinez-Lopez, J. Rodriguez-Cuevas, and A. E. Martynyuk, "Spiraphase-type reflectarray for large reflection elevation angles," *IEEE Trans. Antennas Propag.*, vol. 63, no. 10, pp. 4342–4351, 2015.

[84] H. Rajagopalan, Y. Rahmat-Samii, and W. A. Imbriale, "RF MEMS actuated reconfigurable reflectarray patch-slot element," *IEEE Trans. Antennas Propag.*, vol. 56, no. 12, pp. 3689–3699, 2008.

[85] B. Wu, A. Sutinjo, M. E. Potter, and M. Okoniewski, "On the selection of the number of bits to control a dynamic digital MEMS reflectarray," *IEEE Antennas Wirel. Propag. Lett.*, vol. 7, pp. 183–186, 2008.

[86] J. Perruisseau-Carrier and A. K. Skrivervik, "Monolithic MEMS-based reflectarray cell digitally reconfigurable over a 360° phase range," *IEEE Antennas Wirel. Propag. Lett.*, vol. 7, pp. 138–141, 2008.

[87] T. Debogovic and J. Perruisseau-Carrier, "Low loss MEMS-reconfigurable 1-bit reflectarray cell with dual-linear polarization," *IEEE Trans. Antennas Propag.*, vol. 62, no. 10, pp. 5055–5060, 2014.

[88] H. Moghadas, M. Daneshmand, P. Mousavi, M. R. Chaharmir, and J. Shaker, "Monolithic-Integrated MEMS-Tunable Reflective Cell for Ku-Band Mobile Satellite Two-Way Connectivity," *IEEE Trans. Antennas Propag.*, vol. 63, no. 4, pp. 1384–1392, 2015.

[89] O. Bayraktar, O. A. Civi, and T. Akin, "Beam switching reflectarray monolithically integrated with RF MEMS switches," *IEEE Trans. Antennas Propag.*, vol. 60, no. 2 PART 2, pp. 854–862, 2012.

[90] A. Gaebler, A. Moessinger, F. Goelden, A. Manabe, M. Goebel, R. Follmann, D. Koether, C. Modes, A. Kipka, M. Deckelmann, T. Rabe, B. Schulz, P. Kuchenbecker, A. Lapanik, S. Mueller, W. Haase, and R. Jakoby, "Liquid Crystal-Reconfigurable Antenna Concepts for Space Applications at Microwave and Millimeter Waves," *International Journal of Antennas and Propagation*, vol. 2009, pp. 1–7, 2009.

[91] O. H. Karabey, S. Bildik, S. Bausch, S. Strunck, A. Gaebler, and R. Jakoby, "Continuously polarization agile antenna by using liquid crystal-based tunable variable delay lines," *IEEE Trans. Antennas Propag.*, vol. 61, no. 1, pp. 70–76, 2013.

[92] S. Bildik, S. Dieter, C. Fritzsch, W. Menzel, and R. Jakoby, "Reconfigurable folded reflectarray antenna based upon liquid crystal technology," *IEEE Trans. Antennas Propag.*, vol. 63, no. 1, pp. 122–132, 2015.

[93] J. Perruisseau-Carrier, "Graphene for antenna applications: Opportunities and challenges from microwaves to THz," *LAPC 2012 - 2012 Loughborough Antennas and Propagation Conference*, no. November, pp. 1–4, 2012.

[94] "Graphene antennas: Can integration and reconfigurability compensate for the loss?" *European Microwave Week 2013, EuMW 2013 - Conference Proceedings; EuMC 2013: 43rd European Microwave Conference*, pp. 369–372, 2013.

[95] E. Carrasco and J. Perruisseau-Carrier, "Reflectarray antenna at terahertz using graphene," *IEEE Antennas Wirel. Propag. Lett.*, vol. 12, pp. 253–256, 2013.

[96] Z. Miao, Q. Wu, X. Li, Q. He, K. Ding, Z. An, Y. Zhang, and L. Zhou, "Widely tunable terahertz phase modulation with gate-controlled graphene metasurfaces," *Physical Review X*, vol. 5, no. 4, pp. 1–2, 2015.

[97] Z. Chang, B. You, L. S. Wu, M. Tang, Y. P. Zhang, and J. F. Mao, "A Reconfigurable Graphene Reflectarray for Generation of Vortex THz Waves," *IEEE Antennas Wirel. Propag. Lett.*, vol. 15, pp. 1537–1540, 2016.

[98] "Thermal tuning of mid-infrared plasmonic antenna arrays using a phase change material," *Optics Letters*, vol. 38, no. 3, p. 368, 2013.

[99] "VO2-Based Reconfigurable Antenna Platform with Addressable Microheater Matrix," *Advanced Electronic Materials*, vol. 3, no. 9, pp. 1–8, 2017.

[100] L. Huitema, A. Crunteanu, and H. Wong, "Highly integrated VO2-based antenna for frequency tunability at millimeter-wave frequencies," in *2016 International Workshop on Antenna Technology (iWAT)*. IEEE, feb 2016, pp. 40–43. [Online]. Available: http://ieeexplore.ieee.org/document/7434795/

[101] T. F. Gallacher, D. A. Robertson, and G. M. Smith, "The photo-injected fresnel zone plate antenna: Optoelectronic beam steering at mm-wave frequencies," *IEEE Trans. Antennas Propag.*, vol. 61, no. 4, pp. 1688–1696, 2013.

[102] P. Alizadeh, A. S. Andy, C. Parini, and K. Z. Rajab, "A reconfigurable reflectarray antenna in Ka-band using optically excited silicon," *2016 10th European Conference on Antennas and Propagation, EuCAP 2016*, vol. 1, pp. 1–5, 2016.

[103] D. Kumar, A. S. Siddiqui, H. P. Singh, M. R. Tripathy, and A. Sharma, "A Review: Techniques and Methodologies Adopted for Reconfigurable Antennas," *2018 International Conference on Sustainable Energy, Electronics and coMputing System, SEEMS 2018*, pp. 1–6, 2019.

[104] J. M. Kovitz, H. Rajagopalan, and Y. Rahmat-Samii, "Practical and cost-effective bias line implementations for reconfigurable antennas," *IEEE Antennas Wirel. Propag. Lett.*, vol. 11, pp. 1556–1559, 2012.

[105] W. A. Imbriale, S. S. Gao, and L. Boccia, Eds., *Space Antenna Handbook*. Wiley, may 2012. [Online]. Available: https://onlinelibrary.wiley.com/doi/book/10.1002/9781119945147

[106] "Sending circuit materials into space," https://www.microwavejournal.com/blogs/1-rog-blog/post/21651-sending-circuit-materials-into-space, accessed: 2020-03-15.

[107] L. Zhang, S. Gao, Q. Luo, P. R. Young, W. Li, and Q. Li, "Inverted-s antenna with wideband circular polarization and wide axial ratio beamwidth," *IEEE Trans. Antennas Propag.*, vol. 65, no. 4, pp. 1740–1748, 2017.

[108] P. Naseri, S. A. Matos, J. R. Costa, and C. A. Fernandes, "Phase-delay versus phase-rotation cells for circular polarization transmit arrays—application to satellite ka-band beam steering," *IEEE Trans. Antennas Propag.*, vol. 66, no. 3, pp. 1236–1247, 2018.

[109] J. Wang, "Characteristics of a new class of diode-switched integrated antenna phase shifter," *IEEE Trans. Antennas Propag.*, vol. 31, no. 1, pp. 156–159, jan 1983. [Online]. Available: http://ieeexplore.ieee.org/document/1143014/

[110] J. Huang and R. Pogorzelski, "A ka-band microstrip reflectarray with elements having variable rotation angles," *IEEE Trans. Antennas Propag.*, vol. 46, no. 5, pp. 650–656, 1998.

[111] J. Wang, V. Manohar, and Y. Rahmat-Samii, "Enabling the internet of things with cubesats: A review of representative beamsteerable antenna concepts," *IEEE Antennas Propag. Mag.*, vol. 63, no. 6, pp. 14–28, 2021.

[112] K. Singh, M. U. Afzal, and K. P. Esselle, "Designing efficient phase-gradient metasurfaces for near-field meta-steering systems," *IEEE Access*, vol. 9, pp. 109 080–109 093, 2021.

[113] Y. C. Zhong, Y. J. Cheng, and S. Member, "Generating and Steering Quasi-Non-Diffractive Beam by Near-Field Planar Risley Prisms," *IEEE Trans. Antennas Propag.*, vol. 68, no. c, pp. 7767–7776, 2020.

[114] Y. Sun, J. He, C. Yuan, Q. Zhang, X. Zhao, and L. Yu, "Ku-band radial-line continuous transverse stub antenna with transmit-array lens for high-power microwave application," *IEEE Trans. Antennas Propag.*, vol. 68, no. 3, pp. 2050–2059, 2020.

[115] M. U. Afzal, K. P. Esselle, and M. N. Y. Koli, "A beam-steering solution with highly transmitting hybrid metasurfaces and circularly polarized high-gain radial-line slot array antennas," *IEEE Trans. Antennas Propag.*, vol. 70, no. 1, pp. 365–377, 2022.

[116] K. Debbarma, N. Truong, S. K. Sharma, and J.-C. S. Chieh, "2-d beam steering performance of a triple mode horn antenna integrated with risley prism and phase correcting surface," *IEEE Open Journal of Antennas and Propagation*, vol. 3, pp. 752–761, 2022.

[117] Z. Zhang, Y. C. Zhong, H. Luyen, J. H. Booske, and N. Behdad, "A low-profile, risley-prism-based, beam-steerable antenna employing a single flat prism," *IEEE Trans. Antennas Propag.*, pp. 1–1, 2022.

[118] J. Wang and Y. Rahmat-Samii, "A simplified configuration of beam steerable risley prism antennas: Principles and validation," *IEEE Antennas Wirel. Propag. Lett.*, pp. 1–5, 2022.

[119] A. Li, *Double-Prism Multi-mode Scanning: Principles and Technology.* Springer, 2018, vol. 216.

[120] Y. Sun, F. Dang, C. Yuan, J. He, Q. Zhang, and X. Zhao, "A Beam-steerable Lens Antenna for Ku-band High-Power Microwave Applications," *IEEE Trans. Antennas Propag.*, no. c, pp. 1–1, 2020.

[121] Y. Yang, "Analytic solution of free space optical beam steering using risley prisms," *Journal of Lightwave Technology*, vol. 26, no. 21, pp. 3576–3583, 2008.

[122] Y. Lu, Y. Zhou, M. Hei, and D. Fan, "Theoretical and experimental determination of steering mechanism for risley prism systems," *Appl. Opt.*, vol. 52, no. 7, pp. 1389–1398, Mar 2013.

[123] J. Wang and Y. Rahmat-Samii, "Phase method: A more precise beam steering model for phase-delay metasurface based risley antenna," in *2019 URSI International Symposium on Electromagnetic Theory (EMTS)*, 2019, pp. 1–4.

[124] Y. Rahmat-Samii and Shung-Wu Lee, "Directivity of planar array feeds for satellite reflector applications," *IEEE Trans. Antennas Propag.*, vol. 31, no. 3, pp. 463–470, 1983.

[125] M. N. Y. Koli, M. U. Afzal, K. P. Esselle, and R. M. Hashmi, "A radial line slot-array antenna with low side lobes and a uniform-phase, tapered-amplitude aperture field distribution," *IEEE Access*, vol. 8, pp. 208 532–208 542, 2020.

[126] E. B. Lima, S. A. Matos, J. R. Costa, C. A. Fernandes, and N. J. G. Fonseca, "Circular polarization wide-angle beam steering at ka-band by in-plane translation of a plate lens antenna," *IEEE Trans. Antennas Propag.*, vol. 63, no. 12, pp. 5443–5455, 2015.

[127] S. A. Matos, J. R. Costa, E. B. Lima, P. Naseri, C. A. Fernandes, and N. J. Fonseca, "Wide-angle mechanical scanning Transmit-arrays for Satellite Ka-band user terminals," *2018 IEEE Antennas and Propagation Society International Symposium and USNC/URSI National Radio Science Meeting, APSURSI 2018 - Proceedings*, pp. 1445–1446, 2018.

[128] Q. Tang, B. H. Mcguyer, E. Booen, S. Saraswat, F. Tabatabai, H. Bolandhemmat, C. Von Badinski, and W. H. Theunissen, "Flat-panel mechanical beam steerable array antennas with in-plane rotations: Theory, design and low-cost implementation," *IEEE Open J. Antennas Propag.*, vol. 2, pp. 679–688, 2021.

[129] J. M. Kovitz and Y. Rahmat-Samii, "Using thick substrates and capacitive probe compensation to enhance the bandwidth of traditional cp patch antennas," *IEEE Trans. Antennas Propag.*, vol. 62, no. 10, pp. 4970–4979, 2014.

[130] F. Diaby, L. Di Palma, A. Clemente, L. Dussopt, K. Pham, E. Fourn, and R. Sauleau, "2-bit reconfigurable circularly-polarized unit-cell at ka-band," in *12th European Conference on Antennas and Propagation (EuCAP 2018)*, 2018, pp. 1–3.

[131] H. R. Phelan, "Spiraphase - A new, low cost, lightweight phased array. I," *Microw. J.*, vol. 19, pp. 41–44, Dec 1976.

[132] Z. H. Jiang, L. Kang, T. Yue, W. Hong, and D. H. Werner, "Wideband Transmit-Arrays Based on Anisotropic Impedance Surfaces for Circularly-Polarized Single-Feed Multibeam Generation in the Q-band," *IEEE Trans. Antennas Propag.*, vol. 68, no. 1, pp. 1–1, 2019.

[133] R. J. Mailloux, "Phased array antenna handbook," pp. 15–61, 375–399, 2017.

[134] Y. Rahmat-Samii and S.-W. Lee, "Directivity of planar array feeds for satellite reflector applications," *IEEE Trans. Antennas Propag.*, vol. 31, no. 3, pp. 463–470, 1983.

[135] J. M. Kovitz, Y. Rahmat-Samii, and J. Choi, "Dispersion engineered right/left-handed transmission lines enabling near-octave bandwidths for wideband cp patch arrays," in *2015 IEEE International Symposium on Antennas and Propagation USNC/URSI National Radio Science Meeting*, 2015, pp. 2525–2526.

[136] MACOM, *MACOM MA4AGFCP910*, 2023. [Online]. Available: https://www.macom.com/products/product-detail/MA4AGFCP910

[137] A. Clemente, L. Dussopt, R. Sauleau, P. Potier, and P. Pouliguen, "1-bit reconfigurable unit cell based on pin diodes for transmit-array applications in x-band," *IEEE Trans. Antennas Propag.*, vol. 60, no. 5, pp. 2260–2269, 2012.

[138] D. Wang, L.-Z. Yin, T.-J. Huang, F.-Y. Han, Z.-W. Zhang, Y.-H. Tan, and P.-K. Liu, "Design of a 1 bit broadband space-time-coding digital metasurface element," *IEEE Antennas Wirel. Propag. Lett.*, vol. 19, no. 4, pp. 611–615, 2020.

[139] L. Di Palma, A. Clemente, L. Dussopt, R. Sauleau, P. Potier, and P. Pouliguen, "Experimental Characterization of a Circularly-Polarized 1-Bit Unit-Cell for Beam Steerable Transmitarrays at Ka-Band," *IEEE Trans. Antennas Propag.*, vol. 67, no. 2, pp. 1300–1305, 2018.

[140] P. Hannan and M. Balfour, "Simulation of a phased-array antenna in waveguide," *IEEE Trans. Antennas Propag.*, vol. 13, no. 3, pp. 342–353, 1965.

[141] C. Huang, W. Pan, X. Ma, and X. Luo, "1-Bit Reconfigurable Circularly Polarized Transmitarray in X-Band," *IEEE Antennas Wirel. Propag. Lett.*, vol. 15, pp. 448–451, 2016.

[142] Y. J. Guo and R. W. Ziolkowski, *Advanced Antenna Array Engineering for 6G and Beyond Wireless Communications*. Wiley-IEEE Press, 2022.

[143] M. Z. Chowdhury, M. Shahjalal, S. Ahmed, and Y. M. Jang, "6g wireless communication systems: Applications, requirements, technologies, challenges, and research directions," *IEEE Open Journal of the Communications Society*, vol. 1, pp. 957–975, 2020.

[144] B. J. Xiang, X. Dai, and K.-M. Luk, "A wideband low-cost reconfigurable reflectarray antenna with 1-bit resolution," *IEEE Trans. Antennas Propag.*, vol. 70, no. 9, pp. 7439–7447, 2022.

[145] F. Wu, R. Lu, J. Wang, Z. H. Jiang, W. Hong, and K.-M. Luk, "A circularly polarized 1 bit electronically reconfigurable reflectarray based on electromagnetic element rotation," *IEEE Trans. Antennas Propag.*, vol. 69, no. 9, pp. 5585–5595, 2021.

[146] X. Yang, S. Xu, F. Yang, and M. Li, "A novel 2-bit reconfigurable reflectarray element for both linear and circular polarizations," in *2017 IEEE International Symposium on Antennas and Propagation USNC/URSI National Radio Science Meeting*, 2017, pp. 2083–2084.

[147] J. Wang, V. Manohar, and Y. Rahmat-Samii, "K-band circularly polarized beam steerable reflectarray enabling internet of space: Conceptualization and validation," *IEEE Trans. Antennas Propag.*, vol. 70, no. 8, pp. 6703–6717, 2022.

[148] X. Yang, S. Xu, F. Yang, and M. Li, "Design of a 2-bit reconfigurable reflectarray element using two mems switches," in *2015 IEEE International Symposium on Antennas and Propagation & USNC/URSI National Radio Science Meeting*, 2015, pp. 2167–2168.

[149] B. D. Nguyen, V.-S. Tran, L. Mai, and P. Dinh-Hoang, "A two-bit reflectarray element using cut-ring patch coupled to delay lines," *REV Journal on Electronics and Communications*, vol. 6, no. 1-2, 2016.

[150] L. Liu, F. Yang, S. Xu, and M. Li, "A 2-bit reconfigurable reflectarray unit design using only 2 pin diodes," in *2022 IEEE MTT-S International Microwave Workshop Series on Advanced Materials and Processes for RF and THz Applications (IMWS-AMP)*, 2022, pp. 1–2.

[151] P. C. Theofanopoulos and G. C. Trichopoulos, "A novel 2-bit graphene reconfigurable reflectarray," in *2020 IEEE International Symposium on Antennas and Propagation and North American Radio Science Meeting*, 2020, pp. 1701–1702.

[152] J. Robinson and Y. Rahmat-Samii, "Particle swarm optimization in electromagnetics," *IEEE Trans. Antennas Propag.*, vol. 52, no. 2, pp. 397–407, 2004.

[153] N. Jin and Y. Rahmat-Samii, "Advances in particle swarm optimization for antenna designs: Real-number, binary, single-objective and multiobjective implementations," *IEEE Trans. Antennas Propag.*, vol. 55, no. 3, pp. 556–567, 2007.

[154] R. Pereira, R. Gillard, R. Sauleau, P. Potier, T. Dousset, and X. Delestre, "Dual linearly-polarized unit-cells with nearly 2-bit resolution for reflectarray applications in x-band," *IEEE Trans. Antennas Propag.*, vol. 60, no. 12, pp. 6042–6048, 2012.

[155] J. Huang and J. A. Encinar, *Reflectarray Antennas*. Wiley-IEEE Press, 2008.

[156] J. Kennedy and R. Eberhart, "A discrete binary version of the particle swarm algorithm," in *1997 IEEE International Conference on Systems, Man, and Cybernetics. Computational Cybernetics and Simulation*, vol. 5, 1997, pp. 4104–4108 vol.5.

[157] A. K. Bhattacharyya, *Phased array antennas: Floquet analysis, synthesis, BFNs and active array systems*. John Wiley & Sons, 2006, vol. 179.

[158] R. Hensleigh, H. Cui, Z. Xu, J. Massman, D. Yao, J. Berrigan, and X. Zheng, "Charge-programmed three-dimensional printing for multi-material electronic devices," *Nat. Electron.*, vol. 3, pp. 1–9, 04 2020.

[159] Anycubic 3d printing xxxxx. [Online]. Available: https://www.anycubic.com/products/anycubic-photon-s

[160] Z. Xu, C. S. Ha, R. Kadam, J. Lindahl, S. Kim, H. F. Wu, V. Kunc, and X. Zheng, "Additive manufacturing of two-phase lightweight, stiff and high damping carbon fiber reinforced polymer microlattices," *Addit. Manuf.*, vol. 32, 03 2020.

[161] D. Helena, A. Ramos, T. Varum, and J. N. Matos, "Antenna design using modern additive manufacturing technology: A review," *IEEE Access*, vol. 8, pp. 177 064–177 083, 2020.

[162] K. Kotzé and J. Gilmore, "Slm 3d-printed horn antenna for satellite communications at x-band," in *2019 IEEE-APS Topical Conference on Antennas and Propagation in Wireless Communications (APWC)*, 2019, pp. 148–153.

[163] M. J. Veljovic and A. K. Skrivervik, "Circularly polarized axially corrugated feed horn for cubesat reflectarray applications," in *2020 14th European Conference on Antennas and Propagation (EuCAP)*, 2020, pp. 1–4.

[164] N. Luo, G. Mishra, S. K. Sharma, and X. Yu, "Experimental verification of 3d metal printed dual circular-polarized horn antenna at v-band," in *2019 Antenna Measurement Techniques Association Symposium (AMTA)*, 2019, pp. 1–6.

[165] A. Reinhardt, M. Möbius-Labinski, C. Asmus, A. Bauereiss, and M. Höft, "Additive manufacturing of 300 ghz corrugated horn antennas," in *2019 IEEE MTT-S International Microwave Workshop Series on Advanced Materials and Processes for RF and THz Applications (IMWS-AMP)*, 2019, pp. 40–42.

[166] E. G. Geterud, P. Bergmark, and J. Yang, "Lightweight waveguide and antenna components using plating on plastics," in *2013 7th European Conference on Antennas and Propagation (EuCAP)*, 2013, pp. 1812–1815.

[167] P. T. Timbie, J. Grade, D. van der Weide, B. Maffei, and G. Pisano, "Stereolithographed mm-wave corrugated horn antennas," in *2011 International Conference on Infrared, Millimeter, and Terahertz Waves*, 2011, pp. 1–3.

[168] J.-C. S. Chieh, B. Dick, S. Loui, and J. D. Rockway, "Development of a ku-band corrugated conical horn using 3-d print technology," *IEEE Antennas and Wireless Propag. Lett.*, vol. 13, pp. 201–204, 2014.

[169] J. S. Silva, M. García-Vigueras, T. Debogović, J. R. Costa, C. A. Fernandes, and J. R. Mosig, "Stereolithography-based antennas for satellite communications in ka-band," *Proc. of the IEEE*, vol. 105, no. 4, pp. 655–667, 2017.

[170] A. Macor, E. De Rijk, S. Alberti, T. Goodman, and J.-P. Ansermet, "Note: Three-dimensional stereolithography for millimeter wave and terahertz applications," *Rev. Sci. Instrum.*, vol. 83, no. 4, p. 046103, 2012.

[171] A. I. Dimitriadis, T. Debogović, M. Favre, M. Billod, L. Barloggio, J.-P. Ansermet, and E. De Rijk, "Polymer-based additive manufacturing of high-performance waveguide and antenna components," *Proc. of the IEEE*, vol. 105, no. 4, pp. 668–676, 2016.

[172] J. Teniente, J. C. Iriarte, R. Caballero, D. Valcázar, M. Goñi, and A. Martínez, "3-d printed horn antennas and components performance for space and telecommunications," *IEEE Antennas and Wireless Propag. Lett.*, vol. 17, no. 11, pp. 2070–2074, 2018.

[173] M. Chen and G. Tsandoulas, "A wide-band square-waveguide array polarizer," *IEEE Trans. on Antennas and Propag.*, vol. 21, no. 3, pp. 389–391, 1973.

[174] I. Kim, J. M. Kovitz, and Y. Rahmat-Samii, "Enhancing the power capabilities of the stepped septum using an optimized smooth sigmoid profile," *IEEE Antennas and Propag. Mag.*, vol. 56, no. 5, pp. 16–42, 2014.

[175] C. Shu, J. Wang, S. Hu, Y. Yao, J. Yu, Y. Alfadhl, and X. Chen, "A wideband dual-circular-polarization horn antenna for mmwave wireless communications," *IEEE Antennas and Wireless Propag. Lett.*, vol. 18, no. 9, pp. 1726–1730, 2019.

[176] Y. Huang, J. Geng, R. Jin, X. Liang, X. Bai, X. Zhu, and C. Zhang, "A novel compact circularly polarized horn antenna," in *2014 IEEE Antennas and Propagation Society International Symposium (APSURSI)*, 2014, pp. 43–44.

[177] Z. Jia, F. Liu, X. Jiang, and L. Wang, "Engineering lattice metamaterials for extreme property, programmability, and multifunctionality," *J. Appl. Phys.*, vol. 127, no. 15, p. 150901, 04 2020. [Online]. Available: https://doi.org/10.1063/5.0004724

[178] K.-F. Hung and Y.-C. Lin, "Novel broadband circularly polarized cavity-backed aperture antenna with traveling wave excitation," *IEEE Trans. Antennas Propag.*, vol. 58, no. 1, pp. 35–42, 2010.